Title

Noble gas (He-Ne-Ar) and stable isotope (C-N-O) constraints on volatile sources at convergent and divergent plate boundaries with examples from Indonesia, Iceland and the East African Rift System

Author

Halldorsson, Saemundur A.

Publication Date

2014

UNIVERSITY OF CALIFORNIA, SAN DIEGO

Noble gas (He-Ne-Ar) and stable isotope (C-N-O) constraints on volatile sources at convergent and divergent plate boundaries with examples from Indonesia, Iceland and the East African Rift System

A dissertation submitted in partial satisfaction of the
requirements for the degree Doctor of Philosophy

in

Earth Sciences

by

Saemundur A. Halldorsson

Committee in Charge:

David R. Hilton, Chair
Paterno R. Castillo
James M.D. Day
Barry B. Hanan
James W. Hawkins
Mark H. Thiemens

2014

The Dissertation of Saemundur Ari Halldorsson is approved, and it is acceptable in quality and in form for publication on microfilm and electronically:

Chair

University of California, San Diego

2014

DEDICATION

In memory of my dear friend, Davíð Örn Arnarsson (11.17.1980–11.17.2012) who was instrumental in sparking my interest in the great wonders of Mother Earth.

TABLE OF CONTENTS

LIST OF FIGURES

LIST OF TABLES

SM = See Supplementary Material

ACKNOWLEDGMENTS

First of all, I would like to thank my advisor, **David Hilton**, for his guidance during the course of my PhD during the last five years. David's enthusiasm has been and continues to be the source of enormous motivation and inspiration, and has greatly influenced my scientific approach and thoughts in general. Not only did David open his laboratory to me, but he also gave my the opportunity to be involved in many exciting projects, and exposed me to the many sides of geochemistry by sharing with me his enormous knowledge of the field. In addition, he gave me the opportunity to conduct fieldwork in geologically exciting regions of the world, and provided the funding necessary for me to maintain focus during the last five years and complete this dissertation. Thanks Dave, for always being there for me.

His laboratory, the **Fluids and Volatiles Laboratory,** has been a most pleasant work environment during the last five years. I am forever thankful to Peter Barry, Evelyn Füri, and Doshik Hahm, for getting me started and training me in the laboratory, as well as teaching me the skills needed in a volatile laboratory. I am particularly grateful to Peter Barry for his close friendship and for always being there to answer my questions. Keith Blackmon was instrumental in making things work in the lab during my final experiments during the last two years by providing tremendous help in addition to being extraordinary company. I am also very grateful to Bruce Deck for his wealth of information and his willingness to supply me with all kinds of lab-related assistance throughout the last five years. Larry Finnen also shared his wisdom in the understanding of mass spectrometers.

I would like to thank my **committee members** Pat Castillo, James Day, Jim Hawkins, Mark Thiemens, and Barry Hanan for their constructive comments on my thesis and their helpful insights during our various meetings over the last few years. I am particulary grateful to Pat Castillo and James Day for numerous science-related conversations and to Mark Thiemens for opening up his lab to me, and introducing me to its members. In this respect, Subrata Chakraborty has been an exceptional co-worker and a good friend.

Many thanks to all my **co-authors** for their contributions to the work presented in this dissertation; thanks to Val Troll, Toby Fischer, Paolo Scarsi, Tsegaye Abebe, Jens Hopp, Subrata Chakraborty, Peter Barry, Evelyn Füri and Karl Grönvold, for their valuable comments and suggestions which helped improve the quality of this work.

During **fieldwork** conducted to collect samples for the work presented in this dissertation, I had the pleasure of interaction with some very inspiring individuals; I would like to thank Karl Grönvold, Evelyn Füri, Toby Fischer, Ken Rubin, and John Sinton for their assistance in the field in Iceland. Val Troll and his team, including Lilly Freda, Esther Jolis, and David Budd. In addition, our translator and fixer, Mas Mahjum deserves special thanks for great times in Indonesia. Finally, Pat Castillo, Paolo Scarsi, Tsegaye Abebe, Tyler Evans, and Justin Kulongoski provided invaluable assistance in a particuarly memorable field expedition to Ethiopia.

The **SIO Graduate and GRD office** staff; Denise Darling, Josh Reeves, Cerise Maue, Becky Burrola, Satomi Saito, Jan Hess, Laura Shaefer, Ricky Greer, Monica Bailey, Janet Matsumoto, Azzure Beale, Anne Cressey, and especially, Adam Petersen and Gilbert Bretado have provided exceptional support over the last five years helping me get everything finished up.

Special thanks for my friends and **co-workers in Iceland**. Karl Grönvold, Níels Óskarsson, and Guðrún Sverrisdóttir helped guide my first steps in this endeavor, both by providing me the latitude to make my own mistakes, as well by making time to answer my innumerable questions. Their motivation and encouragement have been invaluable during my doctoral studies. Ólafur Patrick Ólafsson also deserves special appreciation for his support and help throughout the process.

Also a special thanks to Tim Hecker and Lawrence English for their music which kept me company during long and late hours of writing. Very special thanks to all of my new **friends in San Diego**. Last but not least, I'd like to thank my supportive **family**. I would like to acknowledge my parents for their everlasting support. I thank my sister, Kristbjörg and brother Svanur, in addition to Lena Rós Þórarinsdóttir for coming all the way to San Diego to help us out with the three girls.

I will be forever grateful to my three daughters, Anna Signý, Sigríður, and Svanfríður for bringing enormous joy into my life. Finally, my dearest wife, Berglind María Tómasdóttir, has always suppored my endevours in life, and this dissertation would not have seen the light of day without her. Thank you Berglind for being who you are and for for sharing your energy and enthusiasm!

Chapter II, in full, is a reprint of the material as it appeared in *Chemical Geology*, as Sæmundur Ari Halldórsson, David R. Hilton, Valentin R. Troll, Tobias P. Fischer, 2013. Resolving volatile sources along the western Sunda arc, Indonesia. *Chemical Geology*, Volume 339, Pages 263-282. doi.org/10.1016/j.chemgeo.2012.09.042. The dissertation author was the primary investigator and lead author of this paper and conducted all the analyses presented herein.

Chapter III has been submitted, in full, for publication to *Geophysical Research Letters* 2014, Sæmundur Ari Halldórsson, David R. Hilton, Paolo Scarsi, Tsegaye Abebe and Jens Hopp, 2014. A common mantle plume source beneath the entire East African Rift System revealed by coupled helium-neon isotope systematics. The dissertation author was the primary investigator and lead author of this paper and conducted all the analyses presented herein.

VITA

2001-2004	B.Sc. Geology, University of Iceland
2005-2007	M.Sc. Geology, University of Iceland
2005-2007	Teaching Assistant, University of Iceland
2007-2008	Research Fellow, Nordic Volcanological Center, University of Iceland
2008-2014	Graduate Research Assistant, Scripps Institution of Oceanography, University of Californa, San Diego
2010-2013	Teaching Assistant, Scripps Institution of Oceanography, University of Californa, San Diego
2014	Ph.D. Earth Sciences, Scripps Institution of Oceanography, University of Californa, San Diego

PUBLICATIONS

Sæmundur Ari Halldórsson, Niels Óskarsson, Karl Grönvold, Gylfi Sigurðsson, Guðrun Sverrisdótttir and Sigurður Steinþórsson, 2008. Isotope-heterogeneity of the Thjorsa lava – implications for mantle sources and crustal processes within the Eastern Rift Zone, Iceland. *Chemical Geology*, Volume 255, Issues 3-4, Pages 305-316. doi:10.1016/j.chemgeo.2008.06.050.

Evelyn Füri, David R. Hilton, **Sæmundur Ari Halldórsson**, Peter H. Barry, Doshik Hahm, Tobias P. Fischer and Karl Grönvold, 2010. Apparent decoupling of the He and Ne isotope systematics of the Icelandic mantle: The role of He depletion, melt mixing, degassing fractionation and air interaction. *Geochemica Cosmochimica Acta*, Volume 74, Issues 11, Pages 3307-3332. doi:10.1016/j.gca.2010.03.023.

David R. Hilton, **Sæmundur Ari Halldórsson**, Peter H. Barry, Tobias P. Fischer, J. Maarten de Moor, Carlos J. Ramirez, Fredrick Mangasini and Paolo Scarsi, 2011. Helium Isotopes at Rungwe Volcanic Province, Tanzania and the Origin of East African Plateaux. *Geophysical Research Letters* Volume 38, L21304, doi:10.1029/2011GL049589.

Peter H. Barry, David R. Hilton, **Sæmundur Ari Halldórsson**, Doshik Hahm and Kurt Marti, 2012. High precision nitrogen isotope measurements in oceanic basalts using a static triple collection noble gas mass spectrometer. *Geochem. Geophys. Geosyst.*, 13, Q01019, doi:10.1029/2011GC003878.

Halim Mutlu, Nilgün Güleç, David R. Hilton, Harun Aydın, **Sæmundur Ari Halldórsson**, 2012. Spatial variations in gas and stable isotope compositions of thermal fluids around Lake Van: implications for crust-mantle dynamics in Eastern Turkey. *Chemical Geology*, Volume 300-301, Pages 165-176. doi:10.1016/j.chemgeo.2012.01.026.

Sæmundur Ari Halldórsson, David R. Hilton, Valentin R. Troll, Tobias P. Fischer, 2013. Resolving volatile sources along the western Sunda arc, Indonesia. *Chemical Geology*, Volume 339, Pages 263-282. doi.org/10.1016/j.chemgeo.2012.09.042.

Peter H. Barry, David R. Hilton, Evelyn Füri, **Sæmundur Ari Halldórsson** and Karl Grönvold, 2014. Carbon isotope and abundance systematics of Icelandic geothermal gases, fluids and subglacial basalts with implications for mantle plume-related CO_2 fluxes. (accepted for publication in *Geochemica Cosmochimica Acta).*

Sæmundur Ari Halldórsson, David R. Hilton, Paolo Scarsi, Tsegaye Abebe and Jens Hopp, 2014. A common mantle plume source beneath the entire East African Rift System revealed by coupled helium-neon systematics. (accepted for publication in *Geophysical Research Letters).*

ABSTRACT OF THE DISSERTATION

Noble gas (He-Ne-Ar) and stable isotope (C-N-O) constraints on volatile sources at convergent and divergent plate boundaries with examples from Indonesia, Iceland and the East African Rift System

by

Saemundur A. Halldorsson

Doctor of Philosophy in Earth Sciences

University of California, San Diego, 2014

Professor David R. Hilton, Chair

Studies of volatile elements and their isotopes have provided fundamental constraints on the formation and evolutionary history of the many diverse chemical reservoirs that together form the primary building blocks of planet Earth. This largely stems from significant differences in volatile abundances and isotopic characteristics of Earth's dynamically evolving reservoirs, which are prone to modifications following the transfer of volatiles between them. In this

dissertation, I discuss how different volatile sources in the solid Earth can be resolved by means of a combined noble gas and stable isotope approach. I investigate different volatile source regions in the silicate Earth, and the transfer of volatiles from source regions towards the exterior of Earth in various tectonic settings. These settings include the western Sunda arc, Indonesia, as an example of a divergent plate boundary, in addition to two prominent plume-influenced divergent plate boundaries; the East African Rift System (EARS) and Iceland.

Chapter I is intended to provide a general introduction to the use of noble gas and stable isotopes as geochemical tracers, with particular emphasis on their utilization in the elucidation of processes, timescales and source-specific features in the solid Earth. Following this overview, we discuss the main objectives of the various studies of which this dissertation consists.

Chapter II examines the combined He-CO_2-N_2 abundance and isotope systematics of geothermal fluids and gases from volcanic centers along the western Sunda arc, Indonesia. We assess controls on volatile provenance in this major subduction system by resolving volatiles associated with the sub-arc mantle, that includes the subducting slab and mantle wedge, from inputs derived from the over-riding arc crust.

Chapter III describes a combined He-Ne-Ar isotope study of mantle-derived xenoliths and lavas from different segments of the EARS. This coupled approach provides a powerful tool with which to identify volatile provenance from the deep mantle versus shallow lithospheric sources, which allows for a unique investigation of the number of plume sources located in the East African mantle, and the ultimate source of melts being supplied to the different segments of the EARS.

Chapter IV is a detailed study of noble gases and the stable isotopes of carbon and nitrogen trapped in fluid inclusions of mantle-derived xenoliths from the EARS. In considering their coupled systematics, we evaluate a number of mantle/crustal features controlling their elemental and isotope characteristics, and separate the various sources contributing to the volatile components trapped in the fluid inclusions.

Chapter V focuses on the N_2 isotope and abundance systematics of subglacially formed basalts from the Iceland hotspot. After characterization of the nitrogen elemental and isotopic signals of the Iceland mantle plume, we investigate relationships with other isotope and relative abundance systematics in order to discern nitrogen characteristics of the mantle source underlying one of Earth's most prominent hotspots.

Finally, Chapter VI provides concluding remarks on these studies and discusses some future prospects and ways of addressing outstanding questions by, for example, further chemical and isotope characterization of the same sample suite discussed in this dissertation.

Chapter I: Introduction

Major volatiles, such as CO_2 and H_2O, play a fundamental role in initiating melt generation in the mantle but also in governing several physical properties of erupted lavas at the surface (Holloway and Jakobsson, 1986; Dasgupta & Hirschmann, 2010). Mantle-derived melts also contain several trace (rare) gases, most notably nitrogen (N_2) and the noble gases (He, Ne, Ar, Kr, Xe, Rn). Upon transfer from a mantle source reservoir towards the surface, mantle-derived volatiles are exsolved from a melt in a manner described by their solubility in a melt phase leading to partitioning into a vapor phase: this process is regarded as the major factor controlling the transport of volatiles on the terrestrial planets (e.g., Holloway and Jakobsson, 1986). Outgassing of trace gases, such as the noble gases, generally requires the loss of other (major) volatile components which subsequently act as carriers for the noble gases from the mantle source region and to Earth's surface (Porcelli & Ballentine, 2002). At the surface, mantle-derived volatiles are mainly released in passive and/or active gas manifestations or following magmatic activity, either directly or indirectly, in volcanic regions on Earth. In addition, a significant fraction of mantle-derived volatiles can also be transported as dissolved constituents in groundwater and geothermal systems (e.g., Kulongoski & Hilton, 2011).

These rare gases, in particular the noble gases, are powerful geochemical tools for constraining various geological processes that occur during volatile transfer (e.g., Hilton and Porcelli, 2014). Significantly, noble gases provide information not readily available from major element chemistry, due to inherent complexities in these other systems. Thus, noble gas geochemistry has been of enormous use in understanding the evolution of Earth (Allégre, 2008; Ozima & Podosek, 2002). Moreover, the integration of major and minor element chemistry, their isotopes, as well as relative abundance ratios, enables assessment of the origin and interaction history of volatiles between chemical reservoirs located in Earth's interior and exterior reservoirs, as well as their evolution over time. Notably, this approach often allows for the identification of intrinsic mantle characteristics, which can be otherwise obscured due to modifications that occur during melt mixing, degassing, and shallow-level contamination.

To a certain extent, the use of noble gases as a means to constrain processes and timescales in the solid Earth is analogous to the use of lithophile trace elements to constrain processes in igneous petrology. As with common lithophile trace elements in mantle melts, the noble gases have relatively low abundances and are highly incompatible in silicate minerals. However, unlike lithophile trace elements, the noble gases have near-perfect chemical inertness and thus do not form any compounds in nature. Furthermore, the noble gases have a very large isotopic contrast between most major chemical reservoirs on Earth (Ozima & Podosek, 2002; Hilton and Porcelli, 2014) - significantly greater relative to variations provided by the relatively few lithophile elements exploited in a similar manner. In the following discussion, we will provide a general overview of the key isotope tracers utilized in this dissertation to resolve mantle volatile sources, starting with the three light noble gases: He, Ne and Ar.

Helium has two stable isotopes. Its heavier isotope, ^{4}He, is the stable radiogenic daughter product of the radioactive decay of U- and Th-series elements. Significant enrichment in U and Th in the continental crust, relative to the mantle, has thus resulted in the accumulation of significant amounts of ^{4}He with time. In contrast, ^{3}He has been trapped in the terrestrial mantle since its formation and is thus regarded as primordial in origin (Lupton & Craig, 1975; Ozima & Podosek, 2002). The isotope ^{3}He is also generated by bombardment of highly energetic charged particles, known as cosmic rays, in any material exposed to their impact, thus providing a powerful way of determining exposure ages of surface features (Kurz, 1986; Cherling & Craig, 1994; Dunai, 2010). Additionally, ^{3}He can be created by spallation reactions involving Li-rich material in Earth's crust, i.e., via the nuclear reaction: $^{6}\mathrm{Li}(n,\alpha)\rightarrow{}^{3}\mathrm{H}(\beta)\rightarrow{}^{3}\mathrm{He}$ (Ozima & Podosek, 2002). However, relative to the primordial ^{3}He currently degassing from Earth's mantle in volcanically- and tectonically-active regions, these processes do not significantly modify intrinsic ^{3}He characteristics of degassing mantle-volatiles.

Helium isotopes are traditionally reported using the ratio of ^{3}He over ^{4}He (R) relative to the present atmospheric ^{3}He/^{4}He (R_A: 1.4×10^{-6}), i.e., R_{sample}/R_{Air}. Due to the fact that He is not gravitationally bound to Earth, all He brought to Earth's surface by magmatism is eventually lost to space. Therefore, adopting the present atmospheric ratio as the basis for normalization of measured ratios is an elegant way of reporting He isotope variations, as it can be safely assumed that the helium content and isotope ratios of Earth’s atmosphere have remained essentially invariable over recent time, although the subject has been the focus of several inconclusive studies (e.g., Sano et al., 2010; Lupton & Evans, 2004, 2013 Brennwald et al., 2013).

Because of the accumulation of ^{4}He over time, the U- and Th-rich continental material has R/R_A values lower than those of air, and generally varies between 0.01 to 0.1 R_A (O'Nions and Oxburgh, 1988). In contrast, Earth’s upper-mantle, as sampled at mid-ocean ridges, was shown in the mid-1970s to display values both significantly higher than air, but also values that are somewhat uniform (Lupton & Craig, 1975; Craig & Lupton, 1976). Extensive studies on oceanic basalts have now shown that mid-ocean ridges, uninfluenced by any input of mantle plume material, display ^{3}He/^{4}He values between 7 and 9 R_A (see reviews by Graham, 2002; Moreira, 2013). These studies have also shown that mantle-derived volatiles from oceanic, but also mid-plate, continental hot-spots are marked by R/R_A values that significantly exceed values characteristic of mid-ocean ridges. For example, three of the most prominent hot-spots on Earth, Galapagos, Iceland, and Hawaii show values as high as $38R_A$ (Hilton et al., 1999). Furthermore, the proto-Iceland mantle plume, as sampled in 60 to 62-million year-old volcanic rocks from Baffin Island and West Greenland, reaches values more than five times higher than values commonly observed along mid-ocean ridges – up to $50R_A$ (Stuart et al., 2003). Such high ratios of the primordial to radiogenic He-isotopes are regarded as a key argument supporting the existence and survival of a reservoir deep within Earth, which has remained largely un-degassed since its accretion (e.g., Jackson et al., 2010; White, 2010). Recent experimental work has also highlighted the possible role of Earth's core, particularly the early core, in contributing He to the overlying mantle (Porcelli & Halliday, 2001; Bouhifd et al., 2013), presumably by means of a diffusion-related mechanism (Hayden & Watson, 2007).

Neon has three stable isotopes which, when combined, can be used in a powerful manner to identify primordial volatile components in Earth's mantle, and their interactions with nucleogenic and atmospheric neon components (Ozmia and Podosek, 2002). The two stable isotopes – ^{20}Ne and ^{22}Ne – are predominantly primordial in origin, and thus represent trapped primordial volatile components of Earth's primary building blocks. In contrast, ^{21}Ne is predominantly a nucleogenic-produced isotope – generated by the interaction of α and n particles on ^{18}O, and by n and α particles interacting with ^{24}Mg. It should also be noted that ^{21}Ne and ^{22}Ne can also be produced at Earth's surface by cosmic spallation reactions on Mg, Na, Si and Al, and by α and n particle reactions on ^{18}O and ^{19}F (e.g., Dunai, 2010). These are, however, generally insignificant in studies of mantle-derived material and, if present, can be largely avoided by means of vacuum-crushing.

Neon isotopes are traditionally displayed using a three isotope neon plot, i.e., a plot of ^{21}Ne/^{22}Ne versus ^{20}Ne/^{22}Ne (**Figure 1**). Air is a ubiquitous feature of materials erupted onto Earth's surface and largely unavoidable. Consequently, most mantle-derived material form a trajectory intersecting at the air value (^{20}Ne/^{22}Ne = 9.8; ^{21}Ne/^{22}Ne = 0.029), as a reflection of different degrees of contamination of such material with air-derived Ne.

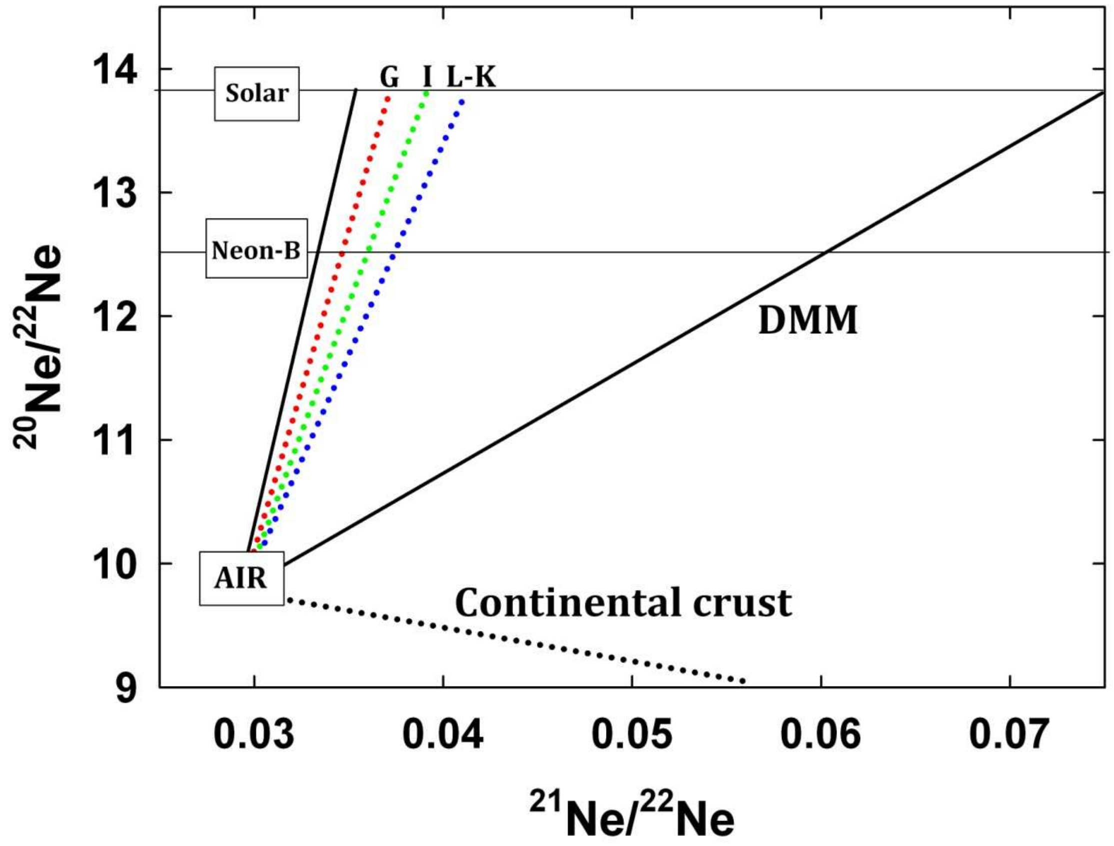

Figure I.1: Three isotope neon plot. The upper horizontal line represents the solar $^{20}Ne/^{22}Ne$ ratio (Benkert et al., 1993), the lower horizontal represents the $^{20}Ne/^{22}Ne$ ratio in the Neon-B meteorite component (e.g., Black, 1972; Trieloff et al., 2000). G=Galapago (red); I= Iceland (green); L-K Lohii-Kilauea (blue). The two solid black lines indicate the solar (left) and DMM trends. Notably, all trends intersect at air ($^{20}Ne/^{22}Ne$ = 9.8, $^{21}Ne/^{22}Ne$ = 0.029). Modified from Jackson et al., (2009).

Thus, the measured Ne-isotope values likely represent a binary mixture between air and different mantle end-members, allowing for straightforward extrapolation to air-free values (e.g., Moreira et al., 1995). However, the end-member ($^{20}Ne/^{22}Ne$) value for the most primitive Ne-component found in Earth's mantle (i.e., Ne captured during its formation) is still debated, with two possibilities prevailing: (i) solar wind compositions, or (ii) Neon-B-like (i.e., compositions identical to those in primitive gas-rich meteorites). In any case, and irrespective of the primitive mantle end-member, the utility of Ne is primarily based on the large contrast associated with different mantle reservoirs (Moreira, 2013; Hilton & Porcelli, 2014). For example, samples from oceanic islands, such as Galapagos, Iceland, and Hawaii (Loihi-Kilauea) generally have much steeper trajectories relative to depleted MORB mantle (DMM) – i.e., for a given ^{21}Ne/^{22}Ne, oceanic island basalts (OIB) samples have a higher ^{20}Ne/^{22}Ne ratio than samples associated with DMM (**Figure 1**) – consistent with the idea that the OIB source has maintained a higher proportion of primordial (solar) gas components so that over time nucleogenic ^{21}Ne in-growth has had less effect on the final ^{20}Ne/^{22}Ne ratio relative to the DMM reservoir (e.g., Sarda et al., 1988; Honda et al., 1991).

Argon has three stable isotopes: ^{40}Ar, ^{38}Ar and ^{36}Ar, with the two latter being stable, whereas the heaviest isotope, ^{40}Ar, represents a radiogenic daughter isotope that has accumulated in the Earth system as a result of the decay of ^{40}K through time. Argon isotope ratios involving the two stable isotopes of ^{38}Ar and ^{36}Ar, have, for the most part, been mostly disregarded in terrestrial mantle studies. However, with the advent of multi-collector noble gas mass spectrometers, this ratio can now be analyzed with far better precision than before, potentially yielding insight into primordial volatile heterogeneities inherited from the early Earth, such as the presence of a possible solar ^{38}Ar/^{36}Ar in the mantle, or lack thereof (Raquin and Moreira, 2009; Moreira, 2013). Largely due to the accumulation of ^{40}Ar over Earth history, the K-Ar isotope system (i.e. the ^{40}Ar/^{36}Ar ratio) has proven most useful for constraining the timing and extent of degassing on Earth since its formation, and the subsequent evolution of Earth's atmosphere (Allégre, 2008). As ^{36}Ar represents a primordial isotope, the ^{40}Ar/^{36}Ar ratio bears witness to the time integrated K/Ar ratio of a given chemical reservoir. For example, an extreme ^{40}Ar/^{36}Ar in the DMM reservoir (as high as 40,000: Burnard et al., 1997; Graham, 2002), relative to the uniform ratio that characterizes the modern atmosphere, is evidence of an ancient degassing process from the solid Earth. Additionally, the uniform atmospheric ratio of 298.6 (Lee et al., 2006) is much higher than the initial ratio of the solar system (<1), consistent with the notion that Ar in the atmosphere is predominantly radiogenic and that degassing must have occurred after Earth accreted (Ozima and Podosek, 2002; Allégre, 2008; Moreira, 2013).

In a manner analogous to He and Ne isotopes, Ar isotopes are generally thought to have preserved different ^{40}Ar/^{36}Ar values among reservoirs within the solid Earth (e.g., Allégre, 2008). Thus, considerable efforts have been made to use Ar isotopes to identify different mantle sources. The lower-mantle source, as sampled at oceanic islands, has been shown to display ^{40}Ar/^{36}Ar ratios that are somewhat closer to the atmospheric value relative to the same ratios of the DMM reservoir. For example, the Iceland mantle source appears to have ^{40}Ar/^{36}Ar ratios no higher than ~6000 (Mukhopadhyay, 2012). Assuming that the Iceland mantle source represents to some extent the volatile characteristics of the lower-mantle, such low ratios are consistent with the idea that the lower mantle has preserved a more primitive Ar isotope composition relative to the upper-mantle. Alternatively, these low ratios, relative to DMM, could indicate that Iceland mantle source has been influenced by contributions from seawater-derived argon that was subducted into the deep mantle (Holland & Ballentine, 2006). However, no consensus has been reached on whether this signature has any bearing on source-specific features of the lower mantle, particularly since ^{40}Ar/^{36}Ar closer to the atmospheric value could also reflect atmospheric contamination associated with shallow eruption features of oceanic island basalts (Graham, 2002; Moreira, 2013).

Finally, a particularly powerful approach favored by noble gas geochemists is to combine noble gas relative abundances as they can reveal important information about source features as well as the mode and extent of degassing. For example, degassing can be constrained by considering the ^{4}He/^{40}Ar* ratio (where * is air-free, radiogenic Ar). These ratios will be thoroughly discussed throughout this dissertation. In general, samples with ^{4}He/^{40}Ar* above the estimated production ratio for Earth's mantle (between ca. 2 to 5) can be considered more degassed relative to samples yielding $^{4}He/^{40}Ar^{*}$ ratios closer to the production ratio (Hilton & Porcelli, 2014).

Carbon has two stable isotopes, ^{12}C and ^{13}C, and one radioactive isotope, ^{14}C, with a half-life of ~5730 years. The ratio of the two stable isotopes is generally reported relative to a Vienna Pee Dee belemnite (VPDB) limestone and is expressed in delta notation as $\delta^{13}C_{PDB}$ (Sharp, 2006). Unlike the noble gases, carbon is chemically reactive and forms a number of carbon-bearing species at different levels in Earth's mantle and in the atmosphere. For example, as the solubility of carbon in iron-rich metal is considerable, it has been proposed that carbon may form stable compounds (e.g., cohenite) in the core. However, the carbon content of Earth's core is not well-constrained (Ni & Keppler, 2013; Wood et al., 2013). The reduced lower mantle (660-2960 km) probably contains a number of possible major iron carbide minerals – whose population may expand greatly with depth (Dasgupta & Hirschmann, 2010; Dasgupta, 2013): this could also apply to Earth's transition zone (410-660 km). However, in the oxidized upper-mantle, carbon dioxide prevails and constitutes the second most abundant major volatile species in the upper-mantle after H_2O, and is thus the most common form of carbon in mantle fluids sampled at Earth's surface. Carbon also forms part of the diamond-bearing mantle beneath the continents (Dasgupta, 2013).

Due to its highly incompatible behavior in basaltic melts, CO_2 strongly partitions into a melt phase, formed during melt extraction (Jambon, 1994). Indeed, during magmatic processes, CO_2 is generally thought to behave like Nb – a highly incompatible lithophile element (e.g., Saal et al., 2002). Thus, CO_2/Nb is an excellent indicator of mantle source characteristics but also degassing-induced CO_2 loss. Furthermore, due to its low solubility in basaltic melts, the CO_2-rich vapor phase readily exsolves during decompression and forms a carrier phase for all other mantle volatiles (Holloway and Jakobsson, 1986). The progressive loss of volatiles upon transfer from the mantle source region towards the surface and during magma emplacement leads to C-isotopic fractionation, so that residual CO_2 in magma becomes progressively depleted in ^{13}C as degassing progresses (Javoy et al. 1978; Mattey, 1991). In contrast to He and Ne, there appears to be no clear isotopic distinction between various mantle reservoirs, with the DMM reservoir having a mean $\delta^{13}C$ of about -5‰ ± 1 ‰ (Marty and Zimmermann, 1999; Cartigny, 2005) which largely overlaps reported estimates for the OIB source (-6 to -3‰: Exley et al., 1986; Gerlach and Taylor, 1990; Hilton et al., 1997; Aubaud et al., 2005; Aubaud et al., 2006; Barry et al., 2014). In part, this could be a reflection of the physiochemical processes governing the isotopic fractionation of CO_2 upon degassing, such that the carbon isotope source specific characteristics have been extensively modified and are therefore no longer diagnostic of their source (e.g., Mattey, 1991).

Nitrogen has two stable isotopes, ^{14}N and ^{15}N, with the ratios between them reported relative to ambient air (i.e., $\delta^{15}N_{AIR}$: Sharp, 2006). Although a major component of Earth's atmosphere, nitrogen is found only at relatively low abundances in the solid Earth (i.e., ppm-level or sub-ppm-level: Cartigny & Marty, 2013). Recent experimental work has confirmed the slightly-to-moderately siderophile behavior of nitrogen at high pressure and temperature, and has demonstrated relatively high partitioning coefficients of nitrogen between metal and silicate, indicating that some nitrogen can be sequestrated in the core (Roskosz et al. 2013). Furthermore, nitrogen appears to have complex speciation in melts under high pressure (Roskosz et al. 2006; Li et al., 2013; Li & Keepler, 2014). For example, nitrides are probably the dominant speciation form of nitrogen under very reducing conditions, similar to those prevailing in the lower mantle, as well as in the lower part of the upper mantle. In contrast, nitrosyl (NO) appears to dominate the nitrogen budget under the more oxidizing conditions of the upper-mantle. Thus, the nitrogen storage capacity of the upper-mantle may have been underestimated, as nitrogen species other than N_2 have been shown to have higher solubility in upper-mantle minerals (Li et al., 2013).

Among mid-ocean ridge basalts, nitrogen (N_2) correlates well with ^{40}Ar, the daughter product of ^{40}K, but not with primordial ^{36}Ar, indicating that the source of mantle nitrogen in the DMM reservoir is tied to the subduction of crustal nitrogen (Marty, 1995; Marty and Humbert, 1997; Marty and Dauphas, 2003; Cartigny & Marty, 2013).

Measurements of δ^{15}N in MORB range from about -10 to +8‰, with a mean value close to -5‰ (e.g., Cartigny & Marty, 2013). Such a mean value is also evident from multiple studies on peridotitic diamonds, indicating that the DMM reservoir has a fairly homogenous composition. However, the nitrogen isotopic composition of Earth's primitive deep-mantle as sampled by OIB is much more controversial than that of the upper-mantle (e.g., Tolstikhin & Marty, 1998; Cartigny and Marty, 2013). Largely based on oxygen isotope constraints, Javoy (1995) proposed that Earth accreted with nitrogen primarily (~70%) derived from enstatite chondrites with a primordial δ^{15}N value as low as ~ -40‰, but that this pristine signature has been progressively diluted as it has interacted with recycled slabs throughout Earth’s history. In order to explain the large nitrogen isotopic contrast between mantle and Earth’s surface, Javoy (1997; 1998) proposed a model invoking heterogeneous accretion of Earth's volatiles in which a late veneer composed of chondritic material, with δ^{15}N values as high as ~ +40‰, supplied about ~30% of Earth’s nitrogen. Mantle degassing would have progressively lowered δ^{15}N of Earth’s surficial reservoirs, whereas recycled slabs would have increased the mantle δ^{15}N value.

Following measurement of highly depleted ^{15}N values in Genesis solar wind samples, Marty (2012) also suggested that a solar N component may be present in Earth’s mantle. However, if the early mantle and/or solar nitrogen component(s) was primarily composed of such depleted nitrogen isotope signatures, the pertinent question arises as to whether this primordial signature may still be preserved in the deep-mantle? Recent studies of deep diamonds show δ^{15}N values that extend to such low values and may bear witness to the survival of this primordial nitrogen in the deep mantle (Palot et al., 2012). Additionally, δ^{15}N values in geothermal gases from the Hengill region in Iceland (Marty et al., 1991) show a large range from -0.5‰ to -10.5‰, consistent with the presence of a nitrogen component that is significantly depleted relative to DMM.

Exley et al. (1986), however, reported that basaltic glasses from Loihi Seamount, Hawaii, had positive $\delta^{15}N$ values and Dauphas and Marty (1999) also measured positive $\delta^{15}N$ values (+ 6.5‰) in deep mantle-derived carbonatites from the Kola Peninsula (380 Ma). Thus, at face value, these latter results are inconsistent with the survival of a relict primordial $\delta^{15}N$ value of ~ -40‰. High $\delta^{15}N$ values (> air) of the deep mantle have gained further support from additional studies. Adopting *in vacuo* crushing techniques, Marty and Dauphas (2003) showed that nitrogen isotopes in OIB glasses have positive values, up to +6 ‰. Marty and Dauphas (2003) noticed that such positive $\delta^{15}N$ values show close association with values of organic matter evident in post-Archean sediments, as well as with values from subduction-related meta-sediments and metamorphosed oceanic crust (Marty and Dauphas, 2003; Halama et al., 2010, 2012). This observation led Marty and Dauphas (2003) to propose that positive $\delta^{15}N$ values in mantle plumes result from recycling of ancient (< Proterozoic) nitrogen from Earth's surface and into the deep mantle by subduction processes.

Oxygen has three stable isotopes: ^{16}O, ^{17}O, and ^{18}O, with the ratios of the heaviest and the lightest isotope (e.g., $^{18}O/^{16}O$) conventionally reported as $\delta^{18}O_{SMOW}$ relative to standard-mean-ocean water (SMOW: Sharp, 2006). The VPDB limestone standard is also used as a standard when oxygen isotopes are reported for carbonate material (i.e., $\delta^{18}O_{PDB}$) – this is commonly adopted in studies on paleoclimate. It should also be noted that oxygen isotope values involving ^{17}O (i.e., $\delta^{17}O$) are not considered in this study. As a primary element in the building blocks of silicates (SiO_4^{4-}), the utility of oxygen isotopes in mantle related studies is primarily based on their sensitivity to fingerprint material which has undergone low-temperature alteration at or near the surface of the solid Earth, but has since been subjected to injection to deeper levels, for example, into the mantle during subduction at divergent plate boundaries (e.g., Taylor & Sheppard, 1986; Eiler, 2001).

The mantle is by far the largest reservoir for oxygen, so any assessment of the oxygen isotopic composition of the mantle is of great importance in determining the isotopic composition of Earth. However, this has not proven a straightforward task and it has been particularly challenging to evaluate the degree of variance in mantle-derived material (Eiler, 2001). Oxygen isotope studies of mantle-derived material underwent significant changes with the advent of laser-based extraction methods, which allowed for much greater precision relative to conventional extraction methods (Sharp, 1990). Basaltic lavas are often affected by input from crustal rocks and hydrothermally altered material (Taylor & Sheppard, 1986), whereas direct mantle-derived samples such as xenoliths, have proven significantly more useful in constraining the oxygen isotopic composition of the mantle. Using laser-based techniques, Mattey et al. (1994), conducted a detailed study of the oxygen isotope composition of mafic mineral separates from a number of mantle peridotite xenoliths, which clearly demonstrated that the mantle is relatively homogeneous in its oxygen isotope composition, with an estimated bulk composition of ~ 5.5 ± 0.4‰. Only a very minor difference (~ 0.5‰) was evident among co-existing mafic minerals (olivine, clino- and ortho-pyroxenes), largely consistent with the expected fractionation between these minerals at mantle temperatures (Matty et al., 1994).

A uniform oxygen isotope composition of the upper-mantle reservoir (DMM) of ~ 5.5 ± 0.4‰ (Mattey et al., 1994) was also confirmed in studies conducted by Harmon and Hoefs (1995), in a compilation of conventional $\delta^{18}O$ data available at that time, and later by Eiler (2001), who compiled high-quality laser-based data only. Such high-quality $\delta^{18}O$ data, analyzed with laser-based methods, have been the subject of a number of studies postulating the occurrence of recycled material in the mantle source regions of oceanic islands and mid-ocean ridge (e.g., Eiler, 2000a; Eiler, 2001; Macpherson et al., 2005; Thirlwall, 2006; Day et al., 2009). Although many oceanic island basalts have mean $\delta^{18}O$ values that are near identical to that of peridotite xenoliths, they often display a significantly greater range of values, both higher and/lower than the canonical DMM value of ~ 5.5‰ (Eiler, 2001; Macpherson et al., 2005; Thirlwall, 2006; Day et al., 2009). In particular, island arc basalts are commonly shifted towards more positive $\delta^{18}O$ values relative to DMM, consistent with the involvement of previously subducted and recycled sedimentary material in their source regions (Eiler et al., 1998; Eiler, 2001; Eiler, 2000b).

From the discussion above, pertaining to the geochemical tracers utilized in this dissertation, it has become evident that elements that exist in more than one oxidation state (e.g., C and N) and form a wide variety of compounds at mantle and crustal conditions, are major constituents of fluids and solids in the solid Earth. Significantly, due to their chemical nature, these elements can be subjected to recycling into the mantle at subduction zones, as they are bound in crustal rocks and marine sediments (Hilton et al., 2002; Marty and Dauphas, 2003). Both carbon and nitrogen appear to be particularly prone to recycling, and several studies have shown that large fractions of these elements enter the mantle, potentially reaching all the way to the deep-mantle (Hilton et al., 2002*)*. In contrast, noble gases, in particular the light noble gases He and Ne, appear not to be recycled into the mantle at subduction zones in any significant amount. In this respect, the concept of the ‘subduction barrier’ was developed to describe the resistance of noble gases to entering the mantle beyond the region of arc magma generation (Staudacher & Allégre, 1988). However, to what extent heavier noble gases are recycled to the (deeper) mantle remains a field of active research and several recent studies have challenged the concept of a ‘subduction barrier’, postulating the return of heavy noble gases through the subduction barrier (Holland & Ballentine, 2006; Kendrick et al., 2011). A recycled origin of the heavy noble gases in the mantle, for example because of their incorporation into hydrous minerals such as serpentinite or amphibole, is a possible solution to the dilemma of Ne, Ar, Kr and Xe in some mantle-dervied material having an isotopic composition very similar to that of the modern atmosphere, as well as containing contributions from radiogenic and solar components (Holland & Ballentine, 2006; Kendrick et al., 2011; Jackson et al., 2013). Furthermore, experimental work has also shown that due to its relatively high solubility in amphibole, He can potentially be transported back into the mantle (Jackson et al., 2013). However, the notable absence of air-like He isotope composition in any mantle-derived material would argue strongly against this possibility.

In this dissertation, we address some of these issues in solid Earth geochemistry by resolving volatile sources at convergent and mantle plume influenced continental and oceanic divergent plate boundaries, using the geochemical tracers listed above. We investigate the origin, transport and behavior of volatiles using a combined noble gas (He-Ne-Ar) and stable isotope (C-N-O) approach, at three different tectonic settings: a) Indonesia, an area of active subduction, b) the East African Rift System, an area of active plume-influenced continental rifting, and c) Iceland, a ridge-centered hotspot.

Chapter II describes the chemical and He-C-N isotope characterization of fumaroles and hydrothermal fluids from the summits and flanks of 19 passively-degassing volcanic centers along the western Sunda arc, Indonesia. Large sections of this arc system, the Sumatra segment in particular, are underlain by thick, Mesozoic continental crust (Hamilton, 1979), composed mainly of granitoids and siliciclastic and carbonate sediments (Hamilton, 1979; Gasparon and Varne, 1995). This unique arc system thus presents a test case of volatile provenance associated with arc volcanism, such as inputs from the over-riding plate versus the sub-arc mantle (subducting slab and mantle wedge). As noted in previous studies of the region (Gasparon and Varne, 1998), a clear-cut resolution between slab-related volatile additions to the mantle source (primary contamination) and shallow-level crustal contamination of magmas en route to the surface (secondary contamination) is not straight-forward, given the chemical and isotopic similarities of incoming sediments on the slab and the arc crust itself. Our approach to the problem lies in applying coupled studies of He, CO_2, and N_2 (isotopes and relative abundances) to resolve upper crustal influences and their potential contribution to arc volcanism. We consider various processes that can occur in the hydrothermal systems which can act to modify intrinsic mantle-source features such as hydrothermal phase separation, calcite precipitation, and degassing. A key finding of this study is that despite the fact that a thick granitic basement underlies large sections of the western Sunda arc, helium isotopes point to the mantle wedge as the principal source of He, with the over-riding crust and associated sediments adding minimal volatiles to volcanic centers. Furthermore, a clear latitudinal effect is apparent in carbon isotope and $CO_2/^3He$ ratios, with higher and more variable values to the north of Sumatra, which we relate to subducted sediment, particularly the Nicobar Fan.

Chapter III examines combined He-Ne-Ar relative abundances and isotopes relationships in mantle-derived xenoliths and lavas from different segments of the East Africa Rift System. A remarkable finding by Craig and Lupton (1977) was that helium isotope ratios in geothermal fluids from the Ethiopian Rift displayed He isotope values exceeding the range of values obtained from normal Mid-Ocean Ridge basalts. They noted that such high values approached those of fumarolic gas from the Kilauea Volcano in Hawaii, which had the highest $^3He/^4He$ ratios at the time. Later work by Marty et al. (1996) and by Scarsi and Craig (1996) confirmed such ratios using mineral separates and ascribed them to a lower mantle component that contributed to petrogenesis throughout Ethiopia. Notably, such high helium isotope values were firmly confined to the Ethiopian rift until Hilton et al. (2011) reported helium isotope ratios greater than the canonical DMM value in Rungwe Volcanic Province (RVP), at the southern tip of the propagating western rift of the Kenya Dome. However, the case was made that He isotopes alone cannot distinguish between the presence of a single plume source, sampled via multiple upwellings, or different mantle plumes that could supply magma individually to each segment of the EARS. The key aim of this study was to conduct measurements of He-Ne-Ar isotopes, to test whether lavas and xenoliths erupted along different segments of the EARS possessed the same unique coupled He-Ne isotopic signature that could identify a single mantle plume source, or if differences between various rift segments reflect individual plumes which have evolved different He-Ne characteristics over time. We show that lavas and xenoliths from the EARS have distinct Ne-isotope anomalies, and a number of samples associated with the two segments of the Kenya rifts plot between DMM and trajectories defined by many oceanic islands on a neon three-isotope plot. Notably, a number of samples associated with the Ethiopian Rift overlap with OIB trajectories, suggesting the presence of a solar-derived Ne component in the East African mantle source. We show that coupled He-Ne systematics can be explained by admixture between a single mantle plume source, common to the entire EARS, and either a DMM or sub-continental lithospheric mantle (SCLM) source. Additionally, we show that the plume source is characterized by low $^{3}He/^{22}Ne_{S}$ ratios, a feature characteristic of oceanic hotspots such as Iceland. We propose that the origin of these unique signatures is the African Superplume (Hansen et al., 2012), which influences magmatism throughout eastern Africa, with the Ethiopia and Kenya domes representing two different heads of the same mantle plume source.

Chapter IV examines the He, CO_2, N_2 and Ar (isotopes and relative abundances) characteristics of trapped volatile components situated within fluid inclusions of mantle xenoliths from nine localities along the strike of the EARS. Several studies on xenolith suites from the EARS (e.g., Rudnick et al. 1993; Baker et al. 1998; Dawson, 2002; Aulbach et al., 2011; Beccaluva et al. 2011), have ascribed their elemental and isotopic composition to mantle metasomatism, i.e., incompatible element enrichment of a normal peridotite mantle which results from the invasion of a mantle fluid, and the associated influx of volatile-rich silicate and/or carbonate melts to the SCLM. For example, clinopyroxene from Olmani in southern Tanzania is consistent with derivation from reactions between peridotite and carbonate melts (Rudnick et al. 1993). However, the origin of the metasomatic melts remains somewhat speculative and is largely based on comparison with experimental melts rather than natural melts. The primary aim of this study is to identify the various sources contributing to the volatile components trapped in the fluid inclusions and to evaluate a number of mantle/crustal factors controlling their elemental and isotope characteristics. After considering processes capable of modifying intrinsic mantle characteristics, we show that the trapped volatile components have compositions consistent with enrichment of the East African SCLM by CO_2-rich mantle fluids from subducted carbonatitic material. Notably, the CO_2 (and N_2) enrichments are associated with low $\delta^{18}O$ values of crystals hosting the fluid inclusions. Such observations reinforce the link between metasomatic fluids and subducted slab fluids. Xenoliths with high $^3He/^4He$ ratios from northern Ethiopia and the Red Sea are also associated with recycled CO_2-rich mantle fluids (i.e., carbonate-melts) and positive $\delta^{15}N$ values, implying that the deep-seated African Superplume supplies the EARS with a mixture of primordial and recycled volatiles. The occurrence of recycled volatiles in the East African SCLM is thus widespread and must be associated with a large-scale mantle process (i.e., the African Superplume) currently supplying mantle material to the EARS. Finally, a key observation is the fact that trapped volatile components, pointing to recycled material, are predominantly found in fluid inclusions from pyroxenite xenoliths, and we discuss the potential link between the formation of a pyroxenite-hybrid mantle source and recycled volatiles on magma genesis along the EARS.

Chapter V focuses on the N_2 systematics, involving both isotope and relative abundance characteristics, of subglacial basaltic glasses from Iceland. We report new nitrogen data for 43 subglacial basaltic glasses collected from the neovolcanic zones of Iceland, a key locality in studies of mantle plume sources and crust-mantle processes. We also report new helium and argon data from new samples to combine with previously published noble gas (He-Ne-Ar: Füri et al., 2010) and carbon characteristics (Barry et al., 2014) on the same sample suite, allowing elemental ratios (e.g., $N_2/^{40}Ar^*$) to be calculated for individual samples. Considerable uncertainties remain regarding the origins and evolutionary history of nitrogen in the mantle (Marty, 2012; Cartigny & Marty, 2013), particularly the deep-mantle. For the most part, the current discussion is centered on a possible relict primordial signature derived from enstatite chondrites with a $\delta^{15}N$ value as low as ~ -40‰ (Javoy, 1995), and/or a possible solar N component (Marty, 2012). On the other hand, others have postulated the importance of dense subducted slabs, which submerge into the deep mantle, in controlling its nitrogen isotopic composition (Marty and Dauphas, 2003). By carefully evaluating a large set of subglacial basalts from Iceland, we aim to better constrain nitrogen elemental and isotopic signals of the Iceland mantle plume, as they may provide a new perspective into the volatile composition of the deep mantle. Our results demonstrate that subglacial glasses show a wide range in $\delta^{15}N$ values, from -2.91 to +11.96‰. In addition, we identified a number of processes that have extensively modified original mantle source compositions. In particular, we note that samples subjected to a large loss of gas are highly susceptible to shallow-level crustal interaction. However, the combined use of $^{4}He/^{40}Ar^{*}$, $N_2/^{40}Ar^{*}$, and $\delta^{15}N$ allows us to identify (and remove) samples potentially affected by degassing-induced fractionation, air interaction and/or crustal contamination. Furthermore, by investigating simple binary mixing scenarios involving both the relative abundance systematics and nitrogen isotopes (i.e., $N_2/^{3}He$- $N_2/^{40}Ar^{*}$-$\delta^{15}N$ systematics), we show that our filtered dataset is consistent with binary mixing involving a high and heterogeneous $\delta^{15}N$ end-member and the DMM reservoir. In addition, we compare our new $\delta^{15}N$ dataset with recent data from the Reykjanes Ridge and consider coupled He-N isotope systematics. A key finding of this study is that recycled and heterogeneous N-component(s) have been integrated into and/or entrained by the Iceland plume source. Finally, by comparison with available radiogenic isotopes from Iceland, and by consideration of extreme $N_2/^{40}Ar^{*}$ ratios, in addition to the very high $\delta^{15}N$ values that characterize Icelandic melts, we are able to offer a possible age of the recycled material entrained by the Iceland plume.

Chapter VI is the final chapter of the dissertation. It summarizes the main findings and conclusions of each study and addresses some possible directions of future research, based on the findings and uncertainties in Chapters II to V.

Chapter II: Resolving volatile sources along the western Sunda arc, Indonesia

Chemical Geology 339 (2013) 263–282

Contents lists available at SciVerse ScienceDirect

Chemical Geology

journal homepage: www.elsevier.com/locate/chemgeo

Resolving volatile sources along the western Sunda arc, Indonesia

Sæmundur A. Halldórsson [a,*], David R. Hilton [a], Valentin R. Troll [b], Tobias P. Fischer [c]

[a] Fluids and Volatiles Laboratory, Scripps Institution of Oceanography, University of California, San Diego, La Jolla, CA 92093-0244, USA
[b] Department of Earth Sciences, CEMPEG, Uppsala University, Villavägen 16, 75236, Sweden
[c] Department of Earth and Planetary Sciences, University of New Mexico, Albuquerque, NM 87131-1116, USA

ARTICLE INFO

Article history:
Accepted 15 September 2012
Available online 4 October 2012

Keywords:
Subduction zones
Indonesia
Volatile recycling
Helium isotopes
Carbon isotopes
Nitrogen isotopes

ABSTRACT

We present the chemical and isotope (He–C–N) characterization of active fumaroles and hydrothermal gases and waters from the summits and flanks of 19 volcanic centers along the western Sunda arc, Indonesia. Samples were collected over two field expeditions (1991 and 2010) and cover 13 volcanic centers in Sumatra, 5 in Java and one in Bali. In addition, we present data from three geothermal sites in Sumatra associated with active fault systems in-between volcanic centers (IBVC). The overall aim is to resolve volatiles associated with the sub-arc mantle (subducting slab and mantle wedge) from inputs derived from the over-riding arc crust. The western Sunda arc is a prime locality to assess controls on volatile provenance at subduction zones due to changes in composition and thickness of over-riding crust and variations in sediment input rates along the strike of the arc.

The dry gas chemistry of the majority of volcanic samples is dominated by CO_2 with inert gas variations ($He-Ar-N_2$) typical of subduction zone gases. However, there is a strong crustal control on the $He-CO_2$ isotope and relative abundance systematics on a number of volcanic centers: this effect is most clearly observed at flank localities and in water phase samples. Filtering the entire database for modifications due to air contamination, degassing-induced fractionation (C-isotopes and $CO_2/^3He$ ratios) and crustal contamination associated with volatile transport within shallow-level hydrothermal systems allows recognition of the magmatic volatile signature of individual volcanoes along the arc. Helium isotopes at all but two volcanic centers (Talang and Dempo on Sumatra) range from 5.3 R_A to 8.1 R_A (R_A = air $^3He/^4He$) pointing to the mantle wedge as the principal source of He but with a small input of crustal (radiogenic) He at some localities. Samples from Java and Bali span an even more limited range (6.6 to 7.9 R_A) implying a relatively smaller input of crustal He. Carbon isotope and $CO_2/^3He$ ratios vary from −1.4‰ to −6.4‰ and 4.38 to 150 ($\times 10^9$), respectively, with higher and more variable values to the north of Sumatra. This latitudinal effect is not apparent in air-corrected N-isotope values ($\delta^{15}N_C = -3.91$ to $+5.92$‰) or various elemental ratios such as N_2/Ar and N_2/He. The three IBVC sites, all located in Sumatra, have significantly lower $^3He/^4He$ ratios (<3.6 R_A) with $CO_2/^3He$ values both higher and lower than volcanic centers. Their $\delta^{13}C$, $\delta^{15}N_C$ and gas ratios overlap with the volcanic centers.

The elemental and isotopic characteristics of carbon and helium have been modified at IBVC sites due to crustal processes. However, based upon relationships between CH_4 and ^3He as well as co-variations between He–C–N isotopes, the over-riding crust and associated sediments add minimal volatiles to volcanic centers throughout the western Sunda arc. In turn, subducted sediment, particularly the Nicobar Fan which supplies Himalayan-derived sediment to the slab off Sumatra, exerts a strong control on the magmatic CO_2 characteristics although it is less influential for N_2. In spite of large sections of incoming sedimentary material being off-scraped during subduction, our data suggest that a significant fraction must enter the trench, enhancing fluid/melt production in the mantle wedge. We propose that subduction-related source contamination plays the dominant role over thick/old crustal basement in supplying the major volatile output budget of the western Sunda arc.

1. Introduction

Carbon dioxide and other volatiles erupted at arc volcanoes trace their origins to the mantle wedge, the subducting slab (including sediments and underlying crust), and the crust through which magmas are erupted (Marty et al., 1989; Poreda and Craig, 1989; Varekamp et al., 1992; Sano and Marty, 1995; van Soest et al., 1998). By resolving contributions from each of these reservoirs to the volcanic arc output, it is possible to constrain the proportion of carbon recycled between trench and arc (shallow recycling) versus the proportion which bypasses the zone of magma generation and

---

[*] Corresponding author.
E-mail address: shalldorsson@ucsd.edu (S.A. Halldórsson).

0009-2541/$ – see front matter © 2012 Elsevier B.V. All rights reserved.
http://dx.doi.org/10.1016/j.chemgeo.2012.09.042

is recycled into the deep mantle (deep recycling) (Hilton et al., 2002).

In this contribution, we present new results on the volatile characteristics of nineteen passively-degassing volcanic centers in the western Sunda arc of Indonesia. Large sections of this arc system, the Sumatra segment in particular, are underlain by thick, Mesozoic continental crust (Hamilton, 1979) composed mainly of granitoids and siliciclastic and carbonate sediments (Hamilton, 1979; Gasparon and Varne, 1995). Gasparon et al. (1994) and Gasparon and Varne (1998) argued that contamination of arc-related magmas by the crust increased in significance from east to west along the Sunda arc, and that the role of subducted sediment on magma chemistry diminished in a complementary fashion. Thus, the western Sunda arc presents a unique test case of volatile provenance associated with arc volcanism, vis-à-vis inputs from the over-riding plate (particularly the crust) versus the subducted slab. Central to this issue, however, is the similar chemical (e.g., trace elements) and radiogenic isotope traits of incoming sediments on the slab and the arc crust itself (Gasparon and Varne, 1998). This also complicates resolution between slab-related volatile additions to the mantle source (primary contamination) and secondary/shallower crustal contamination of magmas en route to the surface.

Coupled studies of He, CO_2 and N_2 (isotopes and relative abundances) can be used in a powerful manner to resolve upper crustal influences and their potential contribution to arc volcanism (e.g., Fischer et al., 2002; Hilton et al., 2002). Applying such an approach to the western Sunda arc is therefore of great interest given the antiquity and composition of the Sundaland crustal core (Fig. 1) and the presence of well-documented sedimentary provinces on the subducting oceanic parts of the Indo-Australian plate, off-Sumatra and west Java (Moore et al., 1980). In this respect, it is of particular interest to compare the Sumatra segment of the Sunda arc with that of Java/Bali where the over-riding crust is thinner and more oceanic in nature (Hamilton, 1979). Thus, our aim is to identify the various sources contributing to the volatile output in the western Sunda arc and to assess first-order controls on their isotopic and abundance characteristics.

2. Geological setting of the western Sunda arc and the Sumatran segment

Indonesia is one of the most volcano-dense regions on Earth with widespread volcanism resulting from the ongoing subduction of the Indian–Australian Plate beneath the Eurasian Plate (Hamilton, 1979; McCaffrey, 2009) (Fig. 1). The continuous Myanmar–Andaman–Sunda–Banda subduction system makes up the present-day volcanic arc, which has been active since the Cretaceous (Hamilton, 1979). In Indonesia, there are two major crustal regimes which are separated at the Progo-Muria fault zone in central Java (Smyth et al., 2007). The western segment of the Sunda arc consists of Sumatra and west Java where the down-going plate is subducting obliquely beneath

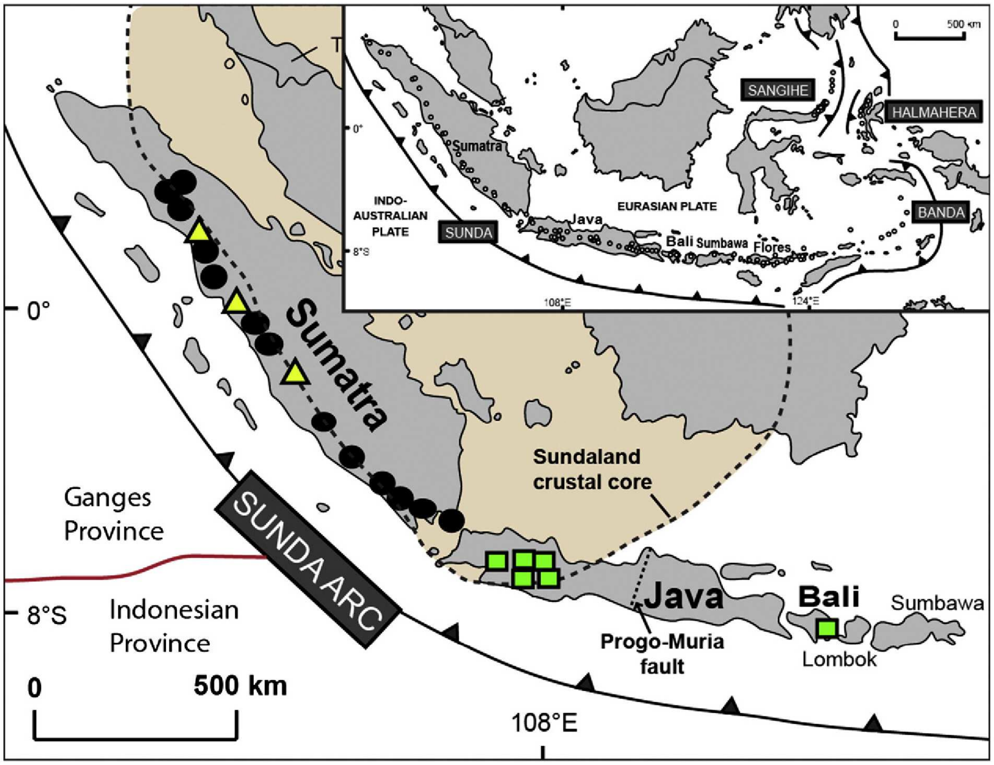

Fig. 1. Map of study area showing the sampling localities (black symbols = Sumatra volcanic centers, yellow triangles = in-between volcanic centers (IBVC) geothermal sites and green boxes = Java/Bali volcanic centers). Sedimentary provinces (Ganges vs. Indonesian) of ocean floor sediments and the Sundaland crustal core are shown for reference. Small inset picture shows the general tectonics of Indonesia, the major plates and arc systems involved. Active and quaternary volcanoes are represented by open symbols (after Gertisser and Keller, 2003).

relatively thick over-riding quasi-continental crust, consisting of the Mesozoic Sundaland core and/or the Sunda Shelf which are composed of continental block fragments. The eastern Sunda and Banda arcs (east Java, Flores, Timor) are built on considerably thinner oceanic crust. In the easternmost part of the arc, the leading-edge of the Australian continent is being subducted (Fig. 1).

The Indo-Australian Plate subducts beneath the Sunda Trench at an orthogonal convergence rate of 50 mm/yr in Sumatra which is considerably lower than ~75 mm/yr in Java and Flores (Von Huene and Scholl, 1991). The age of the subducting lithosphere varies from 50 to 90 Ma from north-to-south along Sumatra and from 100 to 135 Ma from west-to-east in Java (Widiyantoro and van der Hilst, 1996). The dip of the subducting slab changes from ~40° beneath Sumatra to ~60° below Java (Widiyantoro and van der Hilst, 1996). The overall structure and age of the subducting lithosphere strongly influences the style of crustal deformation and associated seismicity along the Sunda arc (Sieh and Natawidjaja, 2000; McCaffrey, 2009). The relatively young age of subducted lithosphere beneath Sumatra has drastic consequences for the depth distribution of earthquake foci, with no earthquakes deeper than ~300 km. In contrast, earthquake focal depths beneath Java extend to the 670 km mantle transition zone (Widiyantoro and van der Hilst, 1996).

Sumatra is situated on the south-western margin of the so-called Sundaland crustal core composed of granitic rocks up to 240 Ma (Gasparon and Varne, 1995). Crustal thickness in Sumatra varies between 25 and 40 km (Sieh and Natawidjaja, 2000; McCaffrey, 2009). During the Triassic to early Jurassic (~250–200 Ma), Sumatra was part of the northern edge of Australia (north of New Guinea) but later rifted from the Australian mainland to form a stable continental margin where it remained until subduction began in the Cretaceous (Hamilton, 1979). The influence of the Sundaland core is clearly evident in the radiogenic isotope systematics of volcanic rocks from Sumatra (e.g., Whitford, 1975). For example, the most radiogenic $^{87}Sr/^{86}Sr$ values along the entire Sunda arc are found in lavas of the great Toba eruption in northern Sumatra (Gasparon and Varne, 1998).

The presently-active volcanic front runs parallel to the Sunda Trench along the length of Sumatra, and coincides with the Barisan Mountains and the Sumatran Fault (McCaffrey, 2009). Recent estimates of sediment delivery rates are 83 km^3/Myr for Sumatra and 54 km^3/Myr for Java (Clift and Vannucchi, 2004). Additionally, a massive accretionary prism has formed offshore Sumatra—forming the Mentawai islands on the fore-arc Simeulue-Enggano ridge, as well as a number of offshore fore-arc basins (Moore and Curray, 1980).

Relatively few petrological and geochemical studies have been reported for Sumatra: however, exceptions include regional studies of Whitford (1975, 1981), Gasparon et al. (1994), Gasparon and Varne (1998) and Turner and Foden (2001). The Toba eruption in northern Sumatra (~75,000 years ago) and the petrology/geochemistry of associated tuffs has been the focus of detailed work (e.g., Chesner et al., 1991; Chesner, 1998; Vazquez and Reid, 2004).

3. Sampling and analytical techniques

Sampling of the western Sunda arc was undertaken in two field expeditions—in 1991 and 2010. In the 2010 expedition, we collected 35 geothermal fluid samples (including 17 duplicates) from 16 localities along a ~2000 km transect of Sumatra, from Rajabasa volcano in the south to Sibayak volcano in the north (see Budd et al., 2012a and Fig. 1). Sampling included the following historically-active stratovolcanoes (from south to north): Dempo, Kaba, Talang, Marapi, Sorik Marapi, Singabung, and Sibayak as well as Rajabasa, Sekincau, and Bual Bauali volcanoes where there is no historical record of eruptive activity (Gasparon, 2005). Three sampling localities are associated with massive caldera-forming lakes and/or caldera floors: Seminung (Ranau caldera) and Panururan (Toba caldera) and the Ratai hydrothermal field by the Hulubelu caldera (Gasparon, 2005). These 13 volcanic centers, which are all passively-degassing, were supplemented by in-between volcanic center (IBVC) geothermal sites associated with active fault systems: from south to north, the Dusan Baru field near Kerinci volcano, the Rimbo Panti field adjacent to Talakmau volcano, and the Helatoba–Tarutung fumarole field. We also collected gas samples from the historically-active Tangkuban Parahu volcano on Java.

The 1991 expedition included Sumatra (including many of the same sampling sites visited in 2010) in addition to five volcanic centers on Java and the island of Bali. With the exception of Talagabodas, all of the volcanoes from Java and Bali (Guntur, Papandayan, Galunggung and Batur) are known to be historically-active. Results of the earlier study helped direct sampling in the 2010 expedition and provided a useful perspective on temporal changes at individual sites over a two-decade period. Thus, the entire sample set (39 gas phase samples and 23 water phase samples) is composed of summit fumaroles (100 °C) from Marapi, Sibayak, Singabung and Papandayan volcanoes, which are classified as volcanic fluids (e.g., Taran and Giggenbach, 2003). The remaining samples are classified as hydrothermal fluids as they were sampled from volcano flanks and/or IBVC. In total, fluid samples were collected from (i) 9 fumaroles, (ii) 12 bubbling acid springs, (iii) 11 hot water springs, making a total of 56 samples (with duplicates) from 32 individual localities on Sumatra. Additionally, 4 fumaroles and 2 water springs from 6 different localities were sampled along the Java/Bali segment (see Table 1).

Sampling protocols and analytical procedures adopted during the 1991 expedition follow closely those described in Hilton et al. (1993). The 2010 samples were similarly collected in evacuated low-He diffusivity glass flasks (1720- or AR-glass) and/or annealed copper tubes, with adoption of the inverted funnel method to collect gas phase samples. Evacuated ~200 mL pyrex flasks, aka Giggenbach bottles, were used for major gas chemistry (2010) or an aliquot was prepared from the AR-glass bottles (1991 expedition).

Analytical protocols for the 2010 samples follow closely those described by Shaw et al. (2003) and Ray et al. (2009). Briefly, samples were released into an ultra high vacuum (UHV) stainless steel purification line where non-condensable gases (He – Ne – N_2) were cryogenically separated from condensable gases (H_2O and CO_2). The light noble gases (He – Ne) were then isolated from the active and heavy noble gas fraction by exposure to an activated charcoal trap at −196 °C and a Ti-getter held at 700 °C, with a calibrated aliquot (~0.5%) transferred to a MAP-215 noble gas mass spectrometer for He isotopic and He/Ne relative abundance analysis. Calibrated aliquots of air, run under identical conditions to samples, were used to gauge mass fractionation and to assess machine sensitivity.

The condensable gas fraction (CO_2) was isolated from water vapor and transferred to a dedicated Pyrex-glass vacuum line for further purification and manometric measurement in a calibrated volume to obtain the total abundance of CO_2. Following measurement, the CO_2 was split and transferred in Pyrex® glass breakseal to a Thermo-Finnigan Delta^{Plus}XP isotope ratio mass spectrometer for $\delta^{13}C$ analysis.

During the course of this study, a new protocol was developed for N_2 isotope measurement of gas and fluid samples. An additional aliquot of gas was collected in a Pyrex glass breakseal on the stainless steel extraction line without exposure to either the charcoal trap or Ti-getter. The aliquot was then transferred to a dedicated N-purification line attached to a static noble gas mass spectrometer (VG5440; Craig et al., 1993). A description of the purification system to prepare the samples for N-isotope measurement is given by Barry et al. (2013–this issue). Briefly, the bulk gas in the breakseal was expanded into the line where residual condensable gases were isolated using a cold finger held at liquid-nitrogen temperature. Gases were then exposed to hot (850 °C) CuO for 10 min in the presence of a Pt-foil catalyst, held at 1000 °C, to enhance the reaction between O_2 and carbonaceous (CO, C_2H_4) and nitrogenous (NO) species, to CO_2 and NO_2, respectively. Excess oxygen was then reabsorbed back onto the CuO finger in two steps, first at 600 °C and then at 450 °C. Throughout the process, the condensable

Table 1

Helium, carbon and nitrogen isotope and relative abundance characteristics of geothermal fluids from Sumatra, Java and Bali.

Location[a]	Sample ID[b]	Sample Type[c]	Latitude (S/N)	Longitude (E)	T (°C)	$^3He/^3He$ R_M/R_A[d]	X[e]	$^3He/^4He$ R_C/R_A[f]	$CO_2/^3He$ ($\times 10^9$)	$\delta^{13}C$ (CO_2) (‰)VPDB	$\delta^{15}N$ (N_2) (‰)AIR	$\delta^{15}N$ (N_2) (‰)$_C$AIR[g]	$[^4He]_C$ cm^{3}STP/gH$_2$O ($\times 10^{-9}$)[h,i]
Sumatra—volcanoes													
Rajabasa	SUM10-2	G-as	S 05°44′53.6″	105°36′58.3″	32	8.05	252	8.08	9.33	−3.0	3.48	3.49 ± 0.46	
	SUM10-3	W-fs	S 05°45′07.0″	105°38′03.0″	54	3.46	6.52	3.91	1023	−4.1	nd	nd	62.8
	725	W-fs	S 05°45′07″	105°38′03″	58	5.52	9.33	6.06	2003	−4.7	nd	nd	4.3
	681	W-fs	S 05°44′54″	105°36′58″	65	3.37	1.77	6.45	724	−2.3	nd	nd	6.7
	726	W-fs				3.03	1.61	6.37	665	−2.7	nd	nd	9.5
Ratai (Hulubelu)	SUM10-4	G-as	S 05°19′53.5″	104°34′22.9″	86	5.25	7.66	5.88	5.03	−3.7	1.55	1.63 ± 0.36	
	SUM10-6	G-as				5.48	9.19	6.02	4.38	−4.5	0.79	0.76 ± 0.74	
Sekincau	SUM10-5	G-as	S 05°05′21.2″	104°18′26.3″	101	5.93	60.1	6.01	9.60	−4.8	4.13	4.18 ± 0.30	
	SUM10-7	G-as				5.46	24.3	5.65	9.00	−4.2	1.52	1.54 ± 0.40	
	694	G-as	S 05°05′21″	104°18′26″	27	6.41	7.97	7.19	75.3	−3.4	nd	nd	
	746	G-as				6.33	8.11	7.08	70.4	−3.4	nd	nd	
Seminung	SUM10-8	W-fs	S 04°52′38.9″	103°55′54.0″	58	3.50	5.59	4.04	229	−8.9	nd	nd	106
	SUM10-9	W-fs				2.49	3.80	3.02	210	−6.2	4.01	5.08 ± 0.51	167
	690	W-fs	S 04°52′39″	103°55′54″	59	2.53	1.37	6.69	141	−6.3	nd	nd	30.8
	649	W-fs				2.6	1.32	7.22	169	−6.3	nd	nd	32.5
Dempo	SUM10-10	W-fs	S 04°10′01.1″	103°04′04.6″	95	1.28	4.57	1.35	200	−3.2	−0.06	−0.36 ± 0.47	52.0
	SUM10-14	W-fs				1.00	2.62	1.00	16.7	−9.6	nd	nd	470
	705	W-fs	S 04°10′01″	103°04′05″	92	2.06	87.2	2.08	70.6	nd	nd	nd	255
	756	W-fs				2.06	65.2	2.08	63.2	nd	nd	nd	302
Kaba	SUM10-11	W-fs	S 03°27′41.2″	102°34′10.7″	48	6.27	27.5	6.47	59.2	−6.9	5.74	5.92 ± 0.43	713
	SUM10-12	W-fs				5.79	15.1	6.13	60.6	−8.2	nd	nd	765
Talang	SUM10-15	W-fs	S 00°55′03.5″	100°40″50.9″	45	1.66	3.35	1.95	442	−5.6	3.88	5.11 ± 0.48	93.1
	SUM10-17	W-fs				1.56	3.37	1.80	471	−4.7	nd	nd	104
Marapi	SUM10-18	G-sf	S 00°23′16.9″	100°27′38.7″	89	6.97	1265	6.98	11.4	−2.6	−2.07	−2.07 ± 0.46	
	SUM10-20	G-sf				7.09	319	7.11	14.1	−1.4	−2.17	−2.18 ± 0.28	
	674	G-sf	S 00°23′17″	100°27′39″	92	6.15	23.5	6.38	22.5	−2.4	nd	nd	
	680	G-sf				6.47	662	6.48	23.3	−2.6	nd	nd	
Sorik Marapi	SUM10-22	G-ff	N 00°42′09.2″	099°33′46.2″	59	5.64	10.2	6.14	38.4	−5.3	2.29	2.43 ± 0.53	
	SUM10-23	G-ff				6.69	57.8	6.79	40.6	−6.4	4.08	4.13 ± 0.38	
	SUM10-27	G-as	N 00°42′20.4″	099°34′43.0″	94	3.46	203	3.47	16.2	−5.3	1.48	1.48 ± 0.36	
	Cu-tube-2	G-as				2.89	21.5	2.99	27.1	−3.8	0.15	0.11 ± 0.41	
	701	G-ff	N 00°42′09″	099°33′46″	88	6.52	65.8	6.6	32.5	−3.0	nd	nd	
	565	G-as	N 00°42′20″	099°34′43″	90	3.32	40.8	3.38	34.4	nd	nd	nd	
	741	G-as				3.33	22.7	3.46	53.3	−3.1	nd	nd	
Bual Buali	SUM10-24	G-ff	N 01°33′59.4″	099°16′05.2″	92	5.92	20.1	6.18	16.3	−1.4	−3.38	−3.61 ± 0.53	
	SUM10-25	G-ff				1.08	2.80	1.12	60.9	−2.8	−2.16	−3.91 ± 0.59	
	615	G-ff	N 01°33′59″	099°16′05″	94	6.47	73.0	6.55	25.8	nd	nd	nd	
	675	G-ff				6.51	88.7	6.58	27.3	−5.3	nd	nd	
Panururan	SUM10-29	G-as	N 02°37′06.6″	098°40′22.7″	62	1.80	4.47	2.03	21.5	−1.6	0.27	0.06 ± 0.64	
	SUM10-30	G-as				5.29	253	5.30	36.9	−2.3	3.76	3.77 ± 0.53	
	665	G-as	N 02°37′07″	098°40′23″	60	5.06	160	5.08	56.8	−4.6	nd	nd	
Singabung	734	G-sf	N 03°10′0″	098°23′30″	120	5.98	34.0	6.14	150	−3.7	nd	nd	
Sibayak	SUM10-26	G-sf	N 03°14′22.9″	098°30′16.5″	95	6.74	1863	6.74	5.74	−3.8	4.33	4.33 ± 0.38	
	SUM10-28	G-sf				6.74	292	6.76	5.96	−2.8	5.52	5.54 ± 0.36	
	Cu-tube-5	W-fs	N 02°57′40.9″	098°52′31.0″	64	4.64	5.36	5.47	46.9	−3.7	nd	nd	19.0
	Cu-tube-6	W-fs				6.40	45.6	6.52	54.5	−4.1	nd	nd	11.9
	Cu-tube-7	W-fs				6.11	24.2	6.33	43.1	−4.0	nd	nd	15.5
	667	W-fs	N 02°57′41″	098°52′31″	44	6.31	7.22	7.17	12.0	−3.9	nd	nd	
	733	G-sf	N 03°14′23″	098°30′17″	106	6.68	1431	6.68	11.5	nd	nd	nd	
Sumatra—IBVC[a]													
Dusan Baru	SUM10-13	G-as	S 01°59′18.9″	101°21′28.1″	58	2.02	437	2.03	14.2	−6.7	3.49	3.50 ± 0.38	
	SUM10-16	G-as				2.00	394	2.00	14.0	−8.0	3.25	3.26 ± 0.55	
	731	W-as	S 01°59′19″	101°21′28″	94	2.03	15.1	2.10	279	−5.6	nd	nd	67.8
Rimbo Panti	SUM10-19	G-as	N 00°20′52.6″	100°04′06.9″	92	3.62	295	3.62	0.38	−4.9	1.75	1.75 ± 0.38	
	SUM10-21	G-as				3.71	312	3.72	nd	nd	1.83	1.83 ± 0.32	
Sumatra—IBVC[a]													
Helatoba–Tarutung	Cu-tube-3	G-as	N 02°04′31.0″	098°56′39.5″	63	1.71	38.7	1.73	1107	−2.1	−0.90	−0.95 ± 0.48	
	Cu-tube-4	G-as				1.62	38.6	1.64	1505	−1.8	−0.54	−0.58 ± 1.19	

gases (mostly CO_2, SO_2 and H_2O) were adsorbed onto a cold finger held at liquid nitrogen temperature. The purified N_2 was then expanded into a VG-5440 mass spectrometer where the ratio of ^{15}N to ^{14}N was analyzed by measuring m/z ratios of 28, 29, and 30, allowing calculation of the N-isotope ratio ($\delta^{15}N$) and application of a comprehensive CO correction to all samples (Barry et al., 2012). Hydrocarbon interferences at masses 28 and 29 are considered negligible. An internal pure N_2 standard, calibrated relative to Scripps-pier air, was repeatedly measured throughout the 23-day run of the western Sunda sample set. In addition, repeated measurements (n = 6) of the Scripps-pier air standard during these runs, following exactly the same analytical protocol as samples, allowed evaluation of uncertainties associated with both sample preparation and mass spectrometer measurement. We take the average reproducibility of our in-house air standard $\delta^{15}N$ value of ±0.26‰ (1σ) as the best estimate of the external reproducibility of our nitrogen system. Throughout the sample runs, procedural N_2 blanks

Table 1 (*continued*)

Location[a]	Sample ID[b]	Sample Type[c]	Latitude (S/N)	Longitude (E)	T (°C)	$^3He/^3He$ R_M/R_A[d]	X[e]	$^3He/^4He$ R_C/R_A[f]	$CO_2/^3He$ ($\times 10^9$)	$\delta^{13}C$ (CO_2) (‰)VPDB	$\delta^{15}N$ (N_2) (‰)AIR	$\delta^{15}N$ (N_2) (‰)$_C$AIR[g]	$[^4He]_C$ cm^3STP/gH_2O ($\times 10^{-9}$)[h,i]
Java—volcanoes													
Tangkuban Parahu	SUM10-1	G-sf	S 06°45′41.2″	107°37′32.9″	51	7.91	338	7.93	13.8	−5.2	1.6	1.6 ± 0.54	
Guntur	721	G-ff	S 07°8′36″	107°50′23″	98	6.75	58.1	6.85	16.4	−2.4	nd	nd	
Papandayan	696	G-sf	S 07°18′53″	107°43′57″	105	6.61	851	6.62	28.2	nd	nd	nd	
Galunggung	711	W-fs	S 07°15′0″	108°3′30″	48	5.44	3.68	7.10	172	−5.5	nd	nd	32.48
Talagabodas	673	G-ff	S 07°12′30″	108°4′0″	95	7.68	1144	7.69	20.2	nd	nd	nd	
Bali—volcano													
Batur	724	W-fs	S 08°15′03″	115°24′03″	32	6.81	6.45	7.87	25.2	nd	nd	nd	200

nd = not determined.

[a] Sample locations given from south to north. IBVC = In-Between Volcanic Centers.

[b] SUM10- and Cu-tube- sampled in October/November 2010, GPS datum WGS84; numbers sampled February/March 1991, map coordinates.

[c] Abbreviations: G = gas; W = water; sf = summit fumarole; ff = flank fumarole; as = gas from acid spring; fs = flank spring.

[d] R_M/R_A notation where R_M = sample $^3He/^4He$ ratio and R_A = atmosphere $^3He/^4He$ ratio ($= 1.4 \times 10^{-6}$).

[e] $X = (^4He/^{20}Ne)_M/(^4He/^{20}Ne)_{air} \times \beta Ne/\beta He$, where M is the measured $^4He/^{20}Ne$ ratio, β represents the Bunsen solubility coefficient assuming a recharge temperature of 15 °C (Weiss, 1971).

[f] R_C/R_A is the air-corrected He isotope ratio $= [(R_M/R_A \times X) - 1]/(X - 1)$.

[g] $\delta^{15}N$ (N_2) (‰)$_C$ is the air-corrected N isotope ratio $= [(\delta^{15}N \times X) - 1]/(X - 1)$. See appendix.

[h] Helium abundance data are corrected for air contamination where $[He]_C = ([He]_M \times (X - 1))/X$.

[i] All errors are reported at the 1σ level; R_C/R_A uncertainty is estimated $< \pm 3\%$, $CO_2/^3He$ uncertainty is estimated ±5%, $\delta^{13}C$ uncertainty is estimated $< \pm 0.5$‰, $[^4He]_C$ is estimated at ±5%.

where monitored prior to each sample analysis. Except for two samples (from Helatoba–Taratunga, blank ~9%), blank contributions were always less than 5% of sample yields and less than 2% in most cases.

Major gas chemistry of the 2010 samples was measured by a GC-quadrupole system at UNM. In this system, CO_2, N_2, $Ar + O_2$, CH_4, and CO are measured on a Gow Mac Gas Chromatograph with Discharge Ionization Detector (DID) [Heyesep and MolSieve columns]. The Ar and O_2 concentrations are measured on a Pfeiffer quadrupole mass spectrometer in dynamic mode. Major gas chemistry of samples from the 1991 expedition (listed in Table 2, identified with numbers only) was measured in the same laboratory using methods outlined previously (Zimmer et al., 2004; Elkins et al., 2006). For that system, samples with very high O_2 concentrations are likely to yield unreliable Ar data due to the difficulty of separating Ar and O_2 in a saturated O_2 separation column (see discussion in Zimmer et al., 2004 and Elkins et al., 2006). Two samples reported in Table 2, shown in italics and underlined, have unusually low N_2/Ar ratios (Seminung = 14.8 and Dempo = 14.6) and are not included in the following discussion.

4. Results

We report $^3He/^4He$, $CO_2/^3He$, C- and N-isotopes, and He abundance results (water phase only) in Table 1 with the major gas chemistry in Table 2. Sample locations are given in Fig. 1, with a filtered version of the dataset (see Section 5.2) plotted as a function of latitude in Figs. 6 to 8.

4.1. Major gas chemistry

The majority of samples is dominated by CO_2 with 34 out of 39 gases and waters having over 80% (dry gas) CO_2 (Table 2). The only localities showing considerably lower CO_2 content are the IBVC Rimbo Panti hydro-thermal site where N_2 dominates the dry gas budget (~58%) and Ratai (~72%). Nitrogen is the most abundant gas among the non-condensable gases but, with the exception of Rimbo Panti and Ratai, is always less than 15% of the total gas budget. Only three localities (Sorik Marapi, Pangururan and Tangkuban Parahu) show hydrogen concentrations higher than 1%, whereas only four of 21 localities (Sorik Marapi, Ratai, Seminung, and Marapi) have greater than ~5% oxygen. Methane is variable but the majority of samples contain less than 1% methane. However, two IBVC hot spring localities, Dusan Baru and Rimbo Panti, have significant amounts of CH_4 (~5% and ~7%, respectively). We also note the relatively high CH_4 (1.5%) at the Sorik Marapi flank locality. Notably, all three of these localities are characterized by relatively low $^3He/^4He$ ratios (2.1 R_A to 3.7 R_A).

In addition to these general features of the major gas chemistry, we use the ternary N_2 – He – Ar inert gas plot (Fig. 2) to distinguish between "mantle-derived" and "arc-type" gases (after Giggenbach, 1996). Arc-related geothermal fluids tend to have high N_2/He (>1000) and N_2/Ar (>83) when compared to mantle-derived fluids as a result of addition of sedimentary-derived nitrogen from the subducting slab (e.g., Giggenbach, 1996). Most samples of the present study fall within the field of arc-related gases but with some notable exceptions: i) gas phase samples from Rimbo Panti (RP) and Sibayak (SII) and water phase samples from Batur (B) have low N_2/Ar ratios and thus fall below the field for mantle-derived gases, ii) samples from Sorik Marapi (SM1), Helatoba–Taratung (HT) and Ratai (R) all have very high ratios of N_2/He (>10,000), iii) samples from Guntur (G), Sorik Marapi (SM) and Singabung (S) all fall outside the proposed field for arc- and mantle-derived fluids, iv) a few samples (e.g., Pangururan and Sibayak) have N_2 – He – Ar systematics consistent with mantle-derived gases.

4.2. $^3He/^4He$ ratios and dissolved helium in water spring samples

Helium isotope results for 32 localities on Sumatra and 6 on Java/Bali are given in Table 1. We plot all measured He isotopes (R_M/R_A) (including duplicates) versus solubility-corrected, air-normalized He/Ne ratio (X) to assess the integrity of the He isotope results (Fig. 3a). Measured $^3He/^4He$ ratios (reported as R_M/R_A where R_M = measured $^3He/^4He$ of sample and $R_A = {}^3He/^4He$ of air; 1.4×10^{-6}) have been corrected (to R_C/R_A) for the presence of atmospheric components using the air-normalized He/Ne ratio multiplied by the ratio of the Bunsen coefficients, assuming an air-equilibration temperature of 15 °C (= X value—see Table 1 footnote for details plus an estimate of the analytical uncertainty). For the most part, the correction results in only minor (<0.3 R_A) changes to the measured $^3He/^4He$ (R_M/R_A) ratio. However, where X values are low (<2), correction to measured values can be large, up to 3.1–4.6 R_A for two water samples (Rajabasa and Seminung). We note also that agreement between duplicate samples generally falls within 0.5 R_A; however, 13 of 24 duplicates agree within 0.1 R_A. In contrast, some samples show poor agreement e.g., Sibayak (5.5 R_A vs. 6.5 R_A), Bual Bual (1.1 R_A

Table 2
Gas chemistry of geothermal fluids from Sumatra, Java and Bali (vol.% dry gas).

Location	Sample ID[a]	Type[b]	CO_2	He [ppm][c]	H_2	Ar[d]	O_2	N_2	CH_4	N_2/Ar	N_2/He	$CH_4/^3He$ (×10^7)
Sumatra—volcanoes												
Rajabasa	G-SUM10-1	G-as	91.86	8.70	nd	0.023	0.29	7.38	0.46	318	8478	4.63
	725	W-fs	99.96	0.077	nd	nd	nd	0.036	nd	nd	4675.3	nd
	681	W-fs	99.79	0.12	nd	nd	nd	0.21	nd	nd	17500	nd
	726	W-fs	99.64	0.17	nd	nd	nd	0.36	nd	nd	21176	nd
Ratai (Hulubelu)	G-SUM10-3	G-as	12.92	3.12	0.0010	0.61	14.0	72.4	0.049	118	232280	1.87
Sekincau	G-SUM10-4	G-as	89.64	11.1	0.16	0.11	1.03	8.44	0.61	74.3	7610	6.55
	694	G-as	99.17	1.31	nd	0.011	nd	0.79	0.04	70.1	6031	2.79
	746	G-as	94.79	1.36	nd	0.010	4.41	0.75	0.04	76.0	5515	2.70
Seminung	690	W-fs	72.01	0.55	nd	*0.034*	26.8	0.51	nd	*14.8*	9273	nd
	649	W-fs	98.85	0.58	nd	0.019	nd	1.13	nd	58.0	19483	nd
Dempo	705	W-fs	93.62	4.56	nd	*0.41*	nd	5.93	0.040	*14.6*	13004	3.03
	756	W-fs	99.22	5.40	nd	nd	nd	0.78	nd	nd	1444	nd
Marapi	674	G-sf	72.23	3.59	nd	nd	26.7	0.56	nd	nd	1560	nd
	680	G-sf	99.97	4.73	nd	nd	nd	0.032	nd	nd	67.7	nd
Sorik Marapi	G-SUM10-9	G-as	81.63	10.4	5.18	0.012	1.60	10.08	1.50	875	9727	29.7
	G-SUM10-10	G-ff	84.36	2.56	0.0070	0.019	2.04	13.48	0.091	694	52748	3.76
	701	G-ff	99.87	3.32	nd	0.0015	nd	0.13	0.0007	87.5	392	0.024
	565	G-as	89.99	5.54	nd	0.014	9.18	0.78	0.055	55.3	1408	2.09
	741	G-as	99.08	3.86	nd	0.00033	0.66	0.23	0.046	703	596	2.49
Bual Buali	G-SUM10-11	G-ff	91.77	6.51	0.076	0.027	2.45	5.20	0.47	195	7999	8.39
	615	G-ff	99.98	4.22	nd	nd	nd	nd	0.019	nd	nd	0.49
	675	G-ff	99.00	3.94	nd	nd	nd	0.98	0.019	nd	2487	0.52
Pangururan	G-SUM10-13	G-as	92.29	3.37	3.66	0.0025	0.98	2.55	0.52	1022	7569	20.80
	665	G-as	99.88	2.47	nd	0.0022	nd	0.1	0.017	46.2	405	0.94
Singabung	734	G-sf	99.91	0.78	nd	0.00086	nd	0.095	nd	110	1218	nd
Sibayak	G-SUM10-15	G-sf	97.23	17.9	0.0060	0.00011	0.61	1.96	0.17	17083	1091	1.02
	G-SUM10-16	G-sf	96.59	17.1	0.011	0.00016	0.45	2.64	0.31	16469	1544	1.89
	733	G-sf	99.96	9.30	nd	0.00086		0.035	0.007	40.6	37.6	0.076
Sumatra—IBVC												
Dusan Baru	G-SUM10-5	G-as	81.30	20.2	0.029	0.21	0.47	11.60	6.39	55.2	5746	112
	G-SUM10-6	G-as	79.98	20.4	0.019	0.098	1.00	11.93	6.95	122	5847	122
	731	W-as	99.54	1.21	nd	nd	nd	0.43	0.028	nd	3554	7.80
Rimbo Panti	G-SUM10-7	G-as	30.14	156	0.0031	1.80	5.05	57.86	5.14	32.2	3701	6.48
	G-SUM10-8	G-as	30.52	156	0.0021	1.77	3.93	58.22	5.52	32.9	3724	6.79
Helatoba–Tarutung	G-SUM10-12	G-as	98.81	0.37	0.054	0.0014	0.32	0.74	0.075	534	20159	84.10
Java—volcanoes												
Tangkuban Parahu	G-SUM10-2	G-sf	86.05	5.62	8.15	0.0013	0.56	5.08	0.16	3894	9034	2.62
Guntur	721	G-ff	96.94	5.46	nd	0.00030	2.83	0.17	0.005	573	311	0.10
Galunggung	711	W-fs	99.87	0.58	nd	nd	nd	0.13	nd	nd	2241	nd
Talagabodas	673	G-ff	99.97	4.59	nd	nd	nd	0.033	nd	nd	71.9	nd
Bali—volcano												
Batur	724	W-fs	99.08	3.57	nd	0.023	nd	0.9	nd	38.3	nd	nd

nd=not determined.

[a] G-SUM10- samples were analyzed with an updated GC system at UNM whereas samples listed with numbers only were analyzed on the old GC system in the same lab.

[b] Abbreviations: G = gas; W = water; sf = summit fumarole; ff = flank fumarole; as = gas from acid spring; fs = flank spring.

[c] Helium conc. are calculated from the $^3He/^4He$ ratios, $CO_2/^3He$ ratios and the CO_2 vol.% dry gas.

[d] Underlined values in italics have been removed from the discussion as the Ar data are not considered reliable.

vs. 6.2 R_A) and Panururan (2.0 R_A vs. 5.1 R_A). We note that the X values for some of these samples are exceptionally low and thus these samples have experienced significant atmospheric contamination (see discussion in Section 5.1.1).

Helium isotope ($^3He/^4He$) values vary considerably along the western Sunda arc, from 1.0 R_A to 8.1 R_A (Table 1), and thus demonstrate a significant contribution of mantle-derived helium, from 13% to 100% (assuming a binary mixing between MORB (8 R_A) and crustal component (~0.01 R_A)). The majority of fluid samples from volcanic centers in Sumatra have $^3He/^4He$ ratios in the range 5.0 to 7.2 R_A, typical of arcs worldwide (Hilton et al., 2002). The one exception is Rajabasa (south Sumatra) where $^3He/^4He$ is coincident with MORB (8.1 R_A). Significant additions of radiogenic helium ($\gg$50% using the same end-members and assuming a binary mixture as above) are found in geothermal fluids from the flanks of Rajabasa (3.9 R_A, 1 sample), Seminung (3.0–4.0 R_A, 2 samples), Dempo (1.0–2.1 R_A, 4 samples), Talang (1.8–2.0 R_A, 2 samples) and Sorik Marapi (3.0–3.5 R_A, 4 samples). Of these, only Dempo and Talang do not show correspondingly higher $^3He/^4He$ ratios from different flank and/or summit fumaroles. Radiogenic He additions are also evident in two gas phase samples from Ratai hydrothermal field near Hulubulu caldera (6.0 R_A).

Fluids from hydrothermal sites associated with fault systems which lie between volcanic centers (IBVC) tend to also show significant radiogenic additions, e.g., Dusan Baru (2.1 R_A, 3 samples), Rimbo Panti (3.6 $R_{A,}$ 2 samples) and Helatoba–Tarutung (1.7 R_A, 2 samples). Other general features of the He isotope results is that the Java and Bali samples show little evidence for significant radiogenic additions, and span a limited range of 6.6 to 7.9 R_A. Finally, there are not significant differences in He isotope systematics between different sample types (gas versus water phase) from the same locality (e.g., Sibayak, Dusan Baru).

The measured dissolved helium abundances in water spring samples (n = 22) are corrected for atmospheric He and reported in Table 1. They range from 11.9 to 765 ncm^3 STP/gH_2O. Thermal springs from the flanks of Kaba volcano show the highest helium contents

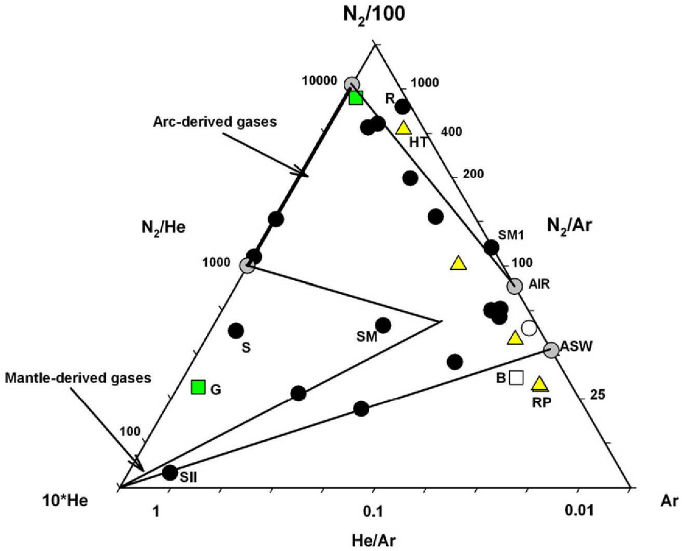

Fig. 2. Ternary plot of the non-reactive gases He – N_2 – Ar. The fields for mantle-derived and arc-type gases, as well as N_2 – Ar ratio of air (83) and air-saturated groundwater (ASW-45) are shown (after Giggenbach, 1996). See text for details on sample identity. Gas phase samples (closed symbols) and water phase samples (open symbols) from volcanic centers on Sumatra are separated from samples collected in-between volcanic centers (IBVC) (yellow triangles). Samples from Java/Bali are shown as boxes: green boxes for gas phase and open boxes for water phase samples.

and they also have amongst the highest $^3He/^4He$ ratios for the water samples (6.1–6.5 R_A). The Kaba springs also had one of the lowest measured temperatures (48 °C).

4.3. $\delta^{13}C$ (CO_2) values

The $\delta^{13}C$ (CO_2) values of all gas and water phase samples (including duplicates) are shown in Fig. 4 (plotted vs. $CO_2/^3He$). The $\delta^{13}C$ values range from −1.4‰ to −9.7‰ with only 6 of 53 samples showing values lower than the mean MORB value of −6.5‰ (Sano and Marty, 1995). Among the gas phase samples, only samples from the Dusan Baru hydrothermal area (Kerinci Valley) show low $\delta^{13}C$ values (−6.7 to −8.0‰) whereas the lowest value is found in a water phase sample from Dempo (−9.7‰). The highest observed values are −1.4‰ in flank fumaroles at Bual Buali and summit fumaroles at Marapi. Water phase samples do not demonstrate systematically different $\delta^{13}C$ values compared to gas samples: water samples vary from −2.3‰ to −9.7‰ whereas gas phase samples vary from −1.4 to −8.0‰. In contrast to He isotopes, the C isotope values observed at IBVC locations show good correspondence with values from the volcanic centers.

4.4. $CO_2/^3He$ ratios

The molar ratio of $CO_2/^3He$ varies by over 4 orders of magnitude for the western Sunda arc samples (Fig. 4), from ~0.4×10^9 to ~2×10^{12} and are thus, with the exception of one sample from Rimbo Panti (0.38×10^9), higher than the global mean for MORB (2×10^9) (Marty and Jambon, 1987). Indeed, the majority of samples have ratios greater than the mean value for worldwide arcs ($16 \pm 11 \times 10^9$) (Sano and Williams, 1996). In contrast to He and C isotopes, water phase samples have significantly higher $CO_2/^3He$ ratios relative to corresponding gases (Fig. 4), presumably because gas samples are less likely than waters to experience elemental fractionation (see Section 5.1.2).

Two samples clearly stand out from the general range of 4.4–150 ($\times 10^9$) observed for gas phase samples: Rimbo Panti acid spring (0.38×10^9) and Helatoba–Tarutung hydrothermal area (1107–1505 ($\times 10^9$)). Notably, both these localities are at a considerable distance from volcanic centers. In contrast, the Dusan Baru hydrothermal site agrees well with ratios generally observed at volcanic centers. Finally, with the exception of the water sample from Galunggung (172×10^9), the Java/Bali samples show a limited range of ratios—14–28 ($\times 10^9$), coincident with the global mean for arcs worldwide (16×10^9).

4.5. $\delta^{15}N$ (N_2) values

In Fig. 3b, we plot measured $\delta^{15}N$ versus the air-normalized He/Ne ratio (X value—see section 4.2 and Table 1 footnote for details). The measured nitrogen isotope data from the 2010 sampling campaign (which includes one value from Tangkuban Parahu on Java) ranges from −3.38‰ to +5.74‰ (Fig. 3), with the majority of samples displaying values greater than air - consistent with values found previously at other arc-related volcanoes (up to +7‰, e.g., Sano et al., 1998; Fischer et al., 2002; Clor et al., 2005; Elkins et al., 2006; Mitchell et al., 2010). Four samples show isotope values identical to that of air.

Measured $\delta^{15}N$ values (reported as $\delta^{15}N$ in Table 1) have been corrected for the presence of atmospheric nitrogen using an approach similar to that used for He isotopes: in the following discussion, we use the air-corrected $\delta^{15}N$ ratio ($\delta^{15}N_C$) based upon this correction. However, an alternative approach to account for air-derived N_2 is based upon measured N_2/He ratios (e.g., Fischer et al., 2002). In the Appendix A, we contrast these two approaches specifically for our dataset.

The most positive $\delta^{15}N_C$ values for our dataset are for a water sample from Kaba volcano (5.92‰) and a summit gas samples from Sibayak volcano (5.54‰). Bual Bual volcano has the lowest (duplicate) values in the dataset: −3.61‰ and −3.91‰. Along with Marapi (−2.07 and

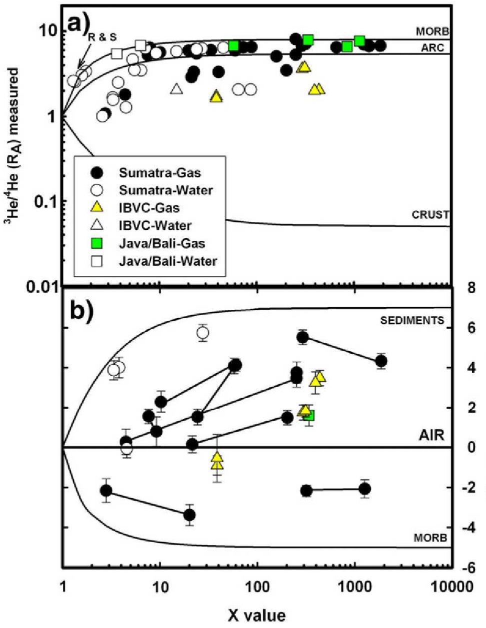

Fig. 3. a) Plot of measured He isotopes versus solubility-corrected, air-normalized He/Ne ratio (X) to assess the integrity of the He isotope results. Curves represent mixing between air-saturated water (1 R_A, X = 1) and MORB (8 R_A), Arc (5.4 R_A) and crust (0.05 R_A). Notably, samples with low X values (<4) and low $^3He/^4He$ ratios are severely air-contaminated. Similarly, samples with high X values and low $^3He/^4He$ ratios are contaminated with radiogenic helium due to crustal contamination. R & S are water samples from Rajabasa and Seminung. b) Plot of measured $\delta^{15}N$ versus the same X value to assess the integrity of the $\delta^{15}N$ results. Tie-lines connect samples from the same locality Curves represent mixing between air-saturated water (0‰ $\delta^{15}N$, X = 1) and MORB (−5‰ $\delta^{15}N$) and sediments (+7‰ $\delta^{15}N$). We note that when duplicate samples from the same locality show poor agreement, the sample with the lowest X almost generally plots closer to the N isotopic composition of air (0‰).

−2.18‰) and Helatoba–Tarutung (−0.58 and −0.95‰), these are the only volcanoes to have solely negative values. We do not observe any marked difference between water and gas samples (Fig. 3). Out of four water phase samples analyzed, Dempo overlaps with the N-isotopic composition of air whereas the remaining three (Seminung, Kaba and Talang) all show positive values (up to 5.92‰).

5. Discussion

5.1. Sample integrity

In this section, we adopt a step-by-step filtering protocol to test the integrity of individual samples to identify those unrepresentative of magmatic gas, due to air contamination, shallow-level crustal contamination and/or elemental fractionation within the hydrothermal systems. This approach is an essential prerequisite to revealing those samples/localities with isotopic and relative abundance He–C–N characteristics of the magma system. Only in this way is it possible to assess the relative importance of mantle source vs. crustal controls on the volatile systematics.

5.1.1. Air contamination

Atmospheric gases can act to mask and/or overwhelm the volatile characteristics of magmatic systems: this is particularly the case for He- and N-isotopes but not so for CO_2 due to the relatively low CO_2 content of air. One way to identify atmospheric contributions is to utilize sample He/Ne ratios (Fig. 3a). For example, two water phase samples from both Rajabasa and Seminung have low X-values so are subject to a large air-correction to measured He isotope compositions. In addition, poor agreement between duplicate samples from these localities further suggests that one or both have experienced severe air-contamination. Generally, when duplicate samples display poor agreement for He-isotopes (>1 R_A), we select the duplicate sample with the higher X value, such as in the case of samples SUM10-29 from Panururan and SUM10-25 from Bual Bauli, as being the least compromised due to air additions.

An alternative approach is to identify atmospheric contributions through the major gas chemistry. For example, N_2/Ar values lower than air (83) but higher than or equal to air-saturated water (ASW) (45) are considered to be contaminated with air and/or affected by mixing with ASW. In this respect, mixing with ASW may apply to the following: Sekincau (G-SUM10-4, 694 and 746), Sorik Marapi II (565), Seminung (649), Dusan Baru (G-SUM10-5) and Pangururan (665). In addition, three samples have N_2/Ar ratios within uncertainty of ASW: gas phase samples from Rimbo Panti (N_2/Ar ~32) and Sibayak II (~41), and a water phase sample from Batur (N_2/Ar ~38). Furthermore, we note that a number of samples have high O_2 which also implies severe air contamination, e.g., sample 690 from Seminung G-SUM-10-3 (Ratai), 674 (Marapi) and 565 (Sorik Marapi II) with O_2 content up to 27%.

The third criterion for identifying air-contaminated samples is the combination of N isotopes, overlapping with air values, and low X values (see Fig. 3b). Two samples fall under this category: Dempo (SUM10-10) and Panururan (SUM10-29).

5.1.2. Processes affecting water phase samples

5.1.2.1. Hydrothermal degassing. Phase separation processes within the hydrothermal systems have the potential to modify original magmatic values, particularly with respect to CO_2 (e.g., Ray et al., 2009). Three localities (Rajabasa, Dusan Baru, Sibayak) allow a direct comparison of He–CO_2 characteristics between gas and water phases. At each of these localities, water phase samples are characterized by higher

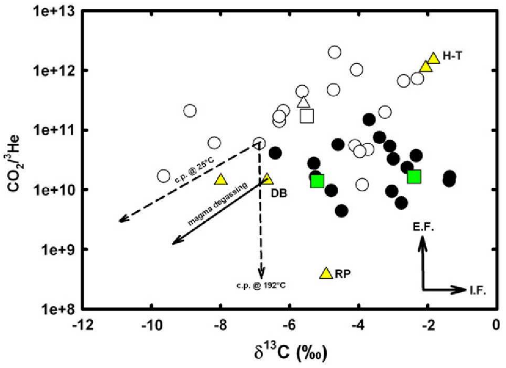

Fig. 4. Plot of $CO_2/^3He$ vs $\delta^{13}C$ for all gas and water phase samples. Trajectories show the effect of temperature dependent calcite precipitation (c. p.) at 25 °C and 192 °C (dashed lines) and magmatic degassing (solid line) from the water and gas phase samples which best represent the arc mantle: Kaba ($CO_2/^3He = 59.2 \times 10^9$, $\delta^{13}C = -6.9‰$) was used in the c. p. model, whereas Dusan Baru ($CO_2/^3He = 14.2 \times 10^9$, $\delta^{13}C = -6.7‰$) was used for the magma degassing model. Observations are inconsistent with both models. The effects of elemental fractionation (E.F.) of $CO_2/^3He$ ratios (vertical line) and isotope fractionation (I.F.) of $\delta^{13}C$ (horizontal line) are also shown. Note the low $CO_2/^3He$ ratio in a sample from Rimbo Panti (RP) and the high $CO_2/^3He$ ratios in samples from Helatoba–Tarutung (H–T). Dusan Baru = DB. Symbols as in Fig. 3.

$CO_2/^3He$ ratios, consistent with phase separation being an active process in fractionating $CO_2/^3He$ ratios. Because of its low solubility in aqueous fluids, helium preferentially enters the vapor phase relative to CO_2 and consequently the $CO_2/^3He$ ratios increases in the residual water phase (Ozima and Podosek, 2002).

Degassing of water phase samples in a hydrothermal system can be readily identified in a plot of $CO_2/^3He$ vs. air-corrected He concentrations (Fig. 5a). There are two notable observations: first, there is a general trend of increasing $CO_2/^3He$ ratios in the water samples with lower He contents. Second, independent of He content, all samples show $CO_2/^3He$ ratios significantly higher than the average values of arcs worldwide (GAA-global arc average) (Sano and Williams, 1996). These observations are consistent with water phase samples containing He and CO_2 which are residual following phase separation event(s).

Phase separation within a hydrothermal system can also potentially fractionate C-isotopes. We plot $\delta^{13}C$ values vs. He concentrations for all water phase samples in Fig. 5b to test for this possibility. The general negative correlation between $\delta^{13}C$ values and He concentrations is consistent with a simple model of degassing-induced isotopic fractionation of $^{13}CO_2$ from $^{12}CO_2$. Indeed, a simple model of open-degassing (Rayleigh fractionation) taking into account the solubility difference between CO_2 and He in water and the carbon isotope fractionation between gaseous CO_2 and various carbon-bearing species dissolved in the geothermal water is in good agreement with the relationship between $[He]_C$, $CO_2/^3He$ and $\delta^{13}C$ (Fig 5a and b).

Finally, we note that three out of the four water samples analyzed for N isotopes have relatively high $[He]_C$ concentrations (>90 ncm^3STP/g H_2O) (Table 1). Although empirical evidence of N isotope fractionation is unavailable, these samples appear relatively undegassed making it unlikely that hydrothermal phase separation has affected their N-isotope values. However, one water phase sample (SUM10-10 from Dempo) has a relatively low He content (52 ncm^3STP/g H_2O), a low X value, and an air-like N isotope composition: taken together, these features are consistent with hydrothermal degassing, followed by late-stage contamination by an air-like N component.

5.1.2.2. Calcite precipitation. Temperature-controlled precipitation of calcite at depth can also potentially modify $CO_2/^3He$ ratios and $\delta^{13}C$ values in water phase samples (Hilton et al., 1998a; van Soest et al., 1998; Ray et al., 2009). In Fig. 4, we compare the $CO_2/^3He$ and $\delta^{13}C$ characteristics of water and gas phase samples. We select Kaba sample SUM10-11 ($CO_2/^3He = 59.2 \times 10^9$, $\delta^{13}C = -6.0‰$), as an illustrative example to model this processes as it has relatively unmodified arc-like characteristics (e.g., Hilton et al., 2002). We superimpose two temperature-dependent calcite precipitation trajectories (c.p. at 25 °C and 192 °C) to show the potential fractionation effects associated with calcite precipitation. Notably, none of the water samples fall between the trajectories indicating they are likely unaffected by calcite precipitation. Even selecting a starting point with higher $\delta^{13}C$ (e.g., −3.9‰ e.g., Sibayak sample 667) fails to encompasses the vast majority of the water samples.

5.1.2.3. Crustal contamination. Low $^3He/^4He$ ratios ($\ll 8\ R_A$) accompanied by high He/Ne values could reflect a dilution of magmatic He components with crustal He in the hydrothermal system. This effect could be caused by (a) gas loss from fluids, with (residual) waters consequently more susceptible to contamination by crustal volatiles rich in ^4He (e.g., van Soest et al., 1998) and (b) significant transit distances between fluid discharge points at the surface and the point where He exsolves from a magmatic system (e.g., Sano et al., 1984).

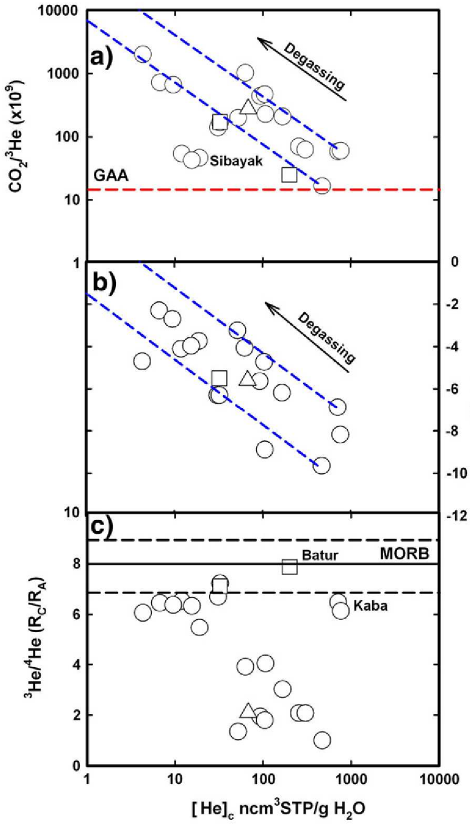

Fig. 5. a) Plot of $CO_2/^3He$ vs. air-corrected He concentrations for water samples only. Except for 3 samples from Sibayak volcano, there is a general trend of decreasing helium concentration in the water phase with higher $CO_2/^3He$ ratios. The global arc average (GAA—red dashed line) is from Sano and Williams (1996). b) Plot of $\delta^{13}C$ values vs. He concentrations for water samples only. The negative correlation is consistent with degassing-induced isotopic fractionation of carbon. c) Plot of He isotopes vs. He concentrations for all water samples. Except for a few samples (e.g., Kaba and Batur) there is a general negative correlation consistent with addition of radiogenic (crustal) He to water phase samples. The range for MORB of $8 \pm 1R_A$ is from Graham (2002). Trajectories for open-degassing are shown as blue dashed curves in panels a and b. The model on panel a uses the equation: $(CO_2/He)_{final} = (CO_2/He)_{initial} \times f^{(\alpha-1)}$ where f is the fraction of He remaining after degassing and α is the fractionation factor calculated at 71.4 °C = 3.00×10^{-2} (following Weis, 1971,1974 and de Leeuw et al. 2010). Similarly, the model in Fig. 5b was constructed using the equation: $\delta^{13}C_{res} = [(1/\alpha) \times (\delta^{13}C_{ini} + 1000) \times f^{(1/\alpha-1)}] - 1000$ where f is the fraction of He remaining after degassing and α is the isotopic fractionation factor between aqueous bicarbonate and gaseous CO_2 calculated at 95 °C = 1.347 (following Szaran, 1997). Two samples from Kaba (SUM10-12) and Dempo (SUM10-14) with the highest [He] are used as starting points for the degassing trends. For model details see de Leeuw et al. (2010). Symbols as in Fig. 3.

To test for crustal contamination within the hydrothermal system, we take advantage of three localities which allow a direct comparison between He isotopes in gas and water phases. At Rajabasa, a gas phase He isotope value of 8.1 R_A is higher than that measured in water samples (3.0 to 5.5 R_A), consistent with preferential addition of radiogenic He to the water phase. However, the case is more equivocal for both Dusan Baru hydrothermal site, where He isotopes show excellent agreement between the two phases, and Sibayak volcano where summit samples show consistent values of 6.7 R_A, overlapping with water phase samples (5.5 and 7.2 R_A) located on the flanks.

In Fig. 5c, we plot He isotopes vs. He concentration for all water samples to assess the general effects of crustal contamination. In this respect, we assume that He addition increases as a function of water-rock interaction within the hydrothermal reservoir such that it represents a proxy for distance traveled from the point of exsolution from the magmatic system. Except for two samples from Kaba volcano and one sample from Batur, there is a significant negative correlation consistent with addition of radiogenic (crustal) He to water phase samples. Thus, the crustal contaminant must have relatively high helium concentrations and a low $^3He/^4He$ ratio. Moreover, by comparing Fig. 5b and c, we note that samples with radiogenic crustal addition displays the lowest $\delta^{13}C$ values, indicating that the contaminant is likely to either contain carbon of organic derivation or has fractionated $\delta^{13}C$ values. As discussed in Section 5.1.2.1 and illustrated in Fig. 5b, it is the high $\delta^{13}C$ values (low [He]) which are consistent with degassing-induced $\delta^{13}C$ fractionated. Therefore, unless the starting $\delta^{13}C$ values are unusually low (i.e., magmas are characterized by organic C-like values) then the former explanation is preferred. In the case of water phase samples from Seminung (3.0 R_A) and Talang (2.0 R_A), they also possess N isotope compositions ($\delta^{15}N_C$) typical of sediments, at 5.08 and 5.11‰, respectively. For these samples, therefore, the origin of the nitrogen is likely to be shallow levels in the crust (Inguaggiato et al., 2004). Although somewhat more equivocal, we note that the most positive $\delta^{15}N_C$ value in the dataset (Kaba at 5.92‰), is characterized by both high He concentrations (713 ncm^3/g H_2O) and mantle-like He-isotopes (6.5 R_A) and $\delta^{13}C$ values (−6.9‰). In this case, it is unlikely that N is derived from shallow organic material.

5.1.3. Processes affecting gas phase samples

5.1.3.1. Magma degassing. Magma degassing will affect not only the elemental abundance of magmatic volatiles, as a function of their different solubilities in melt, but also the isotopic composition of specific volatiles such as CO_2 (e.g., Holloway and Blank, 1994). Degassing of magmatic volatiles will not only lower the $CO_2/^3He$ ratio due to the preferential loss of CO_2 relative to He, (e.g., Hilton et al., 1998b), but also the $\delta^{13}C$ value. Assuming an isotopic fractionation factor of 2‰ between $^{13}CO_2$ in the gas phase and $^{13}CO_2$ remaining in the melt (Mattey, 1991), volatiles residual after degassing will be depleted (i.e., evolve to lower $\delta^{13}C$ values) as degassing progresses. Notably, style of degassing (open vs. closed system) will not affect the general fractionation trends, i.e., $CO_2/^3He$ ratios and $\delta^{13}C$ values will always decrease in the melt, but it will affect the magnitude of any fractionation.

If we select Dusan Baru (SUM10-13) with a $\delta^{13}C$ value (−6.7‰) representative of the mantle wedge (cf. Sano and Marty, 1995), it is clearly seen that no samples fall along the magma degassing trajectory (Fig. 4). Even if we were to choose a different end-member composition with a more positive $\delta^{13}C$ value (e.g., from −6.7‰ to −4.6‰), magma degassing still fails to account for the $\delta^{13}C$ data. Magma degassing can also be disregarded as a viable means to explain the low $CO_2/^3He$ ratio from the Rimbo Panti acid spring as its starting compositions can be considered inappropriate for the arc mantle (i.e., very low $CO_2/^3He$ ratio of 0.38×10^9).

With respect to nitrogen, there is no consensus on degassing-induced isotopic fractionation of nitrogen (see contrasting views in the discussions of Cartigny and Ader, 2003 and Marty and Dauphas, 2003b). Indeed, evidence has been presented against N isotope fractionation during magma degassing based on a study of olivine and geothermal gases collected at the same locations (Fischer et al., 2005). This study shows similar $\delta^{15}N$ values for both types of sampling media.

5.1.3.2. Crustal contamination. The majority of water phase samples have been modified by crustal contamination (Section 5.1.2.3), and the same phenomenon could potentially affect gas phase samples. For example, two gas phase samples from IBVC, i.e., Rimbo Panti (0.38×10^9) and Helatoba–Tarutung ($>1000\times10^9$), fall outside the range of $CO_2/^3He$ ratios typical of all other gas samples (~50×10^9 to ~1×10^{11}). Also, samples from Dusan Baru have the lowest $\delta^{13}C$ values (−6.7 and −8.0‰) among the gas phase samples. Significantly, all three localities are located a considerable distance from volcanic summits and have large relative contributions of radiogenic helium ($^3He/^4He$ between 1.7 R_A and 3.7 R_A). In addition, samples from Rimbo Panti and Dusan Baru have high CH_4 contents (5 and 7 %). Assuming that such high methane concentrations can only be produced by inputs of thermogenically-produced CH_4 from crustal sediments (Taran, et al., 1998), these observations are consistent with these samples having experienced significant crustal contamination. Other likely processes affecting the IVBC samples include: 1) input of CO_2 from the crust, from decarbonation reactions, which may well explain the high $CO_2/^3He$ ratios ($>1000\times10^9$) in samples from Helatoba–Tarutung; and 2) loss of CO_2, presumably by means of carbonate and/or calcite precipitation, which would then produce anomalously low $CO_2/^3He$ ratios as observed at Rimbo Panti.

From a helium isotope perspective, the IBVC samples are the most crustally-contaminated gas samples in the study. In this respect, we might expect a negative relationship between He and N isotopes—assuming that crustal contamination is fingerprinted by high $\delta^{15}N$ (e.g., Inguaggiato et al., 2004). However, no such relationship is evident (e.g., Helatoba–Tarutung has $\delta^{15}N<0$) suggesting an important role for mixing with mantle N components and a muted crustal N input at this locality. Alternatively, mixing with secondary N in a moderate- to low-temperature hydrothermal system at shallow levels of the crust may explain the negative $\delta^{15}N$ values from Helatoba–Tarutung (see Li et al., 2009).

5.1.4. Spatial controls on volatile integrity: flank vs. summit variations

Proximity of sampling sites to volcanic centers or summits is often a primary criterion for sampling pristine magmatic gas, with low He isotope ratios frequently observed at more distal discharge vents (e.g., Sano et al., 1984; Marty et al., 1989; van Soest et al., 1998; Barry et al., 2013–this issue). Three volcanoes in Sumatra allow us to consider this issue: Sorik Marapi, Rajabasa and Sibayak. In the case of two flank localities from Sorik Marapi volcano, sampled only a few km apart, they show contrasting helium isotope ratios in the same sample medium (gas), ~3 R_A (n = 4) vs. 6 R_A (n = 3). Such a large difference in $^3He/^4He$ probably indicates increasing (and heterogeneous) additions of crustal He with distance from the central conduit of the volcano. Different samples on the flanks of Rajabasa volcano (n = 5) vary from 3.0 R_A to 8.1 R_A, with the highest helium isotope ratios (and most MORB-like ratios of $CO_2/^3He$) found in a single gas sample from an acid spring (free gas phase)—all other samples showing lower $^3He/^4He$ ratios are (spring) water phase samples. In contrast, flank samples (n = 4) at Sibayak volcano agree well with summit samples (n = 3) in their He isotopes (and carbon abundance and isotope characteristics). Therefore, if this ‘distance’ effect is to be recognized for gas samples, it has to be taken on a case-by-case basis, with volcanoes with many sampling locations (summit and flank) likely to yield more definitive conclusions. However, for Sorik Marapi and Sibayak, we deem the highest values at both these volcanoes as most representative of the magmatic source with lower values reflecting crustal additions of radiogenic He associated with the hydrothermal system.

5.1.5. Possible temporal variations

Nine volcanic centers and one IBVC locality were sampled in 1991 and 2010, thus enabling combination of the two datasets for assessment of temporal changes. However, there is some uncertainty regarding the exact locations of sampling. Even with this caveat, good agreement (<1 R_A) is found at Sekincau, Dempo, Marapi, Sorik Marapi, Bual Buali, Panururan, Sibayak and Dusan Baru whereas poorer agreement (>2 R_A) characterizes Rajabasa and Seminung. These observations suggest that there has been limited temporal variation in chemical and isotopic composition of emitted gases and fluids over the two-decade hiatus between sampling expeditions. For the most part, differences between the two datasets can be explained by varying degrees of air addition, e.g., samples from the flanks of Seminung and Dempo. When samples of the same medium contain very small contributions of air, i.e., have large X values, $^3He/^4He$ ratios are in excellent agreement—e.g., Sibayak has a $^3He/^4He$ ratios of 6.7 R_A (1991) and 6.7–6.8 R_A (2010).

Interestingly, four summit samples from Marapi, Sumatra's most active volcano, vary beyond analytical uncertainty (<0.2 R_A) from ~6.4 R_A in 1991 to ~7.0 R_A in 2010. GPS coordinates are unavailable from the first sampling expedition so it is impossible to determine if samples were from the same fumarole fields. However, it is possible that an increase in helium isotope ratios accompanied a magma re-charging event at the volcano prior to the renewed activity in 2011 (Smithsonian Institution, 2011).

5.1.6. Summary

In summary, in identifying samples which are likely representative of the magmatic systems of the western Sunda arc, we have confidence in data integrity of samples with a) X values greater than ~3, b) samples which show good agreement between duplicates, and c) samples which show significant deviations from the N isotopic composition of air combined with relatively high X values. A total of 7 samples have experienced sufficient modification by air-contamination that they are unlikely to reflect primary magma characteristics: 681 and 726 (Rajabasa); 690 and 649 (Seminung); SUM10-14 (Dempo); SUM10-25 (Bual Buali); and SUM10-29 (Panururan). However, despite low X values, duplicate samples from Rajabasa (681 and 726) and Seminung (690 and 649) show good agreement after air-correction. Thus, even if water phase samples have been masked by air contamination, they may still preserve $^3He/^4He$ ratios (after correction) that approach primary magma characteristics. However, the majority of water samples have been affected by phase separation within the hydrothermal system and their $\delta^{13}C$ and $CO_2/^3He$ values are likely unrepresentative of the magmatic source. In addition, a number of samples located at a considerable distance from the volcanic centers (i.e., all the IBVC localities: Dusan Baru, Rimbo Panti and Helatoba–Tarutung) and/or at volcanic flank localities (i.e., Rajabasa, Seminung, Dempo, Talang and Sorik Marapi) have experienced significant crustal contamination in the hydrothermal system thus rendering them inappropriate for deducing magmatic sources. Crustal contamination may possibly affect carbon characteristics of gas samples but the effect becomes clear only at low $^3He/^4He$ ratios (i.e., samples from the IBVC localities). In turn, the IBVC samples and water phase flank samples could be important for discerning the likely volatile composition of crustal material in Sumatra.

5.2. The western Sunda arc—along-strike variations

5.2.1. $^3He/^4He$ ratios

In Fig. 6a, we plot the highest $^3He/^4He$ ratio found in water and gas samples from each sample location (summit and flank locations) as a function of latitude. The majority of fluid samples (gas and water) from the western Sunda arc have air-corrected $^3He/^4He$ ratios in the range of 5.1 to 8.1 R_A, typical of arcs worldwide (Hilton et al., 2002). Significantly, additions of radiogenic helium are found in flank water phase samples from Rajabasa, Seminung, Dempo, and Talang, and also in gas phase samples from Sorik Marapi. Additionally, fluids associated with major fault systems lying in between volcanic centers (IBVC), i.e., Dusan Baru, Rimbo Panti and Helatoba–Tarutung, all have significant radiogenic additions.

In Fig. 6b, we plot only the highest $^3He/^4He$ ratio for an individual volcano, and thus the most likely representative value of magma source characteristics. Additions of radiogenic He are still evident among five samples (Talang, Dempo and three IBVC localities) in this filtered dataset. It is important to note that these two volcanic centers are characterized on the basis of a single collection site only, so we cannot rule out the presence of a higher He isotope ratio at these volcanoes, especially since no summit fumaroles were sampled. Beyond these excursions, there is no apparent N–S control on $^3He/^4He$ ratios. Interestingly, our Java and Bali samples show very little evidence for significant radiogenic additions and span a rather limited range of 6.6 to 7.9 R_A but these observations are based on a smaller sample set.

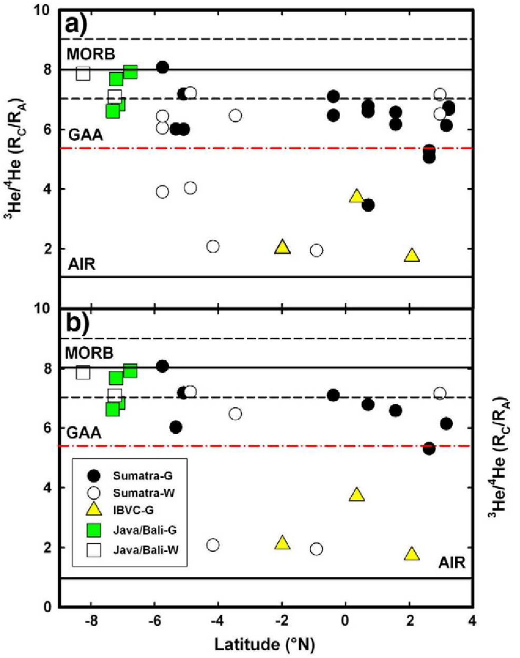

Fig. 6. a) Profile of air-corrected He isotopes vs. latitude for the western Sunda gas and water samples. The highest $^3He/^4He$ ratio found in water and gas samples from each location (flank and summit) is plotted. b) Filtered version of the same dataset as in a) but with only the single highest $^3He/^4He$ ratio for any given volcano plotted. Notably, only water phase samples from Dempo and Talang and samples from the IBVC show significant additions of radiogenic helium. The range for MORB of 8 ± 1 R_A is from Graham (2002) and the global arc average (GAA) of 5.4 R_A from Hilton et al. (2002).

5.2.2. $\delta^{13}C$ (CO_2) values and $CO_2/^3He$ ratios

In Fig. 7a, we plot $\delta^{13}C$ values as a function of latitude for the same samples plotted in Fig. 6a (i.e., summit and flank gas locations but excluding all water phase samples). In contrast to helium isotopes, carbon isotopes tend to show the highest values in the south and north of the western Sunda arc. Significantly, greater heterogeneity is evident from the northern sector of the arc, where the highest values are observed (up to −1.4‰), compared to other sections. Java and Bali samples and samples from IBVC also have high $\delta^{13}C$, i.e., they overlap with other samples of Sumatra.

In Fig. 7b, we plot $CO_2/^3He$ ratios as a function of latitude for the same samples as in Fig. 7a. Except for one sample (Rimbo Panti), $CO_2/^3He$ ratios along the west Sunda arc are always higher than the ratios observed in MORB (~1.5×10^9; Marty and Jambon, 1987). In fact, of the entire dataset (n = 24), only eight samples plot below the GAA (~1.6×10^{10}; Sano and Williams, 1996). When considering gas phase samples from the volcanic centers only (i.e., excluding the IBVC samples), $CO_2/^3He$ ratios increase from south to north along the Sumatran transect, where ratios significantly higher than the GAA become generally more prevalent north of 1°S. Notable

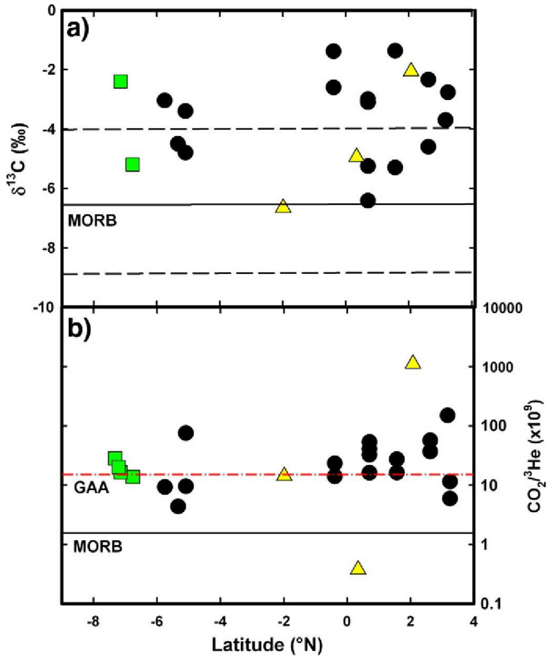

Fig. 7. Along-arc variations in a) δ^{13}C and b) CO$_2$/^{3}He for geothermal gases from the western Sunda arc. Note that only δ^{13}C values and CO$_2$/^{3}He ratios with the highest ^{3}He/^{4}He ratio at any given location is plotted (i.e., Fig. 6a). Dashed and solid horizontal lines show the MORB range of δ^{13}C values: -6.5 ± 2.5 (Sano and Marty, 1995), CO$_2$/^{3}He range for arcs worldwide (GAA) of 1.6×10^{10} (Sano and Williams, 1996) and the MORB range of 1.5×10^9 (Marty and Jambon, 1987). Symbols as in Fig. 3.

exceptions to this trend are two summit samples (~6×10^9) from Sibayak and flank samples (~70×10^9) from Sekincau. Samples from Java and Bali either overlap with GAA or have slightly higher ratios.

5.2.3. N$_2$/He and N$_2$/Ar ratios and δ^{15}N (N$_2$) values

In Fig. 8a–c, we plot the N$_2$ characteristics (N$_2$/Ar and N$_2$/He and δ^{15}N$_C$) as a function of latitude. Note that for δ^{15}N$_C$ we plot the same samples as in Fig. 6a as we have no evidence of sampling bias (Sections 5.1.2 and 5.1.3). Over the whole Java–Bali–Sumatra transect N$_2$/Ar, N$_2$/He and δ^{15}N$_C$, vary from ~40 to ~17,000, ~40 to ~2×10^5, and -3.91 to $+5.92$‰, respectively, consistent with the range found previously in arc-related volcanoes (e.g. Fischer et al., 2002; Elkins et al., 2006; Mitchell et al., 2010). The data, therefore, fall within reported ranges of possible sources contributing to the nitrogen inventory of gases in volcanic arcs, i.e., from typical mantle values (i.e., Marty and Dauphas, 2003a) to values significantly higher, akin to those found in oceanic sediments (see Peters et al., 1978; Fischer et al., 2002). These high ratios, as well as positive δ^{15}N$_C$, are often attributed to a large contribution from degrading organic-rich oceanic sediments on the down-going slab (Fischer et al., 2002; Taran and Giggenbach, 2003). No systematic changes are observed in the N$_2$/Ar and N$_2$/He ratios and δ^{15}N$_C$ systematics along the strike of the arc but in agreement with observations for δ^{13}C values, both higher and lower N$_2$/Ar ratios and δ^{15}N$_C$ values are observed in the southern and northern segments of the arc. The data from the Java and the Bali segments fall within the Sumatra range.

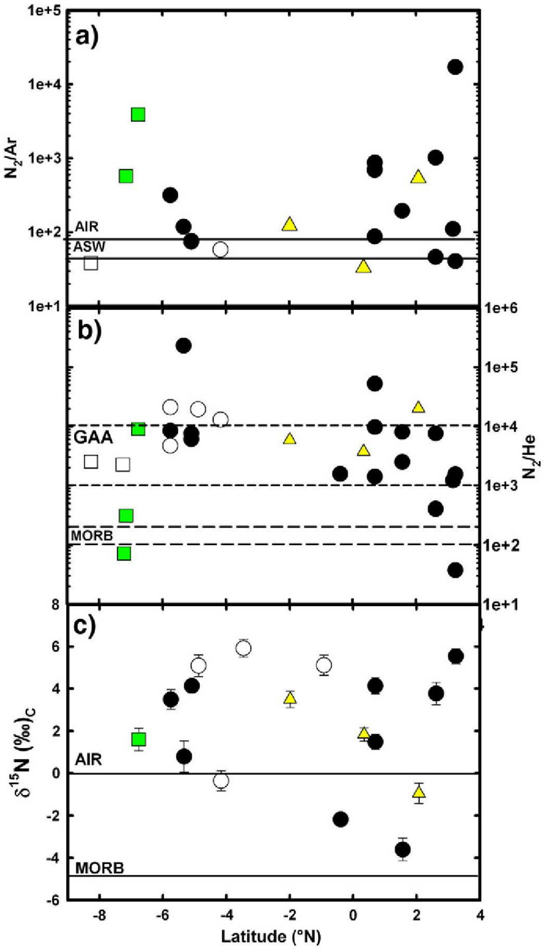

Fig. 8. Profiles of a) N$_2$/He, b) N$_2$/Ar and c) δ^{15}N$_C$ vs. latitude for geothermal gases and fluids from the western Sunda arc. Only δ^{15}N$_C$ values with the highest ^{3}He/^{4}He ratio at any given location are plotted. The solid horizontal lines in a) shows ratios for air (83.5) and air-saturated water (ASW) (45). Dashed, horizontal lines in b) represents the GAA and MORB N$_2$/He range (based on Mitchell et al., 2010). The MORB range in c) is from Marty and Dauphas, 2003a. Symbols as in Fig. 3.

5.3. Major gas provenance along the western Sunda arc segment

The majority of gas samples have CO$_2$ and N$_2$ systematics which are likely to give insight into magmatic source characteristics along the western Sunda arc segment. In this section, we assess the provenance of the magmatic CO$_2$ and N$_2$ and discuss inter-relationships between these two major gas phases.

5.3.1. CO$_2$ provenance

We plot CO$_2$/^{3}He vs. δ^{13}C for all filtered samples (Section 5.1.4) together with possible contributory end-member compositions for MORB-mantle (M), marine carbonate component (limestone) (L) and a sedimentary (S) organic carbon (Fig. 9) (Sano and Marty, 1995). Another potentially important C reservoir in subduction environments is the altered oceanic crust (AOC). We note that Shilobreeva et al. (2011) recently estimated a δ^{13}C value of -4.7‰ as representative of

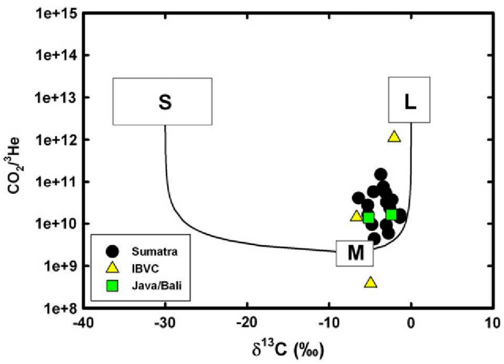

Fig. 9. Plot of $CO_2/^3He$ vs $\delta^{13}C$ for western Sunda arc samples. Superimposed are end-member compositions of a sedimentary-derived carbon source (S), calcareous- or limestone-derived source (L), and mantle-derived (M) following Sano and Marty (1995). Simple binary mixing between mantle and carbonate components cannot explain the data, and up to a 25% contribution from a sedimentary source, hosting organic carbon, is required.

average altered oceanic crust (AOC) which makes it indistinguishable from mantle wedge carbon. This observation, together with arguments by de Leeuw et al. (2007) that it is unlikely the AOC contributes C to the arc inventory, at least in the case of Central America, allows us to discount AOC in the following approach. As L, S and M end-members have distinctive $CO_2/^3He$ and $\delta^{13}C$ ratios (M: 1.5×10^9; -6.5‰; L: 1×10^{13}; 0‰; S: 1×10^{13}; -25‰), it allows determination of CO_2 provenance along the western Sunda arc (Table 3). From Fig. 9 it is apparent that the CO_2 is dominated by mixing between M and L components: however, the carbon characteristics of the samples are inconsistent with simple binary mixing between these two end-members, and require up to a 25% contribution from an organic sedimentary carbon component.

As discussed (Section 5.2.2), higher and more variable $CO_2/^3He$ ratios and generally higher $\delta^{13}C$ values, are observed along the arc towards the north (Fig. 7). This observation can be investigated more closely by comparing the relative contribution of L, M, and S along the strike of the arc. In Fig. 10a, we plot the ratio of CO_2 derived from the two sedimentary components (L+S) relative to that from the mantle component (M) for the same samples as in Fig. 6b, and we note that this ratio increases northward along the arc. If variations to the (L+S)/M ratio are related to the subducted sediments alone, then this observation suggests fundamental changes in the subducting Himalayan sedimentary carbon budget of the down-going Indo-Australian Plate offshore Sumatra. However, if the overlying crust has an impact on this relationship then there are fundamental differences between the Sundaland basement in northern Sumatra and south Sumatra/Java/Bali. This point is discussed in Section 5.4.

Table 3
Quantitative estimates of the relative contribution (%) of mantle (M), limestone (L) and sedimentary (S) sources to western Sunda samples.

Location	Sample ID	Carbon source[a]					Nitrogen source[c]		
		M	L	S	(L+S)/M[b]	S/M[b]	M	S	S/M[b]
Sumatra—volcanoes									
Rajabasa	SUM10-2	10.7	81.5	7.8	8.3	0.7	29.3	70.8	2.4
Ratai (Hulubelu)	SUM10-4	19.9	72.2	7.9			44.8	55.3	
	SUM10-6	22.8	67.1	10.1	3.4	0.4	52.0	48.0	0.9
Sekincau	SUM10-5	10.4	75.8	13.7	8.6	1.3	23.5	76.5	3.3
	SUM10-7	11.1	77.2	11.7			45.5	54.4	
	694	1.3	87.6	11.0					
	746	1.4	87.6	11.0					
Marapi	SUM10-18	8.8	84.5	6.7			75.6	24.4	
	SUM10-20	7.1	89.8	3.1	13.1	0.4	75.6	24.4	0.3
	674	4.4	88.5	7.0					
	680	4.3	88.0	7.7					
Sorik Marapi	SUM10-22	2.6	80.2	17.2			38.1	61.9	
	SUM10-23	2.5	76.7	20.9	39.8	8.5	23.9	76.1	3.2
	SUM10-27	6.2	77.7	16.2			46.0	54.0	
	Cu-tube-2	3.7	84.3	12.0			57.4	42.6	
	701	3.1	87.6	9.3					
	741	1.9	88.2	9.9					
Bual Buali	SUM10-24	6.1	90.6	3.2			88.4	11.6	0.1
	SUM10-25	1.6	89.4	9.0			90.9	9.1	
	675	3.7	79.5	16.9	26.4	4.6			
Panururan	SUM10-29	4.6	91.0	4.3			57.8	42.2	
	SUM10-30	2.7	90.1	7.2	36.0	2.7	26.9	73.1	2.7
	665	1.8	83.3	15.0					
Singabung	734	0.7	87.2	12.2	150.8	18.5			
Sibayak	SUM10-26	17.4	73.7	8.9			22.3	77.8	
	SUM10-28	16.8	77.6	5.6	3.0	0.3	12.2	87.8	7.2
Sumatra—IBVC									
Dusan Baru	SUM10-13	7.0	72.3	20.7	13.2	2.9	29.2	70.8	2.4
	SUM10-16	7.1	67.8	25.1			31.2	68.8	
Rimbo Panti	SUM10-19						43.8	56.3	
	SUM10-21						43.1	56.9	1.3
Helatoba T.	Cu-tube-3	0.1	93.1	6.8			66.3	33.8	0.5
	Cu-tube-4	0.1	93.8	6.1			63.2	36.8	
Java—volcanoes									
Tangkuban P.	SUM10-1	7.2	77.0	15.8	12.8	2.2	45.0	55.0	1.2
Guntur	721	6.1	87.2	6.7	15.4	1.1			

[a] Calculated according to $(^{13}C/^{12}C)_{obs}=M(^{13}C/^{12}C)_M+L(^{13}C/^{12}C)_L+S(^{13}C/^{12}C)_S$, $1/(CO_2/^3He)_{obs}=M/(CO_2/^3He)_M+L/(CO_2/^3He)_L+S/(CO_2/^3He)_S$, and $M+L+S=1$ and with end-members from Sano and Marty (1995).

[b] Ratio is only calculated for the sample with highest R_C/R_A (see Table 1 and Fig. 6b).

[c] Calculated according to $\delta^{15}N_C=f_{sed}\times\delta^{15}N_{sed}+(1-f_{man})\times\delta^{15}N_{man}$ and $f_{man}+f_{sed}=1$ with end-member compositions from Fischer et al. (2002).

5.3.2. N_2 provenance

In a manner analogous to CO_2, the air-corrected (magmatic) N_2 signal is resolved into its various source components using a simple mixing model. Potential sources of nitrogen include the mantle wedge, subducted hemipelagic sediments, shallow crustal sediments, and possibly deep crustal rocks and AOC (e.g., Mitchell et al., 2010). In contrast to organic seafloor sediments with $\delta^{15}N$ values from +5 to +7‰ (Sadofsky and Bebout, 2004; Li and Bebout, 2005), the Earth's upper mantle is characterized by a distinct isotopic composition, estimated at −5‰ (Marty and Dauphas, 2003a). Again, there is considerable overlap between mantle $\delta^{15}N$ values and AOC ($\delta^{15}N$ of −5.2‰; Li et al., 2007) which precludes resolution between these potential sources. As an initial approach, however, we calculate the fraction of sediment-derived and mantle-derived nitrogen in a binary sediment-mantle mixture using the air-corrected $\delta^{15}N$ values ($\delta^{15}N_c$) using the following isotope mass balance equations:

$$\delta^{15}N_c = f_{sed} \times \delta^{15}N_{sed} + (1-f_{sed}) \times \delta^{15}N_{man} \tag{1}$$

$$f_{man} + f_{sed} = 1 \tag{2}$$

where $\delta^{15}N_c$ is the air-corrected $\delta^{15}N_c$ composition of the samples, $\delta^{15}N_{sed}=+7$‰, $\delta^{15}N_{man}=-5$‰, and f_{sed} and f_{man} are the fractions of sediment-derived and mantle-derived nitrogen, respectively. The calculated fractions are given in Table 3 together with the ratio of sedimentary to mantle (S/M) nitrogen for samples with the highest $^3He/^4He$ ratios from each volcano (Fig. 6b). In Fig. 10b, we plot the S/M ratio as

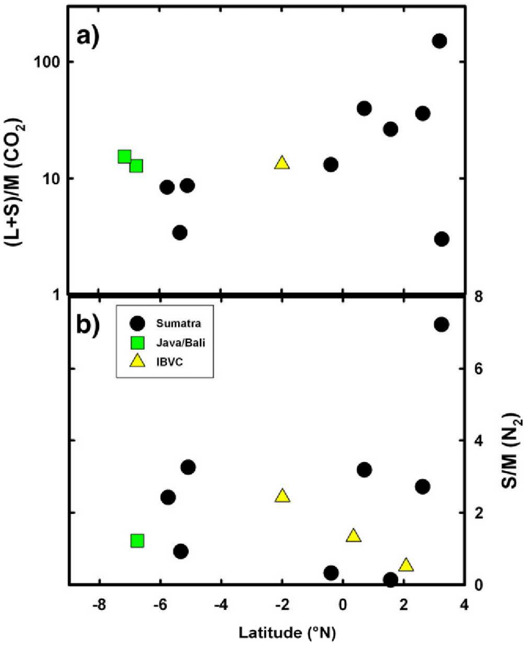

Fig. 10. a) Plot of (L + S)/M (CO_2) as a function of latitude. Preferential contribution from the two sedimentary components (L + S) over the mantle component (M) is evident from south to the north. b) Plot of S/M (N_2) as a function of latitude. No apparent latitudinal changes are observed although we note the high L/M ratio (~7) at Sibayak.

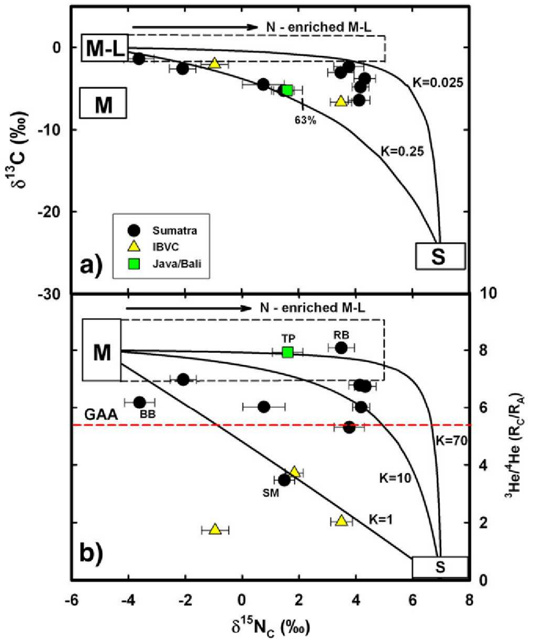

Fig. 11. a) Plot of carbon and nitrogen isotopes (δ^{15}N-corrected for air) in geothermal gases from the western Sunda arc. Binary mixing between a MORB–carbonate mixture (M–L) and a sedimentary component (S) with organically-derived carbon and nitrogen explains the data. Significantly, a component that hosts unmodified mantle wedge volatiles (M) is not likely to play a role, at least not in controlling the carbon characteristics. K mixing values between 0.025 and 0.25 demonstrate significant heterogeneity in the N/C ratio in one or both end-members. Tick indicates 63% mantle-carbonate (M-L) contribution. Dashed horizontal box indicates the possible composition of an N-enriched M–L end-member. b) Plot of helium and nitrogen isotopes (both corrected for air) for the same samples as in a). By adopting a value of 5.4 R_A as the lower limit for the mantle wedge He, a simple binary mixing between the mantle wedge and subducted sediments can explain most of the data. Samples from the volcanic centers can be explained by K values between 1 and 70, and demonstrate large enrichment of the sediment N_2/He ratios, relative to those of the mantle, which is consistent with fluids being dominated by MORB helium and subducted sedimentary nitrogen. Significantly lower K values (≤1) are needed to explain all other samples. Dashed horizontal box indicates the possible composition of a N-enriched M–L end-member. BB: Bual Buali, SM: Sorik Marapi, TP: Tangkuban Parahu, RB: Rajabasa.

a function of latitude. We note that in contrast to results from carbon, there are no major spatial (i.e., latitudinal) changes in the N_2 provenance characteristics along the N-S profile of the western Sunda arc. However, we note that samples from Sibayak have the highest S/M ratios of ~7. We infer that the sedimentary nitrogen contribution is mostly consistent along the strike of the arc although the highest value occurs in the northernmost regions. This observation is consistent with the (sedimentary) origin of CO_2 which also appears enhanced in northern Sumatra (Section 5.3.1 and Fig. 10a).

5.3.3. Co-variations of He, C and N isotopes

The first-order observation of C and N isotope variations along the western Sunda arc suggests that marine carbonate and organic sedimentary material are the dominant contributors of CO_2 and N_2 to the volatile budget, respectively. In Fig. 11a, we plot $\delta^{13}C$ (CO_2) versus $\delta^{15}N_c$ (N_2) for all gas samples from each location containing the highest $^3He/^4He$ together with end-member components M (MORB mantle), M-L (MORB-carbonate hybrid) and S (sediments) (Sano and Marty, 1995; Marty and Dauphas, 2003a; Li and Bebout, 2005). The IBVC samples (triangles) are plotted for comparison. A model of binary mixing between a C-fluxed (M–L hybrid) MORB mantle wedge and carbonate sediments, readily explains these relationships (Fig. 11a). The relative C/N ratios between sedimentary and mantle wedge components is expressed as K-values (where $K = (C/N)_S/(C/N)_M$). K values are ≪1 and range from 0.025 to 0.25, indicating that the sedimentary end-member is characterized by a marked enrichment in its N/C ratio relative to a MORB-carbonate mixture (i.e., M–L). This observation is consistent with calculated S/M ratios in Table 3. Conversely, the relatively high C/N ratio of the MORB-carbonate end-member likely reflects large-scale slab C-devolatilization which enriches the overlying mantle wedge in CO_2. Thus, the mixing relationships are consistent with carbon being derived primarily from the M–L mixture, whereas the nitrogen owes its provenance primarily to the S component.

An alternative explanation involves mixing with N-enriched carbonates in the mantle wedge (e.g., Li and Bebout, 2005). Given that calcareous diatomaceous ooze and breccia may contain up to 200 ppm N with largely positive $\delta^{15}N$ values (up to +5‰) (Li and Bebout, 2005) and assuming that N in the M–L end-member is mantle-like (i.e., [N] = 1 ppm and $\delta^{15}N = -5‰$), a simple mass balance implies that the M–L end-member can have more positive $\delta^{15}N$ values (see dashed horizontal box in Fig. 11a). However, mixing with N-enriched carbonates is not consistent with observed negative $\delta^{15}N$ values.

To further test this mixing scenario, we plot $^3He/^4He$ versus $\delta^{15}N_c$ together with end-member components MORB and sediments (see Fig. 11b caption for details). We also plot the IBVC samples for comparison and explore the role of the N-enriched M–L hybrid end-member (dashed box). Adopting a value of 5.4 R_A as the lower limit for He liberated from the mantle wedge (Hilton et al., 2002), we can

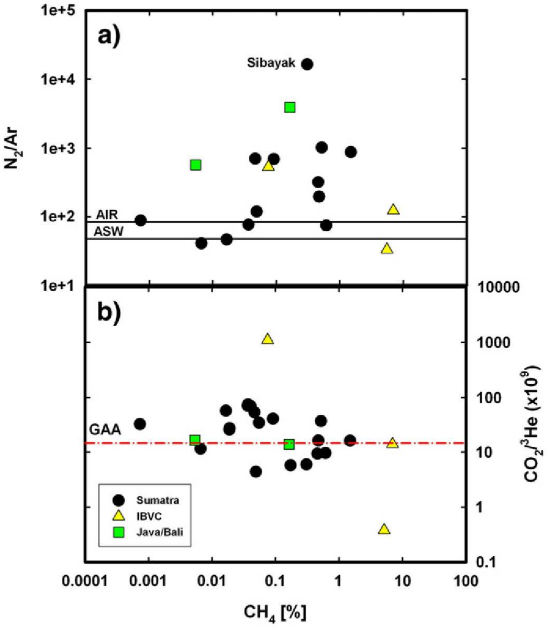

Fig. 12. a) Plot of the N_2/Ar ratio vs. CH_4 [%] content. Note that samples from Rimbo Panti and Dusan Baru (triangles), which have very high CH_4 contents, are not accompanied by high N_2/Ar ratios. Also, Sibayak has a high N_2/Ar ratio but only a modest amount of CH_4. b) Plot of the $CO_2/^3He$ ratio vs. CH_4 [%] content. The lack of correlation argues against any significant shallow level additions of carbon.

readily explain the data which fall above the 5.4 R_A threshold with simple binary mixing between MORB mantle and subducted sediments. Except for one sample from Bual Buali, all data from the volcanic centers can be modeled with K-values between 1 and 70 (where $K = (N/He)_S/(N/He)_M$), demonstrating the relative enrichment of the sedimentary end-member N/He values relative to that of the mantle. Indeed, we note that majority of our data can be explained with K-values between 1 and 10 which is consistent with S/M ratios in Table 3. However, samples from Tangkuban Parahu (SUM10-1) and Rajabasa (SUM10-2) require either extreme N enrichments or He deletion in the S end-member. For these 2 samples, fluids are dominated by MORB-like helium and subducted sedimentary nitrogen such that the N-enriched M-L end-member is capable of explaining the data. Interestingly, samples from the IBCV localities, in addition to one flank sample from Sorik Marapi, all of which have $^3He/^4He < 5.4$ R_A, can only be fitted with significantly lower K values (1 and less). This could suggest that they been affected by mixing with a different sedimentary end-member that has a lower $^3He/^4He$ and/or N/He ratio. We suggest that old crustal basement could have the required features (high He content due to age, and consequent low $^3He/^4He$ ratio due to radiogenic He addition) to satisfy the characteristics of such an end-member (e.g., Hilton et al., 1993).

5.4. Crustal volatile input?

Analogous to the carbon isotope system, the fundamental issue with nitrogen isotopes is that they cannot easily separate shallow crustal sediment components from deep subducted sediments as these end-members have overlapping isotopic characteristics. Thus, an alternative explanation for the C and N isotope relationships along the western Sunda arc involves assimilation and/or addition of volatiles from pre-existing crustal basements of the Sundaland crust. For example, interaction of magmatic volatiles with a crustal limestone component containing essentially no mantle-derived nitrogen, but with embedded organic nitrogen, could potentially represent the S end-members in Fig. 11a and b.

The degree of crustal contamination caused by the interaction between, or by the assimilation of, crustal volatiles can be directly addressed by $^3He/^4He$ ratios where the assimilation of crustal volatiles would be expected to lower the $^3He/^4He$ ratios. We have shown previously (Section 5.1.2.3) that the nature of the contaminant actively affecting water samples is inconsistent with a crustal limestone. Rather, the thick crustal lithologies of the Sundaland crustal core, which the magmas inevitably bypass, are likely to play a role in modifying the volatile budget of the Sumatran arc system. However, given the lack of significant radiogenic additions to the helium inventory of gas samples at volcanic centers along the arc, the effect is likely to be muted. Magmatic helium, therefore, primarily originates from the mantle wedge and reveals the presence of primordial ^3He transferred from the mantle. Those locations showing (minor) additions of radiogenic helium reveal inputs from (1) old and altered subducted oceanic crust, and/or (2) the overriding continental crust (e.g., Hilton et al., 2002). We now consider additional information from methane regarding crustal inputs to the major volatile inventory.

5.4.1. Methane–nitrogen–carbon abundance relationships

The abundance of CH_4, and its relationship to other volatile species, are powerful tracers of shallow-level additions to the volatile inventory (Taran et al., 1998; Taran and Giggenbach, 2003). Some samples in our dataset, particularly those sampled by IBVC, contain significant CH_4 (up to ~7%, see Table 2) so can be considered to be affected by shallow-level volatile additions. Thermal decomposition of sedimentary rocks can potentially also produce N_2, which can be readily identified by high ratios of N_2/Ar and N_2/He (Taran and Giggenbach, 2003). Therefore, hydrothermal fluids with high CH_4 content and high N_2/Ar are likely to have experienced additions of volatiles (shallow-level contamination) from organic material in the crust. This line of reasoning led Taran and Giggenbach (2003) to propose that volcanic gases and hydrothermal fluids could be distinguished by two different relationships as a reflection of their deep (volcanic) versus shallow (hydrothermal) origin. They suggested that volcanic gases from subduction zones are likely to have very little CH_4 but should be characterized by high N_2/Ar (and N_2/He) ratios as a consequence of degradation of subducted organic sediments.

To test this hypothesis, we plot N_2/Ar ratio vs. CH_4 concentration for all gas phase samples (Fig. 12a). We note that some samples with very high CH_4 content (e.g., the IBVC localities: Dusan Baru and Rimbo Panti) do not show correspondingly high N_2/Ar values despite their He isotope ratios being the lowest among our gas phase samples, suggesting that they have not sampled significant N_2 from the underlying crust. Furthermore, we do not observe any indication of a correlation between CH_4 and N_2/Ar for the remaining volcanic center samples from Sumatra and Java. For example, volcanic fluids sampled from active fumaroles at the summit of Sibayak volcano have high N_2/Ar values yet only modest CH_4 (~0.2%). This observation implies that the high N_2/Ar signal is a subducted sediment indicator rather than a crustal feature.

In Fig. 12b, we consider the relationship between $CO_2/^3He$ and CH_4 to assess possible crustal additions to the CO_2 budget. We note that there is no indication of a clear correlation between the CH_4 content and $CO_2/^3He$ for the volcanic centers and/or the IBVC localities. This observation implies that localities, such as the IBVC, which have been clearly affected by input of radiogenic helium, show insignificant addition of CO_2 during the process of crustal contamination. However, decarbonation reactions may explain high $CO_2/^3He$ ratios ($>1000 \times 10^9$) in samples from one of the IBVC localities (Helatoba–Tarutung), but there is no indication in our data that such reactions produced

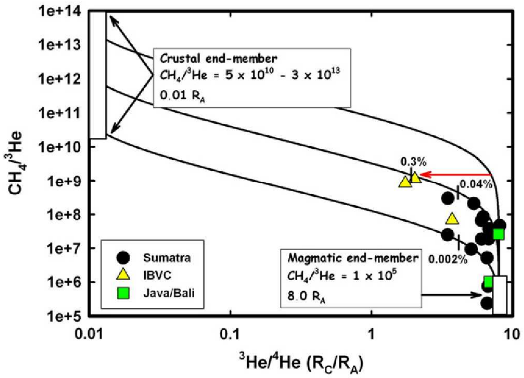

Fig. 13. Plot of $CH_4/^3He$ vs. helium isotopes. Solid lines indicate two-component mixing of magmatic end-member ($CH_4/^3He = 1.0 \times 10^5$, $^3He/^4He = 8.0R_A$) and crustal lithologies with three possible end-members compositions ($CH_4/^3He = 5.0 \times 10^{10}$; 1.3×10^{12}, 3.0×10^{13} with a common $^3He/^4He = 0.01R_A$). Relatively minor inputs from crustal material (<0.3%) are needed to explain the data (assuming 1.3×10^{12} as the value for the crustal end-member $CH_4/^3He$ ratio), including samples from the IBVC localities. The red horizontal arrow shows addition of a pure radiogenic helium crustal component from a point along the uppermost mixing line.

significant CH_4 concentrations. Thus, to conclude, the $CH_4-N_2-CO_2$ abundance relationships at the volcanic centers are inconsistent with CO_2 and N_2 being derived from shallow crustal and/or sedimentary sources. Rather, the CO_2 and N_2 primarily originate from sediment associated with the subducting sedimentary slab beneath the western Sunda arc.

5.4.2. Methane – ^{3}He relationships

As ^{3}He is predominantly derived from the mantle wedge, it can be assumed that unmodified mantle-derived gases should show fairly limited ranges in elemental ratios involving ^{3}He. Therefore, any significant variations in ratios of CH_4 to ^{3}He beyond the constraints provided by MORB would suggest a non-mantle origin. In Fig. 13 we plot $CH_4/^3He$ vs. helium isotopes for all gas phase samples, adopting a two-component crust-mantle mixing model similar to that used by Poreda et al. (1986, 1988) and Jenden et al. (1993) for subduction zone natural gases. Since the $CH_4/^3He$ ratio of the crustal end-member is not well constrained, we adopt three possible end-members compositions ($CH_4/^3He = 5.0 \times 10^{10}$; 1.3×10^{12}, 3.0×10^{13} with a common $^3He/^4He = 0.01\ R_A$). For the magmatic end-member we adopt a typical upper mantle value ($CH_4/^3He = 1.0 \times 10^5$, $^3He/^4He = 8.0\ R_A$) (see also Welhan and Craig, 1983; Poreda et al., 1988; Jenden et al. 1993; Snyder et al., 2003 for discussion on possible end-member compositions).

In Fig. 13, we note the following features of the western Sunda arc data: (1) $CH_4/^3He$ ratios are typical of subduction zone gases, i.e., they range from $\sim 1 \times 10^6$ to 1×10^9 (Snyder et al., 2003), (2) irrespective of the crustal end-member value selected, the mixing model demonstrates the relatively minor input needed from sedimentary material to explain the overall variation in samples from the volcanic centers. In this respect, the highest crustal and/or sediment contribution (<0.3%) is evident for the IBVC localities (assuming 1.3×10^{12} as the value for the crustal end-member $CH_4/^3He$ ratio), and (3) a single value for the crustal end-member $CH_4/^3He$ ratio is inappropriate for all samples. An alternative explanation to a variable crustal end-member involves adding a pure radiogenic helium crustal component from a point along the uppermost mixing line (as shown with the red horizontal arrow in Fig. 13 - from Jenden et al., 1993). In either case, we conclude that the methane–helium relationships again point to a minimal role of (upper) crustal contributions to the volatile inventory in the western Sunda arc.

5.5. Geological and tectonic control on the volatile budget

5.5.1. Crustal control on the volatile budget

Gasparon and Varne (1998) argued that the extent of crustal contamination increases from east to west along the Sunda arc (including Sumatra) with a concomitant diminishing role for subducted sediment influence in the petrogenesis of erupted lavas. They argued that this conclusion was consistent with increased sediment flux into the trench in the eastern part of the arc, and with the fact that large parts of the sediments are scraped off in the fore-arc region off the coast of Sumatra. The evidence presented was primarily based on profiles of radiogenic isotopes (Sr, Nd and Pb) along the Sunda arc which showed increasing radiogenic compositions to the west (see also Whitford, 1975). These results are consistent with the contrasting crustal regime between the western and eastern Sunda arc (Section 2). The Toba volcanics, and other tuffs from Sumatra, showed the highest radiogenic isotope composition in the western Sunda arc although an important caveat is that these samples may not be representative of the Sumatran arc magmas due to prolonged residence time in crustal reservoirs and consequently a large crustal signal (Chesner, 1998; Vazquez and Reid, 2004). Recently, mineral separates from the Toba volcanics have revealed a clear radiogenic helium signature ($R_A < 1.9$) (Budd et al., 2012b), supporting the notion that Toba volcanics are not useful for distinguishing between changes in crustal contamination versus mantle source contamination features along the arc, and should therefore be excluded from such comparisons due to their biased crustal signal. A similar conclusion was reached by Turner and Foden (2001).

Although crustal contamination may be more prominent in Sumatra compared to other sections of the Sunda arc, our study of volatiles in the western Sunda arc system does not support a scenario of extensive crustal controls on the volatile systematics, at least at the volcanic centers. A large number of samples of this study have only experienced relatively minor crustal contamination which only becomes significant at significant distances from the volcanic centers (i.e., IBVC localities). These results may appear somewhat surprising given the relatively thick continental crust on which most of the western Sunda arc is built. However, we note that MORB-like $^3He/^4He$ ratios ($8 \pm 1\ R_A$) (Graham, 2002) as opposed to arc-like ($5.4 \pm 1.9\ R_A$) (Hilton et al., 2002) are a characteristic feature of only very few samples from Sumatra whereas four out of six of our samples from Java and Bali fall within the MORB field. Again, this observation is consistent with along-arc changes in isotope signatures (e.g., Whitford, 1975; Hilton and Craig, 1989; Turner and Foden, 2001) and the contrasting crustal regimes of the Sunda arc. Furthermore, they highlight the sensitivity of helium isotopes to identify upper crustal contamination unrelated to subduction zone processes (Gasparon et al., 1994). We emphasize, however, that upper level contamination, as traced by helium isotopes, has only very minor effects on the major volatile budget for the passively-degassing volcanoes of this study. On the other hand, actively-degassing (i.e., erupting) volcanoes may enhance crustal interaction and liberate additional volatiles unrelated to the magmatic system (cf. Troll et al., 2012).

5.5.2. Subducting sedimentary control on the major volatile budget

A fundamental question regarding understanding the geochemical signatures discussed above is whether the sediments overlying the downgoing oceanic plate are subducted into the mantle or if they are simply scraped off in the fore-arc region. The Nicobar Fan off Sumatra, which constitutes the main part of the sedimentary pile, is supplied with sedimentary material (turbidite sands) from the Bengal Fan, itself derived predominantly from the uplifted Himalaya terrain, and is delivered through the Ganges–Brahmaputra river system (Curray, 1994). Owing to the presence of the structurally-high Ninety

East Ridge, most material carried to the ocean by the Meghna River is deposited west of the Ridge. These sediments are rich in quartz and chlorite-illite clay minerals (Ingersoll and Suczek, 1979), whereas in the fore-arc region off Sumatra, and adjacent to the Java segment, the sediments are mostly derived from the arc itself. They consist mainly of siliceous-clastic sediments and volcano-derived material. Based on observations from the island of Nias, off the coast of Sumatra, Moore and Curray (1980) suggested that large sections of the sediments of the incoming oceanic crust are indeed off-scraped to form the accretionary prism. These estimates are similar to independent estimates reported by Clift and Vannucchi (2004) who calculated 13% accretion efficiency (material accreted relative to material subducted) for Sumatra and 26% for Java.

Additional evidence for significant off-scraping is the lack of ^{10}Be anomalies in the Sunda arc system. ^{10}Be is a ubiquitous tracer of oceanic sediment input to arc volcanics (Morris et al., 1990) and the lack of significant ^{10}Be anomalies in Sunda arc lavas (Tera et al., 1986; Edwards et al., 1993) argues against significant recycling of late- and post Miocene sediments. In order to explain the extremely low ^{10}Be concentrations in Java volcanics, Edwards et al. (1993) argued that sediments which eventually might be related to magma generation processes in the Sunda arc are simply too old to still have active ^{10}Be. Currently, there are no ^{10}Be data available from the Sumatran subduction zone, but its main features, i.e., shallow slab dips, the relatively slow convergence rate, and the occurrence of a massive accretionary prism offshore Sumatra, make it even less likely that significant ^{10}Be anomalies will be found. Also, during off-scraping, the topmost sedimentary part is likely to be preferentially removed, thus leaving older sediments to be subducted: these sediments have very little or no active ^{10}Be remaining once they are dehydrated and eventually contribute to magma generation.

On the basic of U-series and radiogenic isotopes, Turner and Foden (2001) proposed, however, that sediment input must remain high along the Sunda arc, even though the crustal signature is most prominent in Sumatra. On the basis of our volatile data we thus favor a sedimentary, rather than crustal control, on the observed along-arc variation in the carbon systematics (Fig. 10a). In detail, we envision four potential scenarios which could explain our volatile data: 1) subducted sediments of the Nicobar Fan off Sumatra are thicker towards the source and as a result more sediments are subducting in the north (Sumatra) relative to the south (Java). This is supported by observation of Moore et al. (1980) that reported a significant increase in sediment thickness west of Java, with maximum thickness (~5 km) south of Sumatra. Furthermore, Clift and Vannucchi (2004) estimated a significant increase in material subduction rate in Sumatra (72 km^3/my) compared to Java (40 km^3/my), 2) more sediments are being off-scraped in the southern segment relative to northern segment, which is in agreement with observations from central Java and eastwards suggesting that very little sedimentary material enters the mantle owing to the dominance of an erosional subduction regime (Clift and Vannucchi, 2004; Kopp et al., 2006), 3) subduction of fossil spreading centers and/or oceanic plateaux and seamounts in the northeast Indian Ocean may also potentially explain these features, as they are associated with greater sediment thickness (e.g., Singh et al., 2011), 4) a sampling bias due to the fact that we have fewer samples from the south. Regardless of the exact scenario, our data support the dominant control of subducted sediments on the major volatile budget of the western Sunda arc which is in agreement with studies of other arc-systems (e.g., Varekamp et al., 1992; Sano and Marty, 1995).

6. Conclusions

A detailed study of the chemical and isotope (He – C – N) composition of volatiles associated with active fumaroles and hydrothermal fluids from passively-degassing volcanic and other centers along the western Sunda arc has revealed the following observations. Helium isotopes at volcanic centers are consistent with the mantle wedge being the principal He contributor to the arc with only relatively minor additions of radiogenic helium from the crust, most notably on volcanic flanks and on fault-related hydrothermal systems between major volcanic centers. The CO_2 and N_2 results show considerable variation along a N–S transect of the arc, consistent with contributions from both sedimentary and mantle-derived components. However, large input of shallow crustal volatiles to the volcanic centers is not supported by ^{3}He^{4}He – δ^{13}C – δ^{15}N variations or by gas chemistry (e.g., methane relationships). In this case, shallow-level crustal contamination plays only a minor role in the volatile inventory of the western Sunda arc and the subducting slab is the principal provider of volatiles. The increased contribution to the CO_2 budget from sedimentary components in the north of Sumatra likely reflect the thickening of the Nicobar Fan towards its source and consequently higher rates of material subducted in Sumatra compared to Java and Bali.

Acknowledgments

We are very grateful to Dr. Ir. A. Djumarma Wirakusumah (Geological Survey of Indonesia) for support of our 2010 field expedition. Funding for this expedition was provided by the Academic Senate (UC San Diego), discretionary funds of the Fluids and Volatiles Laboratory, Scripps Inst. Oceanography and the Swedish Science Foundation (VR), Uppsala University Centre for Natural Disaster Science (CNDS) and Otterborgska donationsfonde. The 1991 expedition was supported by Dr. Sukamto (Indonesian Geothermal Research Development Center) and funded by the German Science Foundation (DFG) and the Australian Research Council. Assistance in the field was provided by Kardana Hardjadinata, Massimo Gasparon and the late Rick Varne (1991) and Mas Majhum, Ester Jolis, Carmela Freda and David Budd (2010). Konrad Hammerschmidt (Berlin) and Bruce Deck (SIO) are thanked for laboratory assistance. Support of the SIO Fluids & Volatile Laboratory and the UNM Volcanic Fluids Laboratory is provided by the US National Science Foundation (EAR/IF-0651097 and EAR/IF-0743540, respectively). Tobias Fischer's contribution to finalizing the paper was supported by an IRD during an IPA assignment at the US National Science Foundation. Peter Barry provided useful comments on the manuscript and Joe Curray provided essential background on the Sunda arc. We thank two anonymous reviewers for their useful and constructive comments.

Appendix A. Correcting for atmosphere-derived nitrogen in δ^{15}N values

Central to the utility of nitrogen isotopes as a geochemical tracer is the assumption that the atmosphere-derived nitrogen component can be resolved from magmatic and/or sedimentary components contributing to the measured nitrogen inventory. We tested two atmosphere-correction methods, which are described in turn:

Correction based on δ^{15}N and N_2/He ratios

Following Fischer et al. (2002), the atmosphere-component can be subtracted based upon the measured N_2/He ratio. To further understand the N_2 budget of the western Sunda arc, we plot measured N_2/He vs. measured δ^{15}N for the filtered dataset along with mantle (M), sediment (S) and air end-members (A) in Fig. A1. A key advantage of this plot is that it allows visual inspection of samples which either fall within or outside the mixing envelopes defined by end-member compositions. Focusing on samples that fall within the M–S–A mixing envelope (14 out of 24 samples in the present case), we can calculate fractions derived from the N-sources for each sample. We first solve the mass balance equations of Sano et al. (1998), which describe the relative contribution from each of these reservoirs (M, S and A) in the following manner:

$$\delta 15N_{obs} = f_{man} \times \delta^{15}N_{man} + f_{sed} \times \delta^{15}N_{sed} + f_{air} \times \delta^{15}N_{air} \tag{A1}$$

$$1/(N_2/He)_{obs} = f_{man}/(N_2/He)_{man} + f_{sed}/(N_2/He)_{sed} + f_{air}/(N_2/He)_{air} \tag{A2}$$

$$f_{man} + f_{sed} + f_{air} = 1 \tag{A3}$$

where subscripts obs = observed, man = mantle-derived, sed = sediment-derived, air = air-derived and f is the fraction for each of these end-members. Assuming that the air-derived component is not related to endogenic nitrogen so that nitrogen is derived from two sources only, it is possible to resolve the air-corrected $\delta^{15}N_C$ value into its presumed component structure using the following equation:

$$\delta^{15}N_c = f_{sed} \times \delta^{15}N_{sed} + (1 - f_{sed}) \times \delta^{15}N_{man} \tag{A4}$$

where $\delta^{15}N_c$ is the air-corrected $\delta^{15}N_c$ composition of the samples, $\delta^{15}N_{sed} = +7$‰, $\delta^{15}N_{man} = -5$‰, and f_{sed} is the fraction of sediment-derived nitrogen in a binary sediment-mantle mixture.

A clear conclusion when using this method for the western Sunda arc samples is that the sedimentary component dominates the nitrogen signature in the binary mixture. However, we also note that a significant number of data-points (10 put of 24) fall outside the mixing envelope defined by the three end-members (Fig. A1). For example, samples from Bual-Buali volcano display very low $\delta^{15}N$ values accompanied by high N_2/He. Although speculative, this observation could possibly be explained by elemental fractionation of He from N during magma degassing, due to solubility differences in melt (Lux, 1987; Libourel et al., 2003). In addition, two other localities with low N isotope values fall outside the M–A binary mixing curve (i.e., Marapi and Helatoba–Tarutung). This is similar to what has been observed previously in subduction zone fluids and has been attributed to the use of unrepresentative mantle end-member in the mixing model (Clor et al., 2005, Elkins et al., 2006, Mitchell et al., 2010). However, adoption of $\delta^{15}N$ values for the mantle end-member as low as −12‰ (e.g., Mohapatra and Murty, 2004) to accommodate these (outlier) samples is probably unwarranted given arguments that such low values represent experimental artifacts (Yokochi and Marty, 2006). Although we could speculate that He−N solubility differences in magmas of varying composition is the likely explanation for these samples, documented solubility data is first needed to give greater weight to this suggestion.

Correction based on air-normalized He/Ne elemental ratios

The use of the air-normalized He/Ne elemental ratios (multiplied by the ratio of the Bunsen coefficients) to correct for the presence of atmospheric-derived helium has proved successful in correcting measured helium isotope variations for air-He additions (see for example Craig, et al., 1978; Hilton, 1996).

In Fig. 3b, we plot our $\delta^{15}N$ values vs. X-values as a proxy for air contamination (see Section 4.2 and Table 1 footnote) to test the integrity of the correction for measured nitrogen isotope data. We note that if samples from the same locality do not show good agreement in measured $\delta^{15}N$ (outside the reported 1 sigma uncertainty) then values closer to the isotopic composition of air have significantly lower X-values. This applies to all duplicate measurements with the exception of summit samples from Sibayak volcano and Helatoba–Tarutung. Whether this contamination occurred in the field during sample collection and/or in the laboratory is difficult to address. Adopting methods similar to those for He isotopes, we are therefore able to correct for the presence of air N additions using the air-normalized He/Ne ratio using the following equation:

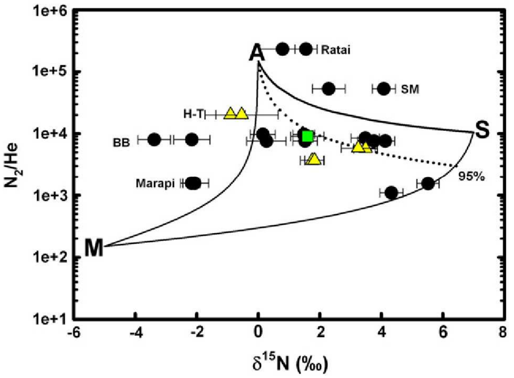

Fig. A1. Plot of N_2/He vs. $\delta^{15}N$ adopting end-members from Fischer et al. (2002), where M=mantle-derived nitrogen, S = sedimentary-derived nitrogen, and A = air-derived nitrogen. Dotted line reflects air addition to a mixture of mantle (5%) and sediment (95%) nitrogen. Samples from Bual Buali (BB), Ratai, Sorik Marapi (SM), Marapi and Helatoba–Tarutung (H–T) fall outside of the mixing envelope. Symbols as in Fig. 3.

$$\delta^{15}N_c = \left[\left(\delta^{15}N_{obs} \times X\right) - 1\right] / (X - 1). \tag{A5}$$

where X is the air-normalized He/Ne elemental ratios (see Table 1 footnote) and $\delta^{15}N_{obs}$ is the measured values. Using this methodology, we corrected the measured $\delta^{15}N$ values (reported as $\delta^{15}N$ in Table 1) to $\delta^{15}N_C$. Notably, only in the case of three samples, two water phase samples (SUM10-9 and SUM10-15) and one sample with very low X value (SUM10-25) did the corrected values differ from measured values by over 1‰ (from 1.01‰ to 1.75‰, respectively). All other corrected values agreed within 0.30‰, i.e., close to the analytical uncertainty of our $\delta^{15}N$ system. For the present dataset, another advantage of this approach is that measured $\delta^{15}N$ values < 0‰ (i.e., SUM10-20, SUM10-25, Cu-tube-3) correct to even lower $\delta^{15}N_c$ values as the air-derived component is subtracted. This is not possible using the N_2/He approach above as these samples fall outside the mixing envelope defined by the A–M end-members.

References

Barry, P.H., Hilton, D.R., Halldórsson, S.A., Hahm, D., Marti, K., 2012. High precision nitrogen isotope measurements in oceanic basalts using a static triple collection noble gas mass spectrometer. Geochemistry, Geophysics, Geosystems 13, Q01019. http://dx.doi.org/10.1029/2011GC003878.

Barry, P.H., Hilton, D.R., Fischer, T.P., de Moor, J.M., Mangasini, F., Ramirez, C.J., 2013. Helium and carbon isotope systematics of cold "mazuku" CO_2 vents and hydrothermal gases and fluids from Rungwe Volcanic Province, southern Tanzania. Chemical Geology 339, 141–156.

Budd, D.A., Troll, V.R., Hilton, D.R., Freda, C., Jolis, E.M., Halldórsson, S.A., 2012a. Traversing nature's danger zone: getting up close with Sumatra's volcanoes. Geology Today 28, 64–70.

Budd, D.A., Troll, V.R., Jolis, E.M., Deegan, F.M., Smith, V.C., Whitehouse, M.J., Harris, C., Freda, C., Hilton, D.R., Halldórsson, S.A., 2012b. Reconstructing the Toba magmatic system: insights from stable isotope geochemistry. Goldschmidt, abstract, Montreal .

Cartigny, P., Ader, M., 2003. A comment to "The nitrogen record of crust–mantle interaction and mantle convection from Archean to Present" by B. Marty and N. Dauphas. Earth and Planetary Science Letters 216, 425–432.

Chesner, C.A., 1998. Petrogenesis of the Toba Tuffs, Sumatra, Indonesia. Journal of Petrology 39, 397–438.

Chesner, C.A., Rose, W.I., Deino, A., Drake, R., Westgate, J.A., 1991. Eruptive history of Earth's largest Quaternary caldera (Toba, Indonesia) clarified. Geology 19, 200–203.

Clift, P., Vannucchi, P., 2004. Controls on tectonic accretion versus erosion in subduction zones: implications for the origin and recycling of the continental crust. Reviews of Geophysics 42, RG2001. http://dx.doi.org/10.1029/2003RG000127.

Clor, L.E., Fischer, T.P., Hilton, D.R., Sharp, Z.D., Hartono, U., 2005. Volatile and N isotope chemistry of the Molucca Sea collision zone: tracing source components along the

Sangihe Arc, Indonesia. Geochemistry, Geophysics, Geosystems 6, Q03J14. http://dx.doi.org/10.1029/2004GC000825.

Craig, H., Lupton, J.E., Horibe, Y., 1978. A mantle helium component in circum-Pacific volcanic gases: Hakone, the Marianas and Mt. Lassen. In: Alexander, E.C., Ozima, M. (Eds.), Terrestrial Rare Gases. Central Academic Publishers, Tokyo, pp. 3–16.

Craig, H., Marti, K., Wiens, R., 1993. A static mass spectrometer with triple collection for nitrogen and neon isotopes. SIO Reference Ser., 93–11. Scripps Inst. of Oceanogr, La Jolla, Calif, p. 1-20A.

Curray, J.R., 1994. Sediment volume and mass beneath the Bay of Bengal. Earth and Planetary Science Letters 125, 371–383.

De Leeuw, G.A., Hilton, D.R., Fischer, T.P., Walker, J.A., 2007. The He – CO_2 isotope and relative abundance characteristics of geothermal fluids in El Salvador and Honduras: new constraints on volatile mass balance of the Central American Volcanic Arc. Earth and Planetary Science Letters 258, 132–146.

De Leeuw, G.A., Hilton, D.R., Güleç, N., Mutlu, H., 2010. Regional and temporal variations in $CO_2/^3He$, $^3He/^4He$ and $\delta^{13}C$ along the North Anatolian Fault Zone, Turkey. Applied Geochemistry 25, 524–539.

Edwards, C.M.H., Morris, J.D., Thirlwall, M.F., 1993. Separating mantle from slab signatures in arc lavas using B/Be and radiogenic isotope systematics. Nature 362, 530–533.

Elkins, L.J., Fischer, T.P., Hilton, D.R., Sharp, Z.D., McKnight, S., Walker, J., 2006. Tracing nitrogen in volcanic and geothermal volatiles from the Nicaraguan volcanic front. Geochimica et Cosmochimica Acta 70, 5215–5235.

Fischer, T.P., Hilton, D.R., Zimmer, M.M., Shaw, A.M., Sharp, Z.D., Walker, J.A., 2002. Subduction and recycling of nitrogen along the Central American margin. Science 297, 1154–1157.

Fischer, T.P., Takahata, N., Sano, Y., Sumino, H., Hilton, D.R., 2005. Nitrogen isotopes of the mantle: insights from mineral separates. Geophysical Research Letters 32 2005GL022792.

Gasparon, M., 2005. Chapter 9: Quaternary volcanicity. In: Barber, A.J., Crow, M.J., Milsom, J.S. (Eds.), Sumatra: Geology, Resources and Tectonic Evolution. Geological Society Memoirs, 31, pp. 120–130.

Gasparon, M., Varne, R., 1995. Sumatran granitoids and their relationship to Southeast Asian terranes. Tectonophysics 251, 277–299.

Gasparon, M., Varne, R., 1998. Crustal assimilation versus subducted sediment input in west Sunda arc volcanics: an evaluation. Mineralogy and Petrology 64, 89–117.

Gasparon, M., Hilton, D.R., Varne, R., 1994. Crustal contamination processes traced by helium-isotopes—examples from the Sunda Arc. Indonesia. Earth and Planetary Science Letters 126, 15–22.

Gertisser, R., Keller, J., 2003. Trace element and Sr, Nd, Pb and O isotope variations in medium-K and high-K volcanic rocks from Merapi volcano, Central Java, Indonesia: evidence for the involvement of subducted sediments in Sunda arc magma genesis. Journal of Petrology 44 (3), 457–489.

Giggenbach, W.F., 1996. Chemical composition of volcanic gases. In: Scarpa, R., Tilling, R. (Eds.), Monitoring and Mitigation of Volcanic Hazards. Springer, pp. 221–256.

Graham, D.W., 2002. Noble gas isotope geochemistry of mid-ocean ridge and ocean island basalts: characterization of mantle source reservoirs. In: Porcelli, D., Ballentine, C.J., Wieler, R. (Eds.), Noble Gases in Geochemistry and Cosmochemistry. : Rev. Mineral. Geochem., vol. 47. Mineral. Soc. Am, Washington, DC, pp. 247–317.

Hamilton, W., 1979. Tectonics of the Indonesian region. U.S. Geol. Surv. Prof. Pap., 1078. 345 pp.

Hilton, D.R., 1996. The helium and carbon isotope systematics of a continental geothermal system: result from monitoring studies at Long Valley caldera (California, U.S.A.). Chemical Geology 127, 269–295.

Hilton, D.R., Craig, H., 1989. A helium isotope transect along the Indonesian archipelago. Nature 342, 906–908.

Hilton, D.R., Hammerschmidt, K., Teufel, S., Friedrichsen, H., 1993. Helium isotope characteristics of Andean geothermal fluids and lavas. Earth and Planetary Science Letters 120, 265–282.

Hilton, D.R., Gronvold, K., Sveinbjornsdottir, A., Hammerschmidt, K., 1998a. Helium isotope evidence for off-axis degassing of the Icelandic hotspot. Chemical Geology 149, 173–187.

Hilton, D.R., McMurtry, G.M., Goff, F., 1998b. Large variations in vent fluid $CO_2/^3He$ ratios signal rapid changes in magma chemistry at Loihi Seamount, Hawaii. Nature 396, 359–362.

Hilton, D.R., Fischer, T.P., Marty, B., 2002. Noble gases and volatile recycling at subduction zones. In: Porcelli, D., Ballentine, C.J., Wieler, R. (Eds.), Noble Gases in Geochemistry and Cosmochemistry. Rev. Mineral. Geochem., vol. 47. Mineral. Soc. Am, Washington, DC, pp. 319–370.

Holloway, J.R., Blank, J.G., 1994. Application of experimental results to C – O – H species in natural melts. In: Carrol, M.R., Holloway, J. (Eds.), Volatiles in Magmas. Rev. Mineral. Geochem., vol. 30. Mineral. Soc. Am, Washington, DC, pp. 187–230.

Ingersoll, R.V., Suczek, C.A., 1979. Petrology and provenance of Neogene sand from Nicobar and Bengal fans, DSDP sites 211 and 218. Journal of Sedimentary Petrology 49, 1217–1228.

Inguaggiato, S., Taran, Y., Grassa, F., Capasso, G., Favara, R., Varley, N., Faber, E., 2004. Nitrogen isotopes in thermal fluids of a forearc region (Jalisco Block, Mexico): evidence for heavy nitrogen from continental crust. Geochemistry, Geophysics, Geosystems 5, Q12003. http://dx.doi.org/10.1029/2004GC000767.

Jenden, P.D., Hilton, D.R., Kaplan, I.R., Craig, H., 1993. Abiogenic hydrocarbons and mantle helium in oil and gas fields. In: Howell, D.G. (Ed.), The Future of Energy Gases: USGS. Prof. Paper, 1570, pp. 31–56.

Kopp, H., Flueh, E.R., Petersen, C.J., Weinrebe, W., Wittwer, A., Meramex Scientists, 2006. The Java margin revisited: evidence for subduction erosion off Java. Earth and Planetary Science Letters 242, 130–142.

Li, L., Bebout, G.E., 2005. Carbon and nitrogen geochemistry of sediments in the Central American convergent margin: insights regarding subduction input fluxes, diagenesis and paleoproductivity. Journal of Geophysical Research 110, B11202. http://dx.doi.org/10.1029/2004JB003276.

Li, L., Bebout, G.E., Idleman, B.D., 2007. Nitrogen concentration and $\delta^{15}N$ of altered oceanic crust obtained on ODP Legs 129 and 185: insights into alteration-related nitrogen enrichment and the nitrogen subduction budget. Geochimica et Cosmochimica Acta 71, 2344–2360.

Li, L., Cartigny, P., Ader, M., 2009. Kinetic nitrogen isotope fractionation associated with thermal decomposition of NH_3: experimental results and potential implications to natural-gas and hydrothermal systems. Geochimica et Cosmochimica Acta 73, 6282–6297.

Libourel, G., Marty, B., Humbert, F., 2003. Nitrogen solubility in basaltic melt. Part I. Effect of oxygen fugacirty. Geochimica et Cosmochimica Acta 67, 4123–4135.

Lux, G., 1987. The behavior of noble gases in silicate liquids: solution, diffusion, bubbles and surface effects, with applications to natural samples. Geochimica et Cosmochimica Acta 51, 1549–1560.

Marty, B., Dauphas, N., 2003a. The nitrogen record of crust–mantle interaction and mantle convestion from Archean to Present. Earth and Planetary Science Letters 206, 397–410.

Marty, B., Dauphas, N., 2003b. "Nitrogen isotopic compositions of the present mantle and the Archean biosphere": reply to comment by Pierre Cartigny and Magali Ader. Earth and Planetary Science Letters 216, 433–439.

Marty, B., Jambon, A., 1987. $C/^3He$ in volatile fluxes from the solid Earth: implication for carbon geodynamics. Earth and Planetary Science Letters 83, 16–26.

Marty, B., Jambon, A., Sano, Y., 1989. Helium isotopes and CO_2 in volcanic gases of Japan. Chemical Geology 76, 25–40.

Mattey, D.P., 1991. Carbon dioxide solubility and carbon isotope fractionation in basaltic melt. Geochimica et Cosmochimica Acta 55, 3467–3473.

McCaffrey, R., 2009. The tectonic framework of the Sumatran Subduction Zone. Annual Reviews of Earth and Planetary Sciences, 37, pp. 345–366.

Mitchell, E.C., Fischer, T.P., Hilton, D.R., Hauri, E.H., Shaw, A.M., de Moor, J.M., Sharp, Z.D., Kazahaya, K., 2010. Nitrogen sources and recycling at subduction zones: insights from the Izu–Bonin–Mariana Arc. Geochemistry, Geophysics, Geosystems 11, Q02X11. http://dx.doi.org/10.1029/2009GC002783.

Mohapatra, R.K., Murty, S.V.S., 2004. Nitrogen isotopic composition of the MORB mantle: a reevaluation. Geochemistry, Geophysics, Geosystems 5, Q01001. http://dx.doi.org/10.1029/2003GC000612.

Moore, G.F., Curray, J.R., 1980. Structure of the Sunda Trench lower slope west of Sumatra from multichannel seismic reflection data. Marine Geophysical Researches 4, 319–340.

Moore, G.F., Curray, J.R., Moore, D.G., Karig, D.E., 1980. Variations in deformation along the Sunda forearc, northeast Indian Ocean. In: Hayes, D.E. (Ed.), Geophys. Monograph. The tectonic and geologic evolution of Southeast Asian seas and islands: Geoph. Mon., vol. 23, pp. 145–160.

Morris, J.D., Leeman, W.P., Tera, F., 1990. The subducted component in island arc lavas: constraints from Be isotopes and B-Be systematics. Nature 344, 31–36.

Ozima, M., Podosek, F.A., 2002. Noble Gas Geochemistry, 2nd ed. Cambridge Univ. Press, New York. 286 pp.

Peters, K.E., Sweeny, R.E., Kaplan, I.R., 1978. Correlation of carbon and nitrogen stable isotope ratios in sedimentary organic matter. Limnology and Oceanography 23, 598–604.

Poreda, R., Craig, H., 1989. Helium isotope ratios in circum-Pacific volcanic arcs. Nature 338, 473–478.

Poreda, R.J., Jenden, P.D., Kaplan, I.R., Craig, H., 1986. Mantle helium in Sacramento basin natural gas wells. Geochimica et Cosmochimica Acta 50, 2847–2853.

Poreda, R.J., Jeffrey, A.W.A., Kaplan, I.R., Craig, H., 1988. Magmatic helium in subduction zone natural gases. Chemical Geology 71, 199–210.

Ray, M.C., Hilton, D.R., Munoz, J., Fischer, T.P., Shaw, A.M., 2009. The effects of volatile recycling, degassing and crustal contamination on the helium and carbon geochemistry of hydrothermal fluids from the Southern Volcanic Zone of Chile. Chemical Geology 266, 38–49.

Sadofsky, S.J., Bebout, G.E., 2004. Nitrogen geochemistry of subducting sediments: new results from the Izu–Bonin–Mariana margin and insights regarding global nitrogen subduction. Geochemistry, Geophysics, Geosystems 5, Q03I15. http://dx.doi.org/10.1029/ 2003GC000543.

Sano, Y., Marty, B., 1995. Origin of carbon in fumarolic gas from island arcs. Chemical Geology 119, 265–274. http://dx.doi.org/10.1016/ 0009-2541(94)00097-R.

Sano, Y., Williams, S.N., 1996. Fluxes of mantle and subducted carbon along convergent plate boundaries. Geophysical Research Letters 23, 2749–2752.

Sano, Y., Nakamura, Y., Wakita, H., Urabe, A., Tominaga, Y., 1984. ^3He emission related to volcanic activity. Science 224, 150–151.

Sano, Y., Takahata, N., Nishio, Y., Marty, B., 1998. Nitrogen recycling in subduction zones. Geophysical Research Letters 25, 2289–2292.

Shaw, A.M., Hilton, D.R., Fischer, T.P., Walker, J.A., Alvarado, G., 2003. Helium and carbon relationships in geothermal fluids from the Central American arc in Costa Rica. Earth and Planetary Science Letters 214, 499–513.

Shilobreeva, S., Martinez, I., Busigny, V., Agrinier, P., Laverne, C., 2011. Insights into C and H storage in the altered oceanic crust: results from ODP/IODP Hole 1256D. Geochimica et Cosmochimica Acta 75, 2237–2255.

Sieh, K., Natawidjaja, D., 2000. Neotectonics of the Sumatran fault, Indonesia. Journal of Geophysical Research 105, 28295–28326.

Singh, S.C., et al., 2011. Aseismic zone and earthquake segmentation associated with a deep subducted seamount in Sumatra. Nature Geoscience 5, 308–311.

Smithsonian Institution, 2011. Marapi. Bulletin of the Global Volcanism Network 36 (7).

Smyth, H.R., Hamilton, P.J., Hall, R., Kinney, P.D., 2007. The deep crust beneath island arcs: inherited zircons reveal a Gondwana continental fragment beneath East Java, Indonesia. Earth and Planetary Science Letters 258, 269–282.

Snyder, G., Poreda, R., Fehn, U., Hunt, A., 2003. Sources of nitrogen and methane in Central American geothermal settings: noble gas and ^{129}I evidence for crustal and magmatic volatile components. Geochemistry, Geophysics, Geosystems 4 (1), 9001. http://dx.doi.org/10.1029/2002GC000363.

Szaran, J., 1997. Achievement of carbon isotope equilibrium in the system HCO^{-}_3 (solution)–CO_2 (gas). Chemical Geology 142, 79–86.

Taran, Y.A., Giggenbach, W.F., 2003. Geochemistry of light hydrocarbons in volcanic and hydrothermal fluids. Society of Economic Geologists Special Publication, 10, pp. 61–74.

Taran, Y., Fischer, T.P., Porovsky, B., Sano, Y., Armienta, M.A., Macias, J.L., 1998. Geochemistry of the volcano-hydrothermal system of El Chichón volcano, Chiapas Mexico. Bulletin of Volcanology 59, 436–449.

Tera, F., Brown, L., Morris, J., Sacks, I.S., Klein, J., Middleton, R., 1986. Sediment incorporation in island-arc magmas: inferences from ^{10}Be. Geochimica et Cosmochimica Acta 50, 535–550.

Troll, V.R., Hilton, D.R., Jolis, E.M., Chadwick, J.P., Blythe, L.S., Deegan, F.M., Schwarzkopf, L.M., Zimmer, M., 2012. Crustal CO_2 liberation during the 2006 eruption and earthquake events at Merapi volcano Indonesia. Geophysical Research Letters 39, L11302. http://dx.doi.org/10.1029/2012GL051307.

Turner, S., Foden, J., 2001. U–Th–Ra disequilibria. Sr–Nd–Pb isotope and trace element variations in Sunda arc lavas: predominance of a subducted sediment component. Contributions to Mineralogy and Petrology 142, 43–57.

van Soest, M.C., Hilton, D.R., Kreulen, R., 1998. Tracing crustal and slab contributions to arc magmatism in the Lesser Antilles island arc using helium and carbon relationships in geothermal fluids. Geochimica et Cosmochimica Acta 62, 3323–3335.

Varekamp, J.C., Kreulen, R., Poorter, R.P.E., van Bergen, M.J., 1992. Carbon sources in arc volcanism with implications for the carbon cycle. Terra Nova 4, 363–373.

Vazquez, J.A., Reid, M.R., 2004. Probing the accumulation history of the voluminous Toba magma. Science 305, 991–994.

von Huene, R., Scholl, D.W., 1991. Observations at convergent margins concerning sediment subduction, subduction erosion, and the growth of continental crust. Reviews of Geophysics 29, 279–316.

Weiss, R.F., 1971. Solubility of helium and neon in water and seawater. Journal of Chemical & Engineering Data 16, 235–241.

Weiss, R.F., 1974. Carbon dioxide in water and seawater: the solubility of a non-ideal gas. Marine Chemistry 2, 203–215.

Welhan, J.A., Craig, H., 1983. Methane, hydrogen and helium in hydrothermal fluids at 21°N on the East Pacific Rise. In: Rona, P.A., Bostrom, K., Laubier, L., Smith, K.L. (Eds.), Hydrothermal Processes at Seafloor Spreading Centers. Plenum Press, New York, pp. 391–409.

Whitford, D.J., 1975. Strontium isotopic studies of the volcanic rocks of the Sunda arc, Indonesia, and their petrogenetic implications. Geochimica et Cosmochimica Acta 39, 1287–1302.

Whitford, D.J., 1981. Neodymium isotopic composition of Quaternary island arc lavas from Indonesia. Geochimica et Cosmochimica Acta 45, 989–995.

Widiyantoro, S., van der Hilst, R., 1996. Structure and evolution of lithospheric slab beneath the Sunda Arc, Indonesia. Science 271, 1566–1570.

Yokochi, R., Marty, B., 2006. Fast chemical and isotopic exchange of nitrogen during reaction with hot molybdenum. Geochemistry, Geophysics, Geosystems 7, Q07004. http://dx.doi.org/10.1029/ 2006GC001253.

Zimmer, M.M., Fischer, T.P., Hilton, D.R., Alvarado, G.E., Sharp, Z.D., Walker, J.A., 2004. Nitrogen systematics and gas fluxes of subduction zones: insights from Costa Rica arc volatiles. Geochemistry, Geophysics, Geosystems 5. http://dx.doi.org/10.1029/2003GC000651.

II. Acknowledgements

In addition to those mentioned within the acknowledgements section of the published work, we also thank Elsevier for allowing us use a reprint of the material as it appeared in Chemical Geology, as Sæmundur Ari Halldórsson, David R. Hilton, Valentin R. Troll, Tobias P. Fischer, 2013. Resolving volatile sources along the western Sunda arc, Indonesia. *Chemical Geology*, Volume 339, Pages 263-282. doi.org/10.1016/j.chemgeo.2012.09.042. The dissertation author was the primary investigator and lead author of this paper and conducted all the analyses presented herein.

Chapter III: A common mantle plume source beneath the entire East African Rift System revealed by coupled helium-neon systematics

III.1 Abstract

We report combined He-Ne-Ar isotope data of mantle-derived xenoliths and/or lavas from all segments of the East Africa Rift System (EARS). Plume-like helium isotope ($^3He/^4He$) ratios (i.e., greater than the Depleted MORB Mantle (DMM) range of 8 ± $1R_A$) are restricted to the Ethiopia Rift and Rungwe, the southernmost volcanic province of the Western Rift. In contrast, neon isotope trends reveal the presence of an ubiquitous solar (plume-like) Ne component throughout the EARS, with $(^{21}Ne/^{22}Ne)_{EX}$ values (where $(^{21}Ne/^{22}Ne)_{EX}$ is the air-corrected $^{21}Ne/^{22}Ne$ ratio extrapolated to Ne-B) as low as 0.034, close to that of solar Ne-B (0.031). Coupling $(^{21}Ne/^{22}Ne)_{EX}$ with $^4He/^3He$ ratios indicates that all samples can be explained by admixture between a single mantle plume source, common to the entire rift, and either a DMM or sub-continental lithospheric mantle (SCLM) source. Additionally, we show that the entire sample suite is characterized by low $^3He/^{22}Ne_S$ ratios (mostly < 0.2) – a feature characteristic of oceanic hotspots such as Iceland. We propose that the origin of these unique noble gas signatures is the deeply rooted African Superplume which influences magmatism throughout eastern Africa. We argue that the Ethiopia and Kenya domes represent two different heads of this common mantle plume source.

III.2 Introduction

The East African Rift System (EARS) is regarded as the classic example of present-day rifting and continental breakup (Yirgu et al., 2006). The topography of the ~3000 km rift is dominated by two prominent plateaux – the Ethiopia and Kenya domes – separated by the low-lying Turkana Depression (Fig. 1). Gravity constraints and seismic imaging of the East African mantle indicate that upwelling of a large, continuous, thermo-chemical mantle plume (the African Superplume), originating at the core-mantle boundary, provides dynamic support for both domes

(Nyblade, 2011; Hansen et al., 2012). High $^3He/^4He$ ratios in volcanic lavas from the Ethiopian Rift in the north (Marty et al., 1996; Scarsi and Craig, 1996; Rooney et al., 2012) and at Rungwe Volcanic Province in the south (Hilton et al., 2011) indicate that a mantle plume component contributes to petrogenesis throughout the East African Rift. However, it remains unclear if one or more mantle plumes impinge the East African lithosphere to support the high plateaux (Ebinger and Sleep, 1998; Rogers, 2006).

Although helium isotopes are a key geochemical tracer of deep seated mantle plumes (Courtillot et al., 2003), taken alone, they cannot distinguish between the presence of a single plume source located in the EARS mantle, and sampled via multiple upwellings, or multiple mantle plumes originating at one or more boundary layers and supplying magma individually to different branches of the EARS. In contrast to extensive studies of He isotopes in eastern Africa (summarized in Pik et al., 2006 and Hilton et al., 2011), the Ne (and Ar) isotope systematics of the EARS remain poorly known in spite of potential to also identify provenance from the deep mantle (Honda et al., 1991; Yokochi and Marty, 2004 Kurz et al., 2009). Measuring He-Ne (and-Ar) isotope variations on the same sample suite offers the opportunity of testing (a) whether lavas and xenoliths erupted along different segments of the EARS possess the same unique coupled He-Ne isotopic signature that could identify a single mantle plume source, or (b) if differences between various rift segments reflect individual plumes which have evolved different He-Ne characteristics over time. Such an analytical strategy can potentially yield greater insight into key features of the EARS mantle in a manner not readily discernible using He isotopes alone.

III.3 Samples and Analytical Techniques

He-Ne-Ar isotope and abundance data of mafic minerals (OL=olivine, PX=pyroxene, GT=garnet) from mantle xenoliths (peridotite and pyroxenites) and basaltic lavas are reported in auxiliary Tables S1-S4. Sample localities are divided between different rift branches of the EARS: (i) Ethiopia Rift; xenoliths and lavas from currently active rift segments of the Red Sea, Afar, Main Ethiopian Rift (MER), in addition to xenoliths and lavas from Tertiary and Quaternary volcanic rocks of the Yerer-Tullu Wellel volcanic lineament and Ethiopian Highlands (Injibara, Lake Tana and the Dilb section), (ii) northern Kenya Rift (north of ~2°N); xenoliths from southern Ethiopia and northern Kenya, (iii) southern Kenya_Rift; xenoliths and lavas from southern Kenya and northern Tanzania, and (iv) Western Rift; lavas from Uganda, the Democratic Republic of the Congo, Rwanda (northern rift) and Rungwe Volcanic Province (RVP) (southern rift). All samples were processed by vacuum crushing, releasing volatiles from fluid and melt inclusions trapped within crystal lattices. Our analytical approach involves two individual crushing steps. First, we identify gas-rich minerals by measuring He isotopes and abundances. Second, we select samples with relatively high He (generally $> 1 \times 10^{-8}$ cm^3 STP/g) for Ne and Ar analyses. A complete description of the analytical methods is given in the auxiliary material.

III.4 Results

In **Figure 1,** we show the He isotope distribution of the EARS – a total of 339 new and published analyses of lavas and xenoliths (see Tables S1 and S2; auxiliary material). Geothermal fluid $^3He/^4He$ ratios are not included as shallow-level fluids can be susceptible to record additions of radiogenic (crustal) He which act to modify primary magmatic values – a likely process given the antiquity of basement lithologies in some parts of the EARS (Pik et al., 2006; Hilton et al., 2011; Barry et al., 2013). Good correspondence between $^3He/^4He$ ratios in xenoliths and phenocrysts are apparent – both within the same sample and between samples from the same location (see auxiliary material) – indicating that both sampling media provide representative (unbiased) He signatures. Sample $^3He/^4He$ ratios identify plume-like He (9-19R_A, n=112), DMM He (8 ± 1R_A: Graham, 2002, n=133), SCLM He (6.1 ± 0.9R_A: Gautheron and Moreira, 2002, n=74) and crustal He (<SCLM, n=20) – **Fig. 1**.

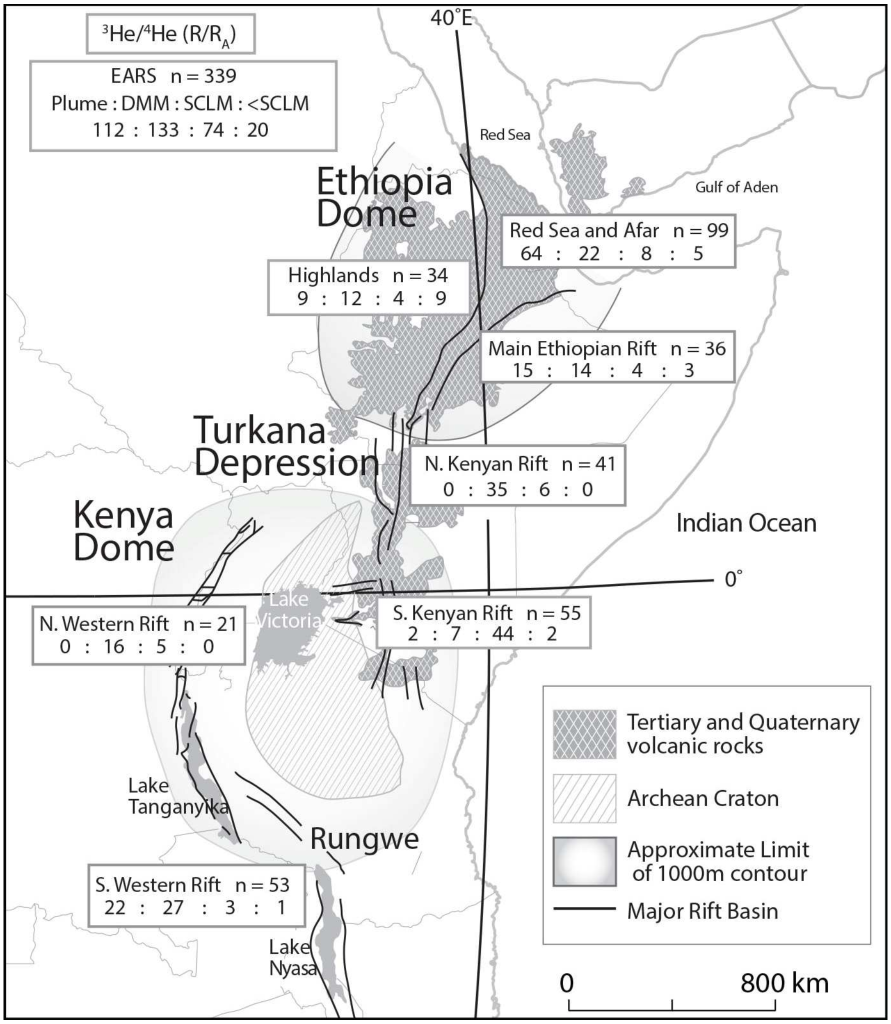

Figure III.1: Helium isotope variations (in R/R_A notation) in lavas and xenoliths of various rift segments of the East Africa Rift System. Results are divided into the following categories: plume-like He (9-19R_A), DMM He (8 ± 1R_A), SCLM He (6.1 ± 0.9R_A) and crustal He (<SCLM). Data sources: Table S1 and S2.

There are several noteworthy features of the He isotope distribution. First, a large number of samples in the Ethiopia Rift (Red Sea, Afar, MER, the Ethiopian Highlands) and RVP in the southern Western Rift (n=88 and 22, respectively) exceed the canonical range of 8 ± 1R_A, diagnostic of DMM. Second, 35 samples from the northern Kenya Rift, in addition to a number of samples from the Ethiopia Rift (n=48) and from the Western Rift (n=43) fall within the canonical DMM range, whereas only 7 samples from the southern Kenya Rift fall within this range. Third, the majority of samples from the southern Kenya Rift (n=44) fall within, or overlap with, SCLM. Finally, 20 samples from various segments display radiogenic He isotope values (<SCLM), diagnostic of crustal contamination – these represent only ~6 % of all samples. We targeted 56 samples containing between 0.8 to 1272 ($\times 10^{-9}$) cm^3STPHe/g for Ne and Ar isotope and abundance characterization (see auxiliary Table S3).

Neon isotopes are shown on a traditional 3-isotope plot in **Figure 2**. For reference, we plot mixing trajectories between air and the hypothetical solar neon end-member, representing neon captured at the time of planetary accretion (aka Neon-B), as well as some relatively well characterized Oceanic Island Basalts (OIB), DMM, and continental crust (Graham, 2002; Honda et al., 1991; Kurz et al., 2009). Notably, all trajectories intersect at the air value ($^{20}Ne/^{22}Ne$ = 9.8; $^{21}Ne/^{22}Ne$ = 0.029), reflecting the largely unavoidable air contamination of materials erupted onto Earth's surface. Of the 56 EARS samples, 25 only are distinct from the neon isotopic composition of air (at the 1σ error), and are plotted. Notably, all samples fall on trajectories steeper than that of DMM. Extrapolating the trend from air through each sample to a $^{20}Ne/^{22}Ne$ ratio of 12.5 (Ne-B: Black, 1972; Ballentine et al., 2005), gives the extrapolated $(^{21}Ne/^{22}Ne)_{EX}$ value, i.e., the air-free mantle $^{21}Ne/^{22}Ne$ ratio (see auxiliary material). There are two features of note: (a) 14 xenoliths and lavas from the Ethiopia Rift and RVP reveal the presence of an unambiguous solar-like Ne component with extrapolated $(^{21}Ne/^{22}Ne)_{EX}$ ratios between 0.034 and 0.039, close to pure Ne-B (Black, 1972; Dixon, 2003; Ballentine et al., 2005; Trieloff and Kunz, 2005), and (b) 10 samples from the Kenyan rifts and one sample from the Ethiopia Rift fall on a trajectory intermediate between DMM and the various OIB trends, and give $(^{21}Ne/^{22}Ne)_{EX}$ ratios between 0.040 and 0.056.

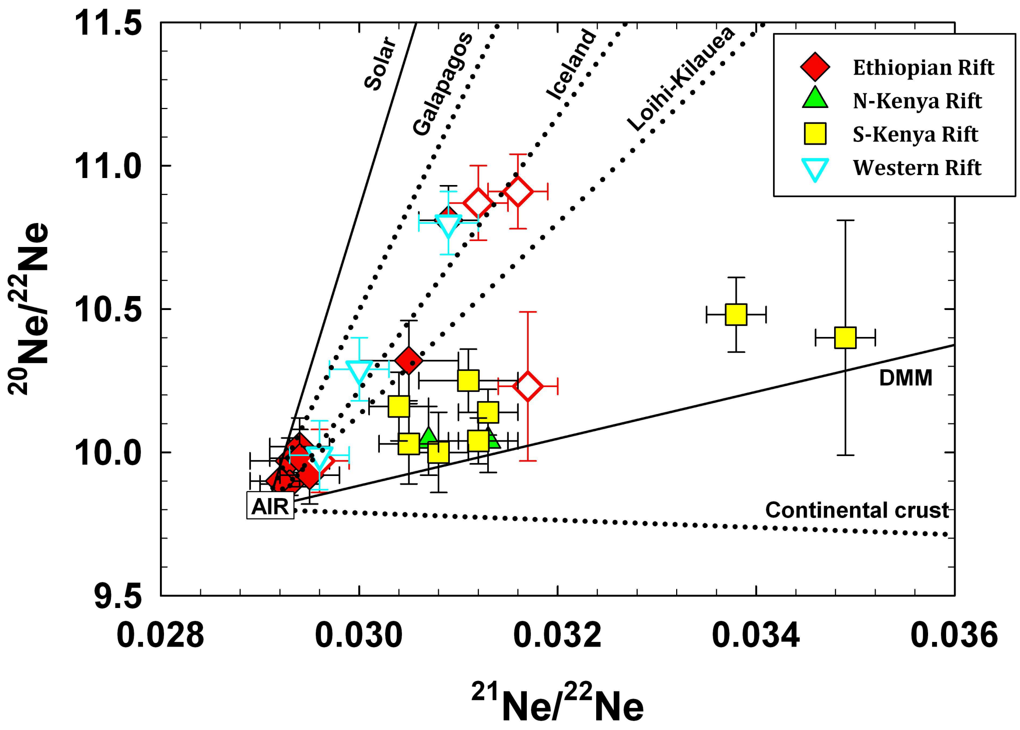

Figure III.2: Three-isotope Ne plot of EARS lavas and xenoliths (n=25). Only samples that display neon isotope compositions distinct from the isotopic composition of air at the 1-sigma level are plotted (Table S3). Also plotted are the solar trajectory, a number of relatively well characterized OIB (Galapagos, Iceland, Loihi-Kilauea), DMM, continental crust and air. Closed symbols = xenoliths; open symbols = lavas.

Therefore, samples do not fall on a single trajectory between air and solar Ne, as in the case of the other OIB in Fig 2, implying that either the $(^{21}Ne/^{22}Ne)_{EX}$ ratio of the EARS has been modified from a diagnostic value that might characterize a single plume source or the EARS mantle is characterized by a heterogeneous distribution of $(^{21}Ne/^{22}Ne)_{EX}$ as might be anticipated if more than one plume were present.

Finally, all 25 samples display $^{40}Ar/^{36}Ar$ ratio >> air (298.6: Lee et al., 2006), reaching values as high as 2950 in the southern Kenya Rift, and with extrapolated values $(^{40}Ar/^{36}Ar)_{EX}$ as high as 16,900 in the northern Kenya Rift (see auxiliary material - Figures S2 & S3).

III.4 Discussion

III.4.1 Helium-Neon Isotope Relationships

In **Figure 3**, we plot the extrapolated neon isotope ratio $(^{21}Ne/^{22}Ne)_{EX}$ versus $^{4}He/^{3}He$ ratios for all 25 samples together with data from previous studies in the region: submarine glasses from the Red Sea (Moreira et al., 1996), ultramafic rocks from Zabargad Island in the Red Sea and xenoliths from Saudi Arabia (Hopp et al., 2004), as well as xenoliths from the Chyulu Hills volcanic field in the southern Kenya Rift (Hopp et al., 2007). Possible mantle end-members relevant to this plot include: (i) a primordial volatile component (PRIM) with a $^{4}He/^{3}He$ ratio identical to solar He = 2580 (280R_A) and a $(^{21}Ne/^{22}Ne)_{EX}$ ratio = 0.03118 (i.e., Ne-B) (Hopp et al., 2004; Trieloff and Kunz, 2005; Hopp et al., 2007), (ii) a mantle plume component (PLUME) with $^{4}He/^{3}He$ ratios of ~35700 (~20R_A), which represents the highest He isotope value observed in the EARS (Marty et al., 1996) with $(^{21}Ne/^{22}Ne)_{EX}$ = 0.034 ± 0.001, defined by many OIB (Graham, 2002), (iii) a DMM component that is identical to Mid Ocean Ridge Basalt (MORB) ($^{3}He/^{4}He$ = 8 ± 1R_A and $(^{21}Ne/^{22}Ne)_{EX}$ = 0.06 ± 0.001) (Graham, 2002; Hopp et al., 2004; Hopp et al., 2007), and (iv) SCLM with $^{3}He/^{4}He$ = 6.1 ± 0.9R_A and $(^{21}Ne/^{22}Ne)_{EX}$ = 0.07 ± 0.001 (Gautheron and Moreira, 2002; Hopp et al., 2004; Hopp et al., 2007), where the postulated Ne isotope composition is significantly more nucleogenic/radiogenic compared to DMM, as commonly found among SCLM xenoliths. Finally, we note that the curvature of the mixing curves between end-members is described by r = $(^{3}He/^{22}Ne)_{DMM}/(^{3}He/^{22}Ne)_{PLUME}$ and/or $(^{3}He/^{22}Ne)_{SCLM}/(^{3}He/^{22}Ne)_{PLUME}$.

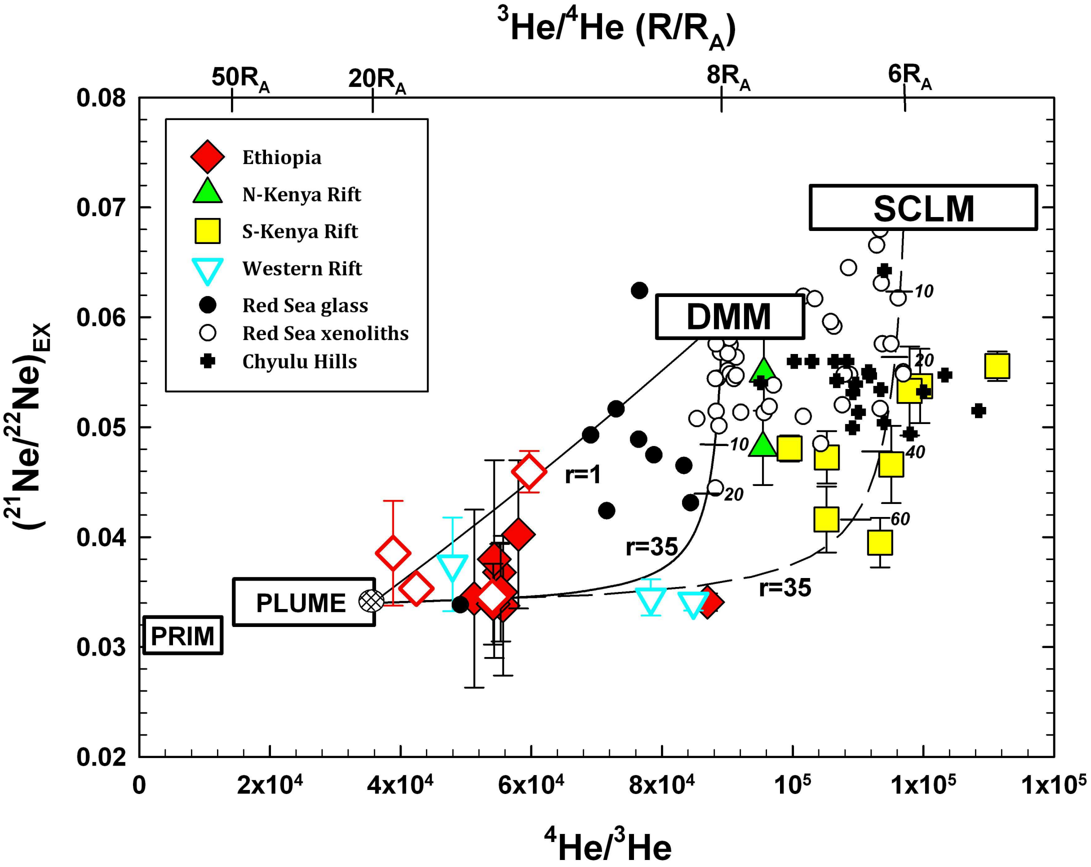

Figure III.3: Extrapolated neon isotopes ($^{21}Ne/^{22}Ne$)$_{EX}$ versus He isotopes ($^4He/^3He$) for all samples from Fig. 2 (n=25). Neon isotopes are extrapolated to Neon-B ($^{20}Ne/^{22}Ne$ = 12.5). Numbers along the curved mixing trajectories indicate the percentage proportions of the PLUME end-member in the binary mixture. Note the extreme sensitivity of Ne isotopes to relatively small additions of the PLUME endmember to DMM and SCLM as a consequence of r >> 1. End-member compositions are defined in the text with the PLUME endmember extending to 50R$_A$ to encompass the highest terrestrial value for $^3He/^4He$ from the proto-Icelandic plume in Baffin Island (Stuart et al., 2003). Cross-hatched circle represents our best estimate of the African Superplume. Closed symbols = xenoliths; open symbols = lavas.

We point out two key features of the coupled He-Ne isotope systematics: (a) samples from the Red Sea and the Ethiopia Rift can be explained by binary mixing between DMM and PLUME with r-values ≥ 1, and (b) samples from the Kenyan rifts as well as the Western Rift cannot be explained by a mixing scenario involving DMM and PLUME (or by mixing between DMM and SCLM as appears to be the case for some xenoliths from the Red Sea area): rather, a hyperbolic mixing trajectory between PLUME and SCLM provides the best fit to data as long as r-values >> 1, i.e., $(^3He/^{22}Ne)_{SCLM}$ >> $(^3He/^{22}Ne)_{PLUME}$. Therefore, irrespective of geographic affinity with the Ethiopia or Kenya domes, all samples share a common PLUME end-member that is characterized by a $(^{21}Ne/^{22}Ne)_{EX}$ ratio close to 0.034 and $^3He/^4He$ ratio ~20R_A. Samples from the Ethiopia and Western rifts plot closer to this end-member (i.e., have a greater proportion of the PLUME component in the mix) compared to samples from the two Kenyan rifts. Thus, the EARS is characterized by a single He-Ne (PLUME) isotopic composition, common to the entire rift, with the apparent heterogeniety in $(^{21}Ne/^{22}Ne)_{EX}$ (Fig. 2) reflecting admixture with different proportions of DMM or SCLM. The most obvious candidate for this common plume component, imaged to underlie the entire EARS, is the deeply rooted African Superplume (Nyblade, 2011; Hansen et al., 2012) (indicated with double hatched symbol in Fig. 3). We point out that a similar mixing scenario can be constructed using He isotopes ($^4He/^3He$) and $(^{40}Ar/^{36}Ar)_{EX}$ ratios, given the assumption that SCLM displays the most radiogenic Ar isotopic compositions (see auxiliary material: Figure S3).

III.4.2 Noble Gas Relative Abundance Ratios

Additional information on mantle end-members involved in EARS petrogenesis are provided by noble gas elemental ratios, particularly $^3He/^{22}Ne_S$ ratios (where $^{22}Ne_S$ = solar ^{22}Ne). A frequently made observation is that mantle plumes displaying $^3He/^4He$ ratios > DMM have $^3He/^{22}Ne_S$ ratios < the nominal upper-mantle value of ~5 (calculated assuming Neon-B): in contrast, glasses from oceanic spreading centers (e.g., the popping rock on the mid-Atlantic Ridge and back-arc basins) generally have $^3He/^{22}Ne$ ratios ≥ the nominal upper-mantle value (Moreira et al., 1998; Honda and McDougall, 1998; Trieloff et al., 2000; Graham, 2002; Dixon, 2003; Mukhopadhyay, 2012; Tucker and Mukhopadhyay, 2013). We test this distinction for our EARS samples by considering the elemental ratio of ^4He to nucleogenic $^{21}Ne^*$ ($^4He/^{21}Ne^* = 2.2 \times 10^7$:

Yatsevich and Honda, 1997), and ^{3}He to solar ^{22}Ne (^{3}He/^{22}Ne$_S$; see auxiliary material for calculation of these values). The ^{3}He/^{22}Ne$_S$ and ^{4}He/^{21}Ne* ratios of EARS lavas and xenoliths are plotted in **Figure 4.**

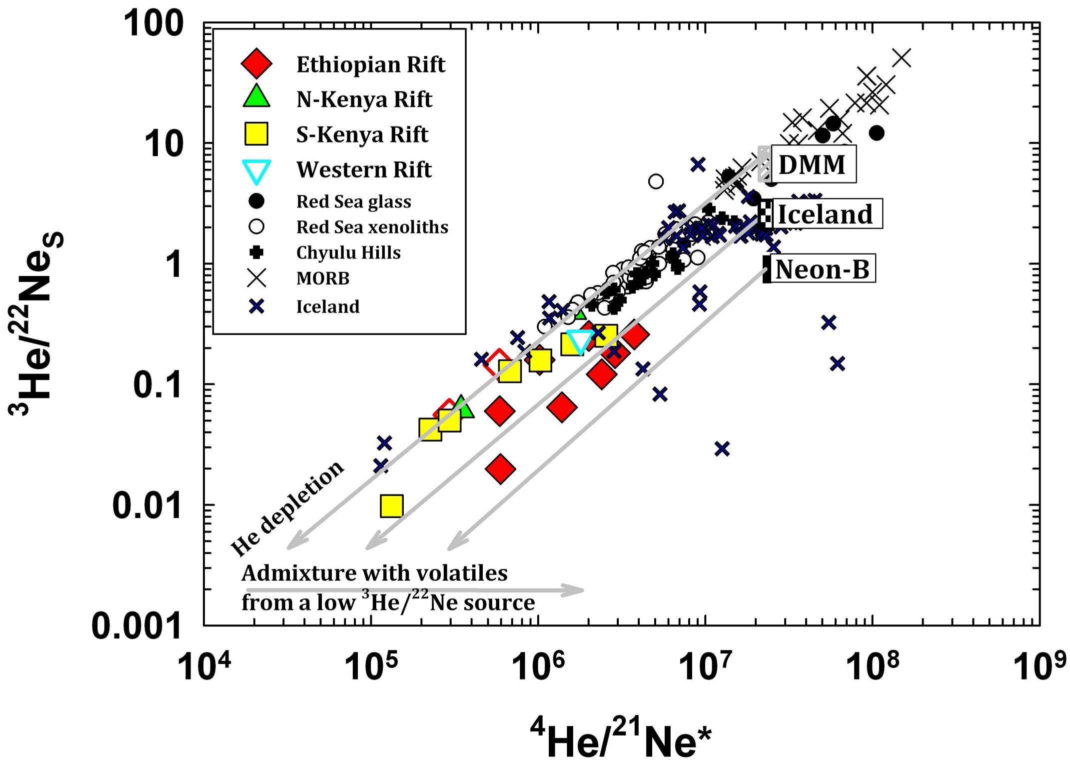

Figure III.4: He-Ne plot incorporating primordial (^{3}He/^{22}Ne$_S$) versus radiogenic/nucleogenic (^{4}He/^{21}Ne*) ratios of EARS lavas and xenoliths (Table S4). MORB glasses (Moreira et al., 1998; Moreira and Allègre, 2002) and Icelandic lavas (Trieloff et al., 2000; Dixon et al., 2000; Moreira et al., 2001; Dixon, 2003; Furi et al., 2010; Mukhopadhyay, 2012) are also plotted. Boxes represent assumed values for DMM (^{3}He/^{22}Ne =5-10: Honda and McDougall, 1998; Trieloff et al., 2000; Graham, 2002; Tucker and Mukhopadhyay, 2013), Iceland (^{3}He/^{22}Ne ~ 3: Mukhopadhyay, 2012) and Neon-B (^{3}He/^{22}Ne$_S$ ~ 1: Black, 1972; Ballentine et al., 2005; Dixon, 2003; Trieloff and Kunz, 2005). All three end-member compositions have the same ^{4}He/^{21}Ne* ratio = 2.2 × 10^7 – see text and Auxiliary material for details and for the calculation of ^{3}He/^{22}Ne$_S$ ratios. Closed symbols = xenoliths; open symbols = lavas.

For comparison, we also plot other samples from the EARS (Moreira et al., 1996; Hopp et al., 2004; Hopp et al., 2007) as well as MORB glasses (Moreira et al., 1998; Moreira and Allègre, 2002) and lavas from the Iceland hotspot (Trieloff et al., 2000; Dixon et al., 2000; Moreira et al., 2001; Dixon, 2003; Furi et al., 2010; Mukhopadhyay, 2012). We note that our data agree with the general trend of OIB in the sense that the He/Ne elemental ratios (^{3}He/^{22}Ne$_S$ and ^{4}He/^{21}Ne*) are lower than the measured and calculated values for DMM. This observation suggests that parental melts sourcing the EARS are characterized by a significant depletion of He relative to Ne. Significantly, any deviation horizontally to the right of the trajectory labeled 'He depletion', is likely caused by admixture with volatiles exsolved from a mantle component that has preserved a lower ^{3}He/^{22}Ne$_S$ ratio relative to DMM. Possibilities include a primitive component approximated by (i) Neon-B with ^{3}He/^{22}Ne$_S$ ~1 (Black, 1972; Ballentine et al., 2005; Dixon, 2003; Trieloff and Kunz, 2005) and/or (ii) other gas-rich meteorites with ^{3}He/^{22}Ne$_S$ ~0.9 (Raquin and Moreira, 2009). Notably, the contribution from this low (primitive) ^{3}He/^{22}Ne$_S$ component is most prominent among Ethiopia Rift samples that display the highest ^{3}He/^{4}He ratios.

Thus, a remarkable feature of the EARS dataset is that all 25 samples that have neon isotopes distinct from air, possess ^{3}He/^{22}Ne$_S$ ratios lower than those of Earth's upper mantle, consistent with observations made previously for oceanic hotspots displaying high ^{3}He/^{4}He ratios. In particular, we point out striking similarities between the EARS and the Iceland hotspot (**Fig. 4**). Additionally, we note that many samples of this study with ^{3}He/^{4}He ratios akin to DMM and/or SCLM, have ^{3}He/^{22}Ne$_S$ elemental ratios which do not overlap DMM. Lower than upper mantle ^{3}He/^{22}Ne$_S$ ratios thus appear to be a general characteristic of the EARS mantle, being pervasive throughout eastern Africa. Given the similarity in ^{3}He/^{22}Ne$_S$ ratios between EARS samples and many OIB displaying high ^{3}He/^{4}He ratios, such a feature clearly represents a deep-seated plume component that has preserved ^{3}He/^{22}Ne$_S$ ratios distinct from the upper mantle, and which currently supplies the EARS with primitive volatile components. The origin of the low ^{3}He/^{22}Ne$_S$ ratios of the deep mantle could be deep solubility controlled degassing (Honda and McDougall, 1998; Yokochi and Marty, 2004) and/or perovskite crystallization (Coltice et al., 2011) in an early terrestrial magma ocean. Alternatively, low ^{3}He/^{22}Ne$_S$ ratios could reflect heterogeneous accretion of the Earth, with the lower mantle having different $^{3}He/^{22}Ne_{S}$ source material than the upper mantle (Mukhopadhyay, 2012). In any case, low $^{3}He/^{22}Ne_{S}$ ratios that characterize EARS magmas, bear witness to long-term and significant noble gas heterogeneities in the deep mantle (Yokochi and Marty, 2004; Mukhopadhyay, 2012).

III.5 Implications for EARS Magmatism

Our results have profound implications for EARS magmatism. First, they imply that magmas erupted within the Ethiopia and Kenya domes have unique volatile isotopic and relative abundance characteristics consistent with a common and deeply rooted mantle plume source underlying both regions. In particular, two independent lines of evidence (coupled He-Ne isotope systematics and low $^{3}He/^{22}Ne_{S}$ ratios) provide compelling evidence that this common plume source can only be the African Superplume, a continuous, thermo-chemical mantle structure that originates at the core-mantle boundary, and provides dynamic support for both main topographic features of the EARS (Nyblade, 2011; Hansen et al., 2012). In effect, our model rules out other plume models that advocate either different styles of mantle convection along the EARS (Pik et al., 2006; Montagner et al., 2007) or multiple plumes impinging the African lithosphere (Rogers, 2006). Our model also negates the need for an oceanic HIMU-type mantle plume to explain low $^{3}He/^{4}He$ ratios evident in the Kenyan rifts (Furman, 2007; Nelson et al., 2012). We show that the SCLM plays the key role in generating the low $^{3}He/^{4}He$ ratios along this segment.

Second, the fact that most Kenya Dome samples (i.e., southern Kenya and the Western Rift) can only be explained by mixing between PLUME and SCLM components (**Fig. 3**), effectively rules out DMM involvement in petrogenesis in this region. Thus, the results argue against the concept of a globally homogeneous upper mantle, fluxing volatiles to both mid-ocean ridges and continental rifts, at least in the case of the southern segment of the EARS as was inferred in a study of Oldoinyo Lengai volcano in northern Tanzania (Fischer et al., 2009). Conversely, DMM-like $^{3}He/^{4}He$ ratios measured along the Kenyan and Western rifts (Pik et al., 2006; Hilton et al., 2011) must therefore represent mixing between SCLM and PLUME (**Fig. 3**), given the absence of DMM involvement. This distinction is not possible using He isotopes alone. Our results are therefore largely consistent with models based on radiogenic isotopes that advocate for three-component mixing involving DMM, SCLM and PLUME components (Rogers, 2006; Castillo et al., 2012). However, we make the case for a ubiquitous and common mantle plume component throughout the EARS with DMM and SCLM end-members predominantly present in the Ethiopia and Kenya domes, respectively.

III.6 Conclusions

Combined He-Ne-(Ar) isotope and relative abundance systematics of mantle-derived xenoliths and lavas from different segments of the EARS, can be explained by admixture between a single mantle plume source, common to the entire rift, and either a DMM or SCLM component but not both. Identical to many oceanic hotspots, such as Iceland, the plume source is also characterized by low $^{3}He/^{22}Ne_{S}$ ratios. The most obvious candidate for this common plume component is the African Superplume that which influences magmatism throughout eastern Africa. We argue that the Ethiopia and Kenya domes thus represent two different heads of the same mantle plume source.

Acknowledgements

This work was supported by the Petrology and Geochemistry program of NSF (EAR-1019489). We thank Pat Castillo for discussions, James Day for useful comments and

Roberta Rudnick for providing selected mantle xenoliths from northern Tanzania. We also thank an anonymous reviewer and Nick Rogers for constructive reviews that helped improve the paper.

Auxiliary Material

Methods and analytical techniques

Sample preparation. Whole rock samples were reduced in size using a diamond rock saw and crushed using a shatter box to a grain size larger than the largest phenocrysts of each sample. Further reduction in grain size was achieved using a pestle and mortar to free phenocrysts of any adhering matrix material. Fresh mineral separates were removed from lavas and broken-up xenoliths and washed in distilled water. This step was followed by cleaning in an ultrasonic bath in a 1:1 acetone-methanol mixture before drying in a hot (~120°C) environment for several (4-6) hours. The cleaned and dried minerals were then examined using a binocular microscope, and minerals free of any surficial alteration were hand-picked and loaded into on-line crushers (Scarsi, 2000) for overnight evacuation to high vacuum prior to He analysis.

Helium analysis of mafic minerals by *in-vacuo* crushing. Olivine (OL), pyroxene (PX) and/or garnet (GT) crystals of mineral separates from lavas and xenoliths were crushed under Ultra High Vacuum (UHV) to determine ^{3}He/^{4}He ratio and He abundance [He] using an MAP215 noble gas mass spectrometer and adopting standard protocols described previously (e.g., Shaw et al. 2006; Furi et al. 2010, Hilton et al., 2011). Throughout all runs, ^{4}He blanks where identical to those reported by Hilton et al. (2011): i.e., ~ 6.0×10^{-11} cm^{3} STP. All ^{3}He/^{4}He ratios and [He] have been corrected for air-derived components using the methodology described in Hilton et al. (2011). The selection of material for combined neon and argon analysis (see below) was guided by those samples having high He abundances. We report ^{3}He/^{4}He ratios and He abundances obtained at Scripps Institution of Oceanography in Table S1 whereas other literature data are given in Table S2.

Neon and argon analysis of mafic minerals by *in-vacuo* crushing. Neon and argon abundance and isotope characteristics of selected mineral separates from lavas and xenoliths previously analyzed for helium were crushed using a custom-built, piston activated *in vacuo* rock-crusher (e.g., Stuart et al. 1994). The released gas was then purified using a dedicated cryogenic separation line, whereby Ne and Ar were separated and analyzed independently. Neon and argon abundances and isotope ratios (as well as He abundances) were measured using a modified VG5440 noble gas mass spectrometer equipped with five Faraday cups and a Daly photo-multiplier detector (see Craig et al., 1993; Furi et al. 2010, Hahm et al., 2012 and Barry et al. 2012) operated in peak jumping mode. Neon results were corrected for procedural blanks and contributions of doubly-charged ^{40}Ar and CO_2 to ^{20}Ne and ^{22}Ne, respectively, following Niedermann et al. (1993). Procedural crusher blanks were between 1.5 and 33 × 10^{-12} cm^3 STP for ^{20}Ne (note that only six samples had blanks > 14 × 10^{-12} cm^3 STP: the mean blank value was 10 ± 7 × 10^{-12} cm^3 STP) and 7 ± 2 × 10^{-9} cm^3 STP for ^{40}Ar, typically representing less than 10% of sample yields. We report He abundances, neon abundances and isotopes, $^{40}Ar/^{36}Ar$ ratios, and argon abundance in Table S3 and derived elemental ratios in Table S4.

Auxiliary Text

1. The East African Rift System He isotope database

We report helium isotope (^{3}He/^{4}He) and abundance characteristics of mineral separates from lavas and mantle xenoliths from 156 different sampling locations throughout the EARS produced at the Scripps Institution of Oceanography (SIO) (Supplementary Table S1). Note that some samples displayed very low He contents ([He]) and were deemed unsuitable for He isotope analyses (indicated as ‘not detectable’: n.d.). For this study, we analyzed a total of 80 mineral separates for He to identify suitable samples for combined Ne-Ar analysis. These new analyses are supplemented with 52 previously reported He analyses of lavas from Rungwe Volcanic Province (Hilton et al., 2011), 8 analyses of xenoliths from the southern Kenya Rift (Hilton et al. 2011), 33 analyses of lavas from the Ethiopia Rift (Scarsi and Craig, 1996), and 11 unpublished data from SIO making a total of 184 ^{3}He/^{4}He ratios. In total, 130 samples have been analyzed for OL, 53 samples for PX, and one sample was analyzed for Garnet. Note that we do not separate OL from PX and Garnet in the plots (Figs. 2-4), as no significant differences were observed in this study. Rather, we focus on the differences between xenoliths (closed symbols) and lavas (open symbols). All SIO data are plotted in **Figure S1a**.

Figure 1 summarises the total helium isotope database for the EARS combining data from Table S1 and the following references: Marty et al. 1993, Marty et al. 1996, Moreira et al. 1996, Hopp et al. 2004, Class et al. 2005, Pik et al. 2006, Furman et al 2006, Hopp et al. 2007, Tedesco et al. 2010, Aulbach et al. 2011, Beccaluva et al. 2011, Rooney et al. 2012, and Medynski et al. 2013. These literature data are given in Table S2 and plotted (^{3}He/^{4}He ratios versus He concentration) in **Figure S1b**. The total EARS He isotope database consists of 300 different sampling localities but 339 analyses as many samples have been analyzed for He using more than one mineral phase.

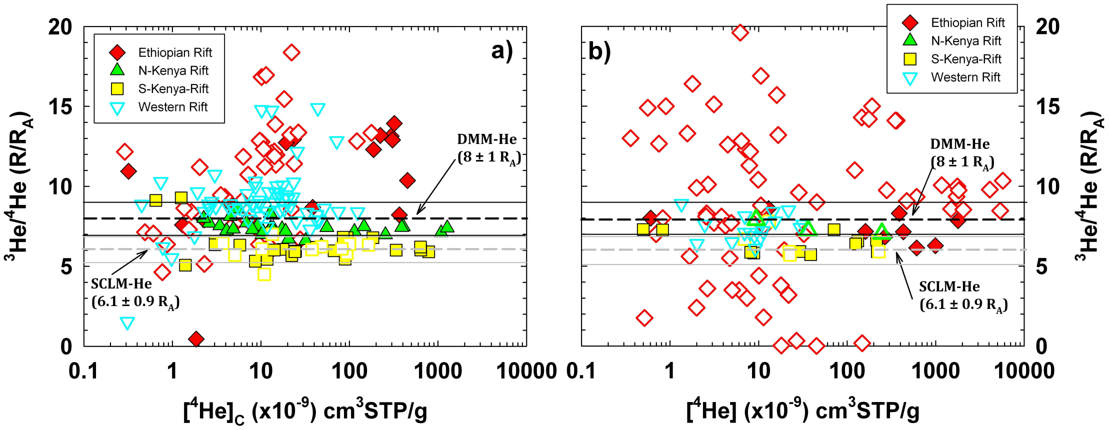

Figure III.S1: Plot of He concentration versus ^{3}He/^{4}He ratio of EARS samples obtained at (a) SIO or (b) from literature sources (see text). He isotopes are reported in the R/R$_A$ notation, where R = sample ^{3}He/^{4}He corrected for a minor air-derived component, and R$_A$ = air ^{3}He/^{4}He) versus He concentration ([He]$_C$ in units of cm^3 STP/g mineral), also corrected for air. (a) Only data obtained at SIO are plotted (n=184). Lavas and gas-rich xenoliths from the EARS span a range from SCLM-like (6.1±0.9 R$_A$) to DMM (8±1 R$_A$) to plume-like He isotope characteristics. (b) Same plot as (a) but only data from literature studies (n=155) are plotted. Closed symbols = xenoliths; open symbols = lavas.

2. Comparison of He isotopes in lavas and xenoliths

A concern with the use of xenoliths to carry a meaningful and unbiased mantle signature to the surface that is identical to the signal carried by phenocrysts in magmas, is the fact they often have a complex origin and can be generated by means of several processes. For example, xenoliths may be formed by extensive crystallization from magmas that are related or unrelated to the host lava (i.e., they represent cumulates), and/or xenoliths may be formed as restites of melting, but later modified by metasomatic processes in the upper mantle or the deep crust (e.g., Nixon, 1987). In order to test if xenoliths carry an unbiased mantle signature equivalent to phenocrysts, we searched our EARS He isotope database in order to identify specific samples where He isotopes have been analyzed using both phenocrysts in host lavas and corresponding xenoliths. Additionally, a comparison of He isotopes in lavas and xenoliths from the same localities, can also provide useful constraints on this issue.

Notably, two mafic (and highly phyric) lavas from Tat' Ali in northern Afar, G-114 and G-115, provide a test case as He isotopes have been measured in mineral phases from the host lava, in addition to minerals phases from the xenoliths hosted by these lavas. Mafic pyroxene minerals in xenoliths from sample G-114 have a $^{3}He/^{4}He$ ratio = $12.82R_A$, in exellent agreement with a value of $12.86R_A$ measured in the olivine phenocrysts from the host lava. The same applies to sample G-115 as olivine phenocrysts have identical $^{3}He/^{4}He$ ratios ($13.37R_A$) to those measured in pyroxene minerals in the xenolith. ($13.35R_A$). Notably, identical He isotope values prevail in both mineral phases/sample types despite almost one order or magnitude difference in He concentrations.

In addition, there is close agreement between phenocrysts and lavas from any given locality along the EARS. For example, lavas from Tat' Ali (G-112, G-113 and G-116) have He isotope ratios that closly resemble those measured in xenoliths from this same location. Other examples include Assab and Afdera, both in Afar. Lavas from various localities in northern Tanzania (Olduvai Gorge, Lake Manyara, Kilimanjaro, Ol Molog, Ol Doinyo Elorori) also show near identical He isotope values to those observed in xenoliths from the same general area (Ol Doinyo Lengai, Eledoi, Pello Hill, Lashine, Olmani) and both sample types, consistently fall within the SCLM range of $6.1 \pm 0.9R_A$(Gautheron and Moreira, 2002). Of all these localities, Labait is the only location which has He isotopes which exceed the SCLM range, consistent with possible plume contributions to this locality as was previously proposed on the basis of Os isotopes (Chesley et al., 1999).

Thus, in summary, comparison between He isotope compositions of phenocrysts and xenoliths from the same samples but also from the same localities, suggest that xenoliths closely resemble the He isotopic characteristics of the host (carrier) magma, and thus they carry a meaningful mantle signature to the surface that is identical to the signal carried by phenocrysts.

3. Calculation of non-atmospheric $^{20}Ne/^{22}Ne$ and $^{21}Ne/^{22}Ne$ ratios

We used the following criteria for selecting samples with non-atmospheric neon assuming that measured Ne isotope values represent a simple two-component mixture between air and mantle Ne (Moreira et al. 1995): (i) measured $^{20}Ne/^{22}Ne$ ratios are distinguishable from air at the 1σ level, (ii) blank contribution was low (<8%, but generally <2%), and (iii) $^{40}Ar/^{36}Ar$ > air (298.6). After identifying samples with non-atmospheric Ne, the measured $^{21}Ne/^{22}Ne$ values are extrapolated along a linear trajectory that passes through the air value towards a primitive mantle component. In all extrapolations for Ne (and Ar), we assumed Ne-B: a primitive implanted solar neon component, identified in gas-rich meteorites and in lunar soils with a $^{20}Ne/^{22}Ne$ ratio of 12.5 (Black, 1972; Trieloff et al., 2005; Ballentine et al. 2005). We note that selecting a more primitive Ne component (the solar wind with $^{20}Ne/^{22}Ne = 13.8$) will not change the conclusions of this study.

4. Generation of low $^{3}He/^{22}Ne$ ratio mantle sources

The notion that low $^{3}He/^{22}Ne_{S}$ ratios represent a feature characteristic of primitive mantle sources commonly sampled at oceanic hotspots (e.g., Honda and McDougall, 1998; Graham, 2002; Hopp & Trieloff, 2008) is challenged by the fact that He can potentially be fractionated from Ne by a number of different processes. If correct, low He/Ne ratios would then primarily represent a process rather than acting to identify a lower mantle source. In the following discussion, we provide an overview of possible processes that may be responsible for these elemental fractionations.

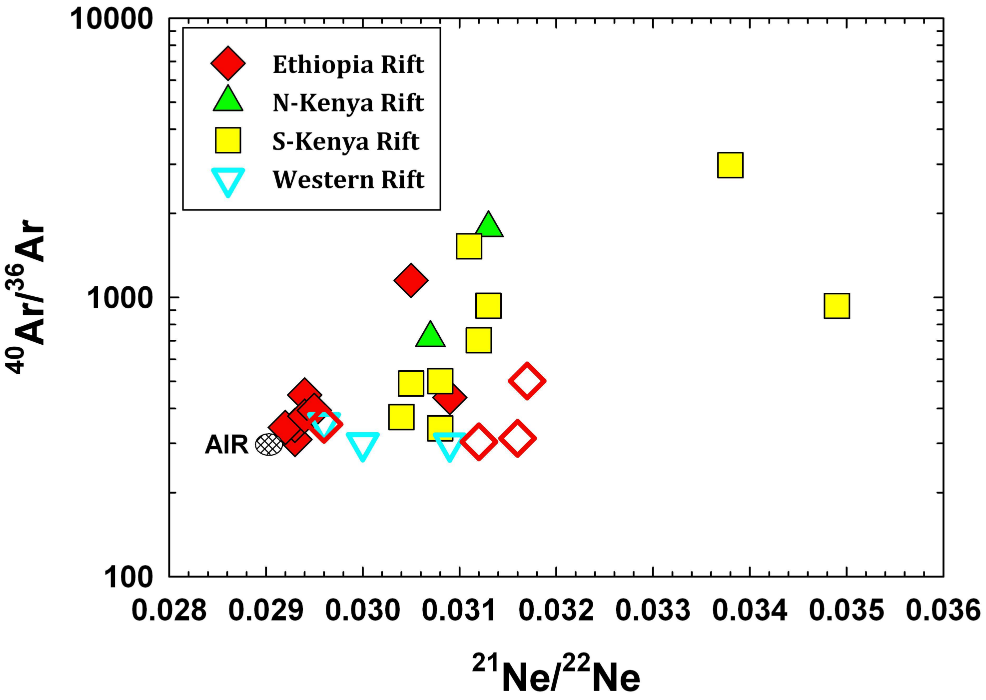

Figure III.S2. ^{40}Ar/^{36}Ar ratios versus ^{21}Ne/^{22}Ne ratios of EARS samples**.** Notably, all 25 samples display ^{40}Ar/^{36}Ar ratio >> air (298.6), reaching values as high as 2946 in the southern Kenya Rift. We also note that lava samples (open symbols) display ^{40}Ar/^{36}Ar ratio that generally lie closer to the air value. However, some xenoliths from the Ethiopian Rift (open symbols) also display ^{40}Ar/^{36}Ar ratios that lie close to air. See text for details.

4.1. *Partitioning of the He, Ne and Ar during partial melting in the upper-mantle*

Helium can be depleted relative to Ne and Ar if it displays more compatible behavior during low-degree partial melting (e.g., Hopp & Trieloff, 2008). However, available partition coefficients for He, Ne and Ar at upper mantle conditions are generally inconsistent with this notion. For example, available partition coefficients (K_D) of He, Ne and Ar between CPX-melt generally reveal lower K_D for He relative to Ne and Ar (Brooker et al., 2003: Heber et al., 2007; Jackson et al., 2013). Although there remain considerable uncertainties regarding relative partition coefficients of He, Ne and Ar between OL-melt (Parman et al., 2005: Heber et al., 2007; Jackson et al., 2013), available data are generally consistent with He having the most incompatible behavior (relative to Ne and Ar) during partial melting. Furthermore, it has also been proposed that Ar is highly compatible in both OL and PX, where K_D of Ar can be as high as ~10^4 (Watson et al., 2007; Thomas et al., 2008). It should be emphasized, however, that large errors reported in some of these studies, in addition to great discrepancy between results of different experimental setups, preclude definitive conclusion regarding K_D values for He, Ne and Ar and additional experimental work is needed.

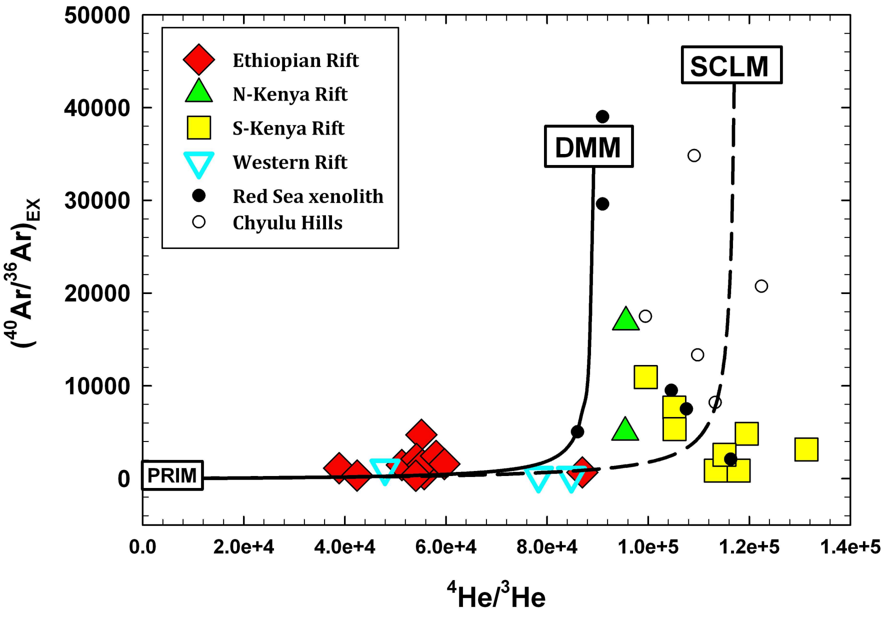

Figure III.S3: Extrapolated argon isotope $(^{40}Ar/^{36}Ar)_{EX}$ versus $^{4}He/^{3}He$ ratios of EARS samples. Notably, $(^{40}Ar/^{36}Ar)_{EX}$ ratios (extrapolated to $^{20}Ne/^{22}Ne=12.5$, i.e., Ne-B) reach values as high as 16,897 in the northern Kenya Rift. Following Buikin et al. (2005) and Hopp et al. (2007), we indicate possible mantle end-members on this plot: (i) PRIM: with primordial values $^{40}Ar/^{36}Ar \approx 0$ (solar, e.g. Benkert et al., 1993), $^{4}He/^{3}He$ ratio identical to solar He = 2580 ($280R_A$), (ii) DMM that is identical to Mid Ocean Ridge Basalt (MORB) ($^{3}He/^{4}He = 8 \pm 1R_A$ and $^{40}Ar/^{36}Ar_{ex} = 35{,}000$) and, (iv) SCLM with $^{3}He/^{4}He = 6.1 \pm 0.9R_A$ and $^{40}Ar/^{36}Ar_{ex} = 45{,}000$, which represents a postulated Ar component that is significantly more radiogenic compared to DMM and found amongst SCLM xenoliths (Buikin et al., 2005; Hopp et al., 2007). We indicate mixing between PRIM and DMM with a solid line and between PRIM and SCLM with a dashed line.

4.2. Diffusive loss of helium relative to neon and argon

Due to its small size and resulting high diffusivity, He can be lost relative to heavier noble gases from fluid inclusions following entrapment in minerals (Yamamoto et al. 2009). This represents another possibility to explain low $^{4}He/^{21}Ne^{*}$, $^{3}He/^{22}Ne_{S}$, $^{4}He/^{40}Ar^{*}$ ratios and possibly also low $^{21}Ne^{*}/^{40}Ar^{*}$ ratios in EARS xenoliths (see Table S4 for the calculation of these ratios). Such low ratios are commonly observed in mantle xenoliths worldwide and have been attributed to the diffusive loss of He, relative to Ne and Ar, to nearby magma channels. This may occur during re-equilibration with mantle-derived melts, either in the source region or during transport of xenoliths to the surface (e.g., Yamamoto et al. 2009).

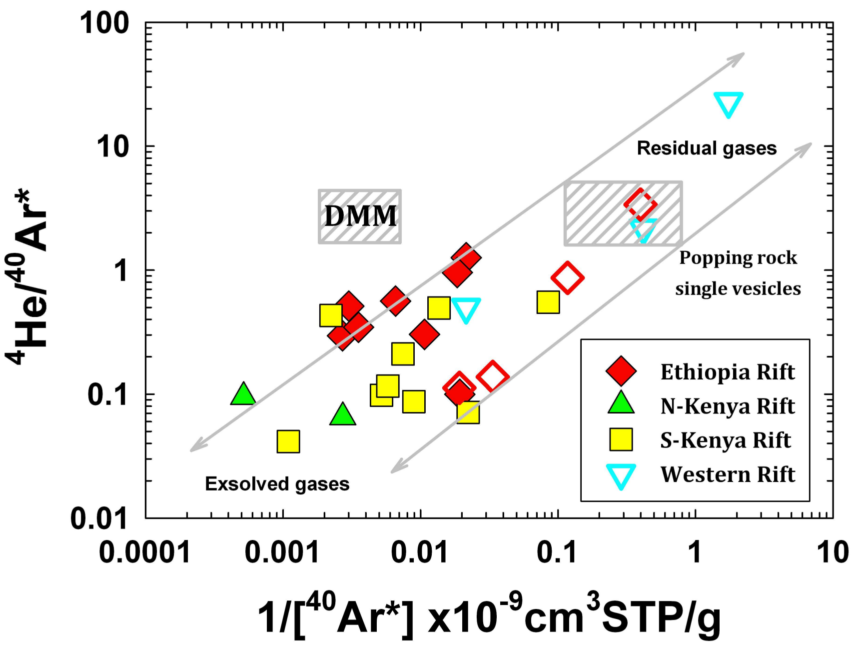

Figure III.S4: $^{4}He/^{40}Ar^{*}$ ratios versus the reciprocal of [$^{40}Ar^{*}$] of the EARS samples. Radiogenic Ar contents [$^{40}Ar^{*}$] found in single vesicles in the 2IID43 popping rock (Burnard et al., 1997) and the predicted ^{40}Ar radiogenic production of the upper mantle (Porcelli & Wasserburg, 1995) in conjunction with the time integrated $^{4}He/^{40}Ar^{*}$ ratio of the upper mantle (1.4 and 4.8). Significantly, we note that there is a good correlation between the enrichment of [$^{40}Ar^{*}$] and decreasing $^{4}He/^{40}Ar^{*}$ ratios. This cannot result from He loss mechanisms: rather, mixing between two exsolved fluids is a more probable explanation. One sample from the Western Rift is consistent with open system degassing as it displays $^{4}He/^{40}Ar^{*}$ > DMM and the 2IID43popping rock.

In **Figure S4** we plot $^{4}He/^{40}Ar^{*}$ versus the reciprocal of [$^{40}Ar^{*}$] to test the possibility that diffusive loss of He can explain low $^{4}He/^{40}Ar^{*}$. Significantly, we note that there is a good anticorrelation between the enrichment of [^{40}Ar*] and ^{4}He/^{40}Ar* ratios that cannot result from He loss mechanisms. Rather, mixing between two fluids is a more probable explanation, where samples with high ^{4}He/^{40}Ar* ratios lie close to [^{40}Ar*] values found in single vesicles in the 2IID43popping rock (Burnard et al., 1997), and the time-integrated ^{4}He/^{40}Ar* ratio of the upper mantle (1.4 and 4.8). Notably, such low [^{40}Ar*] values are somewhat lower than the predicted ^{40}Ar radiogenic production of the upper-mantle (Porcelli & Wasserburg, 1995).

4.3. Solubility controlled fractionation

Finally, Ne (and Ar) may be preferentially fractionated into the exsolved volatile phase derived from a primary melt due to the higher solubility of He relative to Ne in silicate melt resulting in a lower He/Ne ratio in the exsolved phase (Jambon et al. 1986; Lux, 1987; Carroll & Stolper, 1993; Shiabata et al. 1998; Miyazaki et al. 2004; Iacono-Marziano et al. 2010). With regard to the EARS samples, this possibility is supported by the fact that nearly all samples display ^{4}He/^{21}Ne*, ^{3}He/^{22}Ne$_{S}$, ^{4}He/^{40}Ar* and ^{21}Ne*/^{40}Ar* ratios that are lower than upper mantle (i.e., DMM) values (**Figures 4, S4 and S5 a and b**). Indeed, it has been proposed that deep solubility controlled degassing (Honda and McDougall, 1998; Yokochi & Marty, 2004) in an early terrestrial magma ocean was responsible for the apparently low ^{3}He/^{22}Ne$_{S}$ ratios of the deep mantle reservoir.

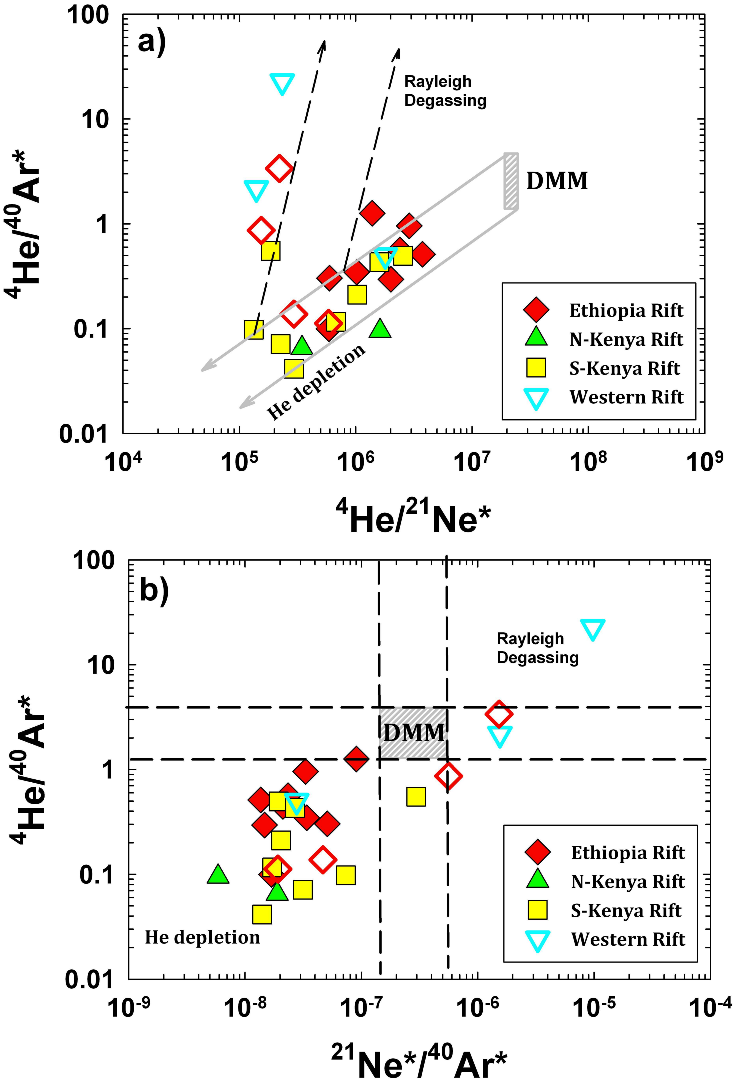

Figure III.S5: (a) ^{4}He/^{21}Ne* versus ^{4}He/^{40}Ar* and (b) ^{21}Ne*/^{40}Ar* versus ^{4}He/^{40}Ar* for EARS samples. The grey squares in both figures represent assumed values for Earth's upper mantle (DMM): (a) and (b) ^{4}He/^{40}Ar* =1.4 and 4.8; (a) ^{4}He/^{21}Ne* = 2.2 × 10^7 (Yatsevich and Honda, 1997); (b) ^{21*}Ne/^{40}Ar* = 1 × 10^{-7} (Valbracht et al., 1996). All ratios are calculated under the assumption that Ne–B is representative of the primordial neon component. In (a) He-Ne-Ar elemental ratios (^{4}He/^{21}Ne* versus ^{4}He/^{40}Ar*) are plotted to demonstrate that EARS lavas and xenoliths of this study are consistently lower than DMM. Notably, 4 lavas (open symbols) and 1 xenolith (closed symbol) have been affected by shallow-level degassing processes (i.e., open system degassing-Rayleigh fractionation) in addition to a deep pre-degassing fractionation event as indicated with trajectories in Figure S5a. In (b) He-Ne-Ar elemental ratios (^{4}He/^{21}Ne* versus ^{21*}Ne/^{40}Ar*) are plotted to demonstrate that EARS lavas and xenoliths of this study are consistently lower than DMM. Notably, nearly all samples plot in the lower left quadrant in Figure S5b. Analogous to Figure S5a, 4 lavas (open symbols) and 1 xenolith (closed symbol) are likely affected by shallow-level degassing processes in addition to a deep pre-degassing fractionation event. These 5 samples are excluded from Figure 4.

Chapter IV: Widespread occurrence of recycled volatiles in the East African sub-continental lithospheric mantle – Evidence from mantle xenoliths

IV.1 Abstract

We report new results on the He-CO_2-N_2-Ar isotope and relative abundances of ultramafic mantle xenoliths from throughout the East African Rift System (EARS). We targeted nine xenoliths localities from the Ethiopian Rift in the north and all the way to the southern Kenya rift in northern Tanzania. All data were obtained by *in-vacuo* crushing techniques and are supplemented with new oxygen isotopes data on the host mafic crystals. The primary aim of this study is to identify the various sources contributing to the volatile components trapped in the fluid inclusions and to evaluate a number of mantle/crustal factors controlling their elemental and isotope characteristics.

We show that volatile components, trapped in fluid inclusions in predominantly pyroxenite xenoliths, have compositions consistent with enrichment of the East African sub-continental lithospheric mantle (SCLM) by CO_2-rich mantle fluids from subducted carbonatitic material. Such CO_2 enrichments ($CO_2/^3He>7x10^9$, $\delta^{13}C$=+0 ‰) are also associated with positive $\delta^{15}N$ values (as high as +3.4 ‰) and unusually low $\delta^{18}O$ values (to +2.4‰) of host crystals, reinforcing the link between the metasomatic fluids and subduction of hydrothermally altered oceanic crust, including the pelagic sedimentary veneer. The occurrence of recycled volatiles in the East African SCLM is widespread and must be associated with a large scale mantle process currently supplying mantle material to the EARS. Notably, xenoliths with high $^3He/^4He$ ratios from northern Ethiopia and the Red Sea are also associated with recycled CO_2-rich mantle fluids (i.e., carbonate-melts) and positive $\delta^{15}N$ values, implying the deep-seated African Superplume mantle plume supplies the EARS with a mixture of primordial and recycled volatiles. Additionally, we propose that these new data provide key constraints on the role of recycled volatiles on magma genesis along the EARS and in particular, on the formation of a pyroxenite-hybrid mantle source.

IV.2 Introduction

Metasomatic enrichment of the sub-continental lithospheric mantle (SCLM) in incompatible trace elements is associated with influx of low-degree volatile-rich melts of either carbonate-rich or silicate-rich composition in addition to C-O-H-rich fluids (e.g., Hawkesworth et al., 1984; Menzies & Hawkesworth, 1987; Rudnick et al., 1993; Schiano et al., 1994; Luth, 2003). Experimental work has shown that such volatile-rich melts react with mantle peridotites to produce clinopyroxene-enriched derivatives (Wallace and Green, 1988) – recognized in numerous mantle xenoliths worldwide (Pearson et al., 2003; Bodinier & Godard, 2003; Downes, 2007). Detailed textural, mineralogical and geochemical studies on mantle xenoliths highlight the complexity of metasomatic changes resulting from the invasion of volatile-rich melts into normal mantle peridotite (e.g., Pearson et al., 2003), and key questions remain about the exact nature, distribution, origin/provenance of the volatile components associated with the metasomatic agents and where they are stored within the SCLM (Menzies & Hawkesworth, 1987; Dunai and Porcelli, 2002).

In this respect, the East Africa Rift System (EARS) is of particular interest as it integrates a variety of mantle and crustal processes resulting in continental rifting which will eventually lead to the formation of a nascent ocean (Kampunza and Lubala, 1991; Yirgu et al., 2006; Dawson, 2008). The source region of magmatism driving the EARS is thought to involve one (Nyblade & Robinson, 1994; Lithgow-Bertelloni & Silver, 1998; Nyblade, 2011; Hansen et al., 2012) or more (e.g., Rogers, 2006; Furman, 2007) deep-seated mantle plume(s) with variable interactions with overlying SCLM and possibly crust. Information on the geochemical nature and history of this key interface, which exists between the chemically heterogeneous lithosphere/crust and the convecting, asthenospheric upper mantle, relies heavily on ultramafic xenoliths – found at numerous localities throughout the EARS (e.g., Nixon, 1987; Dawson, 2008).

A large body of petrological and geochemical research on EARS xenoliths, in particular directed at ultramafic xenoliths from the southern Kenya Rift in Tanzania, bear witness to significant thinning and magmaphile element enrichment of the SCLM following interaction with metasomatic fluids (Cohen et al., 1984; Rudnick et al., 1993; Dawson, 2002; Dawson, 2008; Koornneef et al., 2009; Aulbach et al., 2011; Teklay et al., 2011; Gibson et al., 2013). A number of such studies associate the invading metasomatic fluids to impingement of a mantle plume(s) that supplies heat, mantle melts and fluids/volatiles from the deep-mantle (see Aulbach et al., 2011 for a review). However, limited information is currently available on key volatile tracers such as CO_2 and N_2 – isotope characteristics or relationship to noble gas isotopes (e.g., $CO_2/^3He$) – indicators which could identify provenance, extent of mixing, and other petrogenetic processes related to fluxing of volatiles between mantle (upper and lower) and surficial reservoirs (e.g., Dunai and Porcelli, 2002; Hahm, et al., 2009). In main part, this reflects the difficulty of carrying out precise isotopic and elemental measurements on extremely small quantities of volatiles trapped in ultramafic crystals.

In this contribution, we present new results on the He, CO_2, N_2 and Ar (isotopes and relative abundances) characteristics of trapped volatile components sited within fluid inclusions of mantle xenoliths from nine localities along the strike of the EARS. These locations – in the Red Sea, Ethiopia, Kenya and Tanzania – cover different segments of the EARS from (i) the Ethiopia Rift in the north, through (ii) the northern Kenya Rift (north of ~2°N), and to (iii) the southern Kenya Rift in southern Kenya and northern Tanzania. We supplement these volatile data with oxygen isotope data on the mafic crystals hosting the fluid inclusions. The approach adopted, i.e., obtaining volatile data via *in vacuo* crushing samples, presents a unique test case of provenance associated with a continental-rift environment as studies of these volatile phases can be used in a powerful manner to resolve provenance issues of volatile components. Thus, our aim is to identify the various sources contributing to the volatile components trapped within fluid inclusions and to evaluate which mantle/crustal processes act to control their elemental and isotope characteristics.

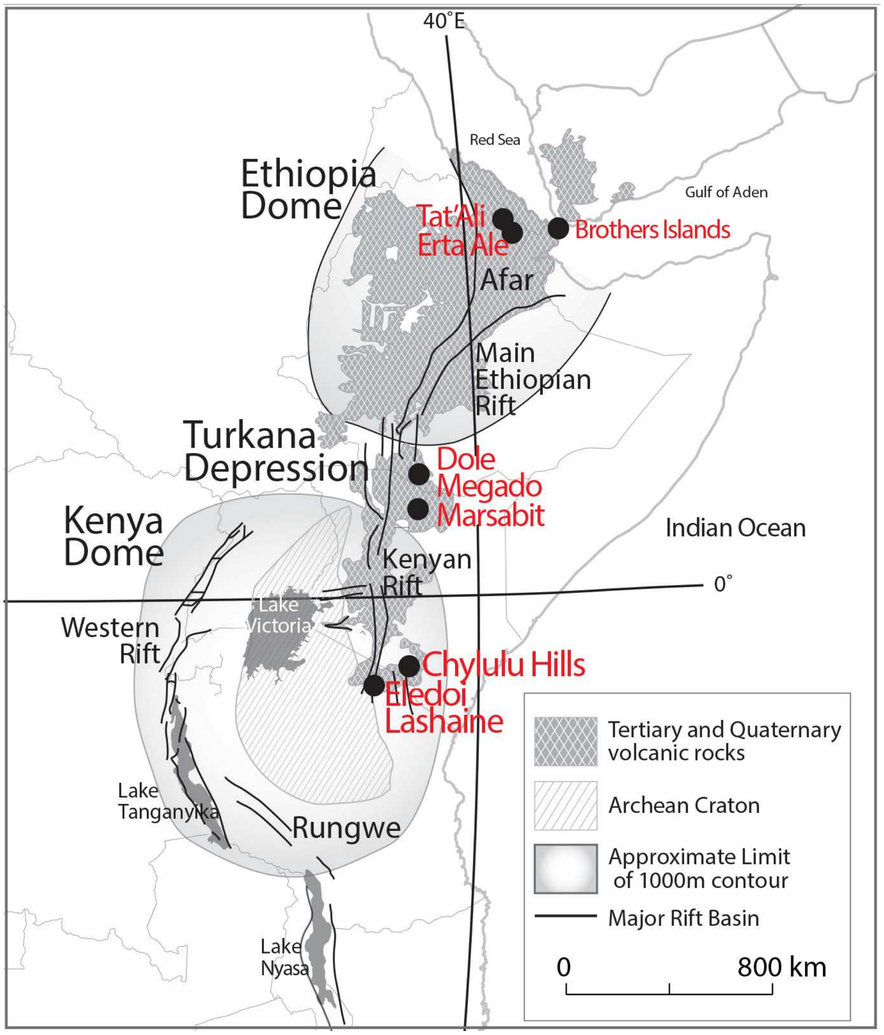

Figure IV.1: The East African Rift System (EARS) showing the Ethiopia and Kenya domes and samples localities along the Ethiopian Rift, the northern Kenya Rift and the southern Kenya Rift (modified from Rogers, 2006; Hilton et al. 2011).

IV.3 Sample selection

We have targeted ultramafic peridotite (n= 6) and pyroxenite (n=19) xenoliths from different segments of the EARS (**Figure 1**) for new He-CO_2-N_2-Ar isotope and relative abundance measurements. Oxygen isotope analyses were carried out on host crystals. A large number (n = 68) of EARS peridotite and pyroxenite xenoliths were first crushed to determine ^{3}He/^{4}He ratio and He abundance characteristics to indentify relatively gas-rich mineral separates (see Section 3 and Halldórsson et al., 2014), and a sub-set of xenoliths with high gas content were selected for further analyses involving CO_2-N_2-Ar-O isotopes. Visual observations can identify fluid inclusions within most crystals of this study, and we note their occurrence either as small clusters of inclusions and/or as trails of inclusions. In general, these observations are similar to those described by Frezzotti et al. (2010) for mantle xenoliths from the Lake Tana region, Ethiopia. Sample details and locations are given in Table S1.

Many of the xenoliths localities of this study have been the focus of prior work (e.g., Dawson & Smith, 1988; Bedini et al., 1997; Bedini & Bodinier, 1999; Roger et al., 1999; Dawson, 2002; Lorand et al., 2003; Reisberg et al., 2004; Aulbach et al., 2011; Orlando et al., 2006; Kaeser, 2006; Meshesha et al., 2011; Beccaluva et al., 2011). However, for the most part, the majority of these studies have focused on the peridotites with relatively little attention paid to pyroxenites xenoliths. In contrast, the focus of this work is largely on the ultramafic pyroxenites as a consequence of the relatively high gas content of these samples. Background detail on the petrology and geochemistry of some key EARS pyroxenites, including those included in this work, can be found in Dawson & Smith (1973), Lloyd (1981), Lloyd et al. (1985), Lloyd (1987), Lloyd et al. (1987), Davies and Lloyd (1989), Lloyd et al. (1991), Dawson & Smith (1992), Henjes-Kunst and Alther (1992), Ulianov et al. (2006), Orlando et al. (2006) and Kaeser et al. (2009). The origin of these pyroxenites is commonly ascribed to multiple metasomatic events interacting with pre-existing mantle peridotites.

In detail, this study has utilized xenoliths from the following regions:

(1) Two peridotite xenoliths from Seven Brothers Island (Sept Frères: 5th and 6th Islands) offshore Djibouti (TF samples), between the Red Sea and the Gulf of Aden.

(2) Pyroxenite xenoliths, dominated by clinopyroxene (CPX), from Tat'Ali (n=3) and Erta Ale (n=3) axial volcanic chains in the Afar area (G samples), some of which were previously analyzed for He isotopes by Scarsi and Craig (1996). In addition, there is one pyroxenite from the central Afar area of Afdera (C-244).

(3) Ultramafic xenoliths from the areas of Megga, Megado and Dilo in southern Ethiopia (i.e., northern Kenya Rift; TAA samples, n=4). Sample descriptions and a discussion of mineralogy and implications of major and trace element geochemistry of these samples are given in Conticelli et al. (1999) and Orlando et al. (2006). Equilibrium pressure of these xenoliths have been constrained to about 1.3-2.3 GPa, which corresponds to a depth of origin of 38-50 km (group C pyroxenites: samples TAA-329B and TAA-345B) to 96 km (group B pyroxenites: samples TAA-332B and TAA-332C) in the SCLM (Orlando et al. 2006).

(4) Pyroxenite xenoliths from Kenya (Ke samples) which includes one xenolith from Marsabit (in the northern Kenya Rift) and four from Chyulu Hills (southern Kenya Rift), some of which are discussed in the study of Hopp et al. (2007). Detailed discussion of the petrology and geochemistry of the Chyulu Hills and Marsabit xenoliths can be found in Henjes-Kunst and Alther (1992), Ulianov et al. (2006) and Garasic (1997), and in Henjes-Kunst and Alther (1992) and Kaeser et al. (2006), Kaeser (2006), Kaeser et al. (2007a), Kaeser et al. (2007b) and Kaser et al. (2009), respectively. On the basis of various thermobarometers, Ulianov et al. (2006) constrained the formation pressure of sample Ke1910/11 from Chyulu Hills to between 1.3 and 2.0 GPa (36 to 60 km) which agrees with previous estimates of ~1 to

~2.6 GPa (30 to 75km) for peridotites and pyroxenites from both Marsabit and Chyulu Hills (Henjes-Kunst & Alther, 1992; Kaeser et al., 2009).

(5) Two peridotite xenoliths from the Eledoi cinder cone, nearby Pello Hill (TAZ samples), and five pyroxenite xenoliths from Lashaine (Las samples), in northern Tanzania, in the southern Kenyan Rift. A general description of Eledoi and Lashaine peridotites can be found in Dawson and Smith (1988), Lee et al. (2000), Dawson (2002) and Rudnick et al. (1994). Dawson and Smith (1973) describe the Lashaine pyroxenites. Notably, and in agreement with our observations, Dawson and Smith (1973) report the occurrence of amphibole in Lashaine pyroxenites but mineral modes are generally dominated by CPX (between 60 and 82%). However, mineral assemblages in the Lashaine pyroxenite are notably poor in Al_2O_3, precluding estimates of formation pressures (Dawson & Smith, 1973).

IV.4 Analytical techniques

IV.4.1 Helium and argon analysis by in-vacuo crushing

Olivine (OL) and/or pyroxene (PX) crystals from the EARS peridotite and pyroxenite xenoliths were crushed under ultra-high-vacuum (UHV) to determine $^{3}He/^{4}He$ ratio and He abundance characteristics using standard procedures described in Hilton et al. (2011). The selection of material for combined neon and argon analysis, and combined carbon and nitrogen analysis, was guided by those samples having relatively high He abundances (see section 4.3). Neon and argon isotope and abundance characteristics obtained by crushing under UHV of xenoliths analyzed for helium used techniques similar to those described in Furi et al. (2010) and Hahm et al. (2012). Argon isotope ratios ($^{40}Ar/^{36}Ar$), argon abundance (^{40}Ar) along with air-corrected radiogenic argon ($^{40}Ar^*$ - see section 4.1) and derived $^{4}He/^{40}Ar^*$ ratios are reported in Table s1, while the full helium dataset of EARS xenoliths along with Ne isotopes is reported elsewhere (Halldórsson et al. 2014).

IV.4.2 Oxygen isotope analysis by laser fluorination

Oxygen isotope analyses were carried out utilizing a CO_2-laser fluorination system that generates O_2 from silicate minerals (Bao and Thiemens, 2000). Mineral separates were handpicked using a stereo microscope. This procedure helped ensure that any minerals affected by secondary alteration, such as the presence of secondary carbonate minerals which might affect $\delta^{18}O$ values, were avoided. An example of an alteration-free mineral separate is given in Figure S1 (supplementary material). All samples were thoroughly washed with acetone and dried at 110°C for 40 to 50 hours. The dried samples are crushed to powder in a porcelain mortar-pestle and transferred into the sample holder of the fluorination chamber which held seven samples and two standards (NBS-28). The fluorination chamber was evaluated to UHV and heated for at least 12 hours before fluorination.

The fluorination chamber and samples were pre-fluorinated (without lasering) twice with BrF_5 to remove any adsorbed moisture from the chamber walls and grain surfaces. Release of any water vapor during the pre-fluorination steps was carefully monitored using a capacitance manometer until water vapor within the sample chamber could not be detected. The amount of oxygen in the second pre-fluorination step, was always < 0.5 micromoles.

Fluorination of samples and standards (each batch of samples was bracketed by the NBS-28 standard) was performed with 30 mbar of BrF_5 which was transferred from a BrF_5-filled Kel-f tube to a liquid nitrogen (LN_2) filled U-trap and pumped to UHV for 5 minutes to remove any non-condensable gases. The clean BrF_5 aliquot was then expanded to the pre-cleaned sample chamber and samples were lasered for 2 minutes using a CO_2-laser. The condensable fluorination products were collected in the U-trap for 10 minutes and the evolved oxygen was collected via a second LN_2 U-trap filled with molecular sieve (5A). The amount of collected oxygen was monitored in a calibrated volume using a capacitance manometer and trapped in a molecular sieve filled sample tube for transfer to a dual-inlet multi collector IRMS (Thermo-Finnigan MAT 253) for oxygen isotope ratio measurement. The standard NBS-28 analyses showed a precision of 0.1‰ in $\delta^{18}O$ from 10 individual analyses.

IV.4.3 Combined carbon and nitrogen analysis by in-vacuo crushing

A new protocol was developed for the simultaneous extraction and collection of CO_2 and N_2 for abundance and isotope analyses during the course of this study. Following the same hand picking and cleaning protocols described above (section 3.1), between 1 and 3 g of fresh mineral chips were loaded into screw-type crushers (constructed from modified Nupro vacuum valves; see details in Stuart et al., 1994; Furi et al., 2010; Hahm et al., 2012), evacuated to UHV and kept at ~100°C overnight. In order to maximize gas yields, gases were released from samples by single-step crushing *in vacuo* using an external hydraulic press capable of 5 tons pressure. During crushing, liberated gases were exposed to LN_2 cooled Pyrex®-glass fingers to both capture the CO_2 and minimize absorption of CO_2 on to any new mineral surfaces created during the crushing stage.

Following trapping of the condensable gas fraction, the non-condensable gases, including N-species, were then inlet into a dedicated metal preparation line described previously in Barry et al. (2012). Briefly, the line acts to purify the released gas by promoting the oxidation of carbonaceous (CO, C_2H_4) and nitrogenous (NO) species to CO_2 and NO_2 with exposing gases to pure O_2, produced by heating a copper oxide (CuO) finger to 850°C in presence of a platinum foil catalyst (at 1000°). After purification, nitrogen abundances and isotope ratios were determined using a modified VG5400 noble gas mass spectrometer, employing static triple collection on masses 28, 29 and 30. A description of the preparation protocol for N-isotope measurement as well as the modified VG5400 instrument is given by Craig et al. (1993) and Barry et al. (2012). The advantage of the multi-collector approach is the increased sensitivity and reproducibility of internal and external standards, and the correction for CO interference. An internal pure N_2 standard, calibrated relative to Scripps-pier air, was repeatedly measured on a daily basis throughout the analyses of this sample suite. In addition, repeated measurements (n=5) of the Scripps-pier air standard during various runs, following the same analytical protocol as samples, allowed evaluation of uncertainties associated with both sample preparation and mass spectrometer measurement. We take the average reproducibility of our in-house air standard $\delta^{15}N$ value of ± 0.47‰ (1σ) as the best estimate of the external reproducibility of the nitrogen system.

Due to anticipated low intrinsic N_2 concentrations in mantle-derived samples, precise characterization of system and sample blanks is essential for high precision N-isotope measurements. Procedural N_2 blanks were run prior to each individual sample as described in Barry et al. (2012) and averaged 3.5 ± 0.6 ($\times10^{-6}$) cm^3STP. With the exception of two peridotite xenoliths from Eledoi, which are characterized by extremely low nitrogen contents, blank contributions were < 20% of sample yields in most cases (see Table 2 for details).

We also tested the crushing efficiency of releasing N_2 in a single crushing step. Two out of four duplicates show excellent agreement in their intrinsic N_2 concentrations: sample TAA-332C gave intrinsic N_2 contents of 33.9 and. 33.4 ($\times10^{-6}$ cm^3STP/g) for sample loads of 1.731 and 2.715 grams, respectively. In this case, the results indicate that the majority of the N_2 is released from fluid inclusions in a single crushing step. However, relatively poor reproducibility between duplicate runs of sample TF-140 (3.2 vs. 9.3 $\times10^{-6}$ cm^3STP/g) and sample G-116 (5.5 vs. 16.6 $\times10^{-6}$ cm^3STP/g) might also suggest that N_2 concentrations may reflect the relative contents (density) of fluid inclusions in individual samples (see section 5.1.1).

IV.4.4 Carbon relative abundance and isotope analysis

The condensable gas fraction released during the N_2 extraction (mostly CO_2) was isolated and transferred to a dedicated Pyrex®-glass vacuum line for purification prior to manometric measurement in a calibrated volume to obtain total abundances (Macpherson et al., 1999). Procedural CO_2 blanks were run prior to each individual sample and averaged 9.3 ± 11.7 ($\times 10^{-6}$) cm^3STP. Blank contributions were significantly less than 1% of sample yields in most cases (except for samples G-114 (1.4%), G-116 (2.8%) and Las-3d (3.1%)). Following abundance measurement, the CO_2 was transferred to a Thermo-Finnigan DeltaPlusXP isotope ratio mass spectrometer in Pyrex®-glass breakseals for $\delta^{13}C$ analysis.

A concern with crushing crystals for CO_2 abundances, and the use of these data to calculate $CO_2/^3He$ ratios (as well as other ratios involving CO_2), is the possibility of inefficient release whereby some volatiles remain within fluid inclusions and/or are lost by adsorption onto fresh mineral surface created during the crushing. To address these concerns, we performed a number of duplicate runs and experimented with a step-wise crushing approach. In the first series of experiments, different amounts of sample were loaded in the crushers to test sample crushing efficiency. Irrespective of the amount of sample loaded, three duplicate analyses (G-115, TAA-329B and Las-3f) agree to within 20%. For example, crushing 2.656 g of sample TAA-332C gave 111 ($\times 10^{-4}$) cm^3STP/g, compared to 92 ($\times 10^{-4}$) cm^3STP/g when 1.114 grams of sample was processed. Somewhat more CO_2 was released in the case of sample Las-3f, with yields of 140 and 165 ($\times 10^{-4}$) cm^3STP/g from 2.776 grams and 1.003 grams, respectively. However, this difference has insignificant (<1%) changes to the derived ratios involving CO_2 (e.g., $CO_2/^3He$). Second, we adopted step-wise crushing, whereby samples were repeatedly crushed without breaking vacuum to test for inefficient release of CO_2 following the first crushing step. We selected samples CH07-

01 and CH07-07, a gas-rich peridotite xenolith samples from the Chisny crater on Reunion Island (Furi et al. 2010), and subjected it to a series of stepwise crushing experiments (Table S3 of the supplementary material). No CO_2 was released during the extended step-wise crushing experiments providing further evidence for complete CO_2 release (and capture in the glass breakseal) during the single step crushing protocol adopted in this study.

IV.5 Results

Helium and argon along with neon isotope ratios and relative abundance systematic on all samples have been reported elsewhere (Halldórsson et al., 2014). For completeness, however, we report the helium and argon isotopes and relative abundance systematics (without neon) in Table S1 along with new oxygen isotope values. Carbon and nitrogen abundance and isotope ratios, including derived elemental ratio CO_2/N_2, $CO_2/^3He$, $CO_2/^{40}Ar^*$ and $N_2/^3He$ are reported in Table S2.

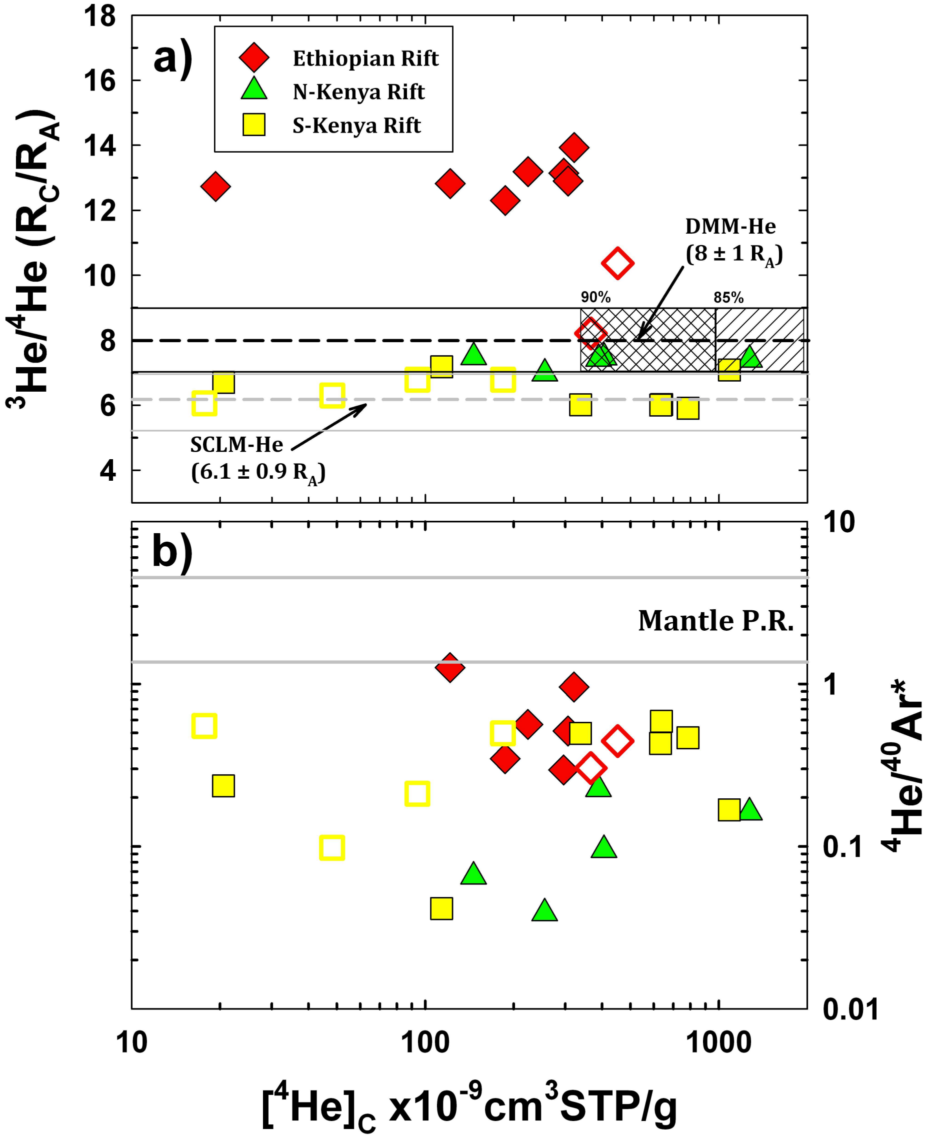

Figure IV.2: Plot of (a) the ^{3}He/^{4}He ratio of each sample (reported in the R/R$_A$ notation where R = sample ^{3}He/^{4}He corrected for a minor air-derived component and R$_A$ = air ^{3}He/^{4}He), (b) ^{4}He/^{40}Ar* ratios (where ^{40}Ar* is the radiogenic Ar corrected for any air) versus He concentration. The He isotope composition of Depleted MORB mantle (DMM) and Sub-Continental Lithospheric Mantle (SCLM) is given in Graham (2002) and Gautheron and Moreira (2002), respectively. Double hatched area in MORB bar signifies that 85% of all reported He abundances in MORB vesicles are ≥1000 ncm3/g, whereas 90% of MORB have [He] ≥350 ncm^{3}STP/g (Macpherson et al., 1998). The production ratio of ^{4}He$_{radiogenic}$/^{40}Ar$_{radiogenic}$ in the mantle lies between 1.4 and 4.8, the former being the time-integrated ratio for 4.5 Ga, and the latter representing present-day instantaneous production. Pyroxenites are denoted with closed symbols whereas peridotites with open symbols.

IV.5.1 Helium and argon abundances and isotopes

In **Figure 2,** we plot (a) He-isotopes and (b) calculated ^{4}He/^{40}Ar* ratios (see footnote to Table 1 for details of the corrections) versus He concentrations ([He]) corrected for the presence of atmospheric helium (see Halldórsson et al., 2014 for details). Helium concentrations range from 18 to 1272 ×10^{-9} cm^{3}STP/g but with only five xenoliths showing concentrations <100 ×10^{-9} cm^{3}STP/g (**Fig. 2a**). The remaining xenoliths have He values >100 ×10^{-9} cm^{3}STP/g, which are significantly higher than typical [He] in phenocrysts from lava flows (e.g., Marty et al., 1993: Marty et al., 1996; Scarsi and Craig, 1996; Class et al., 2005; Pik et al., 2006; Hilton et al., 2011) and xenoliths (Aulbach et al., 2011; Beccaluva et al., 2011; Hopp et al., 2007; Hilton et al., 2011) previously obtained from the EARS using crushing extraction methods. The range obtained here is similar to, or considerably lower than, [He] in the vast majority (85%) of Mid-Ocean Ridge basalts (MORB) glass samples from the major ocean basins (typically between 10^{-6} to 10^{-4} cm^{3}STP/g; Macpherson et al., 1998; Graham, 2002).

The xenoliths display a wide range in He-isotopes from 5.9 to 13.9R$_{A}$ (where R$_{A}$ = air ^{3}He/^{4}He **- Fig. 2a**). We emphasize three points: First, the highest measured values come from 5th Brothers Island (Red Sea) (10.4R$_{A}$) and northern Ethiopia (Tat'Ali and Erta Ale) (12.3-13.9R$_{A}$) with values that greatly exceed the canonical range of 8 ± 1R$_{A}$, diagnostic of the Depleted MORB Mantle (DMM) (Graham, 2002). Second, samples from southern Ethiopia (i.e., the northern Kenya Rift) as well as one sample from the islands off Djibouti fall within this canonical DMM range. Finally, the majority of samples from the southern Kenya Rift (Chyulu Hills, Eledoi and Lashaine), fall within or overlap with SCLM (6.1 ± 0.9 R$_{A}$; Gautheron and Moreira, 2002). Thus, despite an almost two orders of magnitude variation in [He], ^{3}He/^{4}He ratios fall within relatively narrow groupings diagnostic of plume-like, DMM-like and SCLM He affinities, in a general north-to-south direction.

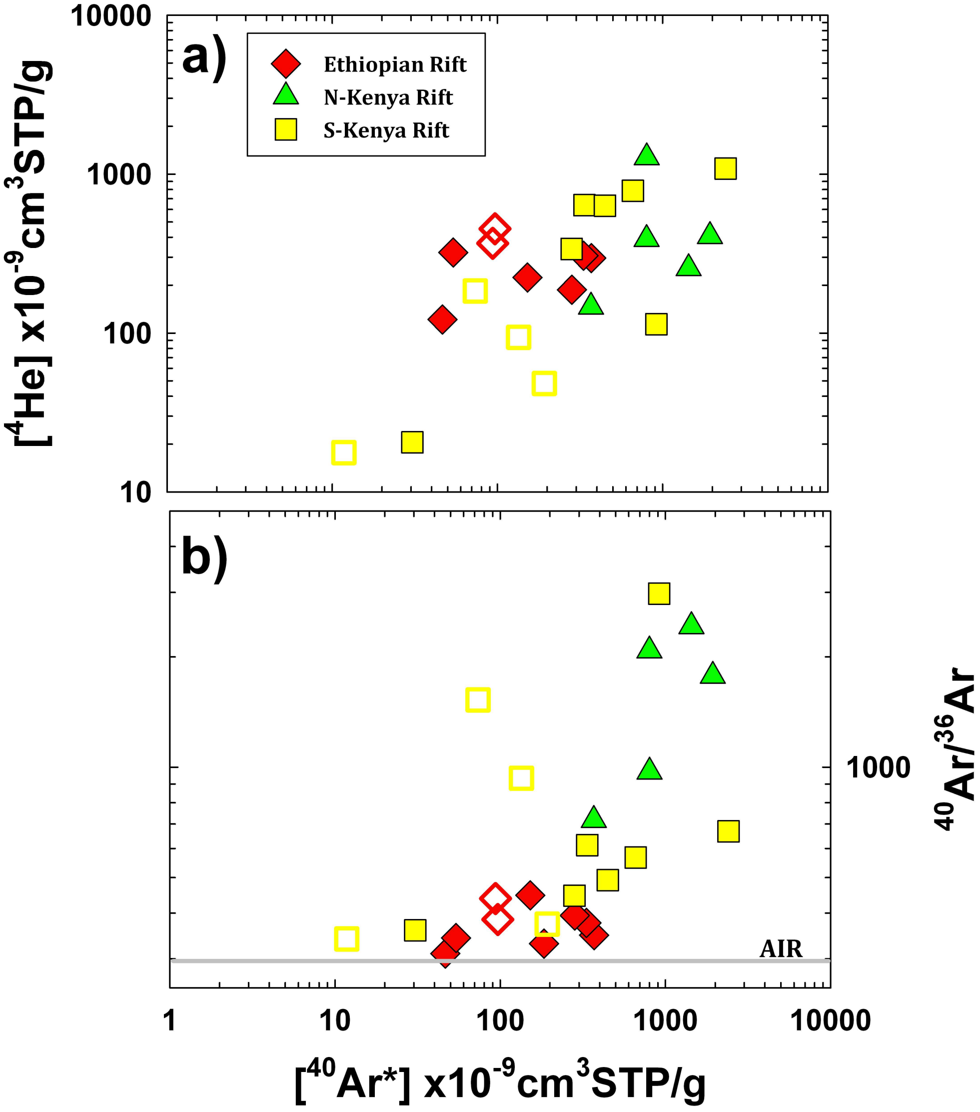

Figure IV.3: (a) [He] and (b) $^{40}Ar/^{36}Ar$ ratios in mantle xenoliths from EARS versus $^{40}Ar^*$. Pyroxenites are denoted with closed symbols whereas peridotites with open symbols.

In **Figure 3**, we plot **(a)** air-corrected He content ($[He]_C$) and **(b)** $^{40}Ar/^{36}Ar$ ratios versus the radiogenic ^{40}Ar content (i.e., corrected for the presence of atmospheric argon - see Table 1 footnotes for details). The radiogenic Ar concentrations [$^{40}Ar^*$] vary from 11.8 to 2408 $\times 10^{-9}$ cm^3STP/g with a generally positive correlation between magmatic helium and radiogenic argon evident in **Fig 3a**. This is consistent with volatiles being released from similar storage sites within the mafic crystals, presumably fluid inclusions (see section 5.1.1). Significantly, all xenoliths, except C-244, have $^{40}Ar/^{36}Ar$ ratios higher than air (298.6 – Lee et al. 2006) and reach values as high as 2976 (**Fig. 3b**). No bulk crushing data are available on other EARS xenoliths but we note that our samples have significantly higher $^{40}Ar/^{36}Ar$ ratios than those obtained on phenocrysts from lavas in the Afar area, where $^{40}Ar/^{36}Ar$ ratios range between air-like to 383.6 (Marty et al., 1993).

All xenoliths, except C-244, have $^{4}He/^{40}Ar^{*}$ ratios lower than the current and time-integrated mantle production ratios (= 1.4 and 4.8, respectively; Porcelli & Ballentine, 2002; Hanyu et al., 2011) and range from 0.04 to 1.26 (**Fig. 2b**). These values are in good agreement with xenoliths from oceanic islands, e.g., Hawaii, Réunion, Samoa and Kerguelen (Graham, 2002) as well as sub-continental xenoliths from localities world-wide (Barford et al. 1998, Matsumoto et al. 1998, 2000, 2005, Yamamoto et al. 2004, 2009, Hopp et al. 2004, 2007, Buikin et al. 2005, Gautheron et al. 2005, Czuppon et al. 2009, 2010,). Again, sample C-244 stands out with air-like $^{40}Ar/^{36}Ar$ ratio, precluding calculation of the $^{4}He/^{40}Ar^{*}$ ratio. The implications of these low $^{4}He/^{40}Ar^{*}$ ratios that characterize the EARS xenoliths are discussed in section 5.1.

IV.5.2 Oxygen isotopes

In **Figure 4,** we plot a histogram showing the distribution of $\delta^{18}O$ values of the mafic xenolith minerals which host the fluid inclusions. Oxygen isotope ($\delta^{18}O$) values of OL and PX crystals span a wide range from +2.4 to +6.5‰ (versus VSMOW). Significantly, OL $\delta^{18}O$ values show a somewhat smaller range (Δ=2.5‰) and vary from +4.0 to +6.5‰ compared to PX $\delta^{18}O$ values which vary from +2.4 to +5.9‰ (Δ=3.5‰). For the most part, this range in OL $\delta^{18}O$ is significantly greater than the range obtained from a wide variety of mantle peridotites xenoliths where $\delta^{18}O_{OL}$ range between +4.8 to +5.5‰ and average +5.18 ± 0.28‰ (2σ). For comparison, coexisting CPX in mantle peridotites range between +5.3 to +5.9‰ (mean value = +5.57 ± 0.32‰), and coexisting orthopyroxenes (OPX) range between +5.4 to +6.1 (mean value = +5.69 ± 0.28‰) (Mattey et al. 1994). Thus, only six samples (3 pyroxenites (including one olivine crystal from sample G-122) and 2 peridotites) overlap with the entire $\delta^{18}O_{OL}$, $\delta^{18}O_{PX}$ and $\delta^{18}O_{OPX}$ range expected for mantle peridotites (+4.8 to +6.1‰) whereas two peridotite samples display $\delta^{18}O$ values > than this range. Notably, one pyroxenite from the Turkana Depression in southern Ethiopia (TAA-332B) has $\delta^{18}O_{PX}$ value of +2.4‰, well below the canonical mantle peridotites range.

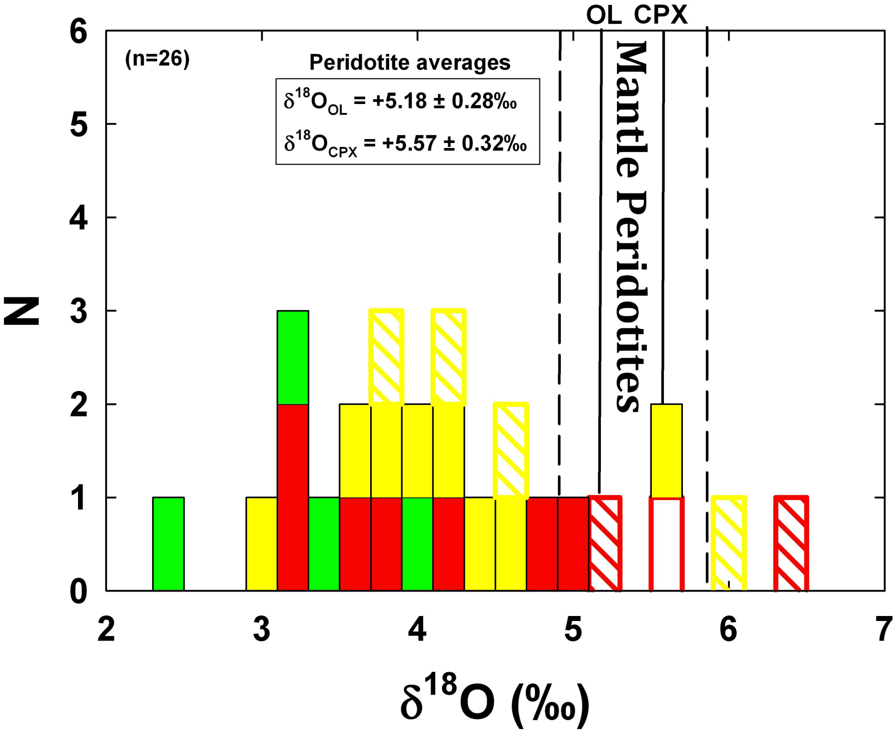

Figure IV.4: Histogram of oxygen isotopes. We indicate the mean values for $\delta^{18}O_{OL}$ (+5.18 ± 0.28‰ (2σ)) and their coexisting CPX (+5.57 ± 0.32‰) in mantle peridotite xenoliths as solid (mean) and dashed (error) vertical lines (Mattey et al., 1994). Pyroxenites are denoted with closed areas whereas peridotites with open hatched areas. Note that one olivine crystal from an Ethiopian pyroxenite (G-122) is indicated as an open area. Blue=Red Sea; Red=Ethiopia; Green=Kenya; Yellow=Tanzania.

With respect to comparative studies, detailed oxygen isotope studies on xenoliths from the EARS are rare but we point out that in contrast to the large range of values reported for our xenoliths, peridotite xenoliths from Plio-Quaternary volcanic fields from the south coast of Yemen (Bir Ali and Ataq) showed a very limited range in oxygen isotope ratios with $\delta^{18}O_{OL}$ and $\delta^{18}O_{CPX}$ that fall within ranges defined by mantle peridotites xenoliths (Chazot et al., 1997). Our oxygen isotope results also differ from the $\delta^{18}O$ values of OL and CPX mineral in basalts and rhyolitic rocks from the Ethiopian-Yemeni large igneous province that erupted 29-31 Ma in Yemen which display $\delta^{18}O$ values that either overlap with mantle peridotites values or show values significantly higher (up to +6.9‰), consistent with significant contributions from the Pan-African crust (Baker et al. 2000).

Finally, and most significantly, we point out similarities of our data with $\delta^{18}O$ values found in eclogite xenoliths of kimberlites found at several localities in southern Africa (Roberts Victor, Kao, Deutsche Erde, Bellsbank) as well as those found in metasomatized peridotite xenoliths, also from southern Africa. These xenoliths all display $\delta^{18}O$ values significantly lower and higher than values expected for pristine mantle peridotites (Garlick et al. 1971; MacGregor and Manton, 1986; Shervais et al. 1988; Ongley et al. 1987; Neal et al. 1990). The EARS xenoliths thus show striking similarities with $\delta^{18}O$ values found in southern African eclogites whose origin is commonly linked to disrupted fragments of ancient subducted oceanic crust/lithosphere (e.g., Jacob, 2004; Smart et al. 2012; Smith et al., 2014).

IV.5.3 Carbon and nitrogen abundances and isotopes

We plot [CO_2] and [N_2] for the EARS xenoliths versus [$^{40}Ar^*$] in **Figure 5**. For comparison, we plot data from MORB that were also obtained by *in vacuo* crushing (Marty and Zimmerman, 1999), allowing for direct comparison with our xenolith data. Carbon dioxide concentrations vary from 0.79 to 153 ($\times 10^{-4}$ cm^3STP/g) and, with the exception of ultramafic peridotites from N-Tanzania (where CO_2 was below detection limit in 2 cases), correlate well with the radiogenic argon content (**Fig. 5a**).

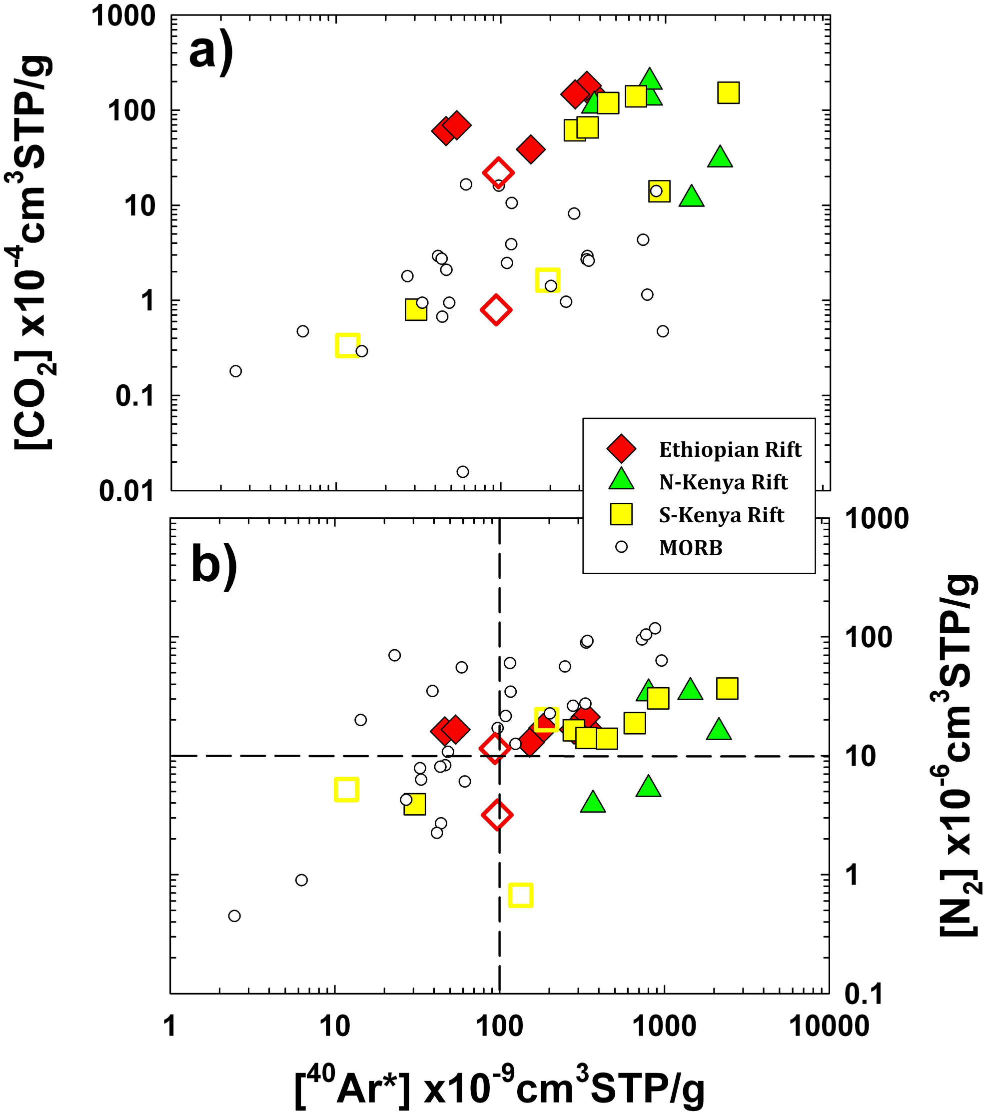

Figure IV.5: Concentrations of CO_2 (upper plot) and N_2 (lower plot) versus ^{40}Ar* where ^{40}Ar* is the radiogenic Ar concentration calculated assuming that all ^{36}Ar is air-derived (see Halldórsson et al., 2014 for details). Data sources: Xenoliths: this work; MORB glasses (Marty and Zimmerman, 1999). Pyroxenites are denoted with closed symbols whereas peridotites with open symbols.

For the most part, both the [CO_2] and the [$^{40}Ar^*$] of the EARS xenoliths, resemble those obtained on MORB glasses. However, two distinct correlations trends are apparent in **Figure 5a**: (i) a trend that strongly overlaps the MORB range and (ii) a trend that characterizes almost all the pyroxenites (filled symbols) with significantly higher [CO_2] for a given [$^{40}Ar^*$] relative to MORB range. We point out that 3 of the 4 OL crystals (open symbols) that yielded measureable [CO_2] belong to trend (i) – potentially a reflection of the greater retentivity of CO_2 in fluid inclusions in PX relative to OL, as has been demonstrated experimentally (Yamamoto et al. 2011). However, we note that the majority of MORB glasses fall on trend (i), implying that the higher [CO_2], for a given [$^{40}Ar^*$] relative to MORB, are indeed a characteristic feature of most pyroxenites.

Nitrogen concentrations ([N_2]) vary from 0.67 to 36.8 ($\times 10^{-6}$) cm^3STP/g, with only six xenoliths showing values > 20 ($\times 10^{-6}$) cm^3STP/g (**Fig. 5b**). These values are, on average, somewhat lower than in MORB glasses where [N_2] reach values as high as ~100 ($\times 10^{-6}$) cm^3STP/g. The relationship between [$^{40}Ar^*$] and [N_2] is less straightforward compared to the [CO_2] and [$^{40}Ar^*$] systematics, but we generally observe N_2 contents > 10 cm^3STP/g $\times 10^{-4}$ when [$^{40}Ar^*$] are > 100 $\times 10^{-9}$ cm^3STP/g (**Fig. 5b** upper right quadrant). This is comparable to CO_2 and He and is consistent with a general coupling of He-C-N-Ar trapped in similar storage sites (i.e., fluid inclusions) in mafic crystals. Thus, volatile concentrations may reflect the relative contents (i.e., density) of fluid inclusions in each sample, consistent with observations on several xenolith suites elsewhere (e.g., Dunai & Baur, 1995; Dunai & Porcelli, 2002 – see also section 5.1.1.).

In **Figure 6a**, we plot carbon isotope values ($\delta^{13}C$-CO_2-VPDB) versus [CO_2]. Notably, three duplicates runs agree to within 0.2‰, well within our conservative estimate for external reproducibility (<0.5‰). The $\delta^{13}C$ values span a limited range from -3.3 to +0.8‰, with only two xenoliths showing values lower than -2.0‰. Such high $\delta^{13}C$ values are at the upper-end of available mantle xenoliths $\delta^{13}C$ data that display a predominant peak at -6‰ but also another at -

25‰ (summarized in Deines, 2002).

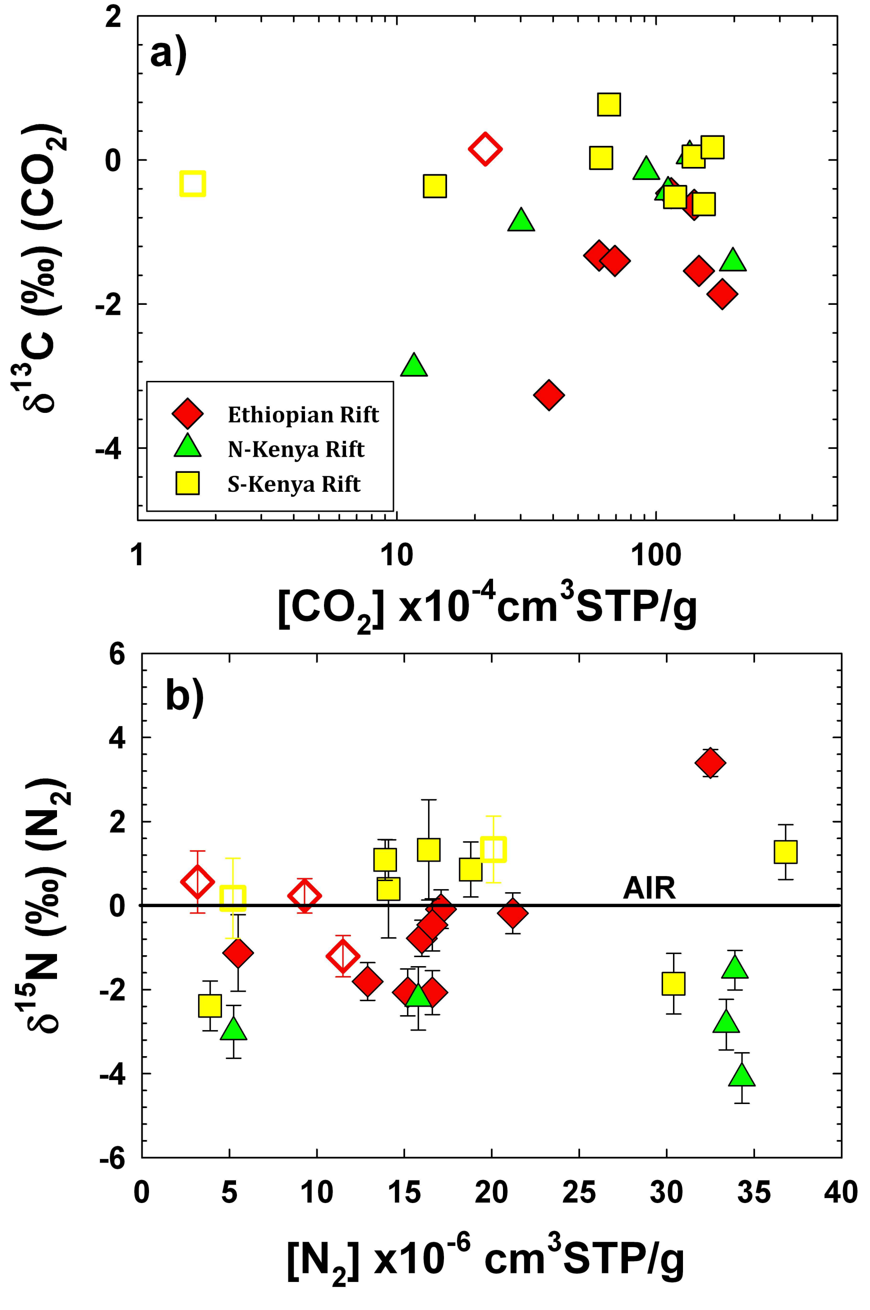

Figure IV.6: Isotope-concentration plots: (a) $\delta^{13}C$ (CO_2) values of all samples (including duplicates) plotted vs. [CO2]. (b) $\delta^{15}N$ (N_2) values of all samples (including duplicates) plotted vs. [N_2]. Solid black line indicates the isotope composition of Air. Data sources: Table 2. Pyroxenites are denoted with closed symbols whereas peridotites with open symbols.

Also, numerous studies on MORB and diamonds have shown upper-mantle carbon ($\delta^{13}C$) of the DMM reservoir to fall within the range -5 ± 1‰ (e.g., Marty and Zimmerman, 1999; Cartigny, 2005), in good agreement with the higher $\delta^{13}C$ peak observed in mantle xenoliths. This point reinforces the notion that our data have significantly higher $\delta^{13}C$ values than DMM. Additionally, our values are also significantly more positive than estimates of the lower mantle, as sampled at hotspot localities that display high $^{3}He/^{4}He$ ratios, such as Loihi Seamount (Exley et al. 1986), the Manus Basin (Shaw et al. 2004) and Iceland (Barry et al. 2014) where $\delta^{13}C$ values are only as high as ~ -4‰. Significantly, the majority of our xenoliths samples plot close to, or overlap with, values reported for marine carbonates of variable age (e.g., Veizer and Mackenzie, 2004) and/or carbonate mineral/veins formed during low-temperature sea-floor alteration (e.g., Alt & Teagle, 1999) which have $\delta^{13}C$ values close to 0 ± 3 ‰. (e.g., Staudigel et al., 1989; Alt & Teagle, 2003; Coggon et al., 2006).

We note that comparative *in-vacuo* crushing studies on SCLM xenoliths are scarce so direct comparison with available data is not possible since most data collected thus far have been obtained via step-vise heating experiments. However, we see no evidence for the presence of mantle carbon significantly depleted in ^{13}C which is commonly observed during such step-vise heating experiments in diamonds, graphite, and/or carbide in mantle minerals (Deines, 2002). The only *in-vacuo* crushing study reporting $\delta^{13}C$ values to date is the recent study of Demény et al. (2010). The carbon isotope compositions of inclusion-hosted CO_2 in that study ranged from –17.8 to –4.8‰, i.e., from mantle-like values to values significantly depleted in ^{13}C. It is also worth pointing out that our results show striking similarities with quenched carbonate-silicate inclusions in Canadian peridotitic clinopyroxene macrocrysts ($\delta^{13}C$ ~ -2.1‰), previously interpreted as consisted with a subducted carbon signature (van Achterbergh et al. 2002).

In **Figure 6b**, we plot nitrogen isotope values ($\delta^{15}N$-N_2-AIR) against [N_2]. Four duplicates runs are in good agreement with the exception of samples G-115 and TAA-332C which deviate outside the 1σ error. For these samples, we only discuss (and plot) $\delta^{15}N$ values that show the largest deviation from air (0‰), assuming that they better represent primary $\delta^{15}N$ values. In contrast to $\delta^{13}C$, $\delta^{15}N$ values of our samples show a wide range from -4.11 to +5.89‰, with the most positive value observed in a PX separate from southern Ethiopia. However, this sample had very low [N_2] (3.87×10^{-6} cm^3STP/g) and thus a relatively high blank contribution (23%). The implication of this highly positive value is questionable, and we choose to omit it from further interpretation as blank corrections exceeding 20% have been shown to be unreliable (Barry et al., 2012). The remaining $\delta^{15}N$ values (-4.11 to +3.39‰) are, for the most part, significantly higher than estimates of the DMM reservoir, as sampled at mid-ocean ridges ~ -5 ± 2‰ (e.g., Marty and Dauphas, 2003).

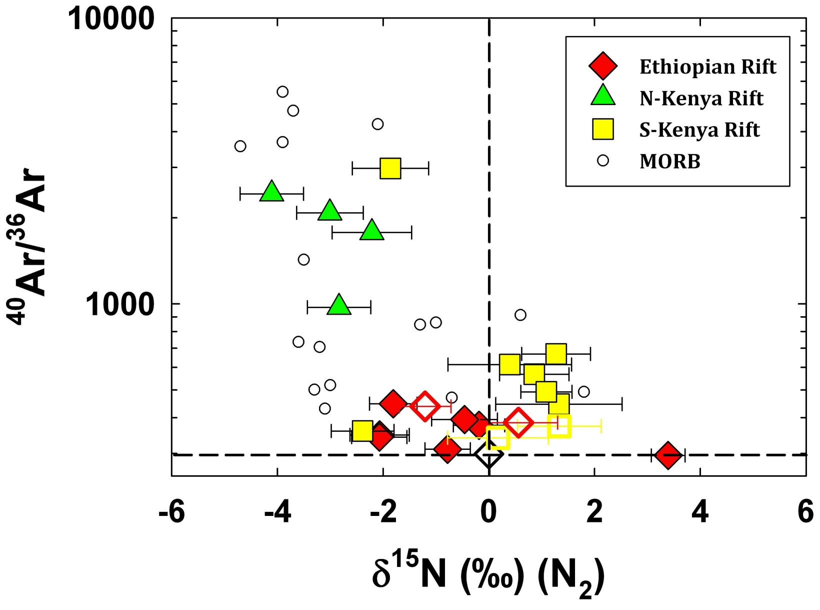

Figure IV.7: Argon isotopes ($^{40}Ar/^{36}Ar$) versus nitrogen isotopes together with Air (diamond) Data sources: xenoliths – Table 1 and 2; MORB glasses – Marty and Zimmerman, 1999. Note that only MORB glasses that fall within the canonical upper-mantle value 8 ± 1R_A are plotted. Pyroxenites are denoted with closed symbols whereas peridotites with open symbols.

In **Figure 7**, we plot $^{40}Ar/^{36}Ar$ ratios versus $\delta^{15}N$ values of the EARS xenoliths, and include MORB glasses that have He isotopic ratios diagnostic of the upper-mantle (DMM) reservoir (8 ± 1R_A) (Marty and Humbert, 1997; Marty and Zimmermann, 1999). We note that despite the fact that our $\delta^{15}N$ values are significantly higher than estimates of the DMM reservoir (-5‰), coupled $^{40}Ar/^{36}Ar$ - $\delta^{15}N$ systematics strongly resembles those observed in MORB. Significantly, we note that the highest $^{40}Ar/^{36}Ar$ ratios also display some of the lowest $\delta^{15}N$ values. We also point out the trend towards $\delta^{15}N$ values > air in samples with relatively low $^{40}Ar/^{36}Ar$ ratios (< 1000), an observation frequently identified in many OIB and attributed to admixture with a recycled crustal nitrogen component (Marty and Dauphas, 2003) (see section 5.3.1).

Finally, with regards to comparative $\delta^{15}N$ studies on SCLM xenoliths, the range of $\delta^{15}N$ values we obtained on EARS xenoliths (-4.11 to +3.39‰) is in generally good agreement with the range of values obtained on southeast Australian xenoliths ($\delta^{15}N$ = –6.0 to +2.0‰: Matsumoto et al., 2002). Additionally, Fischer et al. (2005) obtained a single value of -1.6‰ ± 2.5 for a San Carlos xenolith that falls within the range we obtain for EARS xenoliths. However, our data show significantly less variability when compared to N isotope xenolith data obtained by step-wise heating which show a large range from -17.3 to +30‰ (Mohapatra & Murty, 2000, 2002, Yokochi et al. 2009). As noted by Yokochi et al. (2009), some of these values could have been biased due to (i) contamination by surface N (Marty, 1995), (ii) kinetic effects during gas extraction (Boyd et al., 1993; Pinti et al., 2007), or (iii) analytical problems due to the use of N-reactive metals (Yokochi and Marty, 2006).

IV.5.4 Elemental ratios involving CO_2 and N_2

In **Figure 8**, we plot **(a)** $CO_2/^3He$ ratios, and **(b)** $N_2/^3He$ ratios versus CO_2/N_2 ratios together with MORB data (from Marty and Zimmerman, 1999). In order to demonstrate that EARS xenoliths preserve calculated ratios that are not affected by shallow-level degassing processes, the MORB data have been corrected for degassing fractionation (using their $^4He/^{40}Ar^*$ ratios and equations from Marty, 1995 - see also section 5.1.1.).

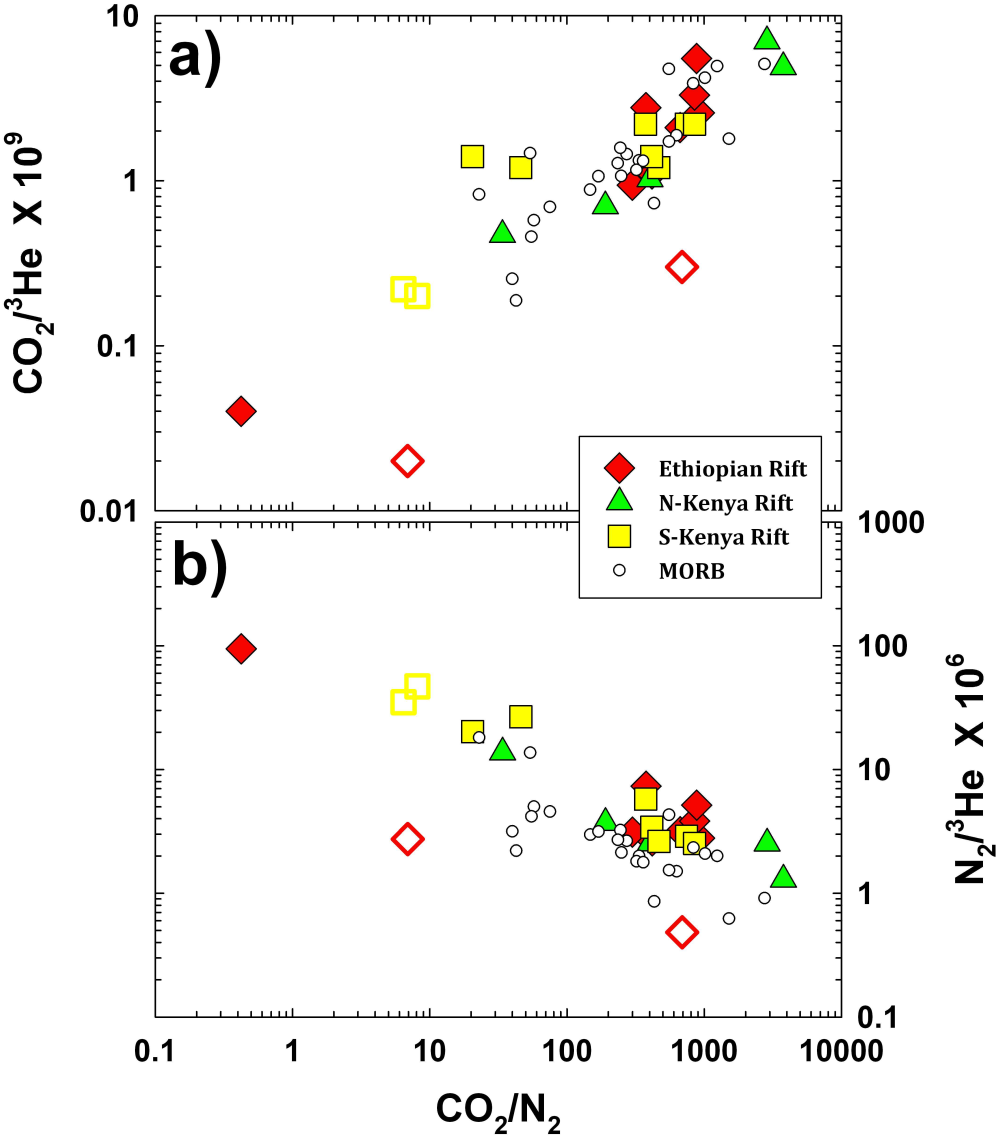

Figure IV.8: Plot of (a) $CO_2/^3He$ ratios and (b) $N_2/^3He$ ratios of each sample versus their CO_2/N_2 ratios. Also plotted are Mid-Ocean Ridge basalts corrected for fractional degassing using $^4He/^{40}Ar^*$ ratios (from Marty, 1995). Note the close association between EARS xenoliths and Mid-Ocean Ridge basalts corrected for fractional degassing, which is consistent with the notion that the xenoliths were not affected by fractional degassing processes. Pyroxenites are denoted with closed symbols whereas peridotites with open symbols.

The xenolith CO_2/N_2, $CO_2/^3He$, and the $N_2/^3He$ ratios vary by many orders of magnitude, from 0.42 to ~3800, 0.020 to 7.0 ($\times 10^9$), and 0.48 to 96 ($\times 10^6$), respectively, and generally show good overlap with the corrected oceanic glasses consistent with the notion that xenoliths derived ratios, have not been extensively modified via shallow level degassing. Notably, two peridotite samples from the Red Sea deviate from the general trend and have somewhat lower $CO_2/^3He$ and $N_2/^3He$ ratios for a given CO_2/N_2 ratio. Also, two peridotites and one pyroxenite lie on the general trend, but extend to lower CO_2/N_2 and $CO_2/^3He$ ratios and higher $N_2/^3He$ ratios compared to oceanic glasses and EARS xenoliths.

Comparative studies reporting combined C-N-He elemental systematics on SCLM and OIB xenoliths are still rare and dominated by the use of stepped-wise heating and/or bulk fusion methods to extract helium and carbon (e.g., Mattey et al., 1989; Porcelli et al., 1992; Trull et al., 1993; Dunai, 1993). The $CO_2/^3He$ ratios reported in these studies ranged from ~ 2 ($\times 10^9$) to ratios significantly higher than values reported here ~ 10^{13}. This is also the case in two studies on xenoliths from Reunion and Samoa (Burnard et al., 1994; 1998) that utilized laser extraction techniques to extract volatiles at the level of a single inclusion. Significantly, the $CO_2/^3He$ ratios of these studies extend from DMM-like values (~2 $\times 10^9$) to ratios as high as ~7 $\times 10^{11}$: however, the case was made that such high ratios were likely affected by surficial contamination. We note that Farley (1995) reported two $CO_2/^3He$ ratios (2.4 and 3.6 $\times 10^9$) obtained for Samoan xenoliths via bulk crushing – i.e., values close to the mean DMM value (~2 $\times 10^9$: Marty & Zimmerman, 1999).

IV.6 Discussion

IV.6.1 Integrity of data

In this section, we evaluate the integrity of our dataset by considering a number of fundamental mechanisms capable of modifying primary mantle volatile elemental and isotope characteristics. Such mechanisms include elemental and isotopic fractionations following degassing before crystal capturing, post-entrapment volatiles loss, and contamination with volatiles from the carrier melt and/or continental crust. By applying this approach, we aim to distinguish between (and identify) volatile characteristics purely of mantle origin from others which reflect secondary and presumably higher-level or shallower processes. Only by identifying the characteristics of EARS mantle-derived volatiles, is it possible to discuss implications and consequences for potential mantle sources contributing to EARS magmatism.

IV.6.1.1 Fluid inclusions as host of mantle volatiles

Noble gases (as well as N_2) strongly partition into CO_2-rich fluids that almost invariably occupy fluid inclusions found in mantle minerals (Dunai & Porcelli, 2002). As a consequence, volatile components found in xenoliths are preferentially located within such fluid inclusions. The abundance (or density) of fluid inclusions in various mantle minerals has been shown to correlate with [He] and [Ar] (Dunai, 1993; Farley et al. 1994; Dunai and Baur, 1995; Burnard et al. 1998), which suggest that concentrations of volatile elements released via *in vacuo* crushing are simply a reflection of inclusion density. The possibility also exists that volatile components can be trapped along grain boundaries at depth. However, Dunai and Porcelli (2002) argued that any volatiles residing along grain boundaries will likely be lost during melting, transport and sample preparation, making it almost impossible to quantify the volatile contents of this component. In this section, we are concerned with two questions: how well do fluid inclusions preserve volatile characteristics and to what extent do the volatiles represent primary mantle volatiles?

IV.6.1.2 Magmatic degassing and entrapment of air-derived components

Two fundamental volatile parameters, $^{4}He/^{40}Ar^{*}$ ratios and $\delta^{13}C$ values, have proven successful in identifying and constraining magmatic degassing processes (e.g., Shaw et al., 2004; Macpherson et al., 2010). Helium is ~10 times more soluble than Ar (and N_2) in silicates melts (Jambon et al., 1986; Lux, 1987) and $^{4}He/^{40}Ar^{*}$ ratios that do not match time-integrated mantle production ratios (between 1.4 and 4.8) must therefore indicate that some fractionation of volatile elements has occurred so that measured elemental ratios no longer represent primary mantle source values. It is commonly observed that MORB glasses display $^{4}He/^{40}Ar^{*}$ ratios $\geq$ the time-integrated mantle production ratios (e.g., Matsuda and Marty, 1995; Sarda and Moreira, 2002), consistent with the notion that glass vesicles have captured magmatic gases which are residual gases following silicate melt degassing. In this respect, magmatic degassing is inconsistent with our data as all xenoliths of this study have $^{4}He/^{40}Ar^{*}$ ratios $\leq$ time-integrated mantle production ratios (**Fig. 2b**). Possible ways of generating $^{4}He/^{40}Ar^{*}$ ratios $\leq$ mantle production ratio are discussed in sections 5.1.3 and 5.1.4.

Observations on natural systems in conjunction with experimental constraints indicate that significant enrichment of ^{13}C occurs in exsolved CO_2 compared to residual carbon left in a melt phase (e.g., Javoy et al, 1978). As a consequence, degassing of CO_2, in either an open or closed system mode or as a combination of both processes, would thus always result in significant ^{13}C depletion in the residual carbon in the melt phase. Significantly, all EARS xenoliths have $\delta^{13}C$ values > the postulated mantle end-members (~ -5‰ ± 1 if DMM-like, Marty and Zimmerman, 1999; Cartigny, 2005) (**Fig. 6a**), which is inconsistent with the notion that EARS xenoliths have captured residual magmatic gases. Finally, we can also identify and remove samples potentially affected by entrapment of air-derived components using $^{40}Ar/^{36}Ar$ ratios found in conjunction with air-like $\delta^{15}N$ values. Of the entire set of EARS xenoliths, no samples fall under this criterion.

IV.6.1.3 Post-entrapment volatile loss

Due to its small size and high diffusivity, preferential He loss from fluid inclusions following entrapment in minerals is a possibility of explaining low $^{4}He/^{40}Ar^{*}$ ratios in EARS xenoliths. Such low ratios have been attributed to diffusive loss of He, relative to Ar, to nearby melt channels that likely exist under magmatic conditions. For example, this process could occur during re-equilibration of xenoliths with mantle-derived melts, either in the source region, or during transport of the xenoliths to the surface (e.g., Yamamoto et al. 2009).

Diffusing loss of He relative to Ar can be readily identified on a plot of $^{4}He/^{40}Ar^{*}$ versus [He] (i.e., **Fig. 2b**) where preferential diffusive loss of He, would result in a positive correlation. In this case, a likely starting composition, is expected to fall within the present and time-integrated mantle production $^{4}He/^{40}Ar^{*}$ ratios (1.4 to 4.8) and have high [He] (i.e., in the upper-right corner of **Fig. 2b**). No clear correlations are observed from such a starting composition that can satisfactory explain the xenoliths data - inconsistent the notion that low $^{4}He/^{40}Ar^{*}$ ratios are due to preferential diffusing loss of He relative to Ar.

To substantiate this conclusion, we plot the reciprocal of [$^{40}Ar^{*}$] versus $^{4}He/^{40}Ar^{*}$ (**Figure 9**). Mixing between any two components will plot as straight lines on this type of plot, thus allowing us to test the possibility that a process other than post-entrapment loss of helium can explain low $^{4}He/^{40}Ar^{*}$. Significantly, we note that there is a good positive correlation between 1/[$^{40}Ar^{*}$] and $^{4}He/^{40}Ar^{*}$ ratios that cannot result from He loss mechanisms since He loss should always plot along horizontal lines (indicated with arrow on the plot). Rather, mixing between two fluids, one with low $^{4}He/^{40}Ar^{*}$ ratios and the other with high $^{4}He/^{40}Ar^{*}$ ratios, is a more probable explanation (as indicated with dashed lines). In this case, samples with high $^{4}He/^{40}Ar^{*}$ ratios lie close to 1/[$^{40}Ar^{*}$] found in single vesicles in the 2IID43popping rock (Burnard et al., 1997) and the time integrated $^{4}He/^{40}Ar^{*}$ ratio of the upper-mantle (1.4 and 4.8). Notably, such [$^{40}Ar^{*}$] are somewhat lower than the predicted ^{40}Ar content due to radiogenic production in the upper-mantle (Porcelli & Wasserburg, 1995) and significantly lower than bulk crushing [^{40}Ar*] of the 2IID43popping rock (Sarda & Graham, 1990).

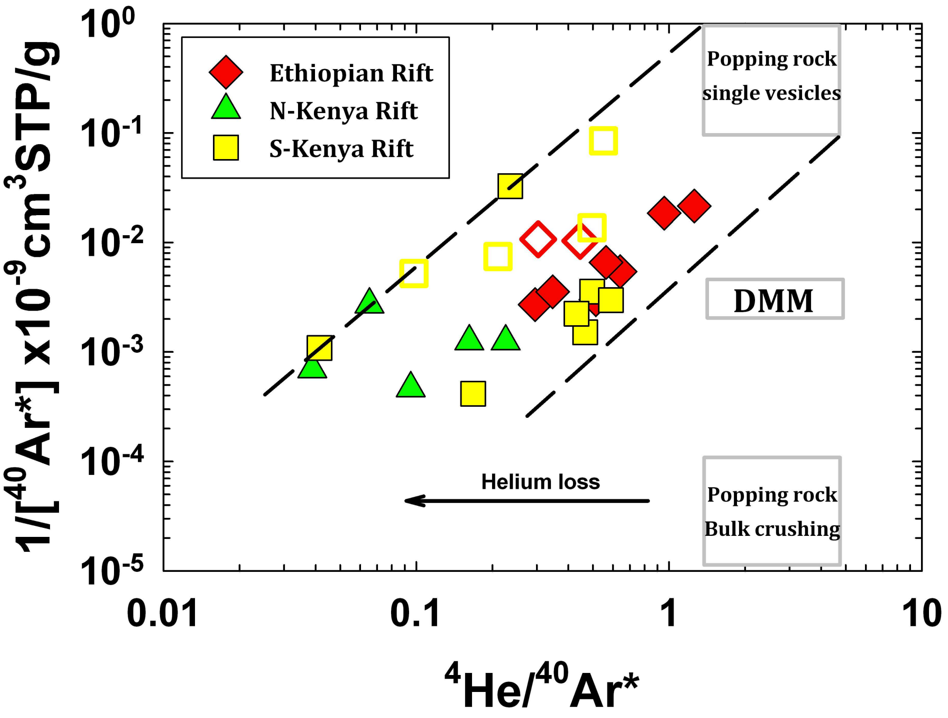

Figure IV.9: The reciprocal of [^{40}Ar*] versus ^{4}He/^{40}Ar. Mixing lines between a low ^{4}He/^{40}Ar* component and a high ^{4}He/^{40}Ar* component is indicated with dashed lines. Helium loss indicated with arrow. We also indicate the ^{4}He/^{40}Ar*-[^{40}Ar*] relationships found in single vesicles in the 2IID43popping rock (Burnard et al., 1997) and the time integrated ^{4}He/^{40}Ar* ratio of the upper-mantle (1.4 and 4.8), in addition to the predicted ^{40}Ar radiogenic production of the upper-mantle (Porcelli & Wasserburg, 1995) and bulk crushing [^{40}Ar*] of the 2IID43popping rock (Sarda & Graham, 1990). Pyroxenites are denoted with closed symbols whereas peridotites with open symbols.

IV.6.1.4 Primary elemental fractionations and exsolved volatiles

To asses first order controls on primary elemental fractionations that characterize melts which likely introduced the volatile elements to the EARS, we note that **Figure 9** implies that one of the two mantle fluids identified must have low ^{4}He/^{40}Ar* ratios (~ 0.04). There are at least two processes capable of producing such low ^{4}He/^{40}Ar* ratios:

(i) helium may be depleted relative to argon due to more compatible behavior during low-degree partial melting. However, such a possibility is generally inconsistent with available partition coefficients (K_D) of He and Ar between CPX-melt (Brooker et al., 2003: Heber et al., 2007; Jackson et al., 2013). Although there remain considerable uncertainties regarding relative partition coefficients of He and Ar between OL-melt (Parman et al., 2005: Heber et al., 2007; Jackson et al., 2013), they are generally consistent with a more incompatible behavior of He during partial melting. Furthermore, is has also been proposed that Ar is highly compatible in both OL and PX, where K_D of Ar can be as high as ~10^4 (Watson et al., 2007; Thomas et al., 2008).

(ii) the partitioning of noble gases (and N_2) between mantle melts and CO_2-rich vapor is controlled by noble gas melt solubilities. Helium is ~10 times more soluble than Ar in silicates melts (Jamon et al., 1986; Lux, 1987) and $^4He/^{40}Ar^*$ ratios < 1.4 must therefore indicate that some fractionation of volatile elements occurred. In addition, these xenoliths also have relatively constant $^{21}Ne^*/^{40}Ar^*$ ratios that are lower than the mantle production ratio (~ 1 x 10^{-7}) (Halldórsson et al., 2014) consistent with the notion that the He/Ar fractionation was accompanied by Ne/Ar fractionation. As discussed in section 5.1.2., lower than mantle $^4He/^{40}Ar^*$ ratios (and $^{21}Ne^*/^{40}Ar^*$) are inconsistent with capture of a residual volatile phase and must therefore represent exsolved gases captured at depth. Assuming an open-system equilibrium degassing scenario (i.e., a Rayleigh process: $^4He/^{40}Ar^*_{exsolved} = {}^4He/^{40}Ar^*_{initial} \times F^{[(1-\alpha)/\alpha]}$, where $\alpha = S_{Ar}/S_{He}$.), an initial $^4He/^{40}Ar^*$ratio of 1.4 (i.e., the present day mantle production ratio) and solubility coefficient (S) between vapor and melt of 5.6 ×10^{-4} cm^3 STP/g for He (Jambon et al., 1986) and 5.9 ×10^{-5} cm^3 STP/g for Ar (Cartigny et al., 2001), we can calculate the % loss of He from the melt to the exsolved phase needed to generate such low $^4He/^{40}Ar^*$ ratios. Significantly, we calculate that loss of 34% of the initial He to the exsolved phase will produce ^{4}He/^{40}Ar* ratios of 0.04 in the exsolved phase and loss of 10% will give a ratio = 0.57, in good agreement with the range of ^{4}He/^{40}Ar* ratios evident among EARS xenoliths.

IV.6.1.5 Contamination with volatiles from the carrier melt and/or continental crust

During transport to the surface, mantle xenoliths may be exposed to volatiles of the carrier melt and, as the melt approaches the surface, xenoliths may also undergo interactions with crustally-derived volatiles. This is particularly the case when a gas phase is present which, in theory, could be incorporated along xenoliths cracks and grain boundaries (Dunai and Porcelli, 2002). However the carrier melt in an unlikely volatile contributor to fluid inclusions trapped in EARS xenoliths for the following reason; (a) xenoliths are transported extremely rapidly through the lithosphere and crust (e.g., Spera, 1984), allowing for minimal interactions with surround melt, (b) any externally-derived volatiles, from the carrier melt and/or the crust, residing in cracks and along grain boundaries will likely be lost during transport and possibly also during sample preparation. Shallow level crustal contamination is also an unlikely process affecting the volatile budget of the EARS xenoliths for the following reasons; (a) formation pressures, as evident from pyroxene thermobarometry (see section 2 above), are consistent with crystallization within the East African lithosphere, making it highly unlikely that crystals and their entrained fluid inclusions were contaminated by shallow level crustal material during crystallization, (b) oxygen isotopes values of crystals hosting the fluid inclusions are dominated by δ^{18}O values that are lower than typical mantle values (+5 to +6‰), contrary to what can be expected from interactions with shallow crustal material of the Pan-African crust (> 6‰: e.g., Baker et al. 2000).

Taken together, various lines of evidence, discussed in sections 5.1.1 through 5.1.5, indicate that it is highly unlikely that volatiles have been affected by degassing loss and/or admixture with atmospheric and/or crustal components. Furthermore, we argue that no significant loss of volatiles occurred following entrapment of volatile components in fluid inclusions at depth within the SCLM. Rather, we suggest that the elemental and isotopic variations reflect primary characteristics of various fluids that introduced the volatiles to the EARS. In the following section, we resolve the volatiles into their various source component structures.

IV.6.2 Resolving volatile sources

IV.6.2.1 Evidence for recycled material in the source of EARS magmatism

There is widespread geological and geochemical evidence for the involvement of recycled crustal material in the source region of EARS magmatism. The presence of 2.0 Ga eclogite-facies rocks in the Usagaran orogeny, that forms the older collisional event of the Mozambique belt surrounding the Tanzanian craton, suggests that subducted oceanic lithosphere was involved in the formation of the lithosphere surround the craton (Möller et al., 1995). The younger collisional event, however, which marks the closure of the Mozambique Ocean and the collision of East and West Gondwana, was the site of arc volcanism with multiple subduction and accretion events during Pan-African times (~615-750 Ma) (e.g., Möller et al., 1998; Möller et al., 2000; Meert et al., 2003).

Additional geochemical evidence of recycled crystal material in the source region of EARS includes, but is not limited to: (a) highly positive Li-isotope values (up to 11.8‰) in pyroxenites from the Island of Zabargad in the Red Sea (Brooker et al. 2004); (b) involvement of a HIMU-mantle component that has been observed in lavas associated with both the Afar and the Kenya plumes and has been attributed to recycling of ancient oceanic crust entrained in the upwelling plumes (e.g., Schilling et al., 1992; Furman et al., 2006); (c) high Cl, Pb and LILE contents of fluid inclusions in metasomatic fluids associated with amphibole-bearing peridotites xenoliths from Quaternary basalts in the Lake Tana region of Ethiopia that have been attributed to contributions from recycled oceanic lithosphere (Frezzotti et al., 2010); (d) high $^{207}Pb/^{204}Pb$ ratios from Nyamuragira volcano in the Western Rift, which indicates derivation from a mantle component with a high time-integrated U/Pb ratio, possibly of Archean age (Chakrabarty et al., 2009); (e) oxygen isotopic composition of eclogite xenoliths in kimberlites in southern Africa (e.g., Garlick et al., 1971; MacGregor and Manton, 1986; Ongley et al., 1987). Taking advantage of the geological and geochemical evidence above for the presence of recycled material in the mantle source underlying the EARS, we investigate in the following sections the nature of the source material of trapped volatile components to ascertain if there is evidence in the volatile record for recycled material.

IV.6.2.2 Co-variation of stable isotopes and elemental ratios involving ^3He: Evidence for ancient recycled volatiles

IV.6.2.2.1 $\delta^{13}C$-$CO_2/^3He$ systematics

In **Figure 10**, we plot $CO_2/^3He$ ratios versus $\delta^{13}C$ values of the EARS xenoliths with the superimposition of possible end-member compositions of DMM, marine carbonate (limestone), and sedimentary organic carbon (S). End-member $CO_2/^3He$ and $\delta^{13}C$ compositions are DMM ($2 \pm 1 \times 10^9$ ± and −5 ± 1‰: Marty and Zimmerman, 1999; Cartigny, 2005), marine carbonate component (L = limestone: $1 \pm 5 \times 10^{13}$ and 0 ± 2‰), and a sediment (S) ($1 \pm 5 \times 10^{13}$ and −30 ± 10‰: Sano and Marty, 1995). Note that another potentially important C reservoir is the altered oceanic crust (AOC) that has bulk $\delta^{13}C$ value of −4.7‰ (Shilobreeva, 2011), indistinguishable from the DMM value but with a poorly constrained $CO_2/^3He$ ratio, so we do not plot this end-member on **Figure 10**. Also, we note that calcite veins in hydrothermally altered oceanic crust have $\delta^{13}C$ values (Staudigel et al., 1989), and potentially also $CO_2/^3He$ ratios, that are identical to marine carbonates so we do not plot this component. As the three major components - DMM, limestone and sedimentary end-members have distinctive $CO_2/^3He$ ratios and $\delta^{13}C$ values, the CO_2 in any sample can be resolved into these components allowing the determination of CO_2 provenance in the SCLM underlying the EARS.

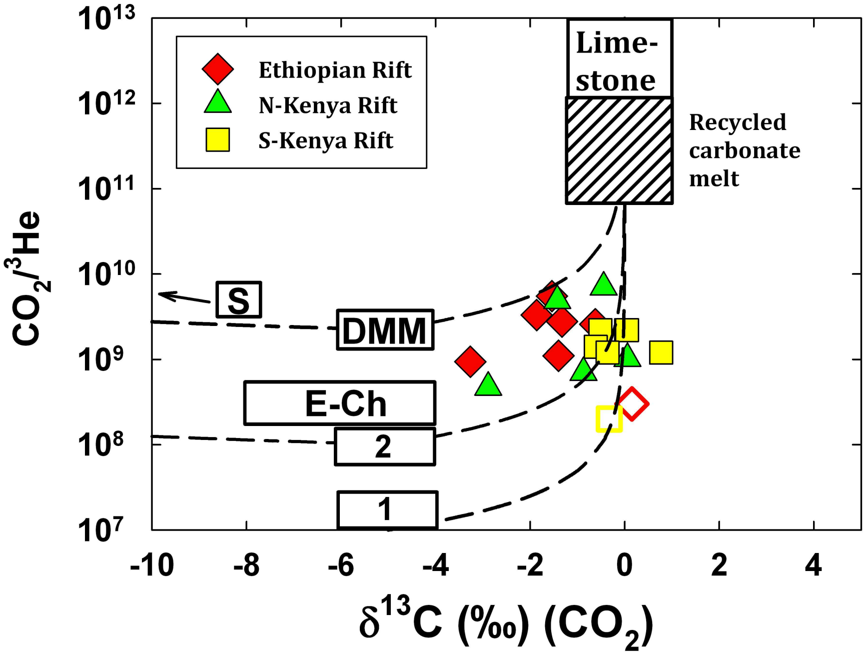

Figure IV.10: $CO_2/^3He$ ratios versus carbon isotopes with possible end-member compositions of DMM, and organic (sedimentary) (S) and Limestone (L) – derived carbon. Also shown is the calculated composition of a recycled carbonate melt in equilibrium with primary silicate melt (see text for details), the field for enstatite chondrites (E-Ch) and variable mantle end-member needed to fit the data (boxes 1 and 2). Binary mixing trajectories between M-S and M-L are shown. Pyroxenites are denoted with closed symbols whereas peridotites with open symbols.

From **Figure 10** it is apparent that the $\delta^{13}C$-$CO_2/^3He$ systematics of the xenoliths lie on one or more binary mixing trajectories where the low $CO_2/^3He$ end-members (box 1 = 1×10^7; box 2 = 1×10^8) clearly fall below the mean DMM value of ~2×10^9 (Marty and Zimmerman, 1999) whereas the high $CO_2/^3He$ end-member is identical to that of marine carbonates. The range of possible low $CO_2/^3He$ end-members encompasses low-end estimates of DMM (~2×10^8) and the mean $CO_2/^3He$ ratio of enstatite chondrite (~3×10^8) (compiled in Marty and Zimmerman, 1999).

Indeed, reported δ^{13}C values of enstatite chondrite (between -8 and -4‰: Javoy, 1995) provide additional support for the role of such compositions as a likely mantle end-member and we indicate this end-member on the plot (E-Ch). Notably, this low end-member for both $CO_2/^3He$ and δ^{13}C is probably the best candidate for unmodified DMM and SCLM end-members, given that the latter was formed by melt extraction from DMM, and the fact that there is no current consensus if these two reservoirs display different δ^{13}C (and δ^{15}N values) (e.g., Fischer et al. 2009). However, we also note that in order to fit two peridotite samples (open symbols) an end-member with a $CO_2/^3He$ ratio of 1×10^7 is needed (labeled 1 and indicated with a box). In any case, and most significantly, taking the $CO_2/^3He$ ratio of 1×10^8 (labeled box 2) as the best estimate of unmodified DMM (and SCLM), our data are consistent with enrichment of the East African SCLM by CO_2-rich mantle fluids from an enriched end-member with $CO_2/^3He$ ratios $>>7\times10^9$ (minimum estimate – from sample TAA-329B) and δ^{13}C ~0‰. These are characteristics of recycled C from subducted carbonate material. Notably, all samples that conform to such a ternary mixing scenario are dominated (>70%) by carbonate-derived CO_2, reaching a maximum value of to 93% CO_2 in the case of sample TAA-329B (see Table S4).

IV.6.2.2.2 $\delta^{15}N$-$N_2/^3He$ systematics

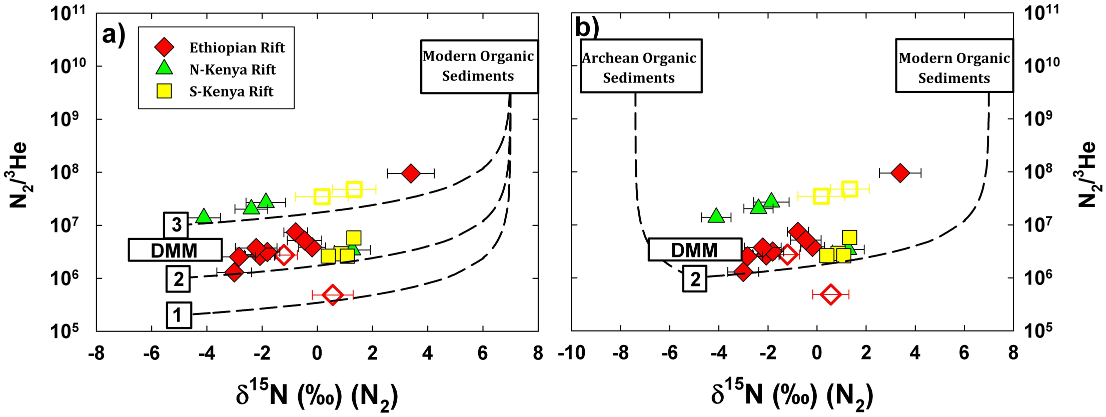

Figure IV.11: (a) Binary mixing model for nitrogen isotopes versus $N_2/^3He$ ratios. Binary mixing trajectories between DMM and sediments are shown. Variable mantle end-member (i.e., with different $N_2/^3He$ ratios) needed to satisfactory fit the data is indicated with boxes 1, 2 and 3. (b) Ternary mixing model for nitrogen isotopes versus $N_2/^3He$ ratios. Binary mixing trajectories between DMM and the two sediments components (persent-day and Archean) are shown. Pyroxenites are denoted with closed symbols whereas peridotites with open symbols.

Further information on the characteristics of the crust ‘recycled’ end-member is available from an analogous plot involving nitrogen. In **Figure 11a**, we plot $N_2/^3He$ ratios versus $\delta^{15}N$ values of the EARS xenoliths and superimpose possible two end-member compositions for DMM ($3.8 \pm 1.2 \times 10^6$; −5 ± 2‰: Marty and Zimmerman, 1999; Marty and Dauphas, 2003) and modern organic sedimentary nitrogen ($1 \pm 5 \times 10^{10}$; +7 ± 3‰: Peters et al. 1978; Sano et al., 1998; Sano et al., 2001). The $\delta^{15}N$-$N_2/^3He$ systematics of the xenoliths likewise fall on binary mixing lines but not towards the DMM end-member. Rather, an end-member $N_2/^3He$ ratio of 1×10^7 is needed to fit most of the Kenyan xenoliths (indicated with box 3) whereas a somewhat lower value of $\sim1\times10^6$ gave a reasonable fit to the Ethiopian and Tanzanian xenoliths (indicated with box 2). A single Red Sea peridotite xenolith has a low $N_2/^3He$ and requires a low $N_2/^3He$ end-member ($\sim2\times10^5$) in any mixing scenario (indicated with box 1). Again, such low ratios are similar to low-end estimates for DMM ($\sim1\times10^6$: Marty and Zimmerman, 1999). Significantly, and irrespective of the actual value of the low $N_2/^3He$ end-member, the data imply binary mixing with a component that has high $N_2/^3He$ ratios $>1\times10^8$ (minimum estimate – from sample C-244) and $\delta^{15}N$ values ~ +7‰. Such a component is similar to recycled N from modern subducted sedimentary material (e.g., Sano et al., 1998).

We note that both plots (**Figure 10 & 11a)** require different mantle end-members to explain different samples, in sharp contrast to the recycled sedimentary component that appears to have relatively fixed $CO_2/^3He$ and $N_2/^3He$ ratios. This is particularly evident for nitrogen as most Kenyan samples, in addition to two other xenoliths, require a $N_2/^3He$ ratio of (1×10^7) in the mantle end-member, significantly higher than estimates for DMM. These variations may represent carbon and nitrogen heterogeneities in the upper-mantle underlying the EARS. However, an alternative explanation is to invoke a ternary mixing scenario with another recycled sedimentary component that has different isotopic compositions than present-day marine sediments (Marty & Dauphas, 2003; Dauphas & Marty, 2004).

Due to the near-absence of oxygen in Archean ocean and thus a lack or oxidized forms of nitrogen, capable of enriching ^{15}N relative to ^{14}N, negative $\delta^{15}N$ values are commonly found in organic matter from Archean cherts (Beaumont & Robert, 1999; Pinti et al., 2001). Assuming that such Archean component has comparable $N_2/^3He$ ratios to modern marine sediments ($\sim1\times10^{10}$) and $\delta^{15}N$ values = -7.4‰ (i.e., pristine values found in Archean organic matter, e.g., Pinti et al. 2001), recycling of Archean organic sediments provides an alternative for the variable enrichments of nitrogen to helium, given that the mantle end-member has a fixed composition. It should be noted that this case is somewhat more equivocal for carbon as $\delta^{13}C$ data from Archean limestone are inconsistent with any major swifts towards negative and/or positive $\delta^{13}C$ values in the Archean (e.g., Veizer and Mackenzie, 2003).

In **Figure 11b**, we plot $N_2/^3He$ ratios versus $\delta^{15}N$ values of the EARS xenoliths. Analogous to the carbon plot, we now superimpose three possible end-member compositions for DMM ($1.0 \pm 1.0 \times10^6$; −5 ± 2‰: i.e., box 2), modern organic sedimentary nitrogen ($1 \pm 5 \times10^{10}$;

+7 ± 3‰: Peters et al. 1978; Sano et al., 1998; Sano et al., 2001) and Archean organic sedimentary component (1 ± 5 $\times 10^{10}$; -7.4 ± 2‰: Pinti et al., 2001; Marty & Dauphas, 2003). Note that our inferred $N_2/^3He$ ratios for DMM (1.0 $\times 10^6$) plots very close to the ratio reported by Marty and Zimmerman (1999) of 3.8 ($\times 10^6$). In **Figure 11b**, it is apparent that the N_2 in most samples is dominated by mixing between mantle and present-day organic sediments components. However, the nitrogen characteristics of EARS xenoliths are inconsistent with simple binary mixing between these two end-members, and require a variable nitrogen contribution from Archean sedimentary component, from between 65% (Marsabit pyroxenite) and 52-54% (for two Chyulu Hils pyroxenites) (see Table S4 for quantitative estimates of the relative contribution (%) of mantle and the two sedimentary components to EARS xenoliths).

IV.6.2.3 Elemental abundance systematics: Evidence for carbonate-melt

The nature of any subducted material, evident among the carbon and nitrogen elemental and isotope systematics, can be constrained further using coupled $^4He/^{40}Ar^*$ and $CO_2/^{40}Ar^*$ ratios. In **Figure 12a**, we plot $^4He/^{40}Ar^*$ and $CO_2/^{40}Ar^*$ ratios of EARS xenoliths, along with MORB glasses (Marty and Zimmerman, 1999) as well as the 2IID43popping rock that it is thought to best represent the volatile composition of primary asthenospheric melt (Burnard et al., 1997). Following Fischer et al. (2009), we also plot the initial $CO_2/^{40}Ar^*$ and $^4He/^{40}Ar^*$ ratios of a primary, and thus undegassed, carbonate-melt in equilibrium with a popping rock-like composition, using the following mass balance equation:

$$(C/Ar)_{carbonatite} = [C]_{carbonatite}/\{[Ar]_{initial}\times F_{carbonatite}\} = [C]_{carbonatite}/\{[Ar]_{initial} \times [C]_{initial}\} \quad (1)$$

where square brackets denote concentrations and $F_{carbonatite}$ is the fraction of a carbonatitic liquid in a binary silicate-carbonatite system.

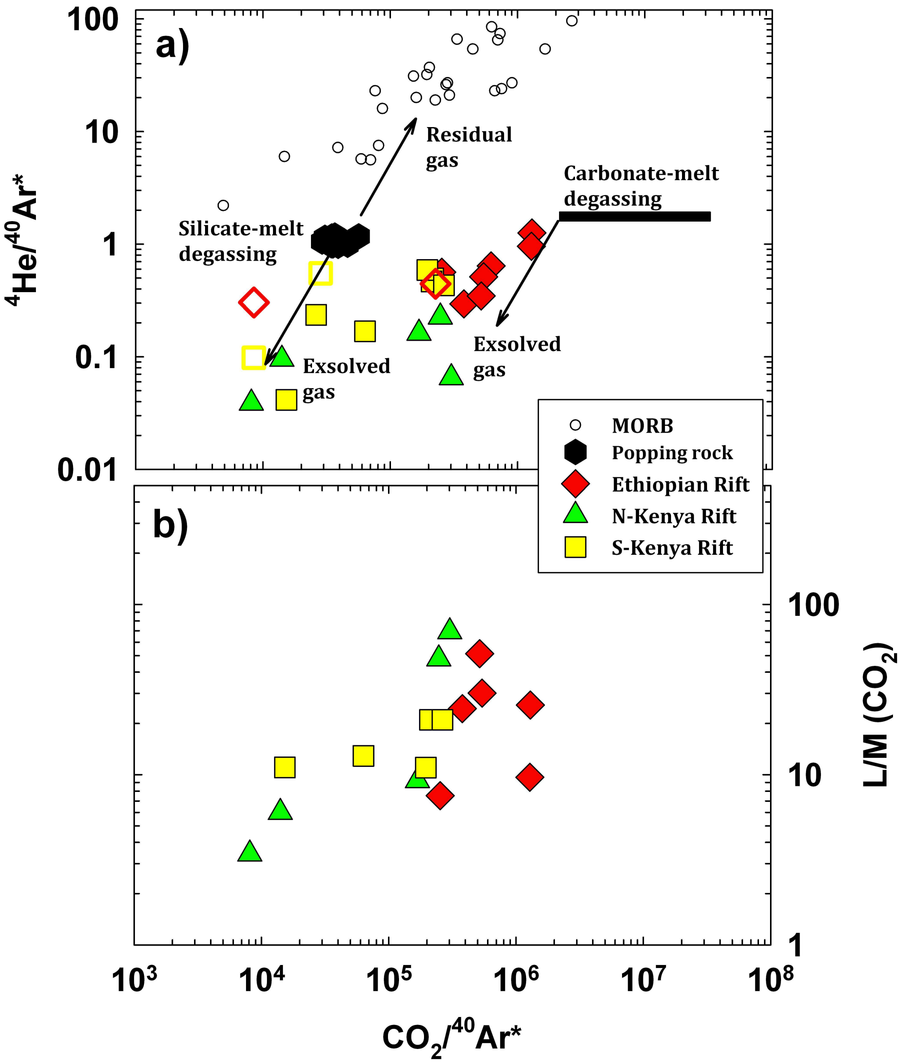

Figure IV.12: (a) ^{4}He/^{40}Ar* ratios versus CO_2/^{40}Ar* ratios. Downward facing arrows indicate exsolved volatiles from silicate magmas and carbonatitic magmas. Elemental ratios of mantle-xenoliths are consistent with mixing of exsolved volatiles from two dominant sources - a silicate-melt source and a carbonate-melt source. (b) Plot of L/M (CO_2) versus CO_2/^{40}Ar* ratios. Quantitative estimates of the relative contribution (%) of mantle (M), limestone (L) and sedimentary (S) sources to EARS xenoliths, required to calculate the L/M ratio, are given in supplementary Table S2. Note the increased carbonate component (L) relative to mantle (M) in xenoliths from Ethiopia and Tanzania. Data sources: xenoliths – Table 1, 2 and S2; MORB glasses – Marty and Zimmerman, 1999. Pyroxenites are denoted with closed symbols whereas peridotites with open symbols.

Since CO_2 contents of the silicate portion of this binary system are very low, it can be safely assumed that the CO_2 is lost to the carbonate portion. Significantly, the solubilities of He and Ar in carbonate melts are very similar to those inferred for silicate melts and thus their concentrations, and thus relative ratios, will be similar in both carbonate and silicate liquids (Burnard et al. 2010). As immiscible carbonate melts must constitute only a small fraction of melts present in the upper mantle, the majority of the He and Ar remain in the silicate portion of the binary system. Using popping rock (Burnard et al., 1997) and carbonate with variable CO_2 contents (between 5% and 35 wt%, the latter being representative composition of carbonate) as starting liquids, the calculated initial carbonate melt $CO_2/^{40}Ar^*$ ratio prior to any degassing lies between 2.3×10^6 and 3.3×10^7. Interestingly, by using these same input parameters and modifying equation (1) for He, the $CO_2/^3He$ ratio of such a carbonate melt can be constrained between 1.3×10^{11} and 1.8×10^{12}, in excellent agreement with that inferred for the recycled carbonate component in **Figure 10**.

$CO_2/^{40}Ar^*$ ratios in EARS xenoliths vary by orders of magnitude from 8.0 to 1295 ($\times 10^3$) and strongly resemble MORB glasses (**Fig. 12a**). However, in contrast to MORB glasses, our data are inconsistent with the notion that EARS xenoliths captured residual volatiles from degassing melts since residual volatiles will likely have $^4He/^{40}Ar^*$ ratios >>2. Therefore, low ratios better represent exsolved gases captured during degassing at depth. Fischer et al. (2009) used this same type of plot to argue that volcanic gases emitted from Oldoinyo Lengai where exsolved from a degassing silicate melt rather than carbonate melt. We note that this is also the case for some xenoliths of this study; most notably, xenoliths from the southern Kenya Rift (**Fig. 12a**). However, in contrast to these xenoliths and the Oldoinyo Lengai gases, most Ethiopian and the remaining xenoliths from Tanzania, coincide with compositions expected from exsolved volatiles from carbonate magmas, possibly followed by mixing with exsolved gases from silicate magmas. Thus, we argue that, at least in the case the Ethiopian Rift, carbonate melts must play a fundamental role in transporting volatiles and other fluid-mobile elements within the upper-mantle. This finding is consistent with several other geochemical studies on mantle-derived xenoliths from the EARS that argue for an important role of carbonate CO_2-rich melts as metasomatic agents in the SCLM (e.g., Rudnick et al. 1993; Baker et al. 1998; Ferrand et al. 2008; Frezzotti et al. 2010; Aulbach et al., 2011; Beccaluva et al. 2011). Significantly, our findings may also relate to the widespread metasomatic enrichment of the East African lithosphere by carbonate and/or silicate melts preceding and/or following initiation of the EARS as inferred from several studies (e.g., Davies & Lloyd, 1989; Baker et al., 1998; Orlando et al., 2006; Kaeser et al. 2009; Beccaluva et al. 2011).

To further investigate the nature of the exsolved fluid phases, we note that **Figure 10** strongly suggest that CO_2-rich mantle fluids (i.e., carbonate melts) have the chemical characteristics of subducted carbonate material and thus will very likely have $\delta^{13}C$ values close to 0‰. We test this possibility by adopting the approach of using $CO_2/^3He$ ratios and $\delta^{13}C$ values, to resolve CO_2 into its various source components (Sano and Marty, 1995). Assuming a mantle end-member (M) with $\delta^{13}C$ = -5‰ and $CO_2/^3He = 1\times10^8$ (i.e., an end-member that captures 16/18 samples within Fig 10), marine carbonate component (L) with $\delta^{13}C$ = 0‰ and $CO_2/^3He = 1\times10^{13}$ and a sedimentary (S) organic carbon with $\delta^{13}C$ = -30‰ and $CO_2/^3He = 1\times10^{13}$ allows determination of CO_2 provenance in the EARS xenoliths. Quantitative estimates of the relative contribution (%) of mantle (M), limestone (L) and sedimentary (S) sources to EARS xenoliths are given in supplementary Table S2.

In **Figure 12b**, we plot the L/M ratio (i.e., the ratio of CO_2 derived from carbonate vs. CO_2 derived from DMM) versus $CO_2/^{40}Ar^*$ ratios. This plot shows that samples with high $CO_2/^{40}Ar^*$ ratios (i.e., samples inferred to be dominated by exsolved gases from carbonate – melts) are associated with high L/M ratios. Interestingly, samples with L/M ratios ≥ 10 are consistent with volcanic gas emitted from subduction zones volcanoes, where carbon has been shown to be actively recycled (e.g., Varekamp et al., 1992; Hilton et al., 2002). This observation suggests that the carbonate -melt component is derived from, or at least affected by, a subduction modified region of the upper-mantle beneath the EARS. Finally, we note that many Ethiopian xenoliths that display high $CO_2/^{40}Ar^*$ and high L/M ratios also have high $^3He/^4He$ ratios - suggesting a link between the African superplume and increased contribution of carbonate-melt fluxing - as discussed in section 5.3.

IV.6.2.4 Implications of lower than mantle oxygen isotope values for recycled material

Oxygen isotope ratios of the EARS span a large range encompassing mantle-like values as well as ratios as low as +2.4‰ (section 4.2). With respect to the origin of such a large range and, in particular, the low oxygen isotope values, we point out three noteworthy features of these results: (i) the large range in $\delta^{18}O$ values precludes segregation of carbonate and/or silicate melts from an isotopically homogeneous mantle peridotite where melts remain in oxygen isotopic equilibrium with the surrounding mantle minerals, (ii) the large $\delta^{18}O$ range (Δ=4.1‰) greatly exceeds the range expected for minerals from primary magmas in equilibrium with mantle peridotite (Mattey et al., 1994; Eiler, 2001) - excluding formation of the EARS pyroxenites via extensive *in situ* crystallization from normal-mantle peridotites as oxygen isotopic fractionation accompanying high-temperature fractionation in the mantle is expected to be minimal, and finally (iii) delamination or contamination with lower continental crustal material (e.g., the Pan African crust) can also be ruled out as source material of the xenoliths, as this would likely result in significantly higher than mantle $\delta^{18}O$ values (> +6.0‰) (e.g., Baker et al. 2000), in contrast to the overall low $\delta^{18}O$ values observed in EARS pyroxenites.

A key question regarding stable isotope variations evident in EARS xenoliths, is how can low $\delta^{18}O$ values be reconciled with recycled sedimentary material that will likely contain $\delta^{18}O$

values >> mantle, in addition to both high δ^{13}C values (in the case of carbonate) and δ^{15}N values? The sedimentary sections, which represent only a small fraction of the entire subducted oceanic lithosphere, are however, not likely to significantly affect the oxygen isotopic signature of the mantle peridotites because of the strong buffering effect of mantle olivine and pyroxene, which dominate the mantle mineral assemblage (e.g., Mattey et al. 1994). In contrast, the underlying crust/lithosphere represents a much larger oxygen isotope reservoir, which has the capacity to significantly alter mantle peridotites δ^{18}O values after its subduction in to the mantle. Overall, this reservoir will have either normal mantle δ^{18}O values, or higher and/or lower than mantle values, as best represented by studies of ophiolite sections (e.g., Eiler, 2001; Perkins et al., 2006). The consistency of lower than mantle δ^{18}O values found in EARS pyroxenites constrains their source material to hydrothermally-altered layer 3 gabbroic and peridotites of the oceanic crust/lithosphere boundary (Perkins et al., 2006). Indeed, on the basis of major and trace element geochemistry, Ulianov et al. (2006) proposed that the pyroxenite xenolith Ke1910/11 (Chyulu Hills) was best represented by a plagioclase-bearing gabbro to gabbro-troctolite protolith. In this respect, we again note the similarities between δ^{18}O values observed in EARS xenoliths and eclogites in kimberlites from southern Africa that are thought to represent disrupted fragments of hydrothermally-altered segments of ancient subducted oceanic lithosphere emplaced into the SCLM during subduction.

IV.6.3 Role of the Africal superplume in supplying recycled volatiles and carbonate-melt – a hybrid plume model

Several studies of peridotite xenoliths from oceanic hotspots, such as Samoa and the Austral Islands (Hauri et al. 1993; Burnard et al. 1998), Grande Comore (Coltorti et al. 1999), Canary Islands (Frezzotti et al., 2002a, b) and Hawaii (Frezzotti & Peccerillo, 2007), reported the occurrence of secondary minerals assemblages (i.e., CPX and apatite) and/or CO_2-rich metasomatic fluids that have been proposed to be derived from recycled crustal components (e.g., Hauri et al. 1993; Frezzotti & Peccerillo, 2007). Notably, xenoliths, lavas and/or geothermal fluids from these oceanic islands (apart from Comore) have $^3He/^4He$ > DMM. With respect to the EARS, we note that Frezzotti et al. (2010) reported the occurrence of chlorine-rich H_2O-CO_2 metasomatic fluids in peridotite xenoliths in Quaternary lavas from Lake Tana in Ethiopia and advocated for their origin as derivations from recycled components.

We also note that in the case of the African Superplume, the source of deep material supplying the EARS, tomographic seismic images indicate that the plume has entrained material of unusually dense composition in the lower mantle (Ni et al., 2002; Simmons et al., 2007). This material is likely to be subduction-derived (Grand, 2002) and will preserve isotopic signatures different from the surrounding ambient lower mantle and thus a possible source of anomalous isotopic compositions associated with the African Superplume. Given evidence above for the presence of recycled material evident among trapped volatiles components in EARS xenoliths, we can now test if this recycled material has any association with entrained material hosted by the African Superplume.

IV.6.3.1 He and N isotope relationships: Evidence for a deep volatile source

Figure 12b raised the possibility that xenoliths with high $^3He/^4He$ ratios are associated with recycled metasomatic CO_2-rich mantle fluids. In **Figure 13a**, we plot $^3He/^4He$ ratios versus $\delta^{15}N$ (N_2) values for EARS xenoliths together with possible end-member components SCLM, DMM and a hybrid African Superplume that has incorporated a mixture of recycled organic sediments, to assess the possible role of the Superplume in supplying recycled volatiles to the EARS.

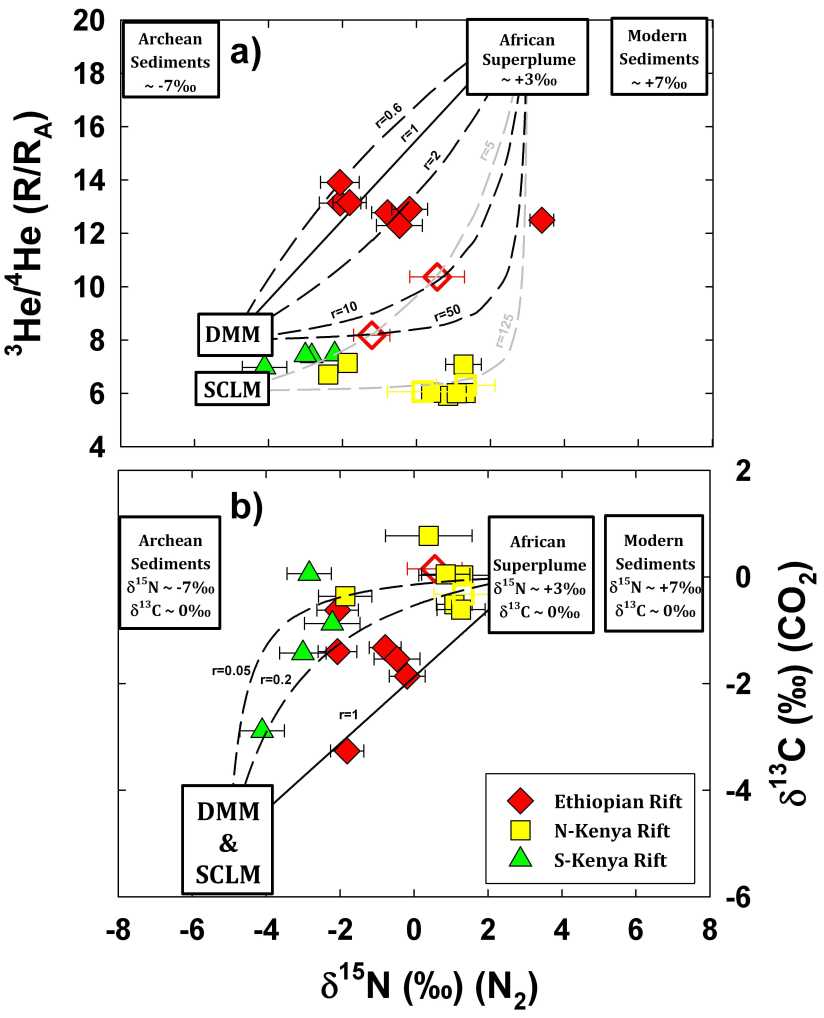

Figure IV.13: Plot of (a) helium and (b) carbon isotopes versus nitrogen isotopes showing binary mixing trajectories between DMM-like, SCLM-like and plume-like end-members. In (a) end-member components are SCLM, DMM and a hybrid African superplume with a high $^{3}He/^{4}He$ ratio of ~$20R_A$, that has incorporated a mixture of recycled organic sediments with $\delta^{15}N = +3 \pm 2$‰. Xenoliths from the Ethiopian Rift with $^{3}He/^{4}He$ > DMM are consistent with a binary mixing between and plume component and DMM. In contrast, xenliths from the two Kenya rifts imply that mixing between the plume component and SCLM dominates. In (a), $r = (N/He)_{PLUME}/(N/He)_{DMM}$. In (b) the recycled plume component is characterized by a mixture of carbonate material and organically-derived nitrogen, entrained within the carbonate matrix ($\delta^{13}C$: ~ 0 ± 2‰; $\delta^{15}N$: +3 ± 2‰). Note that we do not separate DMM and SCLM. All xenoliths are consistent with binary mixing between DMM/SCLM and a hybrid African Superplume. Pyroxenites are denoted with closed symbols whereas peridotites with open symbols.

Following arguments in section 5.2 (i.e., **Figure 11**), the incorporated sedimentary component is composed of two different components with different nitrogen isotopic compositions (~ -7‰; ~ +7‰). Notably, it has been proposed that the deep mantle, as sampled at various oceanic islands worldwide, has nitrogen isotope values that represent admixture between these components but lies somewhat close to the present day organic component (i.e., $\delta^{15}N = +3 \pm 2$‰; Marty & Dauphas, 2003). Finally, we make the assumption that this component has been entrained within a deep mantle source that has a high $^3He/^4He$ ratio of ~$20R_A$, a ratio corresponding to the highest ratios observed in the EARS ($19.6R_A$; Marty et al., 1996).

There are two notable features of this plot. First, a model of binary mixing between DMM and a hybrid African superplume (black mixing lines) readily explains all Ethiopian Rift xenoliths with $^3He/^4He$ ratio > DMM, implying that in addition to supplying primordial volatiles, the deep-seated African superplume also supplies recycled volatiles, most likely in the form of carbonate-melts, to the East African upper-mantle. The relative N/He ratios between plume and DMM components is expressed as r-values (where $r = (N/He)_{PLUME}/(N/He)_{DMM}$). R-values between 0.6 and 50 thus indicate that the plume end-member is characterized by a marked enrichment in its N/He ratio relative to the DMM end-member, consistent with the enrichment of nitrogen and/or depletion of helium in the plume source. Second, xenoliths from the two Kenyan Rifts are inconsistent with a binary mixing between DMM and the African superplume and require an end-member with $^3He/^4He$ ratios similar to the SCLM (i.e., $6.1R_A$) to reasonably fit these samples (grey mixing lines). Significantly, r-values (where $r = (N/He)_{PLUME}/(N/He)_{SCLM}$) in such a binary mixing scenario extend to higher values (r=125), implying considerably greater nitrogen enrichments and/or helium depletions in the plume source relative to DMM-Plume mixing scenario. Alternatively, such high r-values could indicate that the SCLM end-member has a significantly lower N/He ratio relative to the plume source. In any case, the occurrence of recycled volatiles in the East African SCLM is widespread and must be associated with a large scale mantle process (i.e., a mantle plume) currently supplying mantle material to the EARS.

IV.6.3.2 Co-variations of C, N and O isotopes: Constraints on bulk mixing

The first-order observation of C and N isotope variations in EARS xenoliths suggests that marine carbonates and modern/Archean organic sedimentary material, is the dominant contributor of CO_2 and N_2 to the volatile budget preserved in the fluid inclusions (**Figs. 10 and 11**). Significantly, we note that the $\delta^{13}C$-$CO_2/^3He$ systematics (**Fig. 10**) do not require a large contribution (generally < 6%) from a sedimentary component (S) with organically-derived carbon ($\delta^{13}C$ ~ -30‰) in the recycled mixture. This is in agreement with observations from active arc systems that advocate for preferential removal of the uppermost organic-rich sediments, relative to the carbonate-rich sediments and the underlying oceanic crust in the fore-arc region during dehydration and decarbonation of subducting slab (de Leeuw et al., 2007). Furthermore, model calculations imply that the total subducted carbon is dominated (~95%) by carbonates having $\delta^{13}C$ ~ 0‰ with magnesite, the most common phase of carbonates in the subducted slab, later transforming into dolomite II and then to dolomite III at depth, being thermodynamically stable in the lower mantle (Martinez et al., 1998; Coltice et al., 2004; Mao et al., 2011).

However, the $\delta^{15}N$-$N_2/^3He$ systematics (**Fig. 11**) clearly reveals the presence of some form of organic material in the recycled mixture. An alternative explanation to reconcile these conflicting sedimentary end-members, involves mixing with N-enriched carbonates (e.g., Li and Bebout, 2005; Halldórsson et al., 2013). Indeed, on the basis of nitrogen abundance and isotope data from sediments (diatomaceous ooze and breccias) from Ocean Drilling Program legs 170 and 205 offshore of Costa Rica (Li and Bebout, 2005), Halldórsson et al. (2013) argued that a hybrid sedimentary end-member was consistent with coupled N_2 and CO_2 isotope relationships in gas discharges along the western Sunda arc. In the model we present in **Figure 13b**, we thus make the assumption that marine carbonates, characterized by relatively homogenous $\delta^{13}C$ values (~ 0‰), incorporated nitrogen with highly variable $\delta^{15}N$ values (~ -7‰; ~ +7‰), identical to those found in Archean and modern-day sediments. In other words, the recycled plume component is characterized by a mixture of carbonate material and organically-derived nitrogen, entrained within the carbonate matrix (δ^{13}C: ~ 0 ± 2‰; δ^{15}N: +3 ± 2‰).

In **Figure 13b**, we plot δ^{15}N (N_2) versus δ^{13}C (CO_2) together with possible end-member components DMM, SCLM, Archean and modern organic sediments and a hybrid African superplume to test binary mixing relationships between unmodified upper-mantle components (DMM & SCLM) and potential recycled crustal components entrained within the deep-seated African superplume. A model of binary mixing between the upper-mantle and the African superplume readily explains these relationships where xenoliths from southern Tanzania plot closer to the proposed plume end-member. R-values (where $r = (N/C_{plume})/(N/C_{DMM/SCLM})$ in such a binary mixing scenario ≤ 1 and extend to a value of 0.05, implying either significant enrichment of the N/C ratio in the DMM/SCLM end-member relative to the plume end-member, or enrichment of carbon and/or depletion of nitrogen in the plume source. This observation can potentially be explained with more compatible behavior of nitrogen relative to carbon during low-degree partial melting, gaining support from the analogy of N_2 to Ar and CO_2 to Nb - the latter two elements remain highly incompatible during partial meting (e.g., Saal et al. 2002).

The quantity of the recycled component in upper-mantle and plume mixture can be estimated from simple mass balance calculations using the δ^{15}N value of entrained sedimentary end-member (+3‰) and a value representative of the DMM source (-5‰). A large nitrogen contribution (~80%) from this recycled component is required in order to produce a mixture with δ^{15}N of +1.4‰, i.e., a value comparable to the highest δ^{15}N observed among the southern Kenya Rift xenoliths. Interestingly, of all the xenoliths plotted in **Figure 13b**, the southern Kenya Rift xenoliths have the closest geographical proximity to the upwelling focus on the African Superplume (e.g., Ritsema et al., 1999).

We now can further extend a model of recycled material to the oxygen isotopes values of the host crystals. The oxygen isotope geochemistry of the lower mantle as sampled by OIB that display high $^3He/^4He$ ratios has been the subject of several studies (Eiler, 2001 and references therein; Macpherson et al. 2005; Thirlwall et al. 2006). With respect to origin of low $\delta^{18}O$ values in EARS xenoliths, several studies warrant attention. Significant ^{18}O depletion relative to the DMM source in the high $^3He/^4He$ reservoirs has been suggested based on studies of basalts from the Manus Basin, Iceland and Hawaii (Macpherson et al. 2000; Macpherson et al. 2005; Thirlwall et al. 2006; Lassiter and Hauri, 1998). Such ^{18}O depletions were attributed to the presence of recycled oceanic crust/lithosphere in the source of these regions and/or oxygen isotope fractionation between the silicates of the lower mantle and iron alloys of the core. Taking advantage of the evidence above for recycled material in the EARS mantle source we can now test if the oxygen isotopes characteristic of the host crystals can be reconciled with the incorporation of deeply recycled oceanic lithosphere and/or crust.

In **Figure 14**, we plot (**a**) $\delta^{13}C$ values and (**b**) $\delta^{15}N$ values versus $\delta^{18}O$ values to test simple binary mixing relationships between unmodified upper-mantle components (DMM/SCLM: $\delta^{18}O$: +5.5‰; $\delta^{13}C$: -5‰; $\delta^{15}N$: -5‰) and a hybrid African Superplume that incorporated a section of recycle crust/lithosphere, including overlying organic sediments, that was hydrothermally altered (>250°C) prior to subduction ($\delta^{18}O$: +2‰; $\delta^{13}C$: 0‰; $\delta^{15}N$: +3‰). Note that that in both figures we use a $\delta^{18}O$ of +2‰, i.e., a value at the lower-end of values found in ophiolites or ocean-floor drill holes (e.g., Muehlenbachs, 1986; Eiler, 2001) although we note that using a somewhat lower value (e.g., 0‰) could possibly provide a better fit to **Figure 14b.**

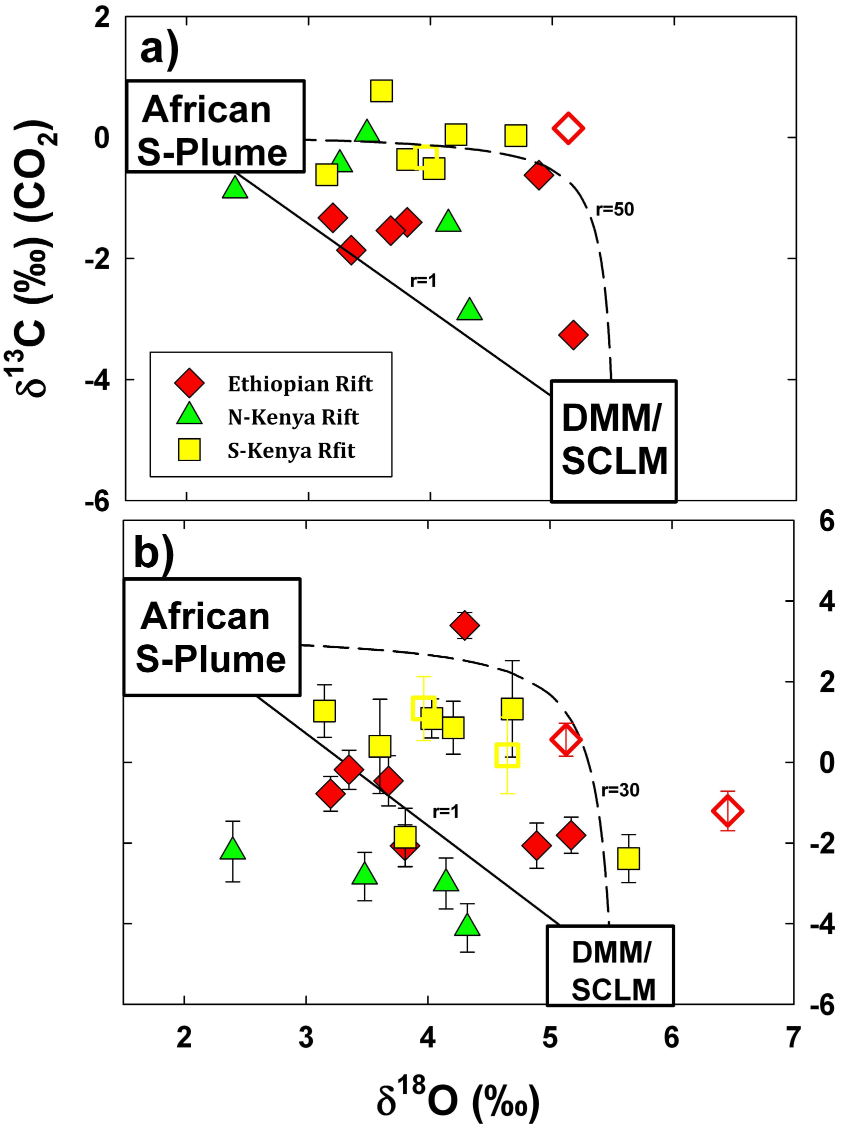

Figure IV.14: (a) Carbon (δ^{13}C) and (b) nitrogen (δ^{15}N) isotopes versus oxygen isotopes for all xenoliths of this work. We show binary mixing relationships between DMM (δ^{18}O: +5.5‰; δ^{13}C: -5‰; δ^{15}N: -5‰) and a hybrid African Superplume that has incorporated recycle crust/lithosphere (δ^{18}O: +2‰; δ^{13}C: 0‰; δ^{15}N: +3‰). In (a) r = $(C/O)_{PLUME}/(C/O)_{DMM}$ and in (b) r = $(N/O)_{PLUME}/(N/O)_{DMM}$. Note that we do not separate DMM and SCLM. Both plots are consistent with binary mixing between DMM/SCLM and a hybrid African Superplume. Pyroxenites are denoted with closed symbols whereas peridotites with open symbols.

A model of binary mixing between DMM/SCML and a hybrid African Superplume, readily explains the relationships between O, C and N isotopes. The relative C/O and N/O ratios between plume and DMM/SCLM components is expressed as r-values (where r = $(C/O)_{PLUME}/(C/O)_{DMM}$; r=$(N/O)_{PLUME}/(N/O)_{DMM}$). R-values between 1 and 50 thus indicate that the plume end-member is characterized by a marked enrichment in its C/O and N/O ratios relative to the DMM/SCLM end-member, consistent with incorporation of recycled carbon and nitrogen in the plume source as oxygen contents can be assume to be approximately the same in both end-members. Notably, significantly higher r-values (up to 50) in **Figure 14a** are consistent with the r-values inferred from **Figure 13b**, demonstrating that the plume source has a higher C/N relative to the upper-mantle.

The amount of subducted crust required to generate the $\delta^{18}O$ range of EARS xenoliths can be estimated from simple mass balance calculations using the $\delta^{18}O$ value of hydrothermally altered oceanic crust (+2‰) and a value representative of the DMM/SCLM source (+5.5‰). These calculations demonstrate that ~90% recycled crust is required in order to produce a mixture with $\delta^{18}O$ of +2.4‰, i.e., the lowest $\delta^{18}O$ value observed in our dataset. A smaller contribution can be accommodated if the recycled crust possesses lower $\delta^{18}O$ value, i.e., a value of 0‰, as indicated by **Figure 14b**.

IV.6.4 Implication for metasomatic agents in the SCLM and the formation of pyroxenite-hybrid mantle beneath the EARS

The elemental and isotopic compositions of peridotite xenoliths from several localities throughout EARS (e.g., Baker et al. 1998; Aulbach et al., 2011; Beccaluva et al. 2011), particularly in those from northern Tanzania (Rudnick et al. 1993: Dawson, 2002), have been interpreted to result from mantle metasomatism, i.e., an influx of volatile-rich silicate and/or carbonate melts to the SCLM. Clinopyroxene from Olmani in southern Tanzania are, for example, consistent with derivation from peridotite and carbonatitic melts (Rudnick et al. 1993).

However, origin of the metasomatic melts remains somewhat speculative and largely based on comparison with experimental melts rather than natural melts.

This work adds to the growing body of evidence that pyroxenites are formed via interactions of mantle volatiles and peridotite (Sobolev et al., 2005; Perkins et al., 2006; Sobolev et al., 2007; Kaeser et al., 2009; Aulbach et al., 2011b) and we argue that the EARS pyroxenites of this study are the product of metasomatic reactions between normal mantle peridotites and slab-derived, volatile-rich silicate/carbonate melts resulting from the partial melting of subducted oceanic crust (i.e., eclogite). This conclusion is consistent with the high volatile content of fluid inclusions in pyroxenites, and their associated subduction-like stable isotope compositions. Thus, EARS xenoliths provide a key link between the petrogenesis of pyroxenite hybrid mantle and recycled volatiles derived from slab fluids of subducted and carbonated oceanic crust.

Additionally, our new data provide constraints on the creation of upper-mantle heterogeneities and the formation of pyroxenites that have been shown to be an important source of basaltic magmas along oceanic and continental spreading centers, and in intra-plate magmatic settings (e.g., Allegre & Turcotte, 1986; Hirschmann & Stolper, 1996; Dasgupta et al. 2007). For example, our data are consistent with models put forward to explain the genesis of OIB that involve generation of compositionally and lithologically (e.g., pyroxenite, eclogite, peridotite) heterogeneous mantle sources containing recycled oceanic crust and lithosphere (Sobolev et al., 2005, 2007; Day et al., 2009). In the case of EARS, such lithologies are entrained within upwelling high-$^{3}He/^{4}He$ mantle material and later experience progressive dilutions by interactions with DMM and SCLM. The importance of pyroxenite hybrid mantle in the petrogenesis of EARS magmas remains to further explored but we note that contributions from recycled pyroxenite components (i.e., CO_2), have recently been proposed to account for high Fe/Mn ratios in Ethiopian lavas (Rogers et al., 2010) and the lack of elevated mantle potential temperatures in the

EARS mantle, which is characterized by abnormally slow seismic velocities (Rooney et al., 2012).

V.7 Conclusions

We present evidence of significant variations in the isotope and concentration characteristics of helium, argon, carbon, nitrogen and oxygen in mantle xenoliths from the EARS. The principal conclusions of this contribution can be summarized as follows:

(1) Volatile components, trapped in fluid inclusions in mantle xenoliths from throughout the East African Rift System, have compositions consistent with enrichment of the SCLM by CO_2-rich mantle fluids from subducted carbonatitic material

(2) Such CO_2 enrichments ($CO_2/^3He>7x10^9$, $\delta^{13}C$=+0 ‰) are also associated with positive $\delta^{15}N$ values (as high as +3.4‰) and unusually low $\delta^{18}O$ values (to +2.4‰) of host crystals, reinforcing the link between the metasomatic fluids and subduction of hydrothermally-altered oceanic crust, including the pelagic sedimentary veneer.

(3) Elemental ratios involving CO_2 suggest that volatile components trapped in EARS xenoliths are formed by mixing of exsolved volatiles from degassing silicate and/or carbonate melts.

(4) Xenoliths with high $^3He/^4He$ ratios (Afar) are also associated with positive $\delta^{15}N$ values and suggest an important role of carbonate-melts. This observation implies that the deep-seated African Superplume supplies the uppermost mantle with a mixture of primordial and recycled volatiles.

(5) The volatile record of EARS xenoliths provides a key link between the petrogenesis of olivine-free hybrid pyroxenite mantle and recycled volatiles derived from slab fluids of subducted carbonated oceanic crust.

Acknowledgements

This work was supported by the Petrology and Geochemistry program of NSF (EAR-1019489). We thank Mark H. Thiemens for access to lab facilities and support and Keith Blackmon and Bruce Deck for lab assistance.

Ke1911/4

Las-3b

Ke1911/15

TAA 325

Ke1911/15

TAA 332

Figure IV.S1: Example of an alteration-free mineral separates used for laser fluorination. Note that the mineral grain shown for Ke1911/4 was avoided due traces of oxidation on its surface. All other grains are representative for the separates we analyzed for oxygen isotopes.

Chapter V: Recycling of Phanerozoic oceanic crust by the Iceland mantle plume: new evidence from nitrogen elemental and isotope systematics of subglacial basalts

V.1 Abstract

We report new nitrogen (N_2) abundance and isotope ($\delta^{15}N$) data for 43 subglacial basaltic glasses collected from the neovolcanic zones of Iceland, a key locality in studies of mantle plume geochemistry and crust-mantle processes. We also report new helium and argon abundance and isotope data to supplement previous studies (Füri et al., 2010), allowing elemental ratios (e.g., $N_2/^{40}Ar^*$) to be calculated for individual samples. Subglacial basaltic glasses with detectable, N_2 (> 3 $\mu cm^3STP/g$) show a wide range in nitrogen isotopes ($\delta^{15}N$), from -2.91 to +11.96‰ (vs. Air), with values > 6‰ only observed at one locality in the Eastern Rift Zone. Elemental ratios involving N_2, i.e., $N_2/^3He$, and $N_2/^{40}Ar^*$, span several orders of magnitude from 2.5 $\times 10^5$ to 9.0 $\times 10^7$, and 12.2 to 6780, respectively. In contrast, $^{40}Ar/^{36}Ar$ ratios are rather limited (air-like to 1330), but glasses span a wide range in helium isotopes (8-26 R_A), with clear distinction between individual rift segments.

A number of processes have extensively modified original mantle source N isotope and relative abundance compositions, most significantly shallow-level crustal interaction. Degassing-induced fractionation and/or air interaction has also affected some samples. We have filtered the entire N dataset (i.e., $N_2/^{40}Ar^*$ and $\delta^{15}N$) using $^{40}Ar/^{36}Ar$ and $^4He/^{40}Ar^*$ ratios to identify (and remove) modified samples. As a result, the resulting samples (n= 22) define the Icelandic mantle N-isotope distribution ($\delta^{15}N$ = -2.29 to +5.71‰).

Using the filtered dataset, we investigate simple binary mixing scenarios involving the relative abundance of nitrogen to noble gases and nitrogen isotopes by considering coupled $N_2/^3He$-$N_2/^{40}Ar^*$-$\delta^{15}N$ systematics. Mixing scenarios are consistent with a recycled component in the Iceland mantle source, defined by a high and heterogeneous $\delta^{15}N$ end-member. Moreover, the high $\delta^{15}N$ end-member may be coupled to the high $^3He/^4He$ signature assuming He loss prior to mixing with the DMM end-member, similar to the two-step model of He depletion followed by open-system degassing (Füri et al., 2010), and/or ii) the presence of excess N_2. The isotopically

high $\delta^{15}N$ end-member needed to explain these mixing relationships strongly suggests the presence of recycled N-component(s) integrated into and/or entrained by the Iceland plume source.

These new results reveal a highly heterogeneous isotopic composition of nitrogen in a hybrid Iceland plume source consistent with models based on trace elements and radiogenic isotopes that advocate for significant heterogeneity of recycled crustal component(s) sampled by the Iceland plume. A relatively young age of the recycled crustal material (i.e., Phanerozoic) is consistent with positive $\delta^{15}N$ values and constraints from radiogenic isotopes (e.g., Pb), thus indicating a relatively short time-interval between subduction of crustal material and entrainment by the Iceland mantle plume.

V.2 Introduction

Although nitrogen is the most abundant gas in the atmosphere, and is found in substantial quantities (up to % levels) in near-surface, low temperature environments, such as biomass, soils and the oceans, it is present at trace levels only (<1 ppm) in Earth's mantle (Bebout et al., 2013). However, due to its mass, the mantle is by far the largest reservoir of nitrogen on Earth. The origins and evolutionary history of nitrogen in the mantle remain uncertain particularly how fundamental processes such early-Earth formation, atmospheric evolution and recycling of surficial material have affected the isotopic composition of nitrogen and its budget in different mantle reservoirs (Marty, 2012; Bebout et al., 2013; Busigny & Bebout, 2013; Cartigny & Marty, 2013). It is noteworthy that in most mantle-derived material, nitrogen strongly correlates with radiogenic ^{40}Ar, indicating that the source of mantle N is subducted crustal rocks in which NH_4^+ has been substituted for K^+ (Marty, 1995; Marty and Humbert, 1997; Marty and Dauphas, 2003a). Because of this affinity for ammonium, nitrogen is more readily subducted and recycled into the mantle than other gases such as the light noble gases, helium and neon. This conclusion is reinforced by the lack of correlation with primordial ^{36}Ar, suggesting that nitrogen in the mantle is not primordial, and thus excluding a history of continuous volatile depletion of the mantle since planetary accretion (Marty, 1995; see also Goldblatt et al., 2009).

Nitrogen isotopes offer a unique opportunity to test the provenance of volatiles in mantle-derived materials, particularly as a tracer of material recycled from surface reservoirs. Their utility is based on the distinct nitrogen isotopic compositions of various terrestrial reservoirs. The nitrogen isotopic composition of the depleted MORB mantle (DMM) reservoir, as sampled at mid-ocean ridges, ranges from about –10 to +8‰, with a mean value of about -5 ± 2‰ (e.g., Sakai et al., 1984; Javoy et al., 1986; Javoy & Pineau,1991; Cartigny et al., 2001; Marty and Humbert, 1997; Marty & Zimmerman 1999; Marty & Dauphas, 2003a). In contrast, organic sediments on the ocean floor are enriched in ^{15}N, with δ^{15}N values from + 4 to + 7 ‰ (Peters et al., 1978; Kienast et al., 2000; Halama et al., 2012). Due to the abundance and isotopic contrasts in terrestrial nitrogen between the upper-mantle (DMM) and the surface, a number of studies have exploited nitrogen as a tracer for volatile recycling between Earth's surface and interior reservoirs. For example, a number of studies of arc systems have shown the utility of nitrogen as a tracer for subducted sediments (e.g., Sano et al., 1998; Fischer et al., 2002).

However, little is known of the extent of nitrogen recycling into the deep(er) mantle, i.e., the mantle beyond the zone of arc magma generation (Cartigny and Marty, 2013). This includes the DMM as well as the source region of mantle plumes, often equated with the mantle below the 670-km seismic discontinuity (e.g., White, 2010). In this contribution, we assess the hypothesis that nitrogen can identify ‘deep recycling’ of subduction-related material by targeting a mantle plume (Iceland), characterized by high ^{3}He/^{4}He, a particularly sensitive tracer of mantle material isolated from the DMM (upper mantle) reservoir and thereby possibility located in the lowermost mantle (Exley et al., 1986; Tolstikhin & Marty, 1998; Dauphas and Marty, 1999; Marty and Dauphas, 2003a; Marty, 2012; Palot et al., 2012). Iceland is one of the one of the few hotspot localities where the nitrogen isotopic signature of high ^{3}He/^{4}He material can be studied due to the ubiquitous presence of rapidly-quenched pillow rims of subglacial basalts which retain original magmatic gases. In addition, such material is erupted under different confining pressures (e.g., Tuffen et al., 2010), and thus records different degrees of degassing, allowing for investigation of secondary controls on any nitrogen elemental and isotope variability, such as volatile degassing and interactions with Icelandic crust, which can act to disturb primary N-isotope features of the Icelandic mantle.

V.3 Geological setting and samples

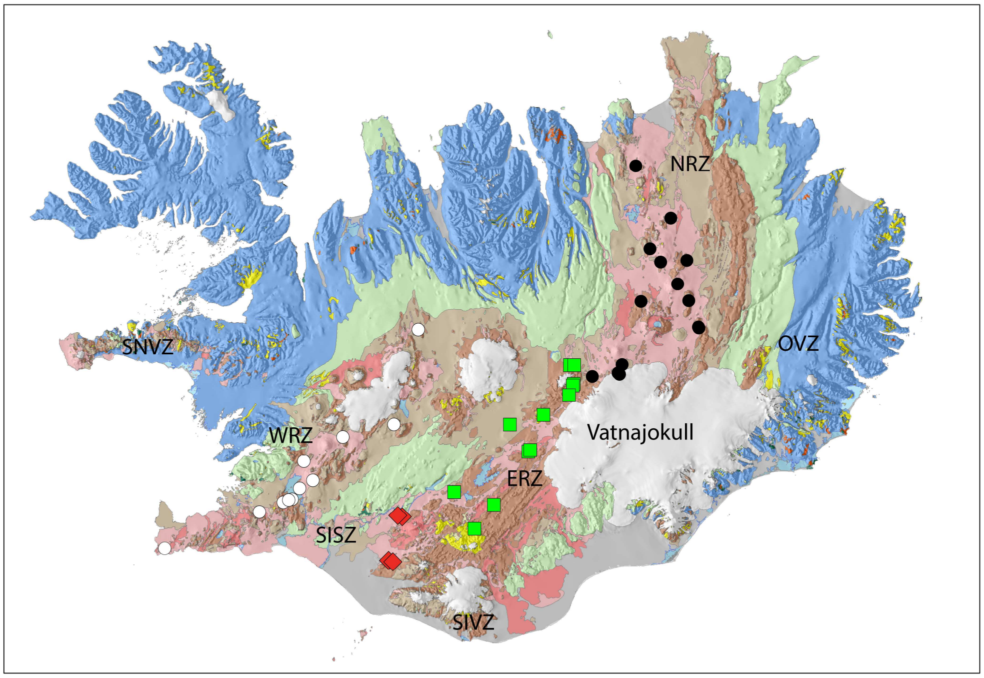

Figure V.1: Map of Iceland showing sampling locations and the neovolcanic zones. These include the axial rift zones: the Western (WRZ), Eastern (ERZ), and Northern rift zones (NRZ), in addition to the off-axis volcanic zones: the South Iceland Volcanic Zone (SIVZ), the Snæfellsnes Volcanic Zone (SNVZ) and the Öræfajökull Volcanic Zone (OVZ). From Jóhannesson and Sæmundsson (1998).

Iceland represents a significant (~100,000 km^2) subaerial segment of the Mid-Atlantic Ridge as is also evident from its enhanced lithosphere thickness resulting from anomalous melting associated with a mantle hotspot (e.g., Bjarnason and Schmeling, 2009). Seismic tomography studies reveal the presence of a low P- and S-wave velocity mantle-zone beneath much of central Iceland, consistent with upwelling of unusually hot asthenosphere (Wolfe et al., 1997). The present-day on-land volcanic activity occurs in two types of neovolcanic zones (**Figure 1**); (i) the axial rift zone, which erupts lavas of tholeiitic composition, passes through Iceland, connecting the adjacent submarine Reykjanes and Kolbeinsey ridges: this rift zone is subdivided into the Western (WRZ), Eastern (ERZ) and Northern (NRZ) Rift Zone segments, and (ii) off-rift volcanic flank zones which erupt lavas of transitional-alkalic to alkalic composition, located to the west on the Snæfellsnes Volcanic Zone (SNVZ) and to the south (South Iceland Volcanic Zone-SIVZ) and south-east (Öræfajökull Volcanic Zone-OVZ) (e.g., Jakobsson et al., 2008). For this study, we targeted 43 subglacially-erupted basalts from different localities, divided between the WRZ (n = 11), ERZ (n = 12), NRZ (n = 15), and SIVZ (n = 5). Sample details and locations are given in **Table 1** and locations are shown in **Figure 1** (see Supplementary Material for sample details).

These samples represent a subset of a larger suite (n=106) of subglacial basaltic glasses from different locations within the neo-volcanic zones, analyzed for helium abundance and isotope characteristics (Macpherson et al., 2005; Furi et al., 2010; this work), to help identify volatile-rich samples for N abundance and isotope measurements. We supplement the sample suite reported by Macpherson et al. (2005) and Füri et al. (2010) with new He abundance and isotopes characteristics on subglacial glass samples from the volcanic flank zones (**Table S1**) in addition to new Ar abundance and isotopes characteristics (**Table S2**).

V.4 Analytical techniques

V.4.1. Helium and argon analysis by in-vacuo crushing

Subglacial basalts (n=16) were crushed under Ultra-High-Vacuum (UHV) to determine their $^3He/^4He$ ratio and He abundance [He] using an MAP215 mass spectrometer and standard protocols described previously (e.g., Shaw et al. 2006; Füri et al. 2010; Hilton et al., 2011). Blanks where identical to those reported by Hilton et al. (2011): i.e., ~ 6.0×10^{-11} cm^3 STP for all runs. All $^3He/^4He$ ratios and [He] were corrected for air-derived He using the methods described in Hilton et al. (2011). High He abundance (generally > 50 cm^3 STP/g) samples were subsequently targeted for nitrogen analysis.

In addition, we analyzed Ar isotope ($^{40}Ar/^{36}Ar$) and abundance characteristics [^{40}Ar] of (n=9) subglacial basalts, adopting *in-vacuo* crushing techniques using a modified VG5440 mass spectrometer equipped with five Faraday cups and a Daly photo-multiplier detector operated in peak jumping mode (see details in: Craig et al., 1993; Füri et al. 2010, Hahm et al., 2012 and Barry et al. 2012). Procedural blanks were typically ~ 7×10^{-9} cm^3 STP for ^{40}Ar.

3.2. Nitrogen analysis by in-vacuo crushing

We targeted 43 helium-rich (13.04 to 3447 $\times 10^{-9}$ cm^3STP/g) basaltic glasses with $^3He/^4He$ ratios between 8.5 and 25.7 R_A and $^{40}Ar/^{36}Ar$ ratios between 292.7 and 1335 for subsequent analyses of N_2 abundances and isotope ratios (Table S1). Using a binocular microscope, we selected fresh glass chips, free of phenocrysts and any visible surficial alteration or large vesicles. The glass was then ultrasonically cleaned in a 1:1 acetone-methanol mixture and dried for ~24 hours. Between 1g and 3 g of fresh glass chips were loaded into screw-type crushers (constructed from modified Nupro vacuum valves; see Stuart et al., 1994), evacuated to UHV, and kept at ~100°C overnight. Nitrogen abundances and isotope ratios were determined on a modified VG5440 mass spectrometer, optimized for static triple collection of nitrogen (see Craig et al., 1993; Barry et al. 2012 for details). A description of the purification system to prepare the samples for N-isotope measurement is given by Barry et al. (2012). In order to maximize nitrogen gas yields; gases were released from samples by single-step crushing *in vacuo* using an external hydraulic press capable of 5 tons pressure. Notably, the N_2/Ar ratio was measured directly after crushing the samples on gas aliquot not utilized for N_2-isotope measurement using a Quadrupole Mass Spectrometer (QMS) interfaced to the purification system as described by Barry et al., (2012).

A pure internal N_2 standard, calibrated relative to Scripps-pier air, was repeatedly measured throughout the run of the Iceland sample set (generally 10-15 times per day). In addition, repeated measurements (n=12) of the Scripps-pier air standard was conducted during these runs, following exactly the same analytical protocol as adopted for samples, allowed evaluation of uncertainties associated with both sample preparation and mass spectrometer measurements. We consider the average $\delta^{15}N$ reproducibility of the Scripps-pier air standard value (± 0.48‰ [1σ]) as the best estimate of the external reproducibility of the system.

Procedural N_2 blanks were run prior to each individual sample and averaged 3.3 ± 1 ($\times 10^{-6}$) cm^3STP for N_2. Blank contributions were (significantly) less than 20% of sample yields in most cases. For samples that yielded blank contributions >20% (n=12), owing to low intrinsic gas contents and/or sample sizes of some samples, results are listed in italics in Table 1. Below, we will only discuss data that had < 30% blank contribution as blank corrections significantly exceeding 20% have been shown to the unreliable (Barry et al., 2012).

To test the reproducibility and the crushing efficiency of our system, we ran 12 samples as duplicates: MID-1, A2, A9, NAL-263, NAL-356, NAL-828, HRD-1, A21/ICE08R-16, A22/ICE08R-17, A35, ICE08R-13, TRI-1. Notably, we analyzed sample MID-1 six times specifically for this purpose. Six duplicates of MID-1 show excellent agreement in [N_2] and range from 21.1 to 31.7 ($\times 10^{-6}$ cm^3STP/g) with an average value of 25.9 ± 4.6 ($\times 10^{-6}$ cm^3STP/g). In this case, our results indicate that the majority of the [N_2] is released from vesicles in a single crushing step. We also note that these values are within the range of values of 13.4 to 58.2 ($\times 10^{-6}$

cm^3N_2STP/g), previously obtained on samples from this same outcrop (i.e., DICE-10 and DICE-11 from Miðfell/Dagmálafell: Marty and Dauphas, 2003). In contrast, out of 12 duplicates, several (n=8) samples show poor agreement in [N_2]: for example sample NAL-263 gave [N_2] of 45.5 and 83.8 ($\times 10^{-6}$ cm^3STP/g) for similar sample loads of 2.537 and 2.105 grams, respectively. This suggests that [N_2] may reflect variable amounts of volatile-rich vesicles in individual samples.

In contrast, we note the good agreement of the $\delta^{15}N$ value of these samples: in the case of NAL-263 the duplicates both gave $\delta^{15}N$ values distinctively more positive than air = +3.70 and +4.71‰. With respect to MID-1, we obtained a range of values for $\delta^{15}N$ of the 6 duplicates: from +0.65 to +3.72‰. Significantly, we note the Marty and Dauphas (2003) reported multiple crushing steps of samples DICE-10 and DICE-11 (i.e., MID-1 = Miðfell/Dagmálafell). The overall of range of values reported by Marty and Dauphas (2003), was between -1.50 to +3.26‰ for $\delta^{15}N$, which is in excellent agreement with the range of values we obtained for $\delta^{15}N$. For this sample, as well as other samples that were run as duplicates, we will only discuss (and plot) $\delta^{15}N$ values that had the lowest blank contribution, assuming that they better represent primary $\delta^{15}N$ values.

4. Results

We report (n=16) new helium isotope and abundance characteristics of transitional-alkalic to alkalic subglacial glasses from volcanic flank zones (SIVZ and SNVZ) in addition to one tholeiitic glass (STAP-1) from the WRZ in Iceland in Table S2 (see supplementary material). These data supplement He data from the previous studies of Macpherson et al. (2005) and Füri et al. (2010), which investigated on-axis Icelandic subglacial basaltic glasses.

In addition, we report new argon isotope and abundance characteristics of (n=9) samples to supplement previous data reported by Füri et al. (2010) in Table S3 (see supplementary material). The combined nitrogen, argon and helium isotope ratios and relative abundance characteristics of the 43 subglacial basaltic glasses that are the focus of this study, are reported in Table S1 along with derived elemental ratio $N_2/^3He$, and $N_2/^{40}Ar^*$ and the $N_2/^{40}Ar$ ratio analyzed straight after crushing samples using a QMS attached to the nitrogen extraction line (see Barry et al., 2012).

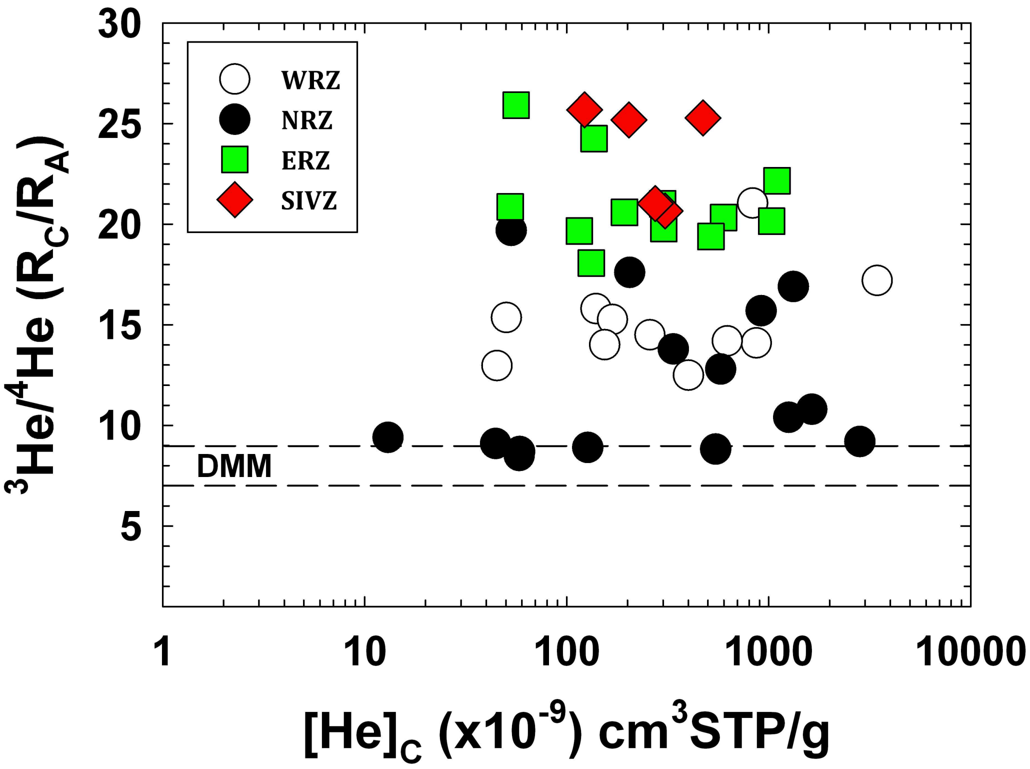

Figure V.2: He-isotopes (reported as R_C/R_A: where R_A = air $^3He/^4He$) versus $[He]_C$ corrected for the presence of atmospheric helium of all subgalcial basalts of this study. The canonical DMM range of 8 ± $1R_A$ is from Graham (2002).

4.1. Helium and argon abundances and isotopes

In **Figure 2**, we plot He-isotopes (reported as R_C/R_A: where R_C is the air-corrected sample $^3He/^4He$ ratio and R_A = air $^3He/^4He$) versus $[He]_C$ (He concentration also corrected for air helium (see footnote for Table S2 for details) of all subglacial basalts of this study relative to the canonical DMM range of 8 ± $1R_A$. Helium concentrations range from 13.04 to 3447 $\times 10^{-9}$ cm^3STP/g with only 1 sample showing concentrations < ~50 $\times 10^{-9}$ cm^3STP/g, in good agreement with the range of values previously reported for most Icelandic subglacial basalts (Condomines et al. 1983; Kurz et al. 1985; Poreda et al. 1986; Harrison et al. 1999; Dixon et al. 2000; Trieloff et al. 2000; Breddam & Kurz, 2000; Dixon, 2003; Macpherson et al. 2005; Füri et al. 2010). In contrast, this concentration range is significantly higher than previously reported values for Icelandic minerals which are generally < 1 $\times 10^{-8}$ cm^3STP/g (Poreda et al. 1986; Hilton et al. 1999; Dixon et al. 2000; Dixon, 2003; Ellan & Stuart, 2004; Brandon et al. 2007; Liccardi et al. 2006; Liccardi et al. 2007; Debaille et al. 2009; Füri et al. 2010; Peate et al. 2010).

The overall range in $^3He/^4He$ is from 8.5 to 25.7 R_A, also comparable with previously reported values from Iceland (Füri et al., 2010 and ref. therein). We note a clear distinction between different rift segments and emphasize four main points: (1) only samples from the NRZ overlap the DMM range, but also extend to higher values. Notably, DMM-like values are predominantly found to the north of the NRZ, whereas higher values (up to $19.7R_A$) occur towards central Iceland, (2) Samples from the WRZ show a more restricted range of values from 12.5 to $21.1R_A$. Indeed, excluding the highest value of $21.1R_A$, the remaining WRZ samples all lie between 12.5 and $17.2R_A$, (3) All samples from the ERZ display $^3He/^4He > 18R_A$, displaying a restricted range of values from 18.1 to $25.9R_A$, and finally, (4) the SIVZ samples, all display $^3He/^4He > 18R_A$ and reach values as high as $25.7R_A$ at Þríhyrningur, in good agreement with the $^3He/^4He$ ratio of $26.2R_A$ obtained previously at this location (Kurz et al., 1985).

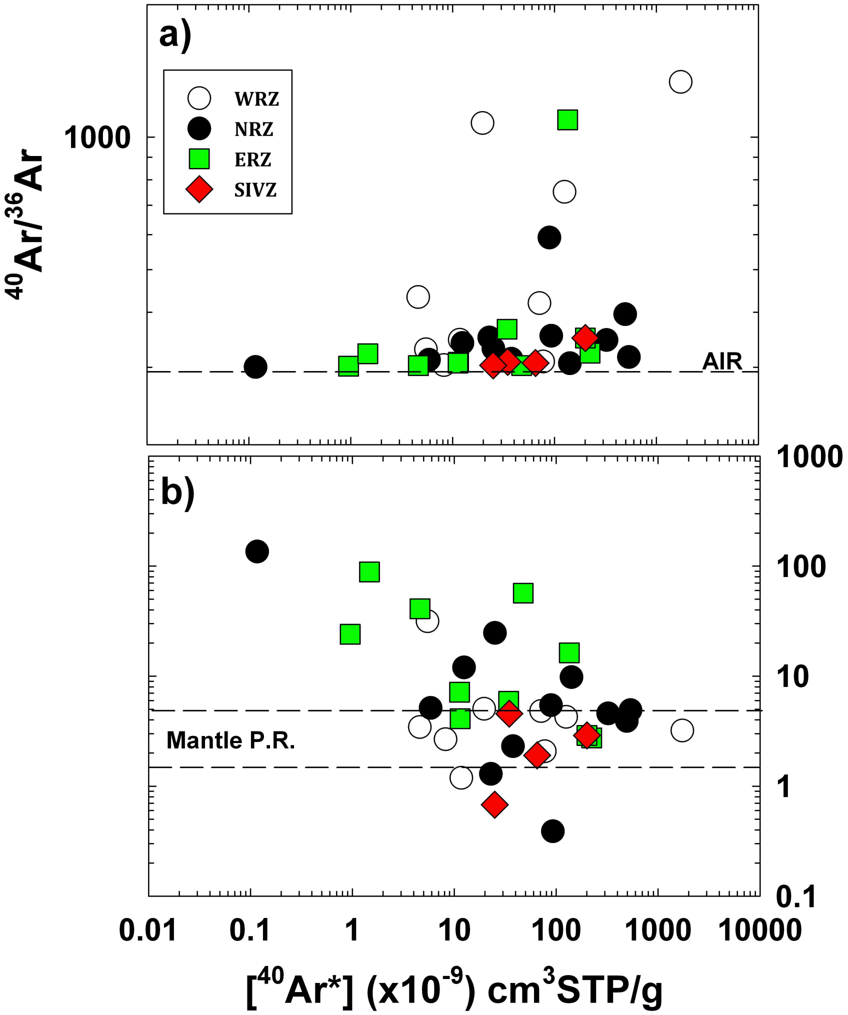

Figure V.3: (a) Argon isotopes ($^{40}Ar/^{36}Ar$) and (b) $^{4}He/^{40}Ar^{*}$ ratios versus radiogenic $^{40}Ar^{*}$. We indicate the present (1.4) and time-integrated (4.8) theoretical $^{4}He/^{40}Ar^{*}$ Production Ratios calculated for the upper-mantle (Porcelli & Ballentine, 2002; Yamamoto and Burnard, 2005; Hanyu et al., 2011). The air $^{40}Ar/^{36}Ar$ value is 298.6 from Lee et al. (2006).

The total ^{40}Ar content, which represents a mixture of air-derived argon in addition to intrinsic radiogenic argon, is corrected for the presence of atmospheric argon (i.e., [$^{40}Ar^{*}$]) assuming that all the ^{36}Ar is atmospheric-derived in the following manner:

$$^{40}Ar^{*} = [^{36}Ar_{m}] \times [(^{40}Ar/^{36}Ar)_{m} - (^{40}Ar/^{36}Ar)_{air}] \qquad (1)$$

Where ^{40}Ar* is radiogenic argon, and ^{36}Ar$_m$ and (^{40}Ar/^{36}Ar)$_m$ are the measured values and (^{40}Ar/^{36}Ar)$_{air}$ is the air ratio (=298.56 ± 31; Lee et al., 2006). In **Figure 3a**, we plot ^{40}Ar/^{36}Ar ratios versus radiogenic ^{40}Ar*. The radiogenic Ar concentrations [^{40}Ar*] vary from 0.1 to 1734 $\times10^{-9}$ cm^{3}STP/g with the highest values found at the MID-1, Miðfell/Dagmálafell (i.e., DICE) locality. This range of values is comparable to the range previously reported for oceanic basalts where [^{40}Ar*] generally lies between ~10^{-9} and ~10^{-6} cm^{3}STP/g (e.g., Yamamoto and Burnard, 2005).

Argon isotopes (^{40}Ar/^{36}Ar) show a rather narrow range of values from atmospheric-like values to 1334. These values are both comparable to and/or lower than those reported previously from Iceland (air-like to ~6500; Burnard et al. 1994; Harrison et al. 1999; Trieloff et al. 2000; Burnard and Harrison, 2005; Füri et al., 2010; Mukhopadhyay, 2012) but much lower than source estimates for oceanic basalts (~5000 to ~ 40,000; e.g., Burnard et al., 1997; Trieloff and Kunz, 2005). Notably, a significant number of samples (n=9) have ^{40}Ar/^{36}Ar near identical to the isotopic composition of air (298.56; Lee et al. 2006).

In **Figure 3b**, we plot ^{4}He/^{40}Ar* ratios versus radiogenic ^{40}Ar*. As noted above, many samples (n=9) have air-like ^{40}Ar/^{36}Ar ratio, precluding calculation of the ^{4}He/^{40}Ar* ratio. Other samples show a wide range in ^{4}He/^{40}Ar* ratios from 0.4 to 135. A significant number of samples fall within the present and time-integrated theoretical ^{4}He/^{40}Ar* production ratio calculated for the upper-mantle (P.R. = 1.4 to 4.8; e.g., Porcelli & Ballentine, 2002; Yamamoto and Burnard, 2005; Hanyu et al., 2011), whereas four samples display ^{4}He/^{40}Ar* ratios < 1.4. As demonstrated by Füri et al. (2010), parental melts of the Iceland plume have undergone noteworthy depletion of helium relative to neon and argon – a likely process responsible for ^{4}He/^{40}Ar* ratios < theoretical upper-mantle values observed in our dataset. We also note that samples with the highest

^{4}He/^{40}Ar* ratios are associated with low [^{40}Ar*] consistent with the preferential loss of ^{40}Ar* relative to ^{4}He following degassing.

4.2. Nitrogen abundances and isotopes

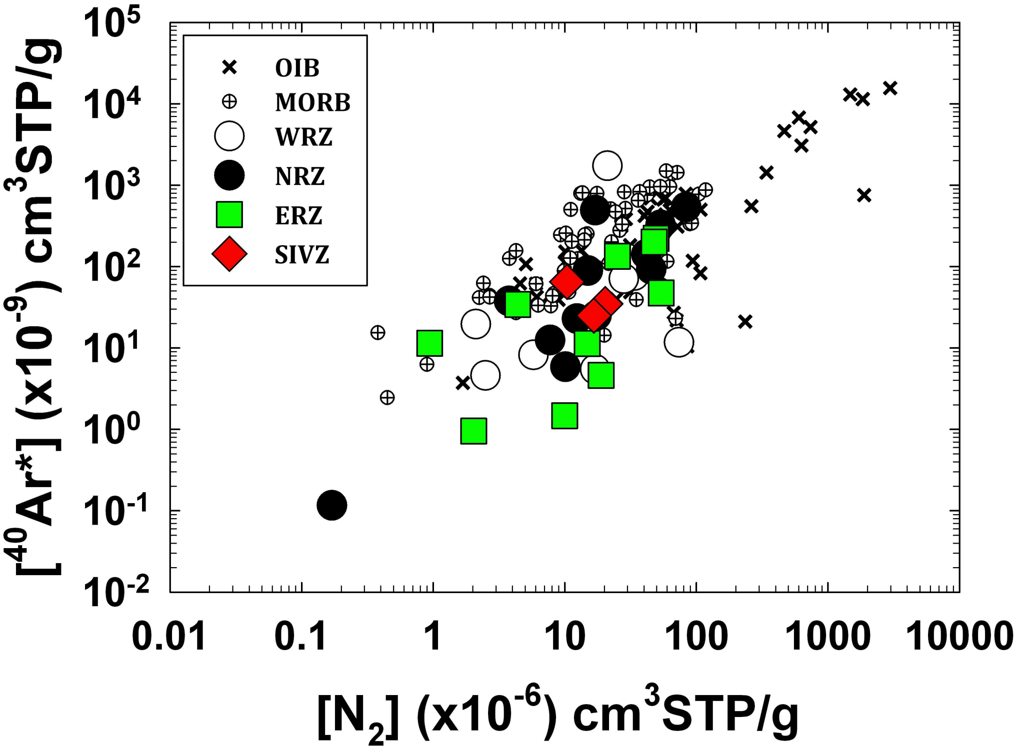

Figure V.4: Argon ([^{40}Ar*]) versus [N_2] concentrations for Icelandic basalts by neovolcanic zone. We also plot data from Mid-Ocean Ridge basalts (MORB) and Oceanic Island Basalts (OIB) that where obtained by in vacuo crushing (Marty and Humbert, 1997; Marty and Zimmerman, 1999; Marty and Dauphas, 2003a).

In **Figure 4**, we plot [^{40}Ar*] versus [N_2]. For comparison we also plot data from mid-ocean ridge basalts (MORB) and oceanic island basalts (OIB) that where obtained by *in vacuo* crushing (Marty and Humbert, 1997; Marty and Zimmerman, 1999; Marty and Dauphas, 2003a), allowing for a direct comparison with our Iceland dataset. Nitrogen concentrations ([N_2]) of the Iceland subglacial basalts vary from 0.17 to 83.2 (×10^{-6}) cm^{3}STP/g. This range is comparable to the range of values previously reported by MORB glasses ~0.4 to ~118 (×10^{-6}) cm^3STP/g but significantly lower than the overall range reported for OIB glasses ~2 to ~2970 (×10^{-6}) cm^3STP/g. However, we note that [N_2] values significantly > ~100 (×10^{-6}) cm^3STP/g are rare in oceanic basalts and are predominantly from Teahitia in the Society Islands (Marty and Dauphas, 2003). Thus, our range is generally consistent with the current [N_2] database reported for oceanic basalts. We observe a generally good correlation between [^{40}Ar*] and [N_2] over several orders of magnitude - consistent with a general coupling of N-Ar trapped in similar storage sites (i.e., vesicles) in subglacial glasses (e.g., Marty, 1995). Thus, the N_2 and Ar concentrations of the Iceland samples may simply reflect the relative density of vesicles in each sample, consistent with observations of other oceanic glasses (Marty, 1995; Marty and Humbert, 1997; Marty and Zimmerman, 1999; Marty and Dauphas, 2003a).

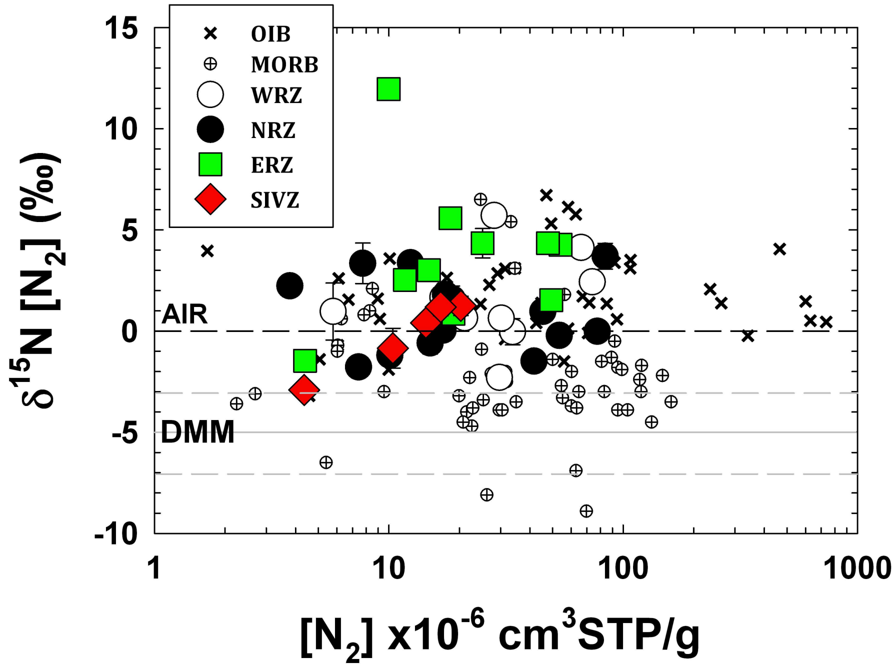

Figure V.5: Nitrogen isotope values (δ^{15}N-N2) versus [N_2] concentrations. We also plot data from MORB and OIB data obtained using in vacuo crushing techniques (Marty and Humbert, 1997; Marty and Zimmerman, 1999; Marty and Dauphas, 2003a). Air is indicated with the dashed black line and the mean δ^{15}N values of the DMM reservoir (-5 ± 2‰) with the solid gray line together with the associated uncertainty with dashed gray lines.

In **Figure 5**, we plot nitrogen isotope values (δ^{15}N-[N_2]-versus Air) versus [N_2] of the Iceland sample-set together with MORB and OIB glasses obtained previously using *in vacuo* crushing techniques (Marty and Humbert, 1997; Marty and Zimmerman, 1999; Marty and Dauphas, 2003a). Note that we do not plot the following samples due their high blank contribution: OLF-1 (41%), MAE-1 (30%), KVIH-1 (87%), A13/ICE08R-09 (47%), A32 (41%): therefore, there are n = 38 Iceland samples plotted in **Figure 5**. The nitrogen isotopes (δ^{15}N) values show a wide range from -2.91 to +11.96‰ and have an average value of +1.62 ± 2.77‰. Notably, this value is significantly higher the value postulated for the DMM end-member of -5 ± 2‰, as sampled at mid-ocean ridges (Marty and Dauphas, 2003a). In addition, the Iceland average is also higher than the average value obtained from the MORB database (-2.00 ± 2.80‰: Marty and Humbert, 1997; Marty and Zimmerman, 1999; Marty and Dauphas, 2003a). We note the values > 6‰ are only observed at one locality in Iceland (A35-Sigalda) and, if we remove this sample, the overall range varies from -2.91 to +5.58‰ and the mean value becomes only slightly less positive (+1.34 ± 2.20‰). In any case, the Iceland data are in excellent agreement with δ^{15}N values previously reported for OIB glasses which range between -3.2 to 6.7‰ and which have a mean value of +1.92 ± 2.43‰ (Marty and Humbert, 1997; Marty and Zimmerman, 1999; Marty and Dauphas, 2003a). However, in contrast to He-isotopes, there appears to be no spatial control on the δ^{15}N dataset as different segments of the neovolcanic zones have overlapping δ^{15}N values.

Published nitrogen isotope values obtained on Icelandic lavas are limited and only three samples have been reported adopting vacuum crushing (Marty & Dauphas, 2003a; Fischer et al., 2005). Fischer et al. (2005) obtained a δ^{15}N of -8‰ for a single Iceland phenocryst sample from Theistareykir in the NRZ - one of the most negative values observed on oceanic basalts so far. We note, however, that this sample had an extremely small quantities of [N_2] (0.88×10^{-6} cm^3STP/g), which is significantly less than our system blank of 3.3 ± 1 ($\times 10^{-6}$ cm^3STP) casting doubt on its integrity. Finally, we note that Mohapatra et al. (2009) analyzed two glass samples from the WRZ by stepped heating and obtained a large range, between -12.5‰ to +16.5‰, that is well beyond the range we observed with vacuum crushing. Again, we have concerns about the validity of these results due to possible modification of the $\delta^{15}N$ values by interaction with hot metal (iridium in this case) crucibles (Yokochi & Marty, 2006).

5. Discussion

5.1. Integrity of data

In the following section, we adopt a step-by-step filtering protocol to test the integrity of individual samples and to identify those that are representative of the mantle source. In the case of the sample suite studied here, modifications of mantle source values may be due to air contamination, degassing, and/or shallow-level crustal contamination. Only through this approach, is it possible to discern primary $\delta^{15}N$ features of the Icelandic mantle source, and to assess the role and extent of these various secondary processes in masking mantle nitrogen features.

5.1.1. Air contamination and entrapment of air-derived components

Atmospheric nitrogen can act to mask, and/or in some cases, overwhelm the characteristics of mantle nitrogen intrinsic to Icelandic melts. To overcome this problem, we have adopted the following criteria to aid in the recognition of primary versus secondary N features:

1. Elemental ratios involving N_2 are employed to help recognize atmospheric contributions. For example, N_2/Ar values lower than air (83), but higher than or equal to air-saturated water (ASW) at 0°C (38) are considered to identify samples contaminated with air and/or affected by mixing with ASW (e.g., Hilton, 1996) . In **Figure 6**, we plot N_2/Ar ratios of the same samples plotted in **Figure 5**, versus [N_2] to identify air-contaminated samples.

Iceland glasses have N_2/Ar ratios between 85 to 425, with a mean ratio of 167 ± 86, somewhat higher than the mean value reported for all types of MORB glasses= 124 ± 40 (Marty and Zimmerman, 1999), and significantly higher than the mean value reported for OIB 74 ± 34 (Marty and Dauphas, 2003a). We note that ratios exceeding 300 are only observed when [N_2] are < 30 ($\times 10^{-6}$ cm^{3}STP/g), whereas [N_2] > 30 ($\times 10^{-6}$ cm^{3}STP/g) always display N_2/Ar ratios < 200. Significantly, no samples overlap with the air value and/or the ASW values as all samples have N_2/Ar ratios <83, indicating that air contamination is minimal.

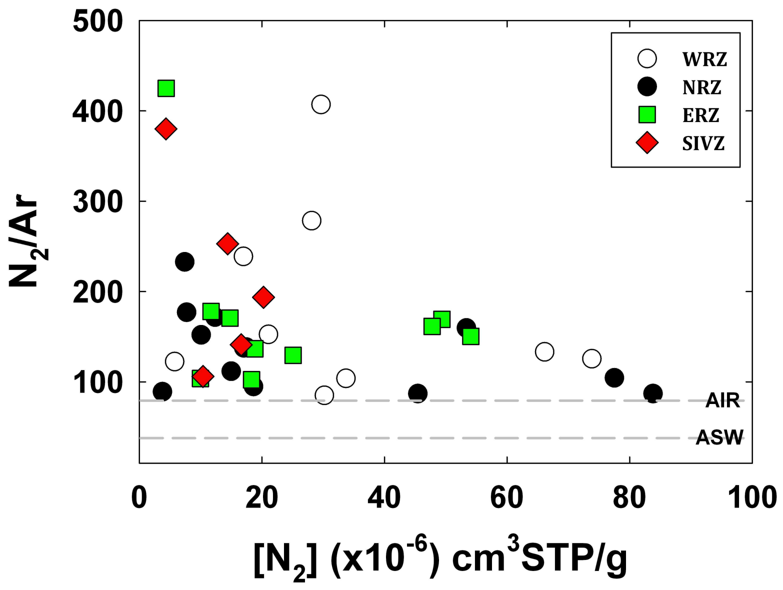

Figure V.6: N_2/Ar ratios of the same samples as Figure 5, versus [N_2] concentrations. The N_2/Ar values of air (83) and air-saturated water (ASW) (38) are indicated by dashed gray lines. Significantly, all samples have N_2/Ar ratios well above the air value, indicating that air contamination does not overwhelm samples.

2. A powerful approach to identifying air-contaminated samples is the combination of N isotopes, overlapping with air-like ^{40}Ar/^{36}Ar ratios. In **Figure 7a**, we plot ^{40}Ar/^{36}Ar ratios versus δ^{15}N values of the Iceland glasses in addition to MORB and OIB glasses (Marty and Humbert, 1997; Marty and Zimmerman, 1999; Marty and Dauphas, 2003a). As noted

previously, Iceland δ^{15}N values are significantly higher than estimates of the DMM reservoir (-5 ±2‰) and also the mean value of MORB database (-2.0 ± 2.8‰), and show better correspondence with OIB glasses.

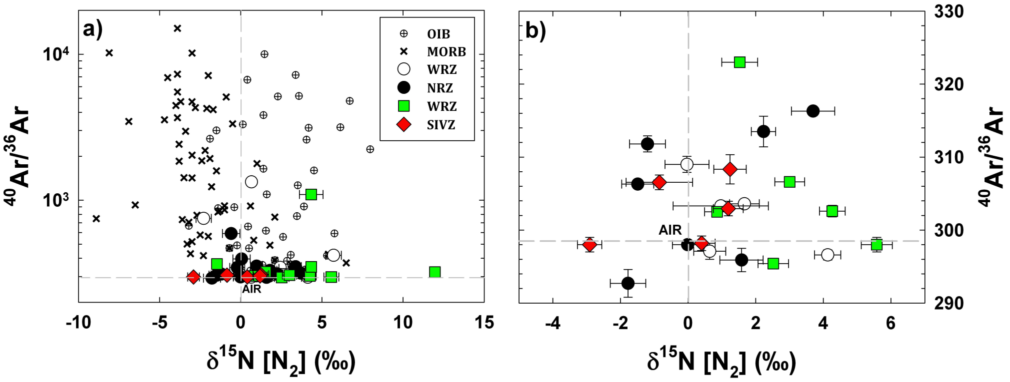

Figure V.7: Argon isotopes ^{40}Ar/^{36}Ar ratios versus δ^{15}N values of the Iceland glasses. In (a), MORB and OIB glasses are plotted (from Marty and Humbert, 1997; Marty and Zimmerman, 1999; Marty and Dauphas, 2003a). The isotopic composition of air (δ^{15}N =0‰ and ^{40}Ar/^{36}Ar =298.6) is indicated with dashed gray lines. In (b), coupled δ^{15}N-^{40}Ar/^{36}Ar systematics are investigated in more detail by adjusting of scale. Notably, two samples (NAL-281 and BHE-43) overlap with air. Additionally, seven sample display ^{40}Ar/^{36}Ar ratios ≤ air. These samples are omitted from further consideration in the discussion.

However, coupled δ^{15}N-^{40}Ar/^{36}Ar systematics of the Iceland glasses differ from both MORB and OIB, as their ^{40}Ar/^{36}Ar ratios do not extend to values significantly greater than ~1000. Only 4 samples have ^{40}Ar/^{36}Ar ratios > 500, indicating that a large component of argon in Icelandic glasses is atmosphere-derived, consistent with prior studies (e.g., Burnard et al. 1994; Harrison et al. 1999; Trieloff et al. 2000; Burnard and Harrison, 2005; Füri et al., 2010; Mukhopadhyay, 2012). In **Figure 7b**, we investigate coupled δ^{15}N-^{40}Ar/^{36}Ar systematics in more detail by only considering samples with air-like isotope signatures (0‰; 298.6). Two samples (NAL-281 and BHE-43) overlap with air δ^{15}N. Additionally, seven samples (NES-1, REY-1, NAL-356, NAL-500, A11, A18/ICE08R-12, TRÍ-2) display ^{40}Ar/^{36}Ar ratios ≤ air. Thus, we omit all 9 samples from further consideration as they have likely incorporated a large component of argon that is atmosphere-derived.

5.1.2. Magmatic degassing and elemental fractionations

In addition to air contamination, another important process capable of modifying intrinsic mantle volatile features is magmatic degassing. Degassing can potentially cause relative abundance fractionation, such that measured elemental ratios are no longer representative of mantle source values (e.g., Cartigny et al., 2001). A robust approach to constrain degassing history and the mode and extent of volatile loss, is the use of the relative noble gas abundance ratio of ^{4}He/^{40}Ar*. This ratio is particularly powerful for modeling the extent of degassing (e.g., Matsuda and Marty, 1995), because He is much more soluble than Ar in basaltic magmas (S_{He}/S_{Ar} = 9.5; Jambon et al., 1986 where S = solubility). As a consequence, the residual medium (i.e., basaltic glass) should display ^{4}He/^{40}Ar* values that increase from the present and time-integrated theoretical production ratios, as degassing proceeds.

In **Figure 8**, we plot elemental ratios involving N_2, i.e., **(a)** N_2/^{3}He and **(b)** N_2/^{40}Ar* (i.e., [N_2] over radiogenic [Ar]; e.g., Cartigny and Marty, 2013) versus ^{4}He/^{40}Ar* ratios. Estimates for the ^{4}He/^{40}Ar*, N_2/^{3}He and N_2/^{40}Ar* ratios of the upper-mantle (DMM: 1.4 to 4.8; 3.76 ± 1.17 ($\times 10^{6}$); 138 ± 65, respectively: Marty and Humbert, 1997; Marty and Zimmermann, 1999; Hanyu et al., 2011; supplementary material) are indicated by the gray boxes. The N_2/^{3}He ratio (**Figure 8a**) varies by well over two orders of magnitude, from 2.5×10^{5} to 9.0×10^{7}, and thus Iceland glasses display N_2/^{3}He ratios that span the range of DMM estimates.

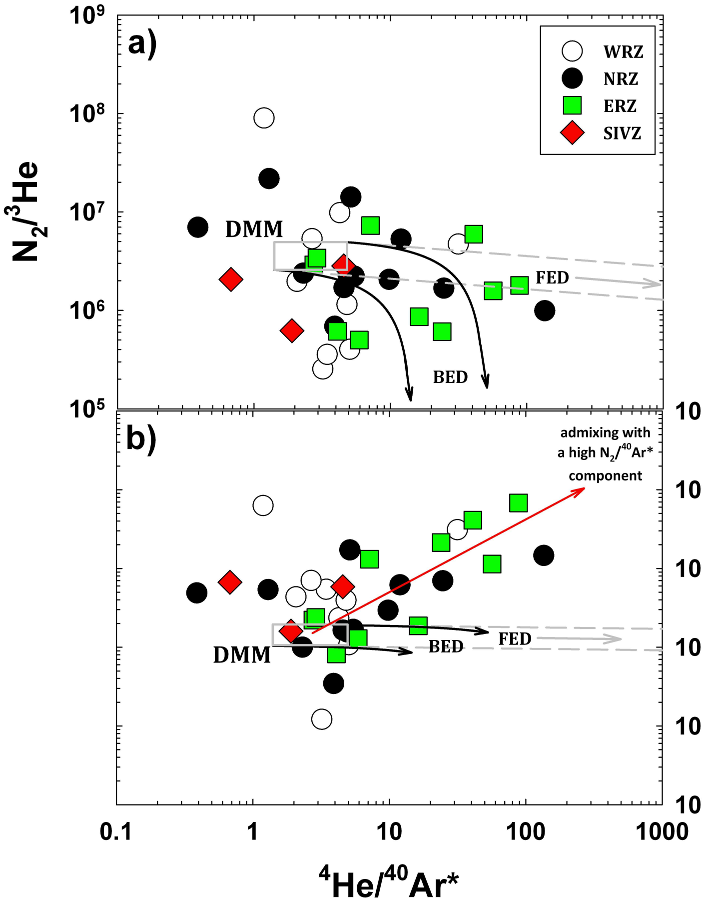

Figure V.8: Plot of (a) $N_2/^3He$ and (b) $N_2/^{40}Ar^*$ versus $^4He/^{40}Ar^*$ ratios. Estimates for the $^4He/^{40}Ar^*$, $N_2/^3He$ and $N_2/^{40}Ar^*$ ratios of the upper-mantle (DMM: 1.4 to 4.8; 3.76 ± 1.17 (×10^6); 138 ± 65, respectively: Marty and Humbert, 1997; Marty and Zimmermann, 1999) are indicated with the gray box. In (a), we superimpose degassing trajectories for open-system degassing (FED) and closed system degassing (BED) assumed starting values of 1.4 for $^4He/^{40}Ar^*$ and of 3.76 ± 1.17 (×10^6) for $N_2/^3He$ and using solubility coefficient described in the text. Notably, 8 samples with $^4He/^{40}Ar^* > 10$ lie very close to the FED trajectories and are thus likely to have modified elemental ratios not representative of their source values. A somewhat lower $N_2/^3He$ starting values (~1 ×10^6) is needed to fit two samples from the ERZ. In (b), we show FED and BED trajectories calculated assumed starting values of 1.4 for $^4He/^{40}Ar^*$ and 138 ± 65 for $N_2/^{40}Ar^*$. The FED trajectory is nearly horizontal irrespective of the $^4He/^{40}Ar^*$ because of the very similar solubilities of Ar and N in basaltic magmas. Significantly, of all the samples that have $^4He/^{40}Ar^* > 10$, only one sample from the ERZ, falls on the FED trajectory. Thus, high $N_2/^{40}Ar^*$ ratios (up to 6780) are well beyond what can be produced by solubility controlled degassing and indicate mixing towards a component with a high $N_2/^{40}Ar^*$ ratio.

In order to test to what extent magmatic degassing is capable of explaining this large variation, we superimpose degassing trajectories for both open-system degassing (FED:

Fractional Equilibrium Degassing) and closed-system degassing (BED: Batch Equilibrium Degassing) using a solubility coefficient for He of (5.60 $\times10^{-4}$ cm^3 STP/g) from Jambon et al. (1986), 6.14 for Ar ($\times10^{-5}$), and 5.12 ($\times10^{-5}$) for N_2, compiled by Cartigny et al. (2001). Additionally, we assume starting values between 1.4 and 4.8 for $^4He/^{40}Ar^*$ and of 3.76 ± 1.17 ($\times10^6$) for $N_2/^3He$ (e.g., Marty and Zimmermann, 1999).

Out of all samples plotted in **Figure 8a**, we note that 10 samples which display $^4He/^{40}Ar^*$ > 10 and fall well outside the DMM box, lie very close to the superimposed degassing trajectories for FED and/or BED. These samples are thus likely to have modified elemental ratios not representative of their source values. Significantly, only when $^4He/^{40}Ar^* > 10$ does the effect of degassing modifications become clearly evident as some samples display characteristics that overlap the DMM field. All other samples have $^4He/^{40}Ar^* < 10$, suggesting only moderate (<20%) amounts of degassing that are unlikely to have extensively modified starting $N_2/^3He$ ratios.

The $N_2/^{40}Ar^*$ varies significantly, from 12.2 to 6780 and, analogous to $N_2/^3He$ ratios, this is well beyond estimates for DMM (**Figure 8b**). Assuming the same solubility coefficients for He, Ar and N as adopted in **Figure 8a**, and a $N_2/^{40}Ar^*$ starting value of 138 ± 65, we construct and superimpose similar FED and BED trajectories. Significantly, of all the samples that have $^4He/^{40}Ar^* < 10$, only 4 sample from the ERZ, falls on the FED trajectory, although we note that there is a considerable overlap with the DMM field. As nitrogen and argon have similar solubilities in basaltic magmas, the FED trajectory is nearly horizontal, irrespective of the $^4He/^{40}Ar^*$, leading to virtually no change in the $N_2/^{40}Ar^*$ value. Thus, magmatic degassing will never be capable of explaining the marked enrichment of N_2 over $^{40}Ar^*$ observed in **Figure 8b**, and the high ratios observed (up to 6780) are well beyond those that could be produced during solubility controlled degassing. Indeed, assuming near 100% degassing, an unlikely process for these samples given that $^4He/^{40}Ar^*$ ratios are all < 140, the $N_2/^{40}Ar^*$ ratios will reach values as low as ~20, but not values > than DMM.

As $^{40}Ar^*$ is the denominator for both ratios plotted in **Figure 8b**, binary mixing should plot as a straight line, as could be the case for samples that have a $^4He/^{40}Ar^*$ ratio > 10. This is illustrated with a binary mixing line (in red) between (i) a mantle component with low $N_2/^{40}Ar^*$ and $^4He/^{40}Ar^*$ ratios, and (ii) a component with high $N_2/^{40}Ar^*$ and $^4He/^{40}Ar^*$ ratios. Significantly, as samples with $^4He/^{40}Ar^* > 10$ have lost significant amounts of volatiles, they become more susceptible to the addition of extraneous volatiles (e.g., crustal and/or atmospheric). Thus, a likely explanation of the high $N_2/^{40}Ar^*$ratios evident in **Figure 8b,** is admixture with a component with a very high $N_2/^{40}Ar^*$, such as organic material embedded in crustal wall rocks (Barry et al., 2014). However, admixture with such a component only becomes evident in samples that have $^4He/^{40}Ar^* > 10$, i.e., degassed samples. This possibility is further tested in section 5.1.4 below.

5.1.3. Magmatic degassing and nitrogen isotope fractionation

In addition to causing relative abundance fractionation, magmatic degassing can potentially generate isotope fractionation of intrinsic mantle nitrogen isotope values. However, with respect to nitrogen, there is no consensus on degassing induced isotopic fractionation of nitrogen (see contrasting views in the discussions of Cartigny and Ader, 2003 and Marty and Dauphas, 2003b). A primary observation commonly used to argue for isotopic fractionation of nitrogen during degassing (Javoy, 1997; Cartigny et al., 2001) is the fact that MORB vesicles, which represent out-gassed (i.e., exsolved) mantle nitrogen, mostly have negative $\delta^{15}N$ values (Javoy and Pineau, 1991; Marty and Humbert, 1997; Marty and Zimmermann, 1999), whereas the residual nitrogen, extracted by fusion, often has higher $\delta^{15}N$ values (e.g., Exley et al., 1986; Cartigny et al., 2001). However, some of these values may be biased due to kinetic effects during gas extraction (Boyd et al., 1993; Pinti et al., 2007; Yokochi et al. 2009) and the use of N-reactive metals (Yokochi and Marty, 2006). Indeed, evidence has been presented against N isotope fractionation during magma degassing, based on a study of olivine and geothermal gases collected at the same locations which shows similar δ^{15}N values for both types of sampling media (Fischer et al., 2005) and consideration of coupled δ^{15}N-^{4}He/^{40}Ar* systematics in oceanic basalts (e.g., Marty and Dauphas, 2003b).

In order to test whether the observed N-isotope variations of the Iceland glasses result from degassing-induced modification of a common mantle source, we plot ^{4}He/^{40}Ar* versus δ^{15}N in **Figure 9a**. Notably, we adopt DMM as the common end-member in our model as there remain considerable uncertainties regarding the selection of another nitrogen mantle component under Iceland. Indeed, on the basis of radiogenic isotopes, DMM has been identified as a mantle end-member in the Iceland mantle source (e.g., Thirlwall et al., 2004 and ref. therein). We adopt a simple open system (FED: Rayleigh fractionation) degassing model to test the possible effects of magmatic degassing. Degassing-induced loss of He and Ar is controlled by fractionation (solubility) factors for He (S_{He}) and Ar (S_{Ar}), and the Rayleigh distillation equation governing the residual ratio $(He/Ar)_r$ in the melt can be describe as follows:

$$(^{4}He/^{40}Ar^*)_r=(^{4}He/^{40}Ar^*)_0 f_{Ar}^{[(SAr/SHe)-1]} \quad (2)$$

where f_{Ar} is the remaining fraction of Ar in the melt. We adopt the same solubility coefficients as described above for He and Ar. Also, in an open system, the δ^{15}N values of the melt are related to the remaining fraction of [N] in the melt (f_N) in the following manner:

$$\delta^{15}N_{melt} = \delta^{15}N_0 + \Delta_i \times \ln f_N \quad (3)$$

where

$$\Delta_i = \delta^{15}N_{ves} - \delta^{15}N_{melt} \qquad (4)$$

Here, Δ_i is the isotopic equilibrium fractionation factor of $\delta^{15}N$ between the vesicles and the melt, and we adopt a value of -1.6‰ from Cartigny et al. (2001). It is important to note the fractionation factor used here is based on observations of vesicles and the melt phases of basaltic glasses from the south-west Indian Ridge, but further experimental work of nitrogen isotope behavior during degassing is needed that confirm this value.

Assuming a fixed $\delta^{15}N$ value of the mantle source but taking its associated uncertainty estimates into account, degassing trajectories are capable of explaining only a small subset of the dataset plotted in **Figure 9a**, and the possible effects of degassing (if any), only become evident as $^{4}He/^{40}Ar^*$ ratio exceeds ~10. Thus, the data are largely inconsistent with degassing induced isotopic fractionation of nitrogen from a single mantle source $\delta^{15}N$ value, and may require heterogeneous starting $\delta^{15}N$ values that are difficult to constrain. In addition, as discussed above, high $N_2/^{40}Ar^*$ ratios in samples associated with $^{4}He/^{40}Ar^*$ ratios > 10, suggest elemental variations are not the result of degassing but instead require a scenario involving mixing of mantle-material that has lost significant amounts of volatiles via degassing and a component with high $N_2/^{40}Ar^*$ ratios. Consideration of additional stable isotope fractionation models such as species- (i.e., solubility- : Mysen & Fogel, 2010) and/or diffusion- (i.e., kinetic- : Yokochi et al., 2009; Roulleau et al., 2012) induced isotopic fractionation, which we deem unlikely at this stage, are provided in the supplementary material.

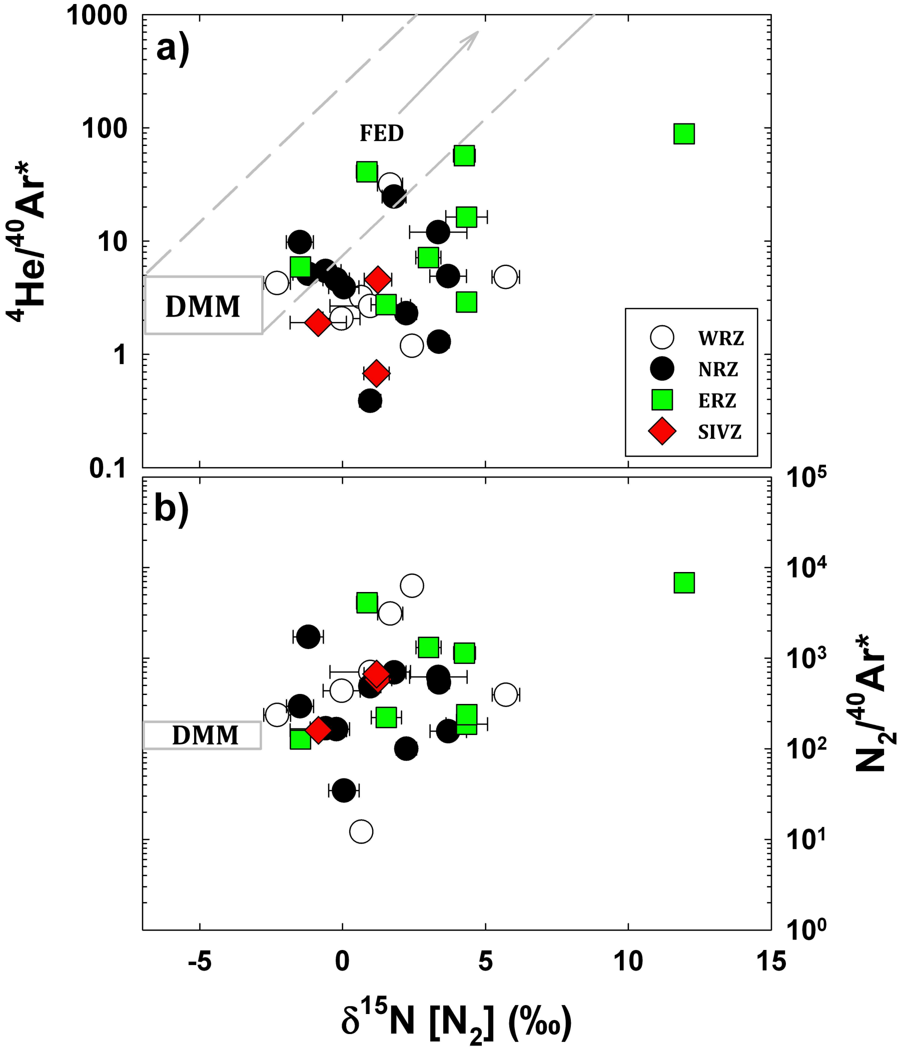

Figure V.9: Plot of (a) ^{4}He/^{40}Ar* and (b) N$_2$/^{40}Ar* ratios versus δ^{15}N. Estimates for the DMM (-5 ± 2‰: 1.4 to 4.8: 138 ± 65) are indicated with the gray box. In (a), we superimpose FED trajectories (see text for details) assuming starting values of 1.4 to 4.8 for ^{4}He/^{40}Ar* and -5 ± 2 ‰ for δ^{15}N to test the possible effects of magmatic degassing on δ^{15}N values. The FED rajectories are only capable of explaining a small subset of the entire dataset assuming a fixed starting value. Possible effects of degassing only become evident as ^{4}He/^{40}Ar* ratio exceed ~10. In (b), N$_2$/^{40}Ar* values are plotted versus δ^{15}N to test the possible effects of crustal contamination on modifying δ^{15}N values. We adopt starting compositions of -7‰ and -3 ‰ (i.e., -5 ±2‰) and 1.4 and 4.8 for δ^{15}N and ^{4}He/^{40}Ar*, respectively. Most samples (7 out of 8) with N$_2$/^{40}Ar* ratios > 1000 have positive δ^{15}N signatures (up to +12‰). Generally, such samples have ^{4}He/^{40}Ar* ratios > 10 (Figure 8b), which is consistent with a significant volatile loss. Thus, the association of high δ^{15}N and high N$_2$/^{40}Ar* ratios in these samples is consistent with admixture of organically-derived nitrogen with δ^{15}N and N$_2$/^{40}Ar* >> DMM to the intrinsic mantle nitrogen component. This would argue against degassing-induced fractionation effects on the δ^{15}N values.

In summary, we conclude that N-isotopes of Icelandic subglacial basalt have not experienced significant degassing-induced fractionation. Significantly, this observation is consistent with previous studies of oceanic basalts (e.g., Marty and Humbert, 1997; Marty and Dauphas, 2003; Fischer et al., 2005), which also suggest that nitrogen isotope variations are independent of degassing and the degree of melting (e.g., Marty and Humbert, 1997).

5.1.4. Contamination with volatiles from the Iceland crust and assimilation of organic material

Now that we can exclude degassing processes as a means of explaining ^{15}N enriched isotope values evident in Icelandic subglacial basalts, we investigate the coupled N- isotope systematics along with elemental ratios involving N_2, in order to assess whether observed co-variations can be explained by crust and/or mantle mixing processes. Enriched δ^{15}N crustal signatures may potentially be generated in Icelandic basalts in two different ways: (i) through the incorporation of deeply recycled oceanic crust (e.g., Hofmann and White, 1982; Marty and Humbert, 1997; Marty and Dauphas, 2003), and/or (ii) by assimilation and/or contamination within existing Iceland crust, acquired during magma emplacement events/eruptions (Marty and Zimmermann, 1999). In the following discussion, we focus on the latter, starting with discussions on the possible nitrogen isotope signature of the Iceland crust.

Although some studies suggest that there is a considerable overlap between mantle δ^{15}N values and bulk δ^{15}N values of the altered oceanic crust (AOC: i.e., δ^{15}N of -5.2%.; Li et al., 2007), such as the Icelandic crust, AOC is generally viewed as being heterogeneous with respect to nitrogen speciation and isotope characteristics (Pinti et al., 2001; Busigny et al., 2005; Li et al., 2007; Busigny et al., 2011; Halama et al., 2012). Indeed, Halama et al., (2012) showed that the AOC displays δ^{15}N value significantly more positive and heterogeneous relative (= -1.2.± 3.7%) to DMM. Thus, there is potential for explaining the range of Iceland δ^{15}N values by assimilation of crustal material during eruption. We also note that Busigny et al. (2005) demonstrated that basalts from Ocean Drilling Program Site 1256, located at the eastern flank of the East Pacific Rise, showed a clear enrichment in nitrogen during the alteration process, with a decrease of $\delta^{15}N$ values with increasing depth. They showed that nitrogen of altered basalts occurs mainly as an ammonium ion (NH_4^+) and is fixed in various secondary minerals (celadonite, K- and Na-feldspars, smectite). These represent typical secondary minerals that have been identified in altered sections of Iceland crust, either in drill-cuts (Mehegan et al., 1982) or in the Tertiary lava pile (e.g., Neuhoff et al., 1999 and 2000). In addition, Busigny et al. (2011) studied ophiolitic meta-gabbros from the western Alps that showed a large range of consistently positive $\delta^{15}N$ values of +0.8 to +8.1‰. The $\delta^{15}N$ values of the metagabbros were shown to correlate with [Cu] (a possible index of hydrothermal alteration), suggesting that leaching of Cu–N compounds, possibly on the form $Cu(NH_3)_2^{2+}$, occurs during hydrothermal alteration.

More recently, Barry et al. (2014) postulated that assimilation of organic material, with low $\delta^{13}C$ signatures in altered Iceland crust, was an important process that generated low $\delta^{13}C$ values (as low as -25‰) in this same sample suite studied here. These authors suggested that the occurrence of organic material within the Iceland crust results from either hydrothermal circulation of organic material (Lang et al., 2006) and/or biological activity during mineralization (Thorseth et al., 1992; Furnes et al., 2001; Fisk et al., 2003). We note that Marty and Humbert (1997) showed that many oceanic basalts with relatively low $^{40}Ar/^{36}Ar$ ratios (<1000) seem to be associated with positive $\delta^{15}N$ values, and proposed that such values reflect contamination of melts by a shallow component enriched in ^{15}N. Seafloor organic matter and sediments have these characteristics and are likely to be found in the Iceland crust. Thus, therefore, there is substantial evidence favoring a predominantly positive $\delta^{15}N$ isotope signature within the Icelandic crust, making shallow level crustal contamination, at least in case of samples with $^4He/^{40}Ar^* < 10$, a viable process for explaining the positive $\delta^{15}N$ signature in Icelandic subglacial basalts.

In **Figure 9b**, we plot $N_2/^{40}Ar^*$ versus $\delta^{15}N$ of the same samples as plotted in **Figure 5.** Estimates for the DMM (138 ± 65: -5 ± 2‰) are indicated by the gray box. Significantly, we note that seven out of eight samples with $N_2/^{40}Ar^*$ ratios > 1000 have positive $\delta^{15}N$ signatures (up to +12‰). Bearing in mind that samples with such high $N_2/^{40}Ar^*$ ratios, generally have $^4He/^{40}Ar^*$ ratios > 10 (**Figure 8b**), which is consistent with a significant loss of volatiles, and thus increased susceptibility to addition of extraneous volatiles, the association of high $\delta^{15}N$ and high $N_2/^{40}Ar^*$ ratios in these samples is thus consistent with admixture of organically-derived nitrogen to the intrinsic mantle nitrogen component.

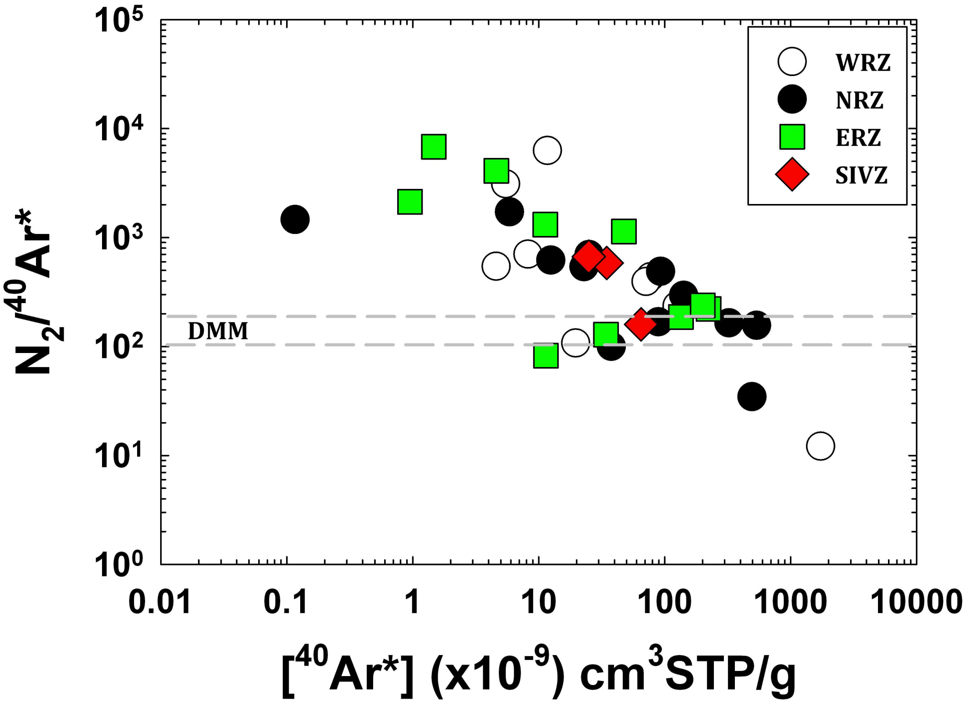

Figure V.10: $N_2/^{40}Ar^*$ ratios versus $[^{40}Ar^*]$ for the same samples as plotted in Figure 5. The DMM range of 138 ± 65 is indicated with the two dashed gray lines. Samples with the highest $N_2/^{40}Ar^*$ ratios (>1000) generally have the lowest $[^{40}Ar^*]$. Such samples become more susceptible to the addition of external volatiles, implying that highly degassed samples have experienced the most significant crustal contamination.

To further test that samples with low volatile concentrations have experienced greater additions of a crustal nitrogen component, in **Figure 10** we plot $N_2/^{40}Ar^*$ ratios versus $[^{40}Ar^*]$ for the same samples as plotted in **Figure 5**. We indicate the DMM range of 138 ± 65, by the gray field. As magmatic degassing should not significantly fractionate N_2 from Ar, any N_2 excess relative to Ar, significantly beyond that DMM range, is likely a result of N_2 addition to initial inventories. Significantly, samples with the highest $N_2/^{40}Ar^*$ ratios (>1000) generally have the lowest [$^{40}Ar^*$]. We also note that the same picture emerges from **Figure 6**, indicating that samples with low [N_2] are associated with high N_2/Ar ratios. As samples with low [$^{40}Ar^*$] and [N_2] are more susceptible to the addition of external volatiles, these observations are consistent with a larger degree of contamination following loss of volatiles via magmatic degassing. Finally, we note, however, that if contamination with shallow-level material during eruption was the only source of ^{15}N enrichment evident in Icelandic subglacial basalts, we would expect to see, a general association of the highest $\delta^{15}N$ values in the lowest [N_2] samples, but no clear relationship is evident between these two parameters (**Figure 5**). In addition, we also note that many samples have $N_2/^{40}Ar^*$ ratios which fall above and below the DMM range, but are inconsistent with a large volatile loss, as evidenced by their $^4He/^{40}Ar^*$ of < 10 (**Figure 8b**).

5.1.5. Summary

In summary, in identifying samples which are likely representative for the Iceland mantle source, we considered coupled $\delta^{15}N$-$^{40}Ar/^{36}Ar$ systematics, and identified a total of 9 samples which have experienced sufficient modification by air-contamination that they are unlikely to reflect primary source features (section 5.1.1.). In addition, we considered possible degassing-induced modification of both elemental (section 5.1.2.) and isotopic (5.1.3.) primary source features. Notably, we have confidence in data integrity of samples with $^4He/^{40}Ar^*$ ratios < 10 only, as samples with $^4He/^{40}Ar^*$ ratios > 10 have modified elemental ratios and isotopic values not representative of their source values. We identified degassing-induced modifications to the primary $N_2/^3He$ ratios in samples with $^4He/^{40}Ar^*$ ratios > 10 whereas no such effect is apparent in the $N_2/^{40}Ar^*$ ratios and $\delta^{15}N$ values. In contrast, $N_2/^{40}Ar^*$ ratios and $\delta^{15}N$ values have experienced significant crustal contamination, but the effect becomes only clear in samples with $^4He/^{40}Ar^*$ ratios > 10 (section 5.1.4.). The remaining samples (n=22) have $^4He/^{40}Ar^* < 10$, suggesting only moderate (<20%) amounts of degassing which we deem to have not extensively modified mantle source characteristics.

5.2. He-N-Ar relationships: evidence for recycled nitrogen in the Iceland mantle source

In the following section, we investigate coupled He-N-Ar elemental and isotope systematics more closely in order to assess whether the ^{15}N enriched crustal component is indeed integrated into the Iceland mantle source, and thus possibly providing information on the nature of recycled material in the deep-mantle. In **Figure 11a**, we plot $N_2/^3He$ versus $\delta^{15}N$ values (only for samples with $^4He/^{40}Ar^* < 10$). We superimpose end-member compositions for DMM ($3.76 \pm 1.17 \times 10^6$; −5 ± 2‰: Marty and Zimmerman, 1999; Marty and Dauphas, 2003a) and a hybrid Iceland mantle plume source that has incorporated a heterogeneous section of recycled crustal material ($1 \pm 6 \times 10^{10}$; +1‰ to +10‰, e.g., Sano et al., 1998; Marty and Dauphas, 2003) that dominates the nitrogen budget of the plume end-member, to assess the possible role of the Iceland plume in supplying recycled volatiles to the surface. Notably, we make the assumption that this recycled crustal material has heterogeneous $\delta^{15}N$ values that vary between +1‰ and +10‰ and, thus incorporates $\delta^{15}N$ values typical of the uppermost section of the subducting slab, i.e., (i) modern organic sedimentary nitrogen (+7 ± 3‰: Peters et al. 1978; Sano et al., 1998; Sano et al., 2001; Halama et al., 2012) , (ii) subduction-related metasediments (+3.2 ± 2.1‰; Halama et al., 2012), (iii) metamorphosed oceanic crust (+4.5 ± 2.1‰; Halama et al., 2010; 2012), and (iv) values proposed to characterize the recycled component evident at many OIB localities (+3 ± 2‰; Marty & Dauphas, 2003a).

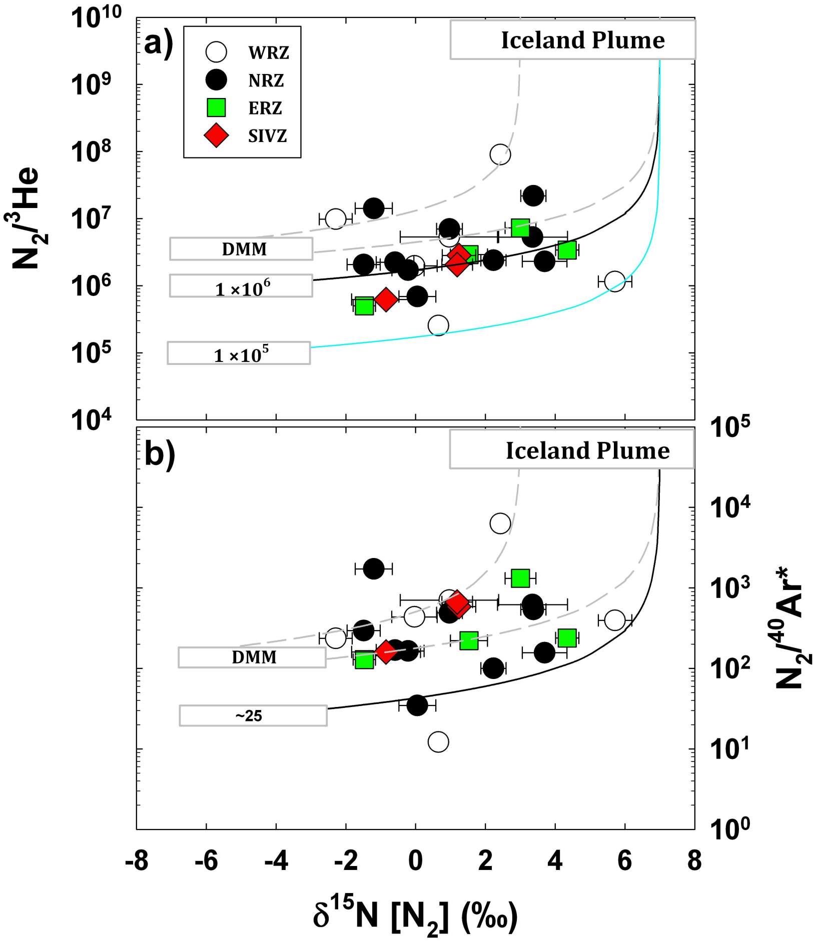

Figure V.11: Plot of (a) $N_2/^3He$ and (b) $N_2/^{40}Ar^*$ ratios versus $\delta^{15}N$ values. Only samples with $^4He/^{40}Ar^* < 10$ are plotted. In (a), two end-member compositions are indicated: for DMM ($3.76 \pm 1.17 \times 10^6$; −5 ± 2‰) and a hybrid Iceland mantle plume source that has incorporated a heterogeneous section of recycled crustal material ($1 \pm 6 \times 10^{10}$; +1‰ to +10‰). Binary mixing trajectories between these end-member compositions are shown with the two dashed gray lines, taking the uncertainties of end-member compositions into account. A binary mixing trajectory from a lower $N_2/^3He$ end-member ($\sim 1 \times 10^6$) is shown with a solid black line whereas a binary mixing curve involving an even lower $N_2/^3He$ end-member ($\sim 1 \times 10^5$) is shown with the cyan colored solid line. In (b), the DMM end-member (138 ± 65; −5 ± 2‰) and a hybrid Iceland mantle plume source ($1 \pm 6 \times 10^5$; +1‰ to +10‰) are indicated with gray boxes. Taking the uncertainty of end-member compositions into account, binary mixing trajectories between these end-member compositions are shown with the two dashed gray lines, whereas binary mixing involving a lower $N_2/^{40}Ar^*$ of 25, is shown with a solid black line. Significantly, data are consistent with binary mixing involving a heterogeneous recycled nitrogen component.

However, binary mixing between these two components, DMM and a hybrid Iceland plume, is capable of explaining only a small subset of the coupled $\delta^{15}N$-$N_2/^3He$ systematics of the

Icelandic subglacial basalts. Even if the uncertainty associated with the mean value reported for DMM ($3.76 \pm 1.17 \times 10^6$) is considered when constructing the binary mixing lines, a better fit to the data is not obtained. Notably, however, most samples are consistent with binary mixing, but not towards the DMM end-member. Rather, an end-member $N_2/^3He$ ratio of ~1 ($\times 10^6$), a ratio similar to uncorrected mean values of DMM (Marty and Zimmerman, 1999), provides a better fit as it incorporates a larger set of samples. We also note that two samples from the WRZ require an even lower $N_2/^3He$ ratio in the DMM end-member of ~1 ($\times 10^5$), and also highlight heterogeneous $\delta^{15}N$ values in the recycled end-member (up to +7‰). Significantly, irrespective of the actual value of the $N_2/^3He$ end-member, the data imply binary mixing with a component that has high $N_2/^3He$ ratios (at least $>1\times 10^8$) and heterogeneous $\delta^{15}N$ values (i.e., that lie at least between +3 to +7‰). Such a component is similar to recycled N from modern subducted sedimentary material and metamorphosed oceanic crust (e.g., Sano et al., 1998; Marty & Dauphas, 2003a; Halama et al., 2010; 2012).

In **Figure 11b**, we plot $N_2/^{40}Ar^*$ versus $\delta^{15}N$ of the same samples as in **Figure 11a** (i.e., samples with $^4He/^{40}Ar^* < 10$), to avoid samples affected by admixture with shallow level crustal material. Again, we superimpose two possible end-member compositions for DMM (138 ± 65; −5 ± 2‰: Marty and Zimmerman, 1999; Marty and Dauphas, 2003a) and a hybrid Iceland mantle plume source ($1 \pm 6 \times 10^5$; +1‰ to +10‰). Note that the $N_2/^{40}Ar^*$ value we adopt for the crustal component is somewhat higher than the highest N_2/Ar (total Ar) ratio of 21,000 reported for oceanic sediment (e.g., Matsuo et al., 1978). This is because oceanic sediments are likely to contain air-derived argon that would lower the N_2/Ar. The $\delta^{15}N$- $N_2/^{40}Ar^*$ systematics of the Icelandic subglacial basalts are consistent with binary mixing between DMM and a hybrid Iceland mantle plume source. We note that relative to the $\delta^{15}N$-$N_2/^3He$ systematics (**Figure 11a**), the DMM end-member provides a significantly better fit to the calculated mixing trajectories (taking the uncertainty of the mean $N_2/^{40}Ar^*$ ratio into account), with only 6 samples falling below the binary mixing trajectory. Five of these samples can be explained by adopting a $N_2/^{40}Ar^*$ ~25 for the DMM end-member, whereas one sample may have an even lower $N_2/^{40}Ar^*$ ratio in the mantle end-member (~10). Significantly, samples that fall below the DMM estimates clearly highlight heterogeneous $\delta^{15}N$ values in the recycled end-member.

Finally, we note that, in general, the $\delta^{15}N$-$N_2/^{3}He$ systematics show more scatter relative to the $\delta^{15}N$- $N_2/^{40}Ar^*$ systematics, and the need for variable mantle (DMM-like) end-members is more problematic for the former. This observation can be explained taking into account that He is more readily fractionated from N_2 than N_2 from Ar, and deep-level fractionation event(s) due to melting and/or solubility controlled fractionation, (e.g., Moreira & Sarda, 2000; Sarda & Moreira, 2002; Füri et al., 2010), are more likely to have occurred. In this respect, **Figure 11b** illustrates the robustness of the $N_2/^{40}Ar^*$ ratio to constrain mantle end-members.

In **Figure 12**, we plot helium isotopes ($^{3}He/^{4}He$) versus $\delta^{15}N$ values to test possible relationships between high $^{3}He/^{4}He$ mantle material in the Iceland plume and $\delta^{15}N$ values. For regional comparison, we include seven samples from the Reykjanes Ridge reported by Barry et al. (2012), helium data by Hilton et al., 2000 and argon data by de Leeuw (2007). These samples all display $^{40}Ar/^{36}Ar$ ratios significantly higher than air, and when available (6 out of 7 samples), also have $^{4}He/^{40}Ar^*$ ratios < 10. We propose possible end-member components: DMM (8 ± $1R_A$; -5 ± 2‰) and a hybrid Iceland plume with a $^{3}He/^{4}He$ ratio of 37 ± $2R_A$ (Hilton et al., 1999), assuming that it has entrained a heterogeneous recycled crustal component, with $\delta^{15}N$ values between +1‰ and +10‰, that dominates the nitrogen budget.

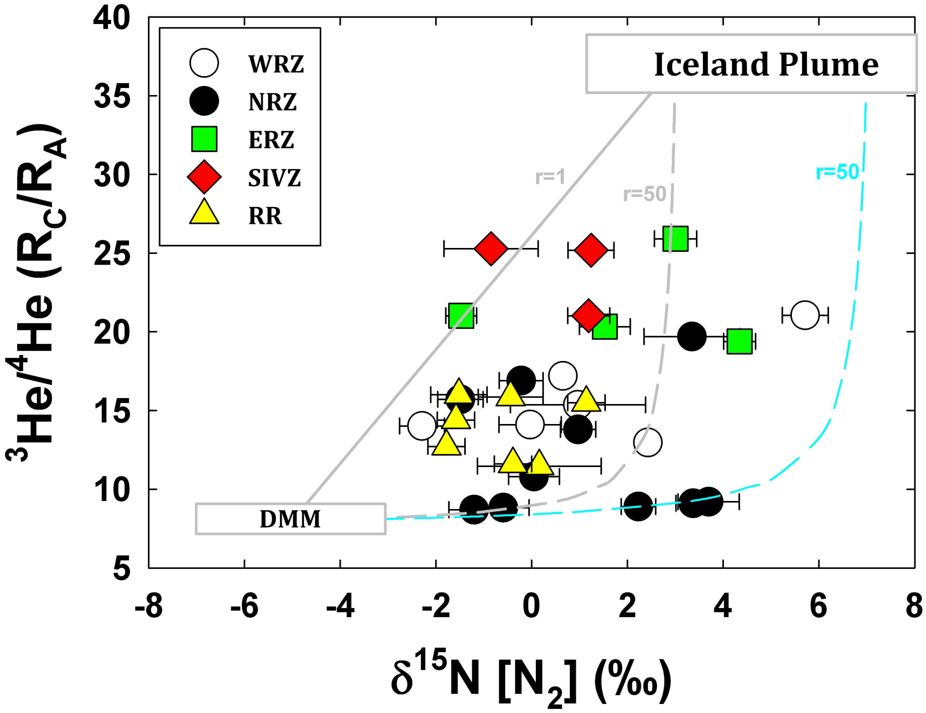

Figure V.12: Helium isotopes ($^3He/^4He$) versus $\delta^{15}N$ values for the same samples plotted in Figure 11. Also plotted are data from the Reykjanes Ridge reported by Barry et al. (2012). Possible end-member components of DMM (8 ± 1R_A; -5 ± 2‰) and a hybrid Iceland plume with a $^3He/^4He$ ratio of 37 ± 2R_A and $\delta^{15}N$ values between +1‰ and +10‰ are shown. Binary mixing trajectories between DMM and a recycled/plume hybrid component evident at many OIB localities (i.e., $\delta^{15}N$ = +3 ± 2‰; Marty & Dauphas, 2003a) are shown with gray mixing lines and binary mixing between DMM and modern organic sediments with $\delta^{15}N$ values of +7 (e.g., Peters et al., 1978; Kienast et al., 2000; Halama et al., 2012) is shown with the cyan mixing line. The relative N/He ratios between plume and DMM components is expressed as r-values (where r = $(N/He)_{PLUME}/(N/He)_{DMM}$). See text for details.

There are two notable features of this plot. First, a model of binary mixing (gray mixing lines) between DMM and a recycled component evident at many OIB localities (i.e., $\delta^{15}N$ = +3 ± 2‰; Marty & Dauphas, 2003a) readily explains the coupled $\delta^{15}N$-$^3He/^4He$ systematics of most samples. The relative N/He ratios between plume and DMM components are expressed as r-values (where r = $(N/He)_{PLUME}/(N/He)_{DMM}$). R-values between 1 and 50 thus indicate that the plume end-member is characterized by a marked enrichment in its N/He ratio relative to the DMM end-member, consistent with the enrichment of nitrogen and/or depletion of helium in the plume source. Second, three samples from the NRZ, in addition to 1 sample from the WRZ and ERZ that plot to the right of mixing trajectory with r=50, are inconsistent with binary mixing between DMM and the common OIB component, and require an end-member with $\delta^{15}N$ up to ~ +7 to reasonably fit these samples (cyan mixing lines). Notably, r-values in such a binary mixing scenario (r=50) are similar to r-values in a mixing scenario involving the common OIB component with +3 ± 2‰ (Marty & Dauphas, 2003a), implying similar nitrogen enrichments and/or helium depletions in the plume source relative to DMM-Plume mixing scenario when adopting a value of +3 ± 2‰. Significantly, r-values > 1 for both scenarios, indicate that the high $^3He/^4He$ signature may in fact be coupled with a high $\delta^{15}N$ end-member that has either i) lost He before mixing with the MORB end-member, similar to the two-step model of He depletion followed by open-system degassing developed by Füri et al. (2010), and/or ii) excess N_2.

In summary, we conclude that the high $\delta^{15}N$ end-member required in order to explain these mixing relationships strongly indicates that the ^{15}N enriched crustal component is integrated into the Iceland mantle source – implying that in addition to supplying primordial volatiles, the deep-seated Icelandic mantle plume also supplies recycled volatiles back to the surface.

5.3. Origin of high $N_2/^{40}Ar^*$ ratios in the Iceland mantle source

A key observation of the present dataset is the fact that $N_2/^{40}Ar^*$ ratios in Icelandic subglacial basalts (459 ± 194; **Figure 11b**) are not only considerably more heterogeneous, but also significantly higher, than DMM (138 ± 65) and OIB (137 ± 24) (Marty and Humbert, 1997; Marty and Zimmermann 1999; Marty & Dauphas, 2003a). Even after applying a robust filtering protocol to obtain values representative for the Iceland mantle source (i.e., section 5.1), the $N_2/^{40}Ar^*$ ratios vary from 100 to 1721 with a mean value of 459 (excluding three outliner values of 12, 35 and 6300). High $N_2/^{40}Ar^*$ ratios of the Icelandic melts relative to the DMM and OIB source may result from:

(i) The complex speciation of nitrogen in melts under high pressure and the possible presence of nitrogen species that are more compatible than Ar (Roskosz et al. 2006). For example, nitrides are probably the main speciation of nitrogen under very reducing conditions, whereas nitrosyl (NO) dominates under more oxidizing conditions (Roskosz et al. 2006). Additionally, recent solubility studies of nitrogen in upper-mantle minerals suggest that the reduced lower part of the upper mantle has a large nitrogen storage capacity, and that, under such reduced conditions, a significant fraction of nitrogen may still be retained following melt extraction (Lee et al., 2013). Extensive melt extraction, from the reduced upper-mantle under Iceland, would thus generate higher $N_2/^{40}Ar^*$ ratios relative to DMM and OIB. However, in contrast to observations from other OIB that display much lower $N_2/^{40}Ar^*$ ratios, such high ratios should also be present at other oceanic hotspots. Unless melting dynamics under Iceland are notably different in comparison with other oceanic hotspot, the idea that mantle-melting involving nitrogen components more compatible than Ar in the upper mantle can explain high $N_2/^{40}Ar^*$ ratios, seems unlikely.

(ii) Contributions from nitrogen in the core to the nitrogen inventory of the lower-mantle. The notion is based on the fact that nitrogen is slightly-to-moderately siderophile at high pressure and temperature whereas Ar is not, and recent metal/silicate nitrogen partitioning experiments suggest that some nitrogen can be sequestrated into the core (Roskosz et al. 2013). If trapped nitrogen interacts with the lower-mantle (e.g., via diffusion as proposed by Hayden & Watson, 2007), it can become entrained by an uprising mantle plume, leading to a high $N_2/^{40}Ar^*$ relative to the DMM. However, direct core contributions to Icelandic magmatism remains unlikely at present given the near uniform $^{186}Os/^{188}Os$ ratio evident in Icelandic picrites (Brandon et al., 2007). Instead, observed $^{187}Os/^{188}Os$ are best explained by incorporation of recycled crust into the Icelandic mantle (Brandon et al., 2007; Sobolev et al., 2008).

(iii) Short residence time of the recycled material in the Iceland mantle source. The low $N_2/^{40}Ar^*$ ratios (<DMM) that characterize many E-MORB as well as OIB, have led to suggestions that link $N_2/^{40}Ar^*$ ratios < DMM to extreme potassium recycling and the mantle residence time of the recycled material and subsequent radiogenic in-growth of ^{40}Ar on a 10^8–10^9 year timescale (Marty and Humbert, 1997; Nishio et al., 1999; Marty and Zimmermann, 1999). This age is largely consistent with the enrichment of radiogenic isotope in E-MORB and OIB that suggest the involvement of recycled components in the source of such regions. In the case of Iceland, extreme $N_2/^{40}Ar^*$, relative to other OIB localities, suggest that the recycled component in Iceland is significantly younger (< 10^9) than recycled components evident elsewhere.

Thus, high $N_2/^{40}Ar^*$ values, in addition to positive $\delta^{15}N$ values that are evidently integrated into the Iceland plume source, have important implications for constraining the age of the recycled component. As discussed above, Marty and Dauphas (2003a) developed ideas on the recycling of post-Archean material (< Proterozoic) from the surface to the deep mantle and proposed that nitrogen in mantle plumes is largely recycled from the surface of the Earth in the form of N_2 rich sedimentary material. A key argument in their discussion was that N isotopic composition of OIB provides a good fit to that of organic matter evident in post-Archean sediments, metamorphic rocks, and subduction-related volcanic rocks. Crustal material from the Archean is not a viable candidate for sourcing nitrogen to mantle plumes as its isotopic composition is not sufficiently enriched (due to the lack of oxygen in the Archean atmosphere). However, such material may potentially supply nitrogen to the upper-mantle – hence the depleted $\delta^{15}N$ value of the DMM source – as the warm and young slabs that dominated plate tectonics in the Archean are more likely to be found in the upper-mantle (Marty & Dauphas, 2003a). In contrast, the old, cold, and nitrogen isotopically enriched slabs that predominate at present are more likely to be subducted to the deep mantle. Significantly, we note that the combination of high $N_2/^{40}Ar^*$ and positive $\delta^{15}N$ values in the Iceland mantle source, which are associated with high $^3He/^4He$ ratios (**Figure 12**), is thus consistent with deep subduction of post-Archean sediments.

5.4. Recycling of Phanerozoic oceanic crust: constraints from other isotope systems

Additional constraints on the age of the recycled crustal material entrained by the Icelandic mantle plume are also available by considering radiogenic isotopes. On the basis of trace elements and radiogenic isotopes, Chauvel and Hemond (2000), and later, Kokfelt et al (2006), proposed that the full compositional spectrum of Icelandic melts was generated through recycling a complete section of oceanic crust entrained into the Icelandic plume. Skovgaard et al. (2001) presented coupled O-Os isotope data to argue for the presence of recycled oceanic lithosphere in the source of lavas from the Theistareykir region, and ocean crust recycling was also favored in the studies of Hanan and Schilling (1997), Hanan et al., (2000), Kempton et al. (2000), Fitton et al. (2003), Stracke et al. (2003), McKenzie et al., (2004), Macpherson et al. (2005) and Magna et al., (2010).

Significantly, Thirlwall et al. (2004) demonstrated that negative $\Delta^{207}Pb$ values (deviation of $^{207}Pb/^{204}Pb$ for a given $^{206}Pb/^{204}Pb$ relative to the Northern Hemisphere Reference Line) associated with DMM-like compositions, characterize many Icelandic lavas, and proposed that such signatures are likely to have formed in a mantle component with higher U/Pb ratio relative to the DMM at a time as recent as ~170 Ma ago, but not earlier than ~450 Ma ago. Iceland is thus a case example of a young HIMU (high-μ) mantle source (e.g., Thirlwall, 1995; 1997). Negative $\Delta^{207}Pb$ in Iceland lavas thus bear witness to involvement of Palaeozoic oceanic crust initially heterogeneous in Pb isotopes. Notably, the region of negative $\Delta^{207}Pb$ appears to correspond with the entire region between 56°N and 70°N (Thirlwall et al., 2004), which is associated with elevated ^{3}He/^{4}He ratios (e.g., Füri et al., 2010) and to some extent, low δ^{18}O values (e.g., Gautason &Muehlenbachs, 1998; Macpherson et al., 2005; Thirlwall et al., 2006). Thus, melts in this whole region of the North-Atlantic are predominantly sourced from a mantle plume source that has incorporated relatively young (i.e., Palaeozoic) recycled oceanic crust and primordial ^{3}He from the deep mantle (Thirlwall et al., 2004). Peate et al., (2010) and Manning and Thirlwall (2014) have also shown that lavas from the Öræfajökull volcano in southern Iceland display positive Δ^{207}Pb that are consistent with small (~0.5%) contributions of recycled sediment in mantle source under Öræfajökull.

In contrast, Kokfelt et al. (2006) proposed that recycled lithosphere with the older age of ~1.5 Ga could account for the Pb isotopic signatures of neovolcanic zone lavas - consistent with Os isotope studies, which suggest a recycled component of < 2 Ga, but possibly as young as 750 Ma (Brandon et al., 2007; Sobolev et al., 2008). We note, however, the Os-studies so far have been mainly directed at two localities – the Reykjanes Peninsula and Theistareykir – they both show the most depleted Pb isotope compositions (e.g., Stracke et al., 2003; Thirlwall et al., 2004), consistent with derivation from the oldest part of the Iceland mantle source. In addition, Re-Os isotope decay model ages are highly dependent on the initial Re/Os ratio of the subducted crust, which remains poorly constrained due to the high mobility of Re during subduction (e.g., Sun et al., 2004). In any case, radiogenic isotopes constrain the age of the recycled component incorporated by the Iceland mantle plume to be (significantly) less than 2 Ga, and possibly as young as 170 Ma, likely pointing to a Phanerozoic age (<541 Ma).

Significantly, the extreme $N_2/^{40}Ar^*$ ratios in the Iceland mantle source relative to other OIB are consistent with the age of the recycled component being significantly younger (at least < 10^9 yr) than recycled component samples from other oceanic hotspot (10^8–10^9 yr). Thus, we favor a Phanerozoic age (<541 Ma) of the recycled component, but note that the Pb isotope models presented by Thirlwall et al. (2004) may possibly constrain the age of this component further to the Palaeozoic era (252 to 541 Ma). In this respect, we point out that in order to account for highly radiogenic ^{87}Sr/^{86}Sr ratios in Hawaiian ultra-depleted melt inclusions, Sobolev et al. (2011) proposed a similar model, involving the recycling of a (young) Phanerozoic (200–550 Myr) oceanic crust. Such a young age for the recycled component in the Hawaiian mantle source significantly predates previous estimates for deep mantle plumes, and indicates a considerably faster mantle circulation timescales, assuming that the subducted crust was delivered to the core–mantle boundary and recycled back to the surface via the Hawaiian mantle plume.

Finally, we note that a major tectonic event, which inevitably affected the upper-mantle structure in the North-Atlantic during the Phanerozoic, was the closure of the Iapetus Ocean by convergence of the protocontinents of Laurentia, Baltica, and Avalonia, between 500 to 400 Ma (e.g., Barker & Geyer, 1984; Bott, 1985; Soper et al., 1992). Evidence for the presence of this ancient subduction system present today in the Caledonian collision zone (i.e., suture) that represents a broad zone of compression found in east Greenland, Scandinavia, Britain, Europe, and Newfoundland (Barker & Geyer, 1984). It thus remains a possibility that recycled crustal components evident in Icelandic melts, have a shallow origin which is mostly confined to the upper-mantle. In this respect, the coupled δ^{15}N-^{3}He/^{4}He systematics would then favor a model involving remobilization of the entrained upper-mantle material by an uprising Iceland mantle plume whose roots may be as deep as the core-mantle boundary (e.g., Helmberger et al., 1997). Future work on these samples, involving radiogenic isotope characterization (Sr-Nd-Hf-Os-Pb) and sulfur isotopes (e.g., ^{33}S), will help to further constrain the age and nature of this recycled component.

Conclusions

Based on the N-Ar-He relative abundance and isotope systematics of subglacial basaltic glasses, we emphasize the following points:

☐ Nitrogen isotopes in subglacial basalts from Iceland span a large range of $\delta^{15}N$ values from -2.91 to +11.96‰ that are generally more positive than values obtained from DMM and largely overlap with $\delta^{15}N$ values obtained from OIB worldwide.

☐ We see no evidence for degassing induced isotopic fractionation of $\delta^{15}N$.

☐ Samples with strong ancillary evidence for degassing show evidence of significant crustal contribution to the nitrogen elemental ($N_2/^{40}Ar^*$) and isotope systematics.

☐ Coupled isotope and relative abundance systematics suggest that a recycled nitrogen component is present in the Icelandic mantle.

☐ We propose that the Iceland mantle plume has incorporated the uppermost section of subducted oceanic crust, whose age may possibly be as young as Phanerozoic as constrained by the combination of positive $\delta^{15}N$ values, radiogenic isotopes (e.g., Pb), and very high $N_2/^{40}Ar^*$ relative to other OIB. This implies a relatively short mantle-residence time for this recycled material.

Acknowledgements

This work was supported by NSF grants EAR-0439122 and EAR-0537618. SAH thanks Ólafur Patrick Ólafsson for assistance in part of the sample collection, Guðrún Sverrisdóttir for providing samples from the Hekla region and Níels Óskarsson for discussions.

Supplementary Material

Sample details

All the subglacial basaltic glasses of this study, belong to the so-called Móberg formation (e.g., Jakobsson and Gudmundsson, 2008) - a general term for Icelandic volcanic rocks formed in single vent and/or fissure eruptions during the Brunhes geomagnetic epoch at the end of the

Pleistocene (0.78–0.01 Ma) (Jóhannesson and Sæmundsson, 1998). We note that most samples are fresh (i.e., free of any surficial alteration), which suggests relatively young formation ages within the epoch. This is consistent with observations in the field, as well as cosmogenic exposure ages (Licciardi et al., 2007) that indicate formation during the last deglaciation. All samples are tholeiitic in composition and only those from the volcanic flank zones (i.e., TRÍ-1, TRÍ-2, TRÍ-3, BHE-43 and BHE-44) are transitional-alkalic to alkali in composition. Additional studies on the major and trace elements chemistry, in addition to radiogenic isotope characteristics on this suite of samples, are currently underway.

$N_2/^{40}Ar^*$ ratios of the DMM, OIB and the Iceland reservoirs

In order to estimate a representative $N_2/^{40}Ar^*$ ratio of the DMM reservoir, we calculated and compiled $N_2/^{40}Ar^*$ ratios using N-Ar data reported by Marty and Zimmermann (1999) and Marty and Humbert (1997). By adopting the same filtering protocols (i.e., using only samples with $^{40}Ar/^{36}Ar > 1000$), as described by Marty and Zimmermann (1999), and by only considering values with He isotope ratios that are within the canonical DMM range 8 ± $1R_A$, we obtained a value of 138 ± 65 (n=28: 2standard error; $2\sigma/n^{1/2}$, where n is the number of values) for the $N_2/^{40}Ar^*$ ratio of DMM. Notably, only slightly lower $N_2/^{40}Ar^*$ ratios are obtained for the DMM reservoir when using the few reported samples with $^{4}He/^{40}Ar^* < 10$, or 122 ± 39 (n=7), which is in good agreement with the N_2/Ar (total argon) value of 124 ± 40 reported for all MORB types by Marty and Zimmermann (1999). Considering only samples with $^{40}Ar/^{36}Ar > 1000$ we obtained a value of 137 ± 24 (n= 27) for the OIB reservoir using data reported by Marty and Zimmermann (1999), Marty and Humbert (1997) and Marty and Dauphas (2003a). Finally, we calculated an average $N_2/^{40}Ar^*$ ratio for Icelandic subglacial basalts of 459 ± 194(n=19) considering only samples with $^{4}He/^{40}Ar^* < 10$. This value is both considerably more heterogeneous and significantly higher than estimates for both the DMM and OIB reservoirs.

Additional stable isotope fractionation models

Additional stable isotope fractionation models such as species- (i.e., solubility-) (e.g., Mysen & Fogel, 2010) and/or diffusion- (i.e., kinetic-) (see below and e.g., Yokochi et al., 2009; Pinti & Hashizume, 2010; Roulleau et al., 2012) induced isotopic fractionation have also been proposed as means of modifying nitrogen isotope characteristics.

Species-induced isotopic fractionation

In the former case, changing abundance of volatile species, such as N_2 and NH_3 (the two major nitrogen-bearing species), dissolved in silicate melts in molecular form and as structural complexes, respectively, may potentially affect stable isotope fractionation during melting and crystallization at high pressure and temperature (Mysen et al., 2008; Mysen & Fogel, 2010). In this case, we note that in fluids of the relatively oxidized upper mantle (e.g., 30-35 kbar = 90-105 km), nitrogen is mostly is the form of N_2, while in the deeper, and more reduced parts of the upper mantle (beyond 60 kbar = 180 km), NH_3 is the dominant nitrogen species (Brandes et al., 1998; Li et al., 2013; Li and Keppler, 2014). Thus, any interpretation of the nitrogen isotope values of melts formed at depths in the oxidized upper mantle should take into account that most of the nitrogen was present as NH_3. However, the isotope fractionation factor (Δ_i) of $\delta^{15}N$ between NH_3 and N_2 is about -1‰ (i.e., $\Delta_i = \delta^{15}N_{NH3} - \delta^{15}N_{N2}$) at 1200°C (Richet et al., 1977), so it is unlikely that even the complete decomposition of NH_3 to N_2 and H_2 in the upper-mantle, can explain highly positive $\delta^{15}N$ values in Icelandic melts.

In addition, provided that the mantle solidus under Iceland is neither particularly wet and/or carbonated, it remains unlikely, at present, that Icelandic melts are formed at such great depth, with the base of the melting region under Iceland generally assumed to be located ≥ 100 km but generally no deeper than ~ 120 km (Maclennan et al., 2001). This view, however, has been challenged by experimental work (Eggler, 1976; Gudfinnson and Presnal, 2005; Dasgupta & Hirschmann 2006; Dasgupta et al. 2007 and 2013) that demonstrates that wet and/or carbonated peridotite may cause the onset of silicate melting for a sub-ridge mantle to occur as deep as 220–300 km – consistent with some geophysical observations for oceanic ridges, such as the presence of the oceanic low-velocity zone and the electrical conductivity structure of the mantle. It is, therefore likely that the presence of small amounts of water and/or carbon in the mantle beneath Iceland may generate small melt fractions (e.g., carbonate melts) at depths several tens of km greater than that of the anhydrous solidus. At such depths, NH_3 is the dominant nitrogen species, but it partially decomposes to N_2 and H_2 at shallower depths.

Diffusion-induced isotopic fractionation

Regarding diffusion- (i.e., kinetic-) induced isotopic fractionation as a result of more rapid diffusion of ^{14}N relative to ^{15}N, we note that some of the available models have been applied to an apparent concentration gradient involving diffusion between fluid inclusions in xenoliths and/or phenocrysts and their host magma (Yokochi et al., 2009; Roulleau et al., 2012). Diffusion is always driven by concentration gradients and given that basaltic glasses can be regarded as a relatively homogenous transport medium of N_2, large concentration gradients are unlikely.

However, we also note that diffusion of the lighter isotope (^{14}N) across the glass-vesicle interface during vesiculation is also a possible process capable of enriching ^{15}N in the melt phase. In this case, vesicles will have lower $\delta^{15}N$ values relative to the initial $\delta^{15}N$ value of the melt before any vesiculation. Although, experimental confirmation of this behavior warrants further studies, we note that such a mechanism is highly dependent on the melt-vesicle equilibrium partitioning, i.e., how much of the initial N goes into the vesicles phase from the melt phase.

However, several studies (e.g., Marty et al., 1983; Jambon et al., 1986; Marty and Zimmermann, 1999) have shown that the partitioning of argon (and thus also nitrogen) between vesicles and melt, generally follows Henry's law, and for vesicularities relevant to MORB glasses, Ar (and N) should be dominantly found in the vesicle phase. Marty and Zimmermann (1999) also argued that additional nitrogen components evident in the melt phase, and recovered by heating (e.g., Exley et al., 1986), is unlikely to result from melt-vesicle equilibrium partitioning and necessitates a secondary contribution from externally-derived nitrogen. They presented measurements of $\delta^{15}N$ values of the melt phase that displayed distinctly more positive $\delta^{15}N$ relative to the dominantly negative values in the vesicle phase and argued that nitrogen extracted by melting was dominated by surficially-derived nitrogen – thus highlighting the robustness of extraction by crushing to reveal a more representative picture of magmatic volatile components (Marty and Zimmermann, 1999).

Chapter VI: Concluding Remarks

I have discussed ways to address and understand processes that influence magmatic volatile characteristics in Earth. By systematically identifying and correcting for these processes, we can better constrain magmatic volatile source characteristics at convergent and divergent plate boundaries. Itook examples from three different tectonic settings: (i) Indonesia, (ii) the East African Rift System and (iii) Iceland. Below, we will briefly summarize the main findings of each of these studies.

Chapter II investigated the He-CO_2-N_2 isotope and abundance characteristics, supplemented with major gas chemistry on selected samples, of active fumaroles, and hydrothermal gases/waters from the western Sunda arc, Indonesia. Although the dry gas chemistry was typical of subduction zone gases, we noted a strong crustal control on the He-CO_2 isotope and relative abundance systematics on a number of volcanic centers, most clearly at flank localities but also in water phase samples associated with active fault systems in between volcanic centers (IBVC). We adopted a robust filtering approach to identify samples whose volatile characteristics have been modified by means of several processes, generally at shallow-level, that take place within hydrothermal systems associated with volcanic activity. This allowed us to characterize magmatic signatures of individual volcanoes along the arc. Helium isotopes are generally consistent with the mantle wedge being the principal source of He, but we noted a significant input of crustal He and carbon at some localities on Sumatra, particularly at the IBVC sites, whereas samples from Java and Bali suggest a smaller input of crustal He. However, on the basis of coupled CH_4 and ^{3}He relationships, we suggested that the over-riding crust and associated sediments add minimal volatiles to volcanic centers throughout the western Sunda arc. Rather, we proposed that subducted sediment exerts a strong control on the magmatic CO_2 characteristics, although it is less influential for N_2. This was supported by carbon systematics along the western Sunda arc that displayed higher and more variable values to the north of Sumatra where such an effect is not apparent in nitrogen systematics. The latitudinal effect is consistent with the presence of the Nicobar Fan which supplies Himalayan-derived sediment to the slab off Sumatra. Finally, we concluded that subduction-related source contamination must play a dominant role relative to basement rocks in supplying the major volatile output budget of the western Sunda arc.

Chapter III reported a comprehensive He, Ne, and Ar relative abundance and isotope dataset of mantle-derived xenoliths and lavas from different segments of the EARS. This dataset, composed of over 100 new He and over 50 new Ne-Ar isotope analyses from the entire EARS, was the first attempt to explore neon isotopes along the EARS, in order to address the question as to whether one or more mantle plumes impinge the upper-mantle below East Africa. The neon isotopes revealed distinct Ne-isotope anomalies relative to DMM. Most notably, we demonstrated that a number of samples associated with the Ethiopian Rift overlap some well defined OIB trajectories, consistent with a solar-Ne component in the East African mantle source. In addition, we considered coupled He-Ne systematics, and showed that they are best explained by binary mixing between a single mantle plume source, best represented by the African Superplume, which would be common to the entire EARS, and either a DMM or a SCLM source. Moreover, we evaluated noble gas elemental ratios to place further constraints on mantle end-members involved in EARS petrogenesis. In agreement with observations from oceanic hotspots, we suggested that the African Superplume source is characterized by low ^{3}He/^{22}Ne$_{S}$ ratios. The similarity in He/Ne ratios between EARS samples from our study and many OIB that display high ^{3}He/^{4}He ratios, prompted us to propose that such a feature represents a deep-seated plume component that has preserved ^{3}He/^{22}Ne ratios distinct from the upper-mantle, and which currently supplies the EARS with primitive volatile components. We discussed some implications of our new dataset for EARS magmatism, concluding that a model involving a common mantle-plume source underlying the entire EARS effectively rules out other plume models that advocate either different styles of mantle convection along the EARS or multiple plumes impinging the African lithosphere, such as an oceanic HIMU-type mantle plume to explain low $^3He/^4He$ ratios evident in the Kenya rifts. Finally, our model shows that the SCLM plays the key role in generating the low $^3He/^4He$ ratios along the EARS, effectively ruling out DMM involvement in petrogenesis in the region surrounding the Kenya Dome.

Chapter IV considered the relative abundances and isotope systematics of He, CO_2, N_2, and Ar trapped within fluid inclusions of mantle xenoliths from the EARS. We also reported new oxygen isotope data on the mafic crystals hosting the fluid inclusions. In total, we examined 26 xenoliths from 9 localities along the strike of the EARS. All data were obtained using *in vacuo* crushing techniques, whereas most data thus far have been produced using stepwise heating that, at least in case of nitrogen, can be biased due to analytical problems associated with the heating of samples. We showed that volatile components trapped in xenolith fluid inclusions generally represent unmodified mantle source features. As there is extensive evidence for recycled material in the source of EARS magmatism, we explored the co-variation of stable isotopes and elemental ratios involving ^3He to investigate the nature of the source material of trapped volatile components to ascertain if there was evidence in the volatile record for recycled material. We showed that the trapped volatile components are consistent with metasomatic enrichment(s) of the East African SCLM by CO_2-rich mantle fluids. Low $\delta^{18}O$ values of crystals hosting the fluid inclusions relative to DMM closely resemble $\delta^{18}O$ values previously obtained from southern African eclogites which are commonly ascribed to disrupted fragments of hydrothermally altered subducted oceanic crust/lithosphere. The combination of $\delta^{13}C$ and $\delta^{15}N$ values significantly higher than DMM, in addition to low $\delta^{18}O$ values, strongly suggests a subducted origin of metasomatic melts and reinforces the link between the metasomatic fluids and subducted slab fluids. The nature of the metasomatic melts was further explored using elemental abundance systematics involving the ratio of $CO_2/^{40}Ar^*$. We suggested that carbonate-melts, in addition to silicate melts, are pervasive throughout the East African upper- mantle. Significantly, we emphasized that xenoliths with high $^3He/^4He$ ratios from the northern Ethiopian Rift show the closest association with such recycled carbonate-melts. Based on these results, we concluded that the deep-seated African Superplume supplies the EARS with a mixture of primordial and recycled volatiles. Finally, we showed that recycled volatile components have a strong association with pyroxenite xenoliths, pointing to a link between the formation of a pyroxenite-hybrid mantle source and recycled volatiles from the African Superplume.

Chapter V described the nitrogen (N_2) abundance and isotope ($\delta^{15}N$) systematics of subglacial basaltic glasses collected from the neovolcanic zones of Iceland. We showed that basaltic glasses with sufficient [N_2] (> 3 μcm^{3}STP/g), span a large range in $\delta^{15}N$ values: from -2.91 to +11.96‰. However, we noted that $\delta^{15}N$ values > 6‰ are only observed at one locality. Elemental ratios (i.e. $N_2/^3He$, and $N_2/^{40}Ar^*$) also showed a wide range and span several orders of magnitude. We carried out detailed evaluation of several processes that are likely to have played a role in modified original mantle source compositions. We considered processes such as air interaction, degassing-induced fractionation of elemental ratios and isotope values, but noted that contamination with volatiles from the Iceland crust, most significantly the assimilation of organic material, was instrumental in modifying the intrinsic mantle characteristics. We demonstrated that the approach of considering coupled N-Ar isotope and relative abundance chacteristics ($N_2/^{40}Ar^*$; $\delta^{15}N$; $^4He/^{40}Ar^*$) provided a very powerful tool with which to identify (and remove) highly degassed and thus modified samples. In contrast to He isotopes, where a clear distinction between individual rift segments is observed, there appears to be little to no spatial control on the filtered $\delta^{15}N$ dataset, apart from the predominance of positive $\delta^{15}N$ values in the Eastern Rift Zone. However, coupled $N_2/^{40}Ar^*$ and $\delta^{15}N$ systematics clearly reveal the presence of a recycled N-component being pervasive throughout the neovolcanic zone. Moreover, coupled He-N isotope systematics suggest that recycled N-component(s) has been entrained by the Iceland plume source. In addition, we used available radiogenic isotopes from Iceland to better constrain the age of the recycled N-component, and demonstrated that a relatively young age of the recycled crustal material (i.e., Phanerozoic; < 541 Ma) could provide a satisfactory explanation for the observed nitrogen systematics of the Iceland plume source. Notably, such a young age of the recycled component would imply a relatively short residence time of volatile elements within the mantle source.

Finally, in this last section, I address some possible directions of future research, based on the findings and uncertainties associated with the discussions in Chapters II to V, with particular emphasis on the suite of samples on which these findings are based.

Chapter II (reprint of Halldórsson et al., 2013)

A critical issue of this chapter was to resolve the volatile characteristics that result from processes that take place within arc hydrothermal systems, such as air contamination, shallow-level crustal contamination, and/or elemental fractionation, from those that are representative of the magma system. Although volatile degassing from volcanic centers is well documented, emissions from flanks, in addition to areas surrounding volcanoes are not well quantified. In this respect, we note that the hydrothermal systems associated with volcanoes along the western Sunda arc act as a medium for the of transfer of volatiles from the magma source towards the surface. Significantly, in-depth studies of individual hydrothermal systems along the Sunda arc, so as to unravel their hydrological characteristics and the proximal versus distal volatile release features would facilitate better understanding of the processes that take place within them.

With respect to magmatic volatiles and their transport within a given hydrothermal system, the most straightforward approach would be to undertake a detailed study on a single volcano and characterize all possible degassing pathways both proximal and distal to the volcano summit, including chemical and isotope characteristics of emitted volatiles. Indeed, ongoing work in the Fluids and Volatiles Laboratory at SIO, aimed at characterizing the carbon footprint of a passively-degassing volcano, has tremendous potential in this respect. The volcano selected as a type locality, in many ways represents a ‘classic’ arc volcano - Mount Lassen in northern California - and preliminary work has elucidated the He and C systematics in groundwater of this currently passively-degassing volcano (Franz, 2012). Significantly, this study showed that a large (~30%) fraction of the total magmatic CO_2 was indeed released via the groundwater system surrounding the volcano. However, the caveat that every volcano and associated hydrothermal system can be very different, should be kept firmly in mind during further studies on arc-related volatiles that use Mount Lassen as an analog of arc volcanoes to constrain volatile fluxes.

We also note that better characterization of subducting sediments would help to advance our binary mixing model involving mantle and recycled slab material. In this respect, we noted that currently there are no ^{10}Be data available from the Sumatran subduction zone, and we proposed that due to shallow slab dips, the relatively slow convergence rate, and the occurrence of a massive accretionary prism off Sumatra, it is unlikely that significant ^{10}Be anomalies will be found. In addition, an important conclusion of this chapter was the apparent minimal contribution from the over-riding crust and associated sediments to the volatile budget of volcanic centers throughout the western Sunda arc. However, we note that improved resolution of the deep lithological structure of the Sundaland crustal core would allow us generate more reliable models of possible crustal volatile input, in particular with respect to the distribution of possible organic sedimentary material embedded within the crustal core that is likely to modify the N_2 and CH_4 characteristics of bypassing mantle-derived volatiles.

In Chapter II, methane-^3He relationships played a fundamental role in elucidating the minimal role of the upper crustal contributions to the volatile inventory in the western Sunda arc. As the $CH_4/^3He$ ratio of the crustal end-member is not well constrained, we adopted three possible end-member compositions ($CH_4/^3He=5.0\times10^{10}$; 1.3×10^{12}, 3.0×10^{13} with a common

$^3He/^4He$ value = 0.01 R_A) to explain coupled $^3He/^4He$- $CH_4/^3He$ systematics. Integration of geological studies of possible crustal material in the Sundaland crust, in conjunction with geochemical characterization, would lead to more reliable geochemical models of volatile sources along the western Sunda arc. However, it should be emphasized that, irrespective of the crustal end-member value selected, our model demonstrated that only a relatively minor input from sedimentary material was needed to explain the overall variation observed in samples from the volcanic centers, and the crustal composition would have to be significantly different from what has been observed elsewhere in order to be of any significance.

We also note that the carbon isotope characterization on hydrothermal CH_4 could open up exciting prospects for future studies, particularly when combined with relative abundance characteristics (e.g., $CH_4/^3He$). Mantle-derived CH_4, which has equilibrated with mantle CO_2, generally has $\delta^{13}C_{CH4}$ values between -18 to -15‰ (Welhan and Craig, 1983). In contrast, typical values of $\delta^{13}C_{CH4}$ for thermogenic methane, produced by thermocatalytic reactions within organic matter in the crust, range from -46 to -32‰, and biogenically-produced methane can yield values significantly lower than -50‰ (down to -110‰). Thus, there is a large isotopic contrast in CH_4 derived from degassing of the mantle and from CH_4 generated by heating of sedimentary material in the crust (i.e., Welhan and Craig, 1983; Schoell, 1988; Welhan, 1988). Indeed, plans are currently in place for a fully operational and dedicated hydrocarbon laboratory at the Fluids and Volatiles Laboratory at SIO. Not only will this new laboratory be able to analyze the relative abundances of different hydrocarbons, but will also be able to obtain $^{13}C/^{12}C$ ratio determination for each of them, i.e., methane, ethane, propane, and butane. Under the supervision of Prof. Hilton, and as a part of his McNair Post-baccalaureate Achievement Program, undergraduate student, Cristian Virrueta has been involved in a project directed at the origin of methane and other hydrocarbons in magmatic systems. Cristian undertook a reconnaissance study of the origin of methane by means of isotope analysis on samples collected from (i) the Salton Sea Geothermal

System in California, (ii) the Tengchong Geothermal Province within the Tibetan–Yunan fold system in China, (iii) the geothermal region in Ethiopia associated with on-axis and off-axis rifted areas and (iv) from the Costa Rica fore-arc system. Initial results demonstrate that the protocols for obtaining reliable $^{13}C/^{12}C$ ratios for methane in geothermal samples have been successfully developed. Thus, this new dataset, in many ways, represents a breakthrough in volatile studies at the Fluids and Volatiles Laboratory, as it allows for additional insight into the origins of hydrocarbons and other volatiles in geothermal systems.

Chapter III

A major conclusion of this chapter was that coupled He-Ne systematics can be explained simply by admixture between a single mantle plume source, common to the entire rift, and either a DMM or SCLM component. This conclusion needs further attention in future geochemical studies of the EARS, particularly since the idea of a single plume source underlying the entire EARS is now well established, from a geophysical viewpoint (Hansen et al., 2012). For example, recent seismic tomographic models of the mantle underlying East Africa, and thus covering the entire Cenozoic Afro-Arabian Rift System, reveal the presence of a laterally near-continuous, low-velocity region in the upper mantle beneath all of eastern Africa and western Arabia, that possibly rises all the way from the core-mantle boundary (e.g., Hansen et al., 2012).

We propose that future work on these now well-characterized samples, involving radiogenic isotope (Sr-Nd-Hf-Os-Pb) in addition to trace elements, should provide additional insight into the binary mixing process involving a single mantle plume source and the two upper-mantle components, DMM and/or SCLM. We note that our model is largely consistent with recent models based on radiogenic isotopes that advocate for three-component mixing between DMM, SCLM, and plume components for the entire EARS (Rogers, 2006). For example, Rooney et al. (2012) have advocated for a three-component model to account for Sr, Nd, Hf, Pb, and He isotopic variations along the Main Ethiopian Rift. In this respect, we also note that collaborative work considering the coupled Sr, Nd, Pb, and He isotope characterization of several samples discussed in this chapter with Prof. Castillo at SIO is currently on-going. Preliminary results, that have been presented as conference meetings (Castillo et al., 2012; Castillo et al., 2013; Castillo et al., 2014), and have led to the development of a three-component mixing model involving a single plume source beneath the EARS - entirely consistent with the model we presented in Chapter III.

Chapter IV

It became evident in this chapter, that pyroxenite xenoliths hold the key to further assessment of mantle volatiles in the EARS, and possibly elsewhere. However, as the volatile characteristics were the primary motivation for this study, petrographic work in conjunction with chemical characterization involving major and trace elements on the various minerals which make-up the EARS xenoliths was not provided. Improved understanding, provided by such (e.g., major and trace element) characterization, will hopefully enable us to generate more robust geochemical models in the future and possibly help us to better interpret isotope and relative abundance results from EARS xenoliths. Also, work on fluid inclusions hosted by mafic minerals of these xenoliths by means of Raman spectroscopy, in addition to micro-thermometry, could provide further insight into formation pressures and volatile characteristics prevailing under the EARS mantle.

A fundamental issue with our models was the use of recycled crustal material entrained by the African-Superplume to place constraints on possible end-member compositions in the mantle. Additional work on these same xenolith samples, involving radiogenic isotope characterization (Sr-Nd-Hf-Os-Pb) and other stable isotope systems could provide ancillary evidence (e.g., $\delta^{13}C$) for recycled components in their mantle source. For example, carbon isotopes in fluid inclusions of the EARS xenoliths highlighted the importance of recycled carbonate material as metasomatic agents in the East African upper mantle. Consideration of additional stable isotope systems could potentially shed further light on this recycled carbonate material in the mantle beneath the EARS. In this respect, the combined use of C-Mg-Ca isotopes, in particular, has enormous potential for tracing subducted carbonate in the mantle. The mantle is homogeneous in its Mg isotope composition (i.e., δ^{26}Mg = −0.25 ± 0.07‰), whereas carbonates have significantly lighter Mg isotope compositions, with δ^{26}Mg values ranging from −5.31 to −1.09‰, making Mg isotopes a potential tracer of recycled carbonate in the mantle (e.g., Yang et al., 2012). Furthermore, Ca isotopes also have great potentially in this respect as the upper-mantle has somewhat more positive values ($\delta^{44/40}$Ca ~ +1.05 ± 0.04‰) relative to marine carbonates ($\delta^{44/40}$Ca ~ 0‰: DePaolo, 2004; Huang et al., 2011).

Additionally, we note that a possible solution to explain highly variable mantle $N_2/^3$He end-members in the EARS mantle was to invoke a different sedimentary end-member with δ^{15}N as low as ~ -7.5‰. Such a sedimentary end-member is only possible assuming that it formed in the absence of oxygen in the Archean. In this respect, consideration of multiple sulfur isotopes (^{33}S, ^{34}S, ^{36}S) could help to further constrain the age and nature of the recycled sedimentary component (e.g., Farquhar et al., 2002; Cabral et al., 2013). For example, significant mass independent ^{33}S anomalies (i.e., Δ^{33}S) in the EARS xenoliths would tie the age of the sedimentary component to the Archean, thus supporting the ternary mixing scenario invoked to explain the coupled $N_2/^3$He- δ^{15}N systematics. On the other hand, the lack of mass independent ^{33}S anomalies would constrain the age of recycled components to the post-Archean - thus arguing against the ternary model - and support binary models with highly variable $N_2/^3$He values in the mantle end-member. Again, some of this work will hopefully form the basis of my postdoctoral research at the Isotope Laboratory at the University of Iceland and in collaboration with Isotope Laboratories elsewhere.

Finally, we note that one segment of the EARS was, for the most part, largely overlooked in Chapters IV and V, mainly due to the lack of samples. The northern part of the western rift, involving volcanically-active areas in Uganda, The Democratic Republic of Congo, Rwanda, and Burundi, remains poorly explored with respect to mantle volatiles studies and mantle geochemistry in general and there is enormous potential for future studies. The potential of the western rift was clearly highlighted by recent work on at the Rungwe Volcanic Province at the southern tip that revealed exciting results, and opened up many doors for further studies. Notable for its low magma volume, the northern part of the western rift contains some of the most diverse igneous rocks on the planet, involving highly silica-undersaturated rocks, carbonate-rich rocks, and potassic rocks (kamafugites), in addition to carbonatites (e.g., Holmes and Harwood, 1932, 1937; Combe and Holmes, 1945; Kampunzu and Mohr, 1991). All these rock-types are generally CO_2-rich, as evidenced by the occurrence of carbonatites and the fact that CO_2 is generally associated with the generation of low silica melts (e.g., Eggler, 1976; Dasgupta et al., 2007).

Very few geochemical studies involving isotope analyses on lavas from the region have been reported and are currently mostly confined to geographically-restricted regions (e.g., Davies & Lloyd, 1989; Rogers et al., 1992, 1998; Chakrabarti et al., 2009; Rosenthal et al., 2009). Furthermore, isotopic studies on geothermal fluids are very rare in the scientific literature (e.g., Bahati et al., 2005; Tedesco et al., 2010). We note in particular that geochemical studies of lavas and geothermal fluids from Uganda are very sparse, whereas the region by Lake Kivu and Mount Nyiragongo in The Democratic Republic of Congo has received more attention in recent years, following the 2002 Nyiragongo eruption. The lack of geochemical studies in Uganda is somewhat surprising due the great variety of volcanic rocks, including ultramafic xenoliths such as pyroxenites, that have been described from the region, so there is exciting potential for future studies aiming to characterize and geochemically map distinct regions of EARS mantle. For example, due to a strong lithosphere signature in mantle-derived melts from the region, the northern part of the western rift is a key region to assess to role of SCLM in EARS magmagenesis. I remain optimistic that I can continue to work on the EARS during my postdoctoral research, and I would greatly welcome in particular, any opportunities to conduct research into the geochemistry of Ugandan lavas and geothermal fluids.

Chapter V

In this chapter, it became evident that degassing models involving elemental ratios rely heavily on solubility coefficients for elements of interest (e.g., $N_2/^{40}Ar^*$). As a result of the similar geochemical behavior of nitrogen and argon, solubility coefficients of these elements are expected to be nearly identical. Thus, realistic and meaningful degassing models involving experimentally- and/or naturally-derived solubility coefficients for nitrogen and argon require well defined solubility coefficients, as relatively minor uncertainties can potentially result in significant changes to the outcome of the model. Our study thus warrants production of further solubility coefficient data for these elements. Ideally, determination of such solubility coefficients would take internal and external variables, such as temperature, pressure, and composition into account, leading to more robust determination.

Similarly, the degassing model developed in this chapter to test degassing induced-fractionation of nitrogen isotopes also depended heavily on well constrained isotopic fractionation factors. In the model adopted in this chapter, we assumed an isotopic equilibrium fractionation factor of $\delta^{15}N$ between the vesicles and the melt, and we adopted a value of -1.6‰. This value was taken from Cartigny et al. (2001), and was based on their observations of the $\delta^{15}N$ difference between vesicles and the melt phases of basaltic glasses from the south-west Indian Ridge. This value has not been confirmed by experimental work and thus requires corroboration. An important conclusion of this study was that Icelandic subglacial basalt did not experience significant degassing-induced fractionation. However, we note that there appears to be no consensus on degassing-induced isotopic fractionation of nitrogen (see contrasting views in the discussions of Cartigny and Ader, 2003 and Marty and Dauphas, 2003) and further studies, involving both experimental melts and well-characterized natural melts that will allow more accurate interpretation of δ^{15}N values in mantle-derived material, are needed.

In this chapter, we also noted that any interpretation of the nitrogen isotope values of melts formed at depths exceeding ~ 180 km, must take into account that most of the nitrogen is likely present as NH_3. By assuming that the mantle solidus under Iceland is neither particularly wet and/or carbonated, we made the assumption that all nitrogen should be in the form of N_2. Clearly, this statement requires further testing, as small amounts of water and/or carbon in the mantle beneath Iceland may generate small melt fractions (e.g., carbonate melts) at depths several tens of km greater than that of the anhydrous solidus (~120 km). Detailed melt inclusion studies of mafic crystals in primitive lavas may provide a feasible way of determining whether the mantle solidus under Iceland is affected by the presence of water and/or carbon.

An important conclusion of this study was that the nitrogen systematics of a number of Icelandic basalts appeared modified, and thus unrepresentative of mantle source characteristics, due to contamination with volatiles from the Iceland crust. This was clearly evident in samples that had lost significant amounts of volatiles and later experienced significant input from the assimilation of organic material in the Icelandic crust. However, the possible role of such organic end-members in the Icelandic crust as a contaminant for Icelandic melts needs more attention. In particular, the formation and preservation of such organic material in the crust is an issue of concern, as it appears unlikely that organic material of substantial quantities can be found in a hot, young, and entirely basaltic crust, similar to the Iceland crust. In addition, contamination of mantle volatiles by organic material should result in coupled enrichments of ^{12}C and ^{15}N, making it difficult to separate such contamination from the degassing induced isotope fractionation that dominates much of the δ^{13}C signature (e.g., Barry et al., 2014). In this respect, we also note that future work on highly degassed samples (i.e., with ^{4}He/^{40}Ar* > 10), involving independent tracers of contamination (e.g., δ^{11}B and δ^{18}O), will help to further constrain the source of positive δ^{15}N signatures observed in Icelandic glasses. Oxygen isotopes are particularly interesting in this respect. Due the high northern latitude of Iceland, and hence isotopically light precipitation, and an unusually thick crust, Iceland remains the case example of a low oxygen anomaly preserved in oceanic basalts worldwide (e.g., Muehlenbachs et al., 1974). This low oxygen anomaly has been widely attributed to assimilation of the low-δ^{18}O Icelandic crust (Muehlenbachs et al., 1974). The notion that shallow level contamination of crustal (organic) material is responsible for the predominantly positive nitrogen isotope values observed in highly degassed basaltic glasses can therefore be tested with oxygen isotopes.

Finally, we note that nitrogen isotope systematics of unmodified Icelandic melts are consistent with significant heterogeneity (i.e., +3 to +7‰) in recycled crustal end-members. Improved knowledge of possible end-member compositions of the recycled materials would help to constrain the mixing model presented in this chapter. For example, future work on these samples, involving radiogenic isotope characterization (Sr-Nd-Hf-Os-Pb) and sulfur isotopes (e.g., ^{33}S), will help to further constrain the age and nature of the recycled components. Some of this work will, indeed, be conducted during my postdoctoral research period at the Isotope Laboratory at the University of Iceland.

References

Allégre, C.J., Turcotte, D.L., 1986. Implications of a two-component marble-cake mantle. Nature 323, 123–127.

Allégre, C., 2008. Isotope Geology. Cambridge University Press. Cambridge, UK, 512 pp.

Alt, J.C., and Teagle, D.A.H., 1999. The uptake of carbon during alteration of ocean crust. Geochim. Cosmochim. Acta 63, 1527–1535.

Alt, J.C., and Teagle, D.A.H., 2003. Hydrothermal alteration of upper oceanic crust formed at fast-spreading ridge: mineral, chemical, and isotopic evidence from ODP Site 801. Chem. Geol. 201, 191–211.

Aubaud, C., Pineau, F., Hékinian, R., and Javoy, M., 2005. Degassing of CO_2 and H_2O in submarine lavas from the Society hotspot. Earth Planet. Sci. Lett., 235, 511-527.

Aubaud, C., Pineau, F., Hékinian, R., and Javoy, M., 2006. Carbon and hydrogen isotope constraints on degassing of CO2 and H2O in submarine lavas from the Pitcairn hotspot (South Pacific). Geophysical research letters, 33(2).

Aulbach, S., Stachel, T., Heaman, L.M., Creaser, R.A., Shirey, S.B., 2011a. Formation of Cratonic Subcontinental Lithospheric Mantle from Hybrid Plume Sources. Contributions to Mineralogy and Petrology 161, 947-960.

Aulbach, S., Rudnick, R. L., McDonough, W. F., 2011b. Lithospheric mantle sources within the East African rift, Tanzania. Invited contribution to "Volcanism and evolution of the African lithosphere" Editors: Beccaluva L, Bianchini G, Wilson M. Geological Society of America Special Paper 478, 105-126.

Bahati, G., Pang, Z., Ármannsson, H., Isabirye, E.M., and Kato, V., 2005. Hydrology and reservoir characteristics of three geothermal systems in western Uganda. Geothermics, 34, 568-591.

Baker, J.A., Chazot, G., Menzies, M., and Thirlwall, M., 1998. Metasomatism of the shallow mantle beneath Yemen by the Afar plume-Implications for mantle plumes, flood volcanism, and intraplate volcanism. Geology 26, 431–434.

Baker, J.A., Macpherson, C.G., Menzies, M.A., and Thirlwall, M.F., 2000. Resolving crustal and mantle contributions to continental flood volcanism, Yemen; Constraints from mineral oxygen isotope data. Journal of Petrology 41, 1805-1820.

Ballentine, C.J, Marty, B., Lollar, B.S., and Cassidy, M., 2005. Neon isotopes constrain convection and volatile origin on the Earth's mantle. Nature 433, 33-38.

Bao, H., and Thiemens, M.H., 2000. Generation of O_2 from $BaSO_4$ using a CO_2-laser fluorination system for simultaneous $\Delta^{18}O$ and $\Delta^{17}O$ analysis. Analytical Chemistry 72(17), 4029-4032.

Barfod, D.N., Ballentine, C.J., Halliday, A.N., and Fitton, J.G., 1999. Noble gases in the Cameroon line and the He, Ne, and Ar isotopic composition of high A (HIMU) mantle. J. Geophys. Res. 104, 29509– 29527.

Barker, A.J., and Gayer, R.A., 1984. Caledonide–Appalachian tectonic analysis and evolution of related oceans. In: Geyer, R.A. (Ed.), The Tectonic Evolution of the Caledonide–Appalachian Orogen. International Monograph Series on Interdisciplinary Earth Science Research and Applications. Friedrich Vieweg 7 Sohn, Braunschweig V, pp. 126–165.

Barry, P.H., Hilton, D.R., Halldórsson, S.A., Hahm D., and Marti K., 2012. High precision nitrogen isotope measurements in oceanic basalts using a static triple collection noble gas mass spectrometer. Geochem. Geophys. Geosyst., 13, Q01019, doi:10.1029/2011GC003878.

Barry, P.H., Hilton, D.R., Fischer, T.P., de Moor, J.M., Mangasini, F., and Ramirez, C., 2013. Helium and carbon isotope systematics of cold “mazuku” CO2 vents and hydrothermal gases and fluids from Rungwe Volcanic Province, southern Tanzania. Chemical Geology 339, 141–156.

Barry, P.H., Hilton, D.R., Füri, E., Halldórsson, S.A. and Grönvold, K., 2014. Carbon isotope and abundance systematics of Icelandic geothermal gases, fluids and subglacial basalts with implications for mantle plume-related CO_2 fluxes. Accepted manuscript, in press at Geochemica Cosmochimica Acta.

Bebout, G.E., Fogel, M.L., and Cartigny, P., 2013. Nitrogen: Highly volatile yet surprisingly compatible, Elements, 9, 333-338.

Beccaluva, L., Bianchini, G., Ellam, R.M., Natali, C., Santato, A., Siena, F., and Stuart, F.M., 2011. Peridotite xenoliths from Ethiopia*:* Inferences about mantle processes from plume to rift settings. Invited contribution to “Volcanism and evolution of the African lithosphere” Editors: Beccaluva L., Bianchini G., Wilson M., Geological Society of America Special Paper 478, 77-104.

Bedini, R.M., Bodinier, J.L., Dautria, J.M., and Morten, L., 1997. Evolution of LILE-enriched small melt fractions in the lithospheric mantle: a case study from the East African Rift. Earth Planet Sci Lett 153:67–83

Bedini, R.M., and Bodinier, J.L., 1999. Distribution of incompatible trace elements between the constituents of spinel peridotite xenoliths: ICP-MS data from the East African Rift. Geochim Cosmochim Acta 63, 3883–3900.

Benkert, J.P., Baur, H., Signer, P., and Wieler, R., 1993. He, Ne, and Ar from the solar wind and solar energetic particles in lunar ilmenites and pyroxenes. Journal of Geophysical Research 98, 13147–13162.

Bjarnason, I.T. and Schmeling, H., 2009. The lithosphere and asthenosphere of the Iceland hotspot from surface waves. Geophysical Journal International, 178, 394-418.

Black, D.C., 1972. On the origins of trapped helium, neon and argon isotopic variations in meteorites—I. Gas-rich meteorites, lunar soil and breccia. Geochimica Cosmochimica Acta, 36, 347-375.

Bodinier, J.L. and Godard, M., 2003. Orogenic, ophiolitic, and abyssal peridotites. In: Carlson, R. W., (ed.) Treatise on Geochemistry, Volume 2 - The Mantle and Core. Amsterdam: Elsevier Pergamon, pp. 103-170.

Bott, M.H.P., 1985. Plate tectonic evolution of the Icelandic transverse ridge and adjacent regions. J. Geophys. Res. 90, 9953–9960.

Bouhifd, M.A., Jephcoat, A.P., Heber, V.S., and Kelley, S.P., 2013. Helium in Earth’s early core. Nature Geoscience, 6, 982–986.

Boyd S.R., Hall, A., and Pillinger, C.T., 1993a. The measurement of $\delta^{15}N$ in crustal rocks by static vacuum mass spectrometry: application to the origin of the ammonium in the Cornubian batholith, southwest England. Geochim. Cosmochim. Acta 57, 1339–1347.

Boyd S.R., Wright, I.P., and Pillinger, C.T., 1993b. Accurate determination of nitrogen concentrations by static vacuum mass spectrometry, Meas. Sci. Technol., 4, 1000–1005.

Brandes, J.A., Boctor, N.Z., Cody, G.D., Cooper, B.A., Hazen, R.M. and Yoder H.S., 1998. Abiotic nitrogen reduction on the early Earth. Nature 395, 365-367.

Brandon, A.D., Graham, D.W., Waight, T., and Gautason, B., 2007. ^{186}Os and ^{187}Os enrichments and high-^{3}He/^{4}He sources in the Earth’s mantle: evidence from Icelandic picrites. Geochim. Cosmochim. Acta 71, 4570–4591.

Breddam, K., Kurz, M.D., and Storey, M., 2000. Mapping out the conduit of the Iceland mantle plume with helium isotopes. Earth Planet. Sci. Lett. 176, 45–55.

Breddam, K., 2002. Kistufell: primitive melt from the Iceland plume. Journal of Petrology 43, 345-373.

Brennwald, M., Vogel, N., Figuraa, S., Vollmer, M.K., Langenfelds, R., Steele, L.,P., Maden, C., and Kipfer, R., 2013. Concentrations and isotope ratios of helium and other noble gases in the Earth's atmosphere during 1978–2011. Earth Planet. Sci. Lett. 366, 27-37.

Brooker, R.A., Du, Z., Blundy, J.D., Kelley, S.P., Allan, N.L., Wood, B.J., Chamorro, E.M., Wartho, J.-A., and Purton, J.A., 2003. The 'Zero charge' partitioning behavior of noble gases during mantle melting, Nature 423, 738-741.

Brooker, R.A., James, R.H., and Blundy, J.D., 2004. Trace elements and Li isotope systematics in Zabargad peridotites: evidence of ancient subduction processes in the Red Sea mantle. Chemical Geology 212, 179-204.

Budd, D.A., Troll, V.R., Hilton, D.R., Freda, C., Jolis, E.M. and Halldórsson, S.A., 2012a. Traversing nature’s danger zone: getting up close with Sumatra’s volcanoes. Geology Today, Volume 28, No. 2, March-April.

Budd, D.A., Troll, V.R., Jolis, E.M., Deegan, F.M., Smith, V.C., Whitehouse, M.J., Harris, C., Freda, C., Hilton, D.R., and Halldórsson, S.A., 2012b. Reconstructing the Toba magmatic system: insights from stable isotope geochemistry. Goldschmidt, abstract, Montreal.

Buikin, A.I., Trieloff, M., Hopp, J., Althaus, T., Korochantseva, E.V., Schwarz, W.H., and Altherr, R., 2005. Noble gas isotopes suggest deep mantle plume source of late Cenozoic mafic alkaline volcanism in Europe. Earth Planetary Science Letters 230, 143–162.

Burnard, P.G., Stuart, F.M., and Turner, G., 1994a. C-He-Ar variations within a dunite nodule as a function of fluid inclusion morphology. Earth and Planetary Science Letters 128, 243-258.

Burnard, P.G., Stuart, F.M., Turner, G., and Oskarsson, N., 1994b. Air contamination of basaltic magmas: implications for high ^{3}He/^{4}He mantle Ar isotopic composition. J. Geophys. Res. –Sol. Earth 99(B9), 17709–17715.

Burnard, P.G., Graham, D.W., and Turner, G., 1997. Vesicle-specific noble gas analyses of “popping rock”: implications for primordial noble gases in the Earth. Science, 276, 568-571.

Burnard, P.G., Farley, K.A., and Turner, G., 1998. Multiple fluid pulsesin a Samoan harzburgite. Chem. Geol. 147, 99–114.

Burnard, P.G., and Harrison, D., 2005. Argon isotope constraints on modification of oxygen isotopes in Iceland basalts by surficial processes. Chemical Geology 216, 143–156.

Burnard, P.G., Toplis, M.J., and Medynski, S., 2010. Low solubility of He and Ar in carbonatitic liquids: implications for decoupling noble gas and lithophile isotope systems. Geochim. Cosmochim. Acta 74, 1672-1683.

Busigny, V., Laverne, C., and Bonifacie, M., 2005. Nitrogen content and isotopic composition of oceanic crust at a superfast spreading ridge: a profile in altered basalts from ODP Site 1256, Leg 206. *Geochem. Geophys. Geosyst.* 6, Q12O01. doi:10.1029/2005GC001020.

Busigny, V., Cartigny, P., and Philippot, P., 2011. Nitrogen isotopes in ophiolitic metagabbros: A re-evaluation of modern nitrogen fluxes in subduction zones and implication for the early Earth atmosphere, Geochim. Cosmochim. Acta 75, 7502–7521.

Busigny, V., and Bebout, G. E., 2013. Nitrogen in the silicate Earth: Speciation and isotopic behavior during fluid-mineral interactions. Elements 9, 353-358.

Cabral, R.A., Jackson, M.G., Rose-Koga, E.F., Koga, K.T., Whitehouse, M.J., Antonelli, M.A., Farquhar, J., Day, J.M.D., and Hauri, E.H., 2013. Recycling of subducted Archean crust from mass-independent sulfur in oceanic hotspot lavas, Nature 496. 490-493.

Carroll, M.R., and Stolper, E., 1993. Noble gas solubilities in silica melts and glasses: new experimental results for argon and the relationship between solubility and ionic porosity. Geochimica Cosmochimica Acta 57, 5039-5051.

Cartigny, P., Jendrzejewski, F., Pineau, F., Petit, E., and Javoy, M., 2001. Volatile (C, N, Ar) variability in MORB and the respective roles of mantle source heterogeneity and degassing: the case of the Southwest Indian Ridge. Earth Planet. Sci. Lett. 194, 241–257.

Cartigny, P., and Ader, M., 2003. A comment to “The nitrogen record of crust-mantle interaction and mantle convection from Archean to Present” by B. Marty and N. Dauphas.” Earth and Planetary Science Letters 216, 425-432.

Cartigny, P., 2005. Stable isotopes and the origin of diamond. Elements 1, 79-84.

Cartigny, P., and Marty, B., 2013. Nitrogen isotopes and mantle geodynamics: The emergence of life and the atmosphere– crust–mantle connection. Elements 9, 359–366.

Castillo, P.R., Hilton, D.R., Halldorsson, S.A., and Wang, R., 2012. The geochemical and Sr-Nd-Pb-He isotopic characterization of the mantle source of Rungwe Volcanic Province: comparison with the Afar mantle domain. Abstract. AGU Fall meeting.

Castillo, P.R., Hilton, D.R., and Halldorsson, S.A., 2013. A single superplume source with multiple heads supplies melt along the East African Rift System. Abstract. ACVOR workshop on Active Volcanism and Continental Rifting, Gisneyi. Rwanda.

Castillo, P.R., Hilton, D.R., and Halldorsson, S.A., 2014. A unified mantle plume hypothesis for the East African Rift System. Abstract. Goldschmidt, Sacramento.

Cerling, T.E., and Craig, H., 1994. Geomorphology and in-situ cosmogenic isotopes, Annu. Rev. Earth Planet. Sci. Lett. 22, 273-317.

Chakrabarti, R., Basu, A.R., Santo, A.P., Tedesco, D., and Vaselli, O., 2009. Isotopic and geochemical evidence for a heterogeneous mantle plume origin of the Virunga volcanics, Western rift, East African Rift system. Chem. Geol. 259, 273–289.

Chauvel, C., and Hemond, C., 2000. Melting of a complete section of recycled oceanic crust: trace element and Pb isotopic evidence from Iceland. Geochem. Geophys. Geosyst. 1(2), 1001, doi:10.1029/1999GC000002.

Chazot, G., Lowry, D., Menzies, M., and Mattey, D., 1997 Oxygen isotopic composition of hydrous and anhydrous mantle peridotites. Geochim Cosmochim Acta 61, 161–169.

Chesner, C.A., Rose, W.I., Deino, A., Drake, R. and Westgate, J.A., 1991. Eruptive history of Earth’s largest Quaternary caldera (Toba, Indonesia) clarified. Geology 19, 200–203.

Chesner, C.A. 1998. Petrogenesis of the Toba Tuffs, Sumatra, Indonesia. Journal of Petrology 39, 397–438.

Class, C., Goldstein, S. L., Stute, M., Kurz, M. D., and Schlosser, P., 2005. Grand Comore Island: A well-constrained "low ^{3}He/^{4}He" mantle plume. Earth Planetary Science Letters 233**,** 391-409.

Clift, P., and Vannucchi, P., 2004. Controls on tectonic accretion versus erosion in subduction zones: implications for the origin and recycling of the continental crust. Rev. Geophys. 42 RG2001, doi:10.1029/2003RG000127.

Clor, L.E., Fischer, T.P., Hilton, D.R., Sharp, Z.D., and Hartono, U., 2005. Volatile and N isotope chemistry of the Molucca Sea collision zone: Tracing source components along the Sangihe Arc, Indonesia. Geochem. Geophys. Geosyst., 6, Q03J14, doi:10.1029/2004GC000825.

Cohen, R.S., O'Nions, R.K., and Dawson, J.B., 1984. Isotope geochemistry of xenoliths from East Africa: Implications for development of mantle reservoirs and their interaction. Earth and Planetary Science Letters 68, 209-220.

Coggon, R.M., Teagle, D.A. H., Cooper, M.J., Hayes, T.E.F., and Green, D.R.H., 2006. Data report: compositions of calcium carbonate veins from superfast spreading rate crust, ODP Leg 206. Proceedings of the Ocean Drilling Program, Scientific Results 206, 1–6.

Coltice, N., Simon, L., and Lécuyer, C., 2004. Carbon isotope cycle and mantle structure. Geo. Res. Lett. 31, L05603, doi:10.1029/2003GL018873.

Coltice, N., Moreira, M., Labrosse, S., and Hernlund, J.W., 2011. Crystallization of a basal magma ocean recorded by Helium and Neon. Earth and Planetary Science Letters 308, 193-199.

Coltorti, M., Bonadiman, C., Hinton, R.W., Siena, F., and Upton, B.G.J., 1999. Carbonatite metasomatism of the oceanic upper mantle: evidence from clinopyroxenes and glasses in ultramafic xenoliths of Grande Comore, Indean Ocean. J Petrol 40, 133–165.

Combe, A., and Holmes, A., 1945. The kalsilite-bearing lavas of Kabirenge and Lyakauli, South-West Uganda. Trans. R. Soc. Edinb. 61, 359–379.

Condomines, M., Grönvold, K., Hooker, P. J., Muehlenbachs, K., O'Nions, R. K., Oskarsson, N., and Oxburgh E. R., 1983. Helium, oxygen and strontium isotopic relationships in Icelandic volcanics. Earth Planet. Sci. Lett. 66, 125–136.

Conticelli, S., Sintoni, M.F., Abebe, T., Mazzarini, F., Manetti, P., 1999. Petrology and geochemistry of ultramafic xenoliths and host basalts from the Ethiopian Volcanic Province: an insight into the upper mantle under Eastern Africa. In: Boccaletti, M., Peccerillo, A., (eds) The Ethiopian rift system. Acta Vulcanol 11,143–159.

Courtillot, V., Davaille, A., Besse, J., and Stock, J., 2003. Three distinct types of hotspots in the Earth's mantle, Earth and Planetary Science Letters 205, 295–308.

Craig, H., and Lupton, J.E., 1976. Primordial neon, helium, and hydrogen in oceanic basalts. Earth and Planetary Science Letters 31, 369-385.

Craig, H., and Lupton, J.E., 1977. Isotope geochemistry and hydrology of geothermal waters in the Ethiopian Rift Valley. Scripps Inst. Oceanography Technical Rpt. 77-14, p140.

Craig, H., Lupton, J.E. and Horibe, Y., 1978. A mantle helium component in circum-Pacific volcanic gases: Hakone, the Marianas and Mt. Lassen. In: E.C. Alexander and M. Ozima, (Editors), Terrestrial Rare Gases. Central Academic Publishers, Tokyo, 3-16.

Craig, H., Marti, K. and Wiens, R., 1993. A static mass spectrometer with triple collection for nitrogen and neon isotopes. Tech. Rep. 93-11, Scripps Inst. Oceanogr., San Diego, p. 37.

Curray, J.R., 1994. Sediment volume and mass beneath the Bay of Bengal. Earth and Planetary Science Letters 125, 371-383.

Czuppon, G., Matsumoto, T., Handler, M.R., and Matsuda, J.-I., 2009. Noble gases in spinel peridotite xenoliths from Mt Quincan, North Queensland, Australia: undisturbed MORB-type noble gases in the subcontinental lithospheric mantle. Chem. Geol. 266, 19–28.

Czuppon, G., Matsumoto, T., Matsuda, J.-I., Everard, J., and Sutherland, L., 2010. Noble gases in anhydrous mantle xenoliths from Tasmania in comparison with other localities from eastern Australia: Implications for the tectonic evolution. Earth and Planetary Science Letters 299, 317–327.

Dasgupta, R., and Hirschmann, M.M., 2006. Melting in the Earth's deep upper mantle caused by carbon dioxide. Nature 440, 659–662.

Dasgupta, R., and Hirschmann M.M., 2007. Effect of variable carbonate concentration on the solidus of mantle peridotite. Am Mineral 92, 370-379.

Dasgupta, R., Hirschmann M.M., and Smith N.D., 2007. Water follows carbon: CO_2 incites deep silicate melting and dehydration beneath mid-ocean ridges. Geology 35, 135-138.

Dasgupta, R., Hirschmann, M.M. and Smith, N.D., 2007. Partial melting experiments of peridotite + CO_2 at 3 GPa and genesis of alkalic ocean island basalts. Journal of Petrology 48, 2093-2124.

Dasgupta, R., and Hirschmann M.M., 2010. The deep carbon cycle and melting in Earth's interior. Earth Planet Sci Lett 298, 1-13.

Dasgupta, R., Mallik, A., Tsuno, K., Withers, A.C., Hirth, G., and Hirschmann, M.M., 2013. Carbon-dioxide-rich silicate melt in the Earth's upper mantle. Nature 493, 211-215.

Dasgupta, R., 2013. Ingassing, storage, and outgassing of terrestrial carbon through geologic time. Reviews in Mineralogy and Geochemistry 75, 183-229.

Dauphas, N., and Marty, B., 1999. Heavy nitrogen in carbonatites of the Kola Peninsula: a possible signature of the deep mantle. Science 286, 2488–2490.

Davies, G.R. and Lloyd, F.E., 1989. Pb–Sr–Nd isotope and trace element data bearing on the origin of the potassic sub-continental lithosphere beneath south-west Uganda. In: Kimberlites and Related Rocks, 2, Geological Society of Australia Special Publication 14, 784–794.

Dawson, J.B., 2008. The Gregory RiftValley and Neogene-RecentVolcanoes of Northern Tanzania. Geological Society, London, Memoirs 33.

Dawson, J.B., 2002. Metasomatism and partial melting in uppermantle peridotite xenoliths from the Lashaine volcano, Northern Tanzania. Journal of Petrology 43, 1749-1777.

Dawson, J.B., and Smith, J.V., 1973. Alkalic pyroxenite xenoliths from the Lashaine volcano, Northern Tanzania. Journal of Petrology 14, 113-131.

Dawson, J.B., and Smith, J.V., 1988. Metasomatised and veined uppermantle xenoliths from Pello Hill, Tanzania: evidence for anomalously light mantle beneath the Tanzanian sector of the East African Rift Valley. Contributions to Mineralogy and Petrology 100, 510-527.

Dawson, J.B. and Smith, J.V., 1992. Olivine-mica pyroxenite xenoliths from northern Tanzania: metasomatic products of upper-mantle peridotite. Journal of Volcanology and Geothermal Research 50, 131-142.

Day, J.M.D., Pearson, D.G., Macpherson, C.G., Lowry, D., Carracedo, J.-C., 2009. Pyroxenite rich mantle formed by recycled oceanic lithosphere: oxygen-osmium isotope evidence from Canary Island lavas. Geology 37, 555-558.

de Leeuw G. A. M., 2007. The noble gas and carbon systematics of divergent, convergent and strike-slip plate boundaries: examples from the Reykjanes Ridge, Central American Arc and North Anatolian Fault Zone. Ph.D. thesis, University of California, San Diego.

de Leeuw, G.A., Hilton, D.R., Fischer, T.P., Walker, J.A., 2007. The He-CO_2 isotope and relative abundance characteristics of geothermal fluids in El Salvador and Honduras: new constraints on volatile mass balance of the Central American Volcanic Arc. Earth and Planetary Science Letters 258, 132–146.

de Leeuw, G.A.M., Hilton, D.R., Güleç, N. and Mutlu, H., 2010. Regional and temporal variations in $CO_2/^3He$, $^3He/^4He$ and $\delta^{13}C$ along the North Anatolian Fault Zone, Turkey. Applied Geochemistry 25, 524-539.

Debaille, V., Trønnes, R.G., Brandon, A.D., Waight, T.E., Graham, D.W., and Lee, C.A., 2009. Primitive off-rift basalts from Iceland and Jan Mayen: Os-isotopic evidence for a mantle source containing enriched subcontinental lithosphere. Geochim Cosmochim Acta 73, 3423–3449.

Deines, P., 2002. The carbon isotope geochemistry of mantle xenoliths. Earth-Sci Rev 58, 247–278.

Demény, A., Dallai, L., Frezzotti, M.-L., Vennemann, T.W., Embey-Isztin, A., Dobosi, G., and Nagy, G., 2010. Origin of CO_2 and carbonate veins in mantle-derived xenoliths in the Pannonian Basin. Lithos 117, 172-182.

DePaolo, D.J., 2004. Calcium isotopic variations produced by biological, kinetic, radiogenic and nucleosynthetic processes. Reviews in Mineralogy and Geochemistry 55, pp. 255–288.

Dixon, E.T., Honda, M., McDougall, I., Campbell, I.H., and Sigurdsson, I.A., 2000. Preservation of near-solar neon isotopic ratios in Icelandic basalts. Earth Planetary Science Letters 180, 309–324.

Dixon, E.T., 2003. Interpretation of helium and neon isotopic heterogeneity in Icelandic basalts. Earth Planetary Science Letters 206, 83–99.

Downes, H., 2007. Origin and significance of spinel and garnet pyroxenites in the shallow lithospheric mantle: ultramafic massifs in orogenic belts in Western Europe and NW Africa. Lithos 99, 1–24.

Dunai, T.J., 1993. Noble gases in the subcontinental mantle and the lower crust. PhD Dissertation. ETH. Zhurich. Switzerland.

Dunai, T.J., and Baur. H., 1995. Helium, neon, argon systematics of the European subcontinental mantle: Implications for its geochemical evolution. Geochim. Cosmochim. Acta 59, 2767–2783.

Dunai, T.J., and Porcelli, D., 2002. Storage and transport of noble gases in the subcontinental lithosphere, Rev. Mineral. Geochem. 47, 371–409.

Dunai, T.J., 2010. Cosmogenic nuclides. Cambridge University Press. Cambridge, UK, 187 pp.

Edwards, C.M.H., Morris, J.D., and Thirlwall, M.F., 1993. Separating mantle from slab signatures in arc lavas using B/Be and radiogenic isotope systematics. Nature 362, 530-533.

Eggler, D.H., 1976. Does CO_2 cause partial melting in low-velocity layer of mantle? Geology 4, 69-72.

Elkins, L.J., Fischer, T.P., Hilton, D.R., Sharp, Z.D., McKnight, S., and Walker J., 2006. Tracing nitrogen in volcanic and geothermal volatiles from the Nicaraguan volcanic front, Geochim. Cosmochim. Acta 70, 5215–5235.

Ellam, R.M., and Stuart F.M., 2004. Coherent He–Nd–Sr isotope trends in high $^3He/^4He$ basalts: implications for a common reservoir, mantle heterogeneity and convection. Earth Planet. Sci. Lett. 228, 511–523.

Eiler, J.M., McInnes, B., Valley, J.W., Graham, C.M., and Stolper, E.M. (1998) Oxygen isotope evidence for slab-derived fluids in the sub-arc mantle, Nature 393, 777-781.

Eiler, J.M., Schiano, P., Kitchen, N., and Stolper, E.M., 2000a. Oxygen isotope evidence for recycled crust in the sources of mid-ocean ridge basalts. Nature 403, 530-534.

Eiler, J.M., Crawford, A., Elliott, T., Farley, K.A., Valley, J.W., and Stolper, E.M., 2000b. Oxygen isotope geochemistry of oceanic-arc lavas. Journal of Petrology 41, 229-256.

Eiler, J.M., 2001. Oxygen isotope variations of basaltic lavas and upper mantle rocks. In: Valley JW, Cole DR (eds) Stable isotope geochemistry, Reviews Mineral Geochemistry vol 43. Mineral Soc Amer, Washington DC, pp 319–364.

Exley, R.A., Mattey, D.P., Clague, D.A., and Pillinger C.P., 1986. Carbon isotope systematics of a mantle hotspot: a comparison of Loihi seamount and MORB glasses. Earth Planet. Sci. Lett. 78, 189–199.

Exley, R.A., Boyd, S.R., Mattey, D.P., and Pillinger, C.T., 1986. Nitrogen isotope geochemistry of basaltic glasses: implications for mantle degassing and structure? Earth Planet. Sci. Lett. 81, 163–174.

Farley, K.A., 1995. Rapid cycling of subducted sediments into the Samoan mantle plume. Geology 23, 531–34.

Farquhar, J., Wing, B.A., McKeegan, K.D., Harris, J.W., Cartigny, P., and Thiemens, M.H., 2002. Mass-independent sulfur of inclusions in diamond and sulfur recycling on early Earth. Science 298, 2369-2372.

Ferrando, S., Frezzotti, M.L., Neumann, E.R., Astis, D.G., Peccerillo, A., Dereje, A., Gezahegn, Y., and Teklewold, A., 2008. Composition and thermal structure of the lithosphere beneath the Ethiopian plateau: evidence from mantle xenoliths in basanites, Injibara, Lake Tana Province. Mineral Petrol 93, 47–78.

Fischer, T.P., Hilton, D.R., Zimmer, M.M., Shaw, A.M., Sharp, Z.D., and Walker, J.A., 2002 Subduction and recycling of nitrogen along the Central American margin. Science 297, 1154–1157.

Fischer, T.P., Takahata, N., Sano, Y., Sumino, H., and Hilton, D.R., 2005. Nitrogen isotopes of the mantle: insights from mineral separates. Geophys. Res. Lett. 32, 2005GL022792.

Fischer, T. P., et al., 2009. Upper-mantle volatile chemistry at Oldoinyo Lengai volcano and the origin of carbonatites. Nature 459, 77–80.

Fisk, M. R., Storrie-Lombardi, M. C., Douglas, S., Popa, R., McDonald, G., and Di Meo-Savoie, C., 2003. Evidence of biological activity in Hawaiian subsurface basalts, Geochem. Geophys. Geosyst. 4 2003GC000387.

Fitton, J.G., Saunders, A.D., Kempton, P.D., and Hardarson, B.S., 2003. Does depleted mantle form an intrinsic part of the Iceland plume? Geochem. Geophys. Geosyst. 4, 1032. doi:10.1029/2002GC000424.

Franz, B., 2012. He-CO_2 systematics in groundwaters at Mount Lassen Volcano, Northern California. M.Sc. Thesis. University of California, San Diego.

Frezzotti, M.L., and Peccerillo, A., 2007. Diamond-bearing COHS fluids in the mantle beneath Hawaii. Earth Planet. Sci. Lett. 262, 273–283.

Frezzotti, M.L., Ferrando, S., Peccerillo, A., Petrelli, M., Tecce, F., and Perucchi, A., 2010 Chlorine-rich metasomatic H_2O-CO_2 fluids in amphibole-bearing peridotites from Injibara (Lake Tana region, Ethiopian plateau): nature and evolution of volatiles in the mantle of a region of continental flood basalts. Geochim Cosmochim Acta 74, 3023–3039.

Furman, T., Kaleta, K.M., Bryce, J.G., Hanan, B.B., 2006. Tertiary mafic lavas of Turkana, Kenya: constraints on east African plume structure and the occurrence of high-μ volcanism in Africa. Journal of Petrology 47, 1221-1244.

Furman, T., 2007. Geochemistry of East African Rift basalts: An overview. Journal African Earth Science 48, 147-160.

Furnes, H., Muehlebachs, K., Torsvik, T., Thorseth, I.H., and Tumyr, O., 2001. Microbial fractionation of carbon isotopes in altered basaltic glass from the Atlantc Ocean, Lau Basin and Costa Rica Rift. Chem. Geol. 173, 313–330.

Füri, E., Hilton, D.R., Halldórsson, S.A., Barry, P.H., Hahm, D., Fischer, T.P., and Grönvold, K., 2010. Apparent decoupling of the He and Ne isotope systematics of the Icelandic mantle: The role of He depletion, melt mixing, degassing fractionation and air interaction. Geochemica Cosmochimica Acta 74, 3307-3332.

Füri E., Hilton D.R., Murton B.J., Hemond C., Dyment, J., and Day, J.M. D., 2011. Helium isotope variations between Réunion Island and the Central Indian Ridge (17º-21ºS): New evidence for ridge-hotspot interaction. J. Geophys. Res. 116, B02207, doi:10.1029/2010JB007609.

Garasic, V., 1997. Mantel xenolithe als Dokumente der thermischen Entwicklung des Erdmantels unter den Chyulu Hills, Kenia. PhD thesis, University of Heidelberg, Germany.

Garlick, G.D., MacGregor, I.D., and Vogel, D.E., 1971. Oxygen isotope ratios in eclogites from kimberlites. Science 172, 1025–1027.

Gasparon, M., Hilton, D.R., and Varne, R., 1994. Crustal contamination processes traced by helium-isotopes—Examples from the Sunda Arc, Indonesia, Earth Planet. Sci. Lett. 126, 15–22.

Gasparon, M., and Varne, R., 1995. Sumatran granitoids and their relationship to Southeast Asian terranes. Tectonophys 251, 277-299.

Gasparon, M., and Varne, R., 1998. Crustal assimilation versus subducted sediment input in west Sunda arc volcanics: an evaluation. Mineralogy and Petrology 64, 89-117.

Gasparon, M., 2005. Chapter 9: Quaternary volcanicity. In: Barber, A.J., Crow, M.J. & Milsom, J.S. (eds). Sumatra: Geology, Resources and Tectonic Evolution. Geological Society Memoirs 31, 1–6.

Gautason, B., and Muehlenbachs, K., 1998. Oxygen isotopic fluxes associated with high-temperature processes in the rift zones of Iceland. Chem. Geol. 145, 275–286.

Gautheron, C., and Moreira, M., 2002. Helium signature of the subcontinental lithospheric mantle. Earth Planetary Science Letters 199, 39–47.

Gautheron, C., Moreira, M., and Allegre, C., 2005. He, Ne and Ar composition of the European lithospheric mantle. Chemical Geology 217, 97– 112.

Gerlach, T.M., and Taylor, B.E., 1990. Carbon isotope constraints on degassing of carbon dioxide from Kilauea volcano. Geochim. Cosmochim. Acta. 54, 2051–2058.

Giggenbach, W.F., 1996. Chemical composition of volcanic gases. In: Scarpa, R., Tilling, R. (Eds.), Monitoring and Mitigation of Volcanic Hazards. Springer, 221–256.

Goldblatt, C., Matthews, A.J., Claire, M.W., Lenton, T.M., Watson A.J., and Zahnle, K.J., 2009. Nitrogen-enhanced greenhouse warming on early Earth, Nature Geoscience 2, 891-896.

Graham, D.W., 2002. Noble gas isotope geochemistry of mid-ocean ridge and ocean island basalts: characterization of mantle source reservoirs. In: Porcelli, D., Ballentine, C.J., Wieler, R. (Eds.), Noble Gases in Geochemistry and Cosmochemistry. Rev. Mineral. Geochem. Mineral. Soc. Am., vol. 47. Washington, DC, 247–317.

Grand, S.P., 2002. Mantle shear-wave tomography and the fate of subducted slabs. Philosophical Transactions: Mathematical, Physical and Engineering Sciences 360, 2475-2491.

Green, D.H. and Wallace, M.E., 1988. Mantle metasomatism by ephemeral carbonatite melts. Nature 336, 459–462.

Gudfinnsson, G., and Presnall, D.C., 2005. Continuous gradations among primary carbonatitic, kimberlitic, melilititic, basaltic, picritic, and komatiitic melts in equilibrium with garnet lherzolite at 3-8 GPa. J. Petrol. 46, 1645-1659.

Hahm, D., Hilton, D.R., Cho, M. Wei, H., and Kim, K.R., 2008. Geothermal He and CO_2 variations at Changbaishan intra-plate volcano (NE China) and the nature of the sub-continental lithospheric mantle. Geophys. Res. Lett., 35, L22304, doi:10.1029/2008GL035955.

Hahm, D., Hilton, D.R., Castillo, P.R., Hawkins, J.W., Hanan, B.B., and Hauri, E.H., 2012. An overview of the volatile systematics of the Lau Basin – resolving the effects of source variation, magmatic degassing and crustal contamination. Geochemica Cosmochimica Acta 85, 88-113.

Halama R., Bebout, G.E., John, T., and Schenk, V., 2010. Nitrogen recycling in subducted oceanic lithosphere: The record in high- and ultrahigh-pressure metabasaltic rocks, Geochimica et Cosmochimica Acta 74, 1636-1652.

Halama R., Bebout, G.E., John, T., and Scambelluri, M., 2012. Nitrogen recycling in subducted mantle rocks and implications for the global nitrogen cycle, International Journal of Earth Sciences (Geologische Rundschau), doi: 10.1007/s00531-012-0782-3.

Halldórsson, S.A., Hilton, D.R., Troll, V.R., and Fischer, T.P., 2013. Resolving volatile sources along the western Sunda arc, Indonesia. Chemical Geology 339, 263-282.

Halldórsson, S.A., Hilton, D.R., Scarsi, P., Abebe, T., and Hopp, J., 2014. A common mantle plume source beneath the entire East African Rift System revealed by coupled helium-neon isotope systematics. In revision at Geophys. Res. Lett.

Hamilton, W., 1979. Tectonics of the Indonesian region, U.S. Geol. Surv. Prof. Pap., 1078, 345 pp.

Hanan, B.B., and Schilling, J.-G., 1997. The dynamic evolution of the Iceland mantle plume: the Pb isotope perspective. Earth and Planetary Science Letters 151, 43-60.

Hanan, B.B., Blichert-Toft, J., Kingsley, R., and Schilling, J., 2000. Depleted Iceland mantle plume geochemical signature: Artifact of multicomponent mixing? Geochem. Geophys. Geosyst. 1,1003.

Hansen, S., Nyblade, A.A., and Benoit, M., 2012. Mantle structure beneath Africa and Arabia from adaptively parameterized P-wave tomography: Implications for the origin of Cenozoic Afro-Arabian tectonism. Earth Planetary Science Letters 319-320, 23–34.

Hanyu, T., Tatsumi, Y., and Kimura, J.-I., 2011. Constraints on the origin of the HIMU reservoir from He-Ne-Ar isotope systematics. Earth Planet Sci Lett 307, 377–386.

Harmon, R.S., and Hoefs, J., 1995. Oxygen-isotope heterogeneity of the mantle deduced from global ^{18}O systematics of basalts from different geotectonic settings. Contrib Mineral Petrol 120, 95-114.

Harrison, D., Burnard, P., and Turner, G., 1999. Noble gas behaviour and composition in the mantle: constraints from the Iceland Plume. Earth Planet. Sci. Lett. 171, 199–207.

Hauri, E.H., Shimizu, N., Dieu, J.J., and Hart, S.R., 1993. Evidence for hotspot-related carbonatite metasomatism in the oceanic upper mantle. Nature 365, 221–227.

Hawkesworth, C.J., Rogers, N.W., Van Calsteren, P.W.C. and Menzies, M.A., 1984. Mantle enrichment processes. Nature 311, 331-335.

Hayden, L.A., and Watson, E.B., 2007. A diffusion mechanism for core-mantle interaction. Nature 450, 709-711.

Heber, V.S., Brooker, R.A., Kelley, S.P., and Wood, B.J., 2007. Crystal-melt partitioning of noble gases (helium, neon, argon, krypton, and xenon) for olivine and clinopyroxene. Geochimica Cosmochimica Acta 71, 1041–1061.

Helmberger, D., Wen, L., and Ding, X., 1998. Seismic evidence that the source of the Iceland hotspot lies at the core–mantle boundary. Nature 396, 251–258.

Henjes-Kunst, F., and Altherr, R., 1992. Metamorphic petrology of xenoliths from Kenya and NorthernTanzania and implications for geotherms and lithospheric structures. Journal of Petrology 33, 1125-1156.

Hilton, D.R., and Craig, H., 1989. A helium isotope transect along the Indonesian archipelago. Nature 342, 906–908.

Hilton, D.R., Hammerschmidt, K., Teufel, S., and Friedrichsen, H., 1993. Helium isotope characteristics of Andean geothermal fluids and lavas. Earth Planet. Sci. Lett. 120, 265–282.

Hilton, D.R., 1996. The helium and carbon isotope systematics of a continental geothermal system: result from monitoring studies at Long Valley caldera (California, U.S.A.). Chemical Geology 127, 269-295.

Hilton, D.R., McMurtry, G.M., and Kreulen, R., 1997. Evidence for extensive degassing of the Hawaiian Mantle Plume from helium-carbon relationships at Kilauea Volcano. Geophysical research letters 24, 3065-3068.

Hilton, D.R., Grönvold, K., Sveinbjornsdottir, A., and Hammerschmidt, K., 1998a. Helium isotope evidence for off-axis degassing of the Icelandic hotspot Chem. Geol. 149, 173–187.

Hilton, D.R., McMurtry, G.M., and Goff, F., 1998b. Large variations in vent fluid $CO_2/^3He$ ratios signal rapid changes in magma chemistry at Loihi Seamount, Hawaii. Nature 396, 359–362.

Hilton, D.R., Grönvold, K., Macpherson, C.G., and Castillo, P.R., 1999. Extreme $^3He/^4He$ ratios in northwest Iceland: constraining the common component in mantle plumes. Earth and Planetary Science Letters 173, 53-60.

Hilton, D.R., Thirlwall, M.F., Taylor, R.N., Murton, B.J., and Nichols, A., 2000. Controls on degassing along the Reykjanes Ridge with implications for the helium paradox. Earth and Planetary Science Letters 183, 43-50.

Hilton, D.R., Fischer, T.P., and Marty, B., 2002. Noble gases and volatile recycling at subduction zones, in: D. Porcelli, C.J. Ballentine, R. Wieler (Eds.), Noble Gases in Geochemistry and Cosmochemistry, Rev. Mineral. Geochem., vol. 47, Mineral. Soc. Am.,Washington, DC, 319–370.

Hilton, D.R., Halldórsson, S.A., Barry, P.H., T. Fischer, T.P., de Moor, J.M., Ramirez, C.J., Mangasini, F., and Scarsi, P. (2011). Helium isotopes at Rungwe Volcanic Province, Tanzania, and the origin of East African Plateaux. Geophysical Research Letters 38, L21304.

Hilton, D.R. and Porcelli D., 2014. Noble Gases as Tracers of Mantle Processes. Treatise on Geochemistry, 2nd Edition, Vol. 3. (Turekian KK, Holland HD, Eds.). 327-353., Oxford: Elsevier Science.

Hirschmann, M.M., and Stolper, E.M., 1996. A possible role for garnet pyroxenite in the origin of the “garnet signature” in MORB. Contrib. Mineral. Petrol. 124, 185–208.

Hofmann, A.W., and White, W.M., 1982. Mantle plumes from ancient oceanic crust. Earth Planet. Sci. Lett. 57, 421-436.

Holland, G., and Ballentine, C.J., 2006. Seawater subduction controls the heavy noble gas composition of the mantle. Nature 441, 186-191.

Holloway, J.R., and Jakobsson, S., 1986. Volatile solubilities in magmas: Transport of volatiles from mantles to planet surfaces. Journ. Geophys. Res., 91.B4, D505-D508.

Holloway, J.R., and Blank, J.G., 1994. Application of Experimental Results to C-O-H Species in Natural Melts, in: M. R. Carrol and J. Holloway (Eds.), Volatiles in Magmas. Rev. Mineral. Geochem., vol. 30, Mineral. Soc. Am., Washington, DC, 187–230.

Holmes, A., and Harwood, H.F., 1932. Petrology of the volcanic fields east and southeast of Ruwenzori, Uganda. Q. J. Geol. Soc. Lond. 88, 370–442.

Holmes, A., and Harwood, H.F., 1937. The Volcanic Area of Bufumbira (Part II). Geol. Surv. Uganda Memoir, Kampala. 300 pp.

Honda, M., McDougall, I., Patterson, D.B., Doulgeris, A., and Clague, D.A., 1991. Possible solar noble gas component in hawaiian basalts. Nature 349, 149-151.

Honda, M., and McDougall, I., 1998. Primordial helium and neon in the Earth – a speculation on early degassing. Geophys. Res. Lett. 25(11), 1951–1954.

Hopp, J., Trieloff, M., and Altherr, R., 2004. Ne isotopes in mantle rocks from the Red Sea reveal large scale plume-lithosphere interaction. Earth Planetary Science Letters 219, 61-76.

Hopp, J., Trieloff, M., and Altherr, R., 2007a. Noble gas compositions of the lithospheric mantle below the Chyulu Hills volcanic field, Kenya. Earth Planetary Science Letters 261, 635-64.

Hopp. J., Trieloff, M., Buikin, A.I., Korochantseva, E.V., Schwarz, W.H., Althaus, T., and Altherr, R., 2007b. Heterogeneous mantle argon isotope composition in the subcontinental lithospheric mantle beneath the Red Sea region. Chemical Geology 240, 635-64.

Hopp, J., and Trieloff, M., 2008. Helium deficit in high-^{3}He/^{4}He parent magmas: Predegassing fractionation, not a "helium paradox". Geochem. Geophys. Geosyst. 9, Q03009, doi:10.1029/2007GC001833.

Huang, S., Farkaš, J., and Jacobsen, S.B., 2011. Stable calcium isotopic compositions of Hawaiian shield lavas: evidence for recycling of ancient marine carbonates into the mantle. Geochimica et Cosmochimica Acta 75, 4987–4997.

Iacono-Marziano, G., Paonita, A., Rizzo, A., Scaillet, B., and Gaillard F., 2010. Noble gas solubilities in silicate melts: New experimental results and a comprehensive model of the effects of liquid composition, temperature and pressure. Chemical Geology 279, 36-53.

Ingersoll, R.V., and Suczek C.A., 1979. Petrology and provenance of Neogene sand from Nicobar and Bengal fans, DSDP sites 211 and 21., Journal of Sedimentary Petrology 49, 1217-1228.

Inguaggiato, S., Taran, Y., Grassa, F., Capasso, G., Favara, R., Varley, N., and Faber, E., 2004. Nitrogen isotopes in thermal fluids of a forearc region (Jalisco Block, Mexico): Evidence for heavy nitrogen from continental crust. Geochem. Geophys. Geosyst., 5, Q12003, doi:10.1029/2004GC000767.

Jackson, M.G., Kurz, M.D., and Hart S.R., 2009. Helium and neon isotopes in phenocrysts from Samoan lavas: Evidence for heterogeneity in the terrestrial high ^{3}He/^{4}He mantle. Earth Planet. Sci. Lett. 287, 519–528.

Jackson, M.G. et al., 2010. Evidence for the survival of the oldest terrestrial mantle reservoir. Nature 466, 853-856.

Jackson, C.R.M., Parman, S.W., Kelley, S.P., and Cooper, R.F., 2013. Noble gas partitioning at the conditions of spinel-peridotite melting. Earth Planetary Science Letters 348, 178-187.

Jackson, C.R.M., Parman, S.W., Kelley, S.P. and Cooper, R.F., 2013. Noble gas transport into the mantle facilitated by high solubility in amphibole. Nature Geoscience 6, 562-565.

Jacob, D.E., 2004. Nature and origin of eclogite xenoliths from kimberlites. Lithos 77, 295-316.

Jakobsson, S.P., and Gudmundsson, M.T., 2008. Subglacial and intraglacial volcanic formations in Iceland. Jökull 58, 179-197.

Jambon, A., Weber, H., and Braun, O., 1986. Solubility of He, Ne, Ar, Kr and Xe in a basalt melting in the range 1250-1600°C. Geochemical Implications, Geochimica Cosmochimica Acta 50, 401-408.

Jambon, A., 1994. Earth degassing and large-scale geochemical cycling of volatile elements. In Volatiles in magmas, editors M. R. Carroll, and J. R. Holloway, volume 30 of Rev. Mineral. Geochem., 479–517. Mineral. Soc. Am., Washington, DC.

Javoy, M., Pineau, F., and Iiyama, I., 1978. Experimental determination of the isotopic fractionation between gaseous CO_2 and carbon dissolved in tholeiitic magma; a preliminary study. Cont. Mineral. Petrol. 67, 35–39.

Javoy, M., Pineau, F., and Delorme, H., 1986. Carbon and nitrogen isotopes in the mantle. Chem. Geol. 57, 41–62.

Javoy, M., Pineau, F., 1991. The volatile record of a popping rock from the Mid-Atlantic Ridge at 14°N: Chemical and isotopic composition of gases trapped in the vesicles. Earth Planet. Sci. Lett. 107, 598–611.

Javoy, M., 1995. The integral Enstatite Chondrite model of the Earth. Geophys. Res. Lett. 22, 2219-2222.

Javoy, M., 1997. The major volatile elements of the Earth: their origin, behavior, and fate. Geophys. Res. Lett. 24, 177–180.

Javoy, M., 1998. The birth of the Earth’s atmosphere: the behaviour and fate of its major elements. Chem Geol 147, 11–25.

Jochum, K.P., Hofmann, A.W., Ito, E., Seufert, H.M., and White, W.M., 1983. K, U and Th in mid-ocean ridge glasses and heat production, K/U and K/Rb in the mantle. Nature 306, 431-436.

Jóhannesson, H., and Sæmundsson, K., 1998. Geological map of Iceland. Bedrock geology, scale 1:500.000. Náttúrufræðistofnun Islands, Reykjavík (2nd edition).

Kaeser, B., 2006. Mantle xenoliths from theMarsabit volcanic field: a case study on the evolution of the lithospheric mantle in a continental rift environment. Ph.D. thesis, University of Neuchatel, 207 pp.

Kaeser, B., Kalt, A., and Pettke, T., 2006. Evolution of the lithospheric mantle beneath the Marsabit volcanic field (northern Kenya): constraints from textural, P-T and geochemical studies on xenoliths. J. Petrol. 47, 2149–2184.

Kaeser, B., Kalt, A., and Pettke, T., 2007a. Crystallisation and breakdown of metasomatic phases in graphite-bearing peridotite xenoliths from Marsabit (Kenya). J. Petrol. 48, 1725–1760

Kaeser. B., Kalt, A., and Ludwig, T., 2007b. Li, Be, and B abundances in minerals of peridotite xenoliths from Marsabit (Kenya): Disequilibrium processes and implications for subduction zone signatures. Geochemistry Geophysics Geosystems, 8, 9, 1-25.

Kaeser, B., Olker, B., Kalt, A., Altherr, R., and Pettke, T., 2009. Pyroxenite xenoliths from Marsabit (Northern Kenya): evidence for different magmatic events in the lithospheric mantle and interaction between peridotite and pyroxenite. Contrib Mineral Petrol 157, 453–472.

Kampunzu, A.B., and Mohr, P., 1991. Magmatic evolution and petrogenesis in the East African Rift system. In: Kampunzu, A.B., Lubala, R.T. (Eds.), Magmatism in Extensional Structural Settings: the Phanerozoic African Plate. Springer, Berlin, pp. 85–136.

Kampunza, A.B., and Lubala, R.T., (Eds.) 1991. Magmatism in Extensional Structural Settings: The Phanerozoic African Plate, 637 pp., Springer, Berlin.

Kempton, P.D., Fitton, J.G., Saunders, A.D., Nowell, G.M., Taylor, R.N., Hardarson, B.S., Pearson, G., 2000. The Iceland plume in space and time: a Sr-Nd-Pb-Hf study of the North Atlantic rifted margin. Earth Planet. Sci. Lett. 177, 255–271.

Kendrick, M.A., Scambelluri, M., Honda, M., Phillips, D., 2011. High abundances of noble gas and chlorine delivered to the mantle by serpentine subduction. Nature Geoscience 4, 807-812.

Kienast, M., 2000. Unchanged nitrogen isotopic composition of organic matter in the South China Sea during the last climatic cycle: global implications, Paleoceanography 15, 244-253.

Kokfelt, T.F., Hoernle, K., Hauff, F., Fiebig, J., Werner, R., and Garbe-Schonberg, D., 2006. Combined trace element and Pb-Nd–Sr-O isotope evidence for recycled oceanic crust (upper and lower) in the Iceland mantle plume. J. Petrol. 47, 1705–1749.

Koornneef, J.M., Davies, G.R., Döpp, S.P., Vukmanovic, Z., Nikogosian, I.K. and Mason, P.R.D., 2009. Nature and timing of multiple metasomatic events in the sub-cratonic lithosphere beneath Labait, Tanzania. Lithos 112, 896-912.

Kopp, H., Flueh, E.R., Petersen, C.J., Weinrebe, W., Wittwer, A., and Meramex Scientists 2006. The Java margin revisited: Evidence for subduction erosion off Java. Earth and Planetary Science Letters 242, 130-142.

Kulongoski, J.T., and Hilton, D.R., 2011. Applications of groundwater helium. Handbook of environmental isotope geochemistry. (Baskaran, M., Ed.)., Berlin; London: Springer.

Kurz, M.D., Meyer, P.S., and Sigurdsson, H., 1985. Helium isotopic systematics within the neovolcanic zones of Iceland. Earth Planet. Sci. Lett. 74, 291–305.

Kurz, M.D., 1986. Cosmogenic helium in a terrestrial igneous rock. Nature 320, 435-439.

Kurz, M.D., Curtice, J., Fornari, D., Geist, D., and Moreira, M., 2009. Primitive neon from the center of the Galápagos hotspot. Earth and Planetary Science Letters 286, 23-34.

Lang, S.Q., Butterfield, D.A., Lilley, M.D., Johnson, H.P., and Hedges, J.I., 2006. Dissolved organic carbon in ridge-axis and ridge-flank hydrothermal systems. Geochim. Cosmochim. Acta 70, 3830–3842.

Lassiter, J., and Hauri, E.H., 1998. Osmium-isotope variations in Hawaiian lavas: evidence for recycled oceanic lithosphere in the Hawaiian plume. Earth Plan Sci Lett 164, 483–496.

Lee, C.-T., Rudnick, R.L., McDonough, W.F. and Horn, I., 2000. Petrologic and geochemical investigation of carbonates in peridotite xenoliths from northeastern Tanzania. Contributions to Mineralogy and Petrology 139, 470-484.

Lee, J.Y., Marti, K., Severinghaus, J.P., Kawamura, K., Yoo, H.S., Lee, J.B., and Kim, J.S., 2006. A redetermination of the isotopic abundances of atmospheric Ar. Geochim. Cosmochim. Acta 70, 4507–4512.

Li, L., and Bebout, G.E., 2005. Carbon and nitrogen geochemistry of sediments in the Central American convergent margin: Insights regarding subduction input fluxes, diagenesis and paleoproductivity, J. Geophys. Res., 110, B11202, doi:10.1029/2004JB003276.

Li, L., Bebout, G.E., and Idleman, B.D., 2007. Nitrogen concentration and δ^{15}N of altered oceanic crust obtained on ODP Legs 129 and 185: insights into alteration-related nitrogen enrichment and the nitrogen subduction budget. Geochimica et Cosmochimica Acta 71, 2344–2360.

Li, L., Cartigny, P., and Ader, M., 2009. Kinetic nitrogen isotope fractionation associated with thermal decomposition of NH_3: Experimental results and potential implications to natural-gas and hydrothermal systems. Geochim. Cosmochim. Acta 73, 6282-6297.

Li, Y., Wiedenbeck, M., Shcheka, S., and Keppler, H., 2013. Nitrogen solubility in upper mantle minerals. Earth Planet Sci Lett 377-378, 311-323.

Li, Y., and Keppler, H., 2014. Nitrogen speciation in mantle and crustal fluids. Geochimica et Cosmochimica Acta 129, 13-32.

Libourel, G., Marty, B., and Humbert, F., 2003. Nitrogen solubility in basaltic melt. Part I. Effect of oxygen fugacity. Geochim. Cosmochim. Acta 67, 4123–4135.

Licciardi, J.M., Kurz, M.D., and Curtice, J.M., 2007. Glacial and volcanic history of Icelandic table mountains from cosmogenic ^{3}He exposure ages. Quaternary Science Reviews 26, 1529-1546.

Licciardi, J.M., Kurz, M.D., and Curtice, J.M., 2006. Cosmogenic ^{3}He production rates from Holocene lava flows in Iceland. Earth and Planetary Science Letters 246, 251–264.

Lithgow-Bertelloni, C., and Silver, P.G., 1999. Dynamic topography, plate driving forces and the African Superswell. Nature 395, 269–272.

Lloyd, F.E., 1981. Upper-mantle metasomatism beneath a continental rift: clinopyroxenes in alkali mafic lavas and nodules from South West Uganda. Mineralogical Magazine 44, 315-23.

Lloyd, F.E., Arima, M., and Edgar, A.D., 1985. Partial melting of a phlogopite–clinopyroxinite nodule from south-west Uganda: an experimental study bearing on the origin of highly potassic continental rift volcanics. Contributions to Mineralogy and Petrology 91, 321–329.

Lloyd, F.E., 1987. Characterisation of mantle metasomatic fluids in spinel lherzolites and alkali clinopyroxenites from West Eifel and south west Uganda. In Menzies M. & Hawkesworth C. J. eds, Mantle Metasomatism, pp. 91-124. Academic Press, New York.

Lloyd, F.E., Nixon, P.H., Hornung, G., and Condliffe, E., 1987. Regional K-metasomatism in the mantle beneath the west branch of the East African rift: alkali clinopyroxenite xenoliths in highly potassic magmas. In: Nixon, P.H. (Ed.), Mantel Xenoliths. Wiley, Lond., pp. 641–659.

Lloyd, F.E., Huntingdon, A.T., Davies, G.R., and Nixon, P.H., 1991. Phanerozoic volcanism of southwest Uganda: a case for regional K and LILE enrichment of the lithosphere beneath a domed and rifted continental plate. In: Magmatism in Extensional Structural Settings. The Phanerozoic African Plate (Edited by Kampunzu, A. B. And Lubala, R. T.) 23-72. Springer-Verlag, Heidelberg.

Lorand, J.P., Reisberg, L., and Bedini, R.M., 2003. Platinum-group elements and melt percolation processes in Sidamo spinel peridotite xenoliths, Ethiopia, East African Rift. Chem Geol 196, 57–75.

Lupton, J.E., and Craig, H., 1975. Excess ^{3}He in oceanic basalts: evidence for terrestrial primordial helium. Earth and Planetary Science Letters 26, 133-139.

Lupton, J.E. and Evans, L., 2004. The atmospheric helium isotope ratio: is it changing? Geophysical Research Letters. 31(13).

Lupton, J.E. and Evans, L., 2013. Changes in the atmospheric helium isotope ratio over the past 40 years. Geophysical Research Letters. 40(23).

Luth, R.W., 2003. Mantle volatiles: distribution and consequences. In: Holland, H. D. & Turekian, K. K. (eds), Treatise on Geochemistry. Amsterdam: Elsevier, pp. 319-361.

Lux, G., 1987. The behavior of noble gases in silicate liquids: Solution, diffusion, bubbles and surface effects, with applications to natural samples, Geochim. Cosmochim. Acta 51, 1549-1560.

Maclennan, J., McKenzie, D.P., and Grönvold, K., 2001. Plume-driven upwelling under central Iceland. Earth and Planetary Science Letters 194, 67-82.

Macpherson, C.G., Hilton, D.R., Sinton, J.M., Poreda, R.J., and Craig, H., 1998. High 3He/4He ratios in the Manus backarc basin: Implications for mantle mixing and the origin of plumes in the western Pacific Ocean. Geology 26, 1007–1010.

Macpherson, C.G., Hilton, D.R., Newman, S., and Mattey, D.P., 1999. CO_2, $^{13}C/^{12}C$ and H_2O variability in natural basaltic glasses: A study comparing stepped heating and FTIR spectroscopic techniques. Geochim. Cosmochim. Acta 63, 1805–1813.

Macpherson, C.G., Hilton, D.R., Mattey, D.P., and Sinton, J.M., 2000. Evidence for an ^{18}O-depleted mantle plume from contrasting $^{18}O/^{16}O$ ratios of back-arc lavas from the Manus Basin and Mariana Trough. Earth Planet. Sci. Lett. 176, 171–183.

Macpherson, C.G., Hilton, DR., Day, J.M.D., Lowry, D., and Grönvold, K., 2005. High $^3He/^4He$, depleted mantle and low-$\delta^{18}O$, recycled oceanic lithosphere in the source of central Iceland magmatism. Earth. Plan. Sci. Lett. 233, 411–427.

Macpherson, C.G., Hilton, D.R., and Hammerschmidt, K., 2010. No slab-derived CO_2 in Mariana Trough back-arc basalts: implications for carbon subduction and for temporary storage of CO_2 beneath slow spreading ridges. Geochem. Geophys. Geosyst. 11, Q11007, doi:10.1029/2010GC003293.

Magna, T., Wiechert, U., Stuart, F.M., Halliday, A.N., and Harrison, D., 2011. Combined Li–He isotopes in Iceland and Jan Mayen basalts and constraints on the nature of the North Atlantic mantle. Geochimica et Cosmochimica Acta 75, 922-936.

Mao, Z., Armentrout, M., Rainey, E., Manning, C.E., Dera, P., Prakapenka, V.B., Kavner, A., 2011. Dolomite III: A new candidate lower mantle carbonate. Geophys. Res. Lett. 38, L22303, doi:10.1029/2011GL049519,.

Marty, B., Zashu, S., and Ozima, M., 1983. Two noble gas components in a Mid-Atlantic Ridge basalt. Nature 302, 238–240.

Marty, B., Gunnlaugsson, E., Jambon, A., Oskarsson, N., Ozima, M., Pineau, F., and Torssander, P., 1991. Gas geochemistry of geothermal fluids, the Hengill Area, southwest rift zone of Iceland. Chem. Geol. 91, 207–225.

Marty, B., and Jambon, A., 1987. $C/^3He$ in volatile fluxes from the solid Earth: implication for carbon geodynamics. Earth Planet. Sci. Lett., 83, 16–26.

Marty, B., Jambon, A., and Sano, Y., 1989. Helium isotopes and CO_2 in volcanic gases of Japan. Chem. Geol. 76, 25–40.

Marty, B., Appora, I., Barrat, J.A., Deniel, C., Vellutini, P., and Vidal, P., 1993. He, Ar, Sr, Nd and Pb isotopes in volcanic rocks from Afar: evidence for a primitive mantle component and constraints on magmatic sources. Geochemical Journal 27, 219–228.

Marty, B., 1995. Nitrogen content of the mantle inferred from N_2–Ar correlation in oceanic basalts. Nature 377, 326–329.

Marty, B., Pik, R., and Gezahegn, Y., 1996. Helium isotopic variations in Ethiopian plume lavas: Nature of magmatic sources and limit on lower mantle contribution. Earth Planetary Science Letters 144, 223–237.

Marty, B., and Humbert, F., 1997. Nitrogen and argon isotopes in oceanic basalts, Earth Planet. Sci. Lett. 152, 101-112.

Marty, B., and Zimmermann, L., 1999. Volatiles (He, C, N, Ar) in mid-ocean ridge basalts: assessment of shallow-level fractionation and characterization of source composition. Geochim. Cosmochim. Acta 63, 3619–3633.

Marty, B., and Dauphas, N., 2003a. The nitrogen record of crust-mantle interaction and mantle convestion from Archean to Present. Earth Planet. Sci. Let. 206, 397-410.

Marty, B., and Dauphas, N., 2003b. “Nitrogen isotopic compositions of the present mantle and the Archean biosphere”: Reply to comment by Pierre Cartigny and Magali Ader. Earth and Planetary Science Letters, 216, 433–439.

Marty, B., 2012. The origins and concentrations of water, carbon, nitrogen and noble gases on Earth. Earth Planet. Sci. Lett. 313-314, 56-66.

Martinez, I., et al., 1998. Experimental investigation of silicate-carbonate system at high pressure and high temperature. J. Geophys. Res., 103, 5143– 5163.

Matsuda, J.I., and Marty, B., 1995. The $^{40}Ar/^{36}Ar$ ratio of the undepleted mantle; A reevaluation. Geophys. Res. Lett. 22, 1937–1940.

Matsuo, S., Susuki, M., and Mizutani, Y., 1978. Nitrogen to argon ratio in volcanic gases. in Terrestrial Rare Gases (eds. E.C. Alexander & M. Ozima) center for Academic Publishing Japan, Tokyo, pp. 17- 25.

Matsumoto, T., Honda, M., McDougall, I., and O'Reilly, S.Y., 1998. Noble gases in anhydrous lherzolites from the Newer Volcanics, southeastern Australia: a MORB-like reservoir in the subcontinental mantle. Geochim. Cosmochim. Acta 62, 2521–2533.

Matsumoto, T., Honda, M., McDougall, I., O'Reilly, S.Y., Norman, M., and Yaxley, G., 2000. Noble gases in pyroxenites and metasomatised peridotites from the Newer Volcanics, southeastern Australia: implications for mantle metasomatism. Chem. Geol. 168, 49–73.

Matsumoto, T., Pinti, D.L., Matsuda, J., and Uminjo, S., 2002. Recycled noble gas and nitrogen in the subcontinental lithospheric mantle: implications from N–He–Ar in fluid inclusions of SE Australian xenoliths. Geochem. J. 36, 209–217.

Matsumoto, T., Morishita, T., Matsuda, J., Fujioka, T., Takebe, M., Yamamoto, K., Arai, S., 2005. Noble gases in the Finero phlogopite-peridotites, western Italian Alps. Earth Planet. Sci. Lett. 238, 130–145.

Mattey, D.P., Exley, R.A., Pillinger, C.T., Menzies, M.A., Porcelli, D.R., Galer, S., and O'Nions, R.K., 1989. Relationships between C, He, Sr and Nd isotopes in mantle diopsides. Spec. Publ. - Geol. Soc. Aust. 4 (2), 913–921.

Mattey, D.P., 1991. Carbon dioxide solubility and carbon isotope fractionation in basaltic melt. Geochim. Cosmochim. Acta. 55, 3467–3473.

Mattey, D.P., Lowry, D., and Macpherson, C.G., 1994. Oxygen isotope composition of mantle peridotite. Earth Planet. Sci. Lett. 128, 231–241.

McGregor, I.D., and Manton, S.R., 1986. Roberts Victor eclogites: ancient oceanic crust. J. Geophys. Res. 91, 14063–14079.

McCaffrey, R., 2009. The tectonic framework of the Sumatran Subduction Zone Annual Reviews of Earth and Planetary Sciences 37, 345-366.

McKenzie, D., Stracke, A., Blichert-Toft, J., Albarede, F., Grönvold, K., and O'Nions, R.K., 2004. Source enrichment processes responsible for isotopic anomalies in oceanic island basalts. Geochimica et Cosmochimica Acta 68, 2699–2724.

Medynski, S., et al., 2013. Controls on magmatic cycles and development of rift topography of the Manda Hararo segment (Afar, Ethiopia): Insights from cosmogenic ^{3}He investigation of landscape evolution. Earth and Planetary Science Letters 367, 133–145.

Meert, J.G., 2003. A synopsis of events related to the assembly of eastern Gondwana. Tectonophysics 362, 1–40.

Mehegan, J., Robinson, J., and Delaney, J., 1982. Secondary mineralization and hydrothermal alteration in the Reydarfjordur Drill Core, East Iceland, J. Geophys. Res., 87, 6511 – 6524.

Menzies, M.A., and Hawkesworth, C.J., 1987. Mantle Metasomatism. NewYork: Academic Press.

Meshesha, D., Shinjo, R., Matsumura, R., and Chekol, T., 2011. Metasomatized lithospheric mantle beneath Turkana depression in southern Ethiopia (the East Africa Rift): geochemical and Sr–Nd–Pb isotopic characteristics. Contrib Mineral Petrol 162, 5, 889-907.

Mitchell, E.C., Fischer, T.P., Hilton, D.R., Hauri, E.H., Shaw, A.M., de Moor, J. M., Sharp, Z.D., and Kazahaya, K., 2010. Nitrogen sources and recycling at subduction zones: Insights from the Izu-Bonin-Mariana Arc. Geochem. Geophys. Geosyst., 11, Q02X11, doi:10.1029/2009GC002783.

Miyazaki, A., Hiyagon, H., Siugiura, N., Hirose, K., and Takahashi, E., 2004. Solubilities of nitrogen and noble gases in silicate melts under various oxygen fugacities: implications for the origin and degassing history of nitrogen and noble gases in the earth, Geochemica Cosmochimica Acta 68, 387-401.

Mohapatra, R.K., and Murty, S.V.S., 2000. Search for the mantle nitrogen in the ultramafic xenoliths from San Carlos, Arizona. Chem. Geol. 164, 305–320.

Mohapatra, R.K., and Murty, S.V.S., 2002. Nitrogen and noble gas isotopes in mafic and ultramafic inclusions in the alkali basalts from Kutch and Reunion—implications for their mantle sources. J. Asian Earth Sci. 20, 867–877.

Mohapatra, R.K., and Murty, S.V.S., 2004. Nitrogen isotopic composition of the MORB mantle: A reevaluation, Geochem. Geophys. Geosyst., 5, Q01001, doi:10.1029/2003GC000612.

Mohapatra, R.K., Harrison, D., Ott, U., Gilmour, J.D., and Trieloff, M., 2009. Noble gas and nitrogen isotope components in Ocean Island Basalts. Chem. Geol. 266, 29–37.

Montagner, J.P., Marty, B., Stutzmann, E., Sicilia, D., Cara, M., Pik, R., Lévêque, J-J., Roult, G., Beucler, E., and Debayle, E., 2007. Mantle upwellings and convective instabilities revealed by seismic tomography and helium isotope geochemistry beneath eastern Africa. Geophysical Research Letters, 34, L21303.

Moore, G.F., and Curray, J.R., 1980. Structure of the Sunda Trench lower slope west of Sumatra from multichannel seismic reflection data: Marine Geophys. Res. 4, 319-340.

Moore, G.F., Curray, J.R., Moore, D.G., and Karig, D.E., 1980. Variations in deformation along the Sunda forearc, northeast Indian Ocean: in: Hayes, D.E., ed., Geophys. Monograph The Tectonic and Geologic Evolution of Southeast Asian Seas and Islands, Geoph. Mon., vol. 23, 145-160.

Moreira, M., Staudacher, T., Sarda, P., Schilling, J.-G., and Allègre, C.J., 1995. A primitive plume neon component in MORB: The Shona ridge-anomaly, South Atlantic (51-52°S), Earth Planetary Science Letters 133, 367-377.

Moreira, M., Valbracht, P., Staudacher, T., and Allègre C.J., 1996. Rare gas systematics in Red Sea Ridge Basalts. Geoph. Res. Lett. 23, 2453-2456.

Moreira, M., Kunz, J., and Allègre, C.J., 1998. Rare gas systematics on popping rock: estimates of isotopic and elemental compositions in the upper mantle. Science 279, 1178-1181.

Moreira, M., and Sarda, P., 2000. Noble gas constraints on degassing processes. Earth Planet. Sci. Lett. 176, 375– 386.

Moreira, M., Breddam, K., Curtice, J., and Kurz, M.D., 2001. Solar neon in the Icelandic mantle: evidence for an undegassed lower mantle. Earth Planetary Science Letters 185, 15-23.

Moreira, M., and Allègre, C.J., 2002. Rare gas systematics on Mid Atlantic Ridge (37°-40°). Earth Planetary Science Letters 198, 401-416.

Moreira, M., 2013. Noble gas constraints on the origin and evolution of Earth's volatiles. Geochemical Perspectvies 2 (2), 229-230.

Morris, J.D., Leeman, W.P., and Tera, F., 1990. The subducted component in island arc lavas: constraints from Be isotopes and B-Be systematics. Nature 344, 31-36.

Muehlenbachs, K., Anderson, A.T., and Sigvaldason, G.E., 1974. Low-O^{18} basalts from Iceland. Geochim. Cosmochim. Acta 38, 577–588.

Muehlenbachs, K., 1986. Alteration of the oceanic crust and ^{18}O history of seawater. In Stable Isotopes in high temperature geological processes (eds. J.W. Valley, H.P. Taylor Jr., J.R. ONeil). Reviews in Mineralogy 16, Washington DC, pp 425–444.

Mukhopadhyay, S., 2012. Early differentiation and volatile accretion recorded in deep-mantle neon and xenon. Nature 486, 101-104.

Mysen, B.O., Yamashita, S., and Chertkova, N., 2008. Solubility and Solution Mechanisms of NOH Volatiles in Silicate Melts at high Pressure and Temperature--Amine Groups and Hydrogen Fugacity. Amer. Mineral. 93, 1760-1770.

Mysen, B.O., and Fogel, M.L., 2010. Nitrogen and Hydrogen Isotope Compositions and Solubility in Silicate Melts in Equilibrium with Reduced (N+H)-bearing Fluids at High Pressure and Temperature: Effects of Melt Structure. Amer. Mineral. 95, 987-999.

Möller, A., Appel, P., Mezger, K. and Schenk, V., 1995. Evidence for a 2Ga subduction zone: eclogites in the Usaragan Belt of Tanzania. Geology 23, 1067–1070.

Möller, A., Mezger, K., and Schenk, V., 1998. Crustal age domains and the evolution of the continental crust in the Mozambique belt of Tanzania: combined Sm-Nd, Rb-Sr and Pb-Pb isotopic evidence. J. Petrol. 39, 749–783.

Möller, A., Mezger, K., and Schenk, V., 2000. U-Pb dating of metamorphic minerals: Pan-African metamorphism and prolonged slow cooling of high pressure granulites in Tanzania, east Africa. Precambrian Res 104, 123–146.

Neal, C.R., Taylor, L.A., Davidson, J.P., Holden, P, Halliday, A.N., Nixon, P.H., Paces, J.B., Clayton, R.N., and Mayeda, T.K., 1990. Eclogites with oceanic crustal and mantle signatures from the Bellsbank kimberlite, South Africa, 2. Sr, Nd, and O isotope geochemistry. Earth Plan Sci Lett 99, 362–379.

Nelson, W.R., Furman, T., van Keken, P.E., Shirey, S.B., and Hanan, B.B., 2012. Os-Hf isotopic insight into manlte plume dynamics beneath the East African Rift System, Chemical Geology 320-321, 66-79.

Neuhoff, P.S., Fridriksson, T., Arnórsson, S., and Bird, D.K., 1999. Porosity changes and mineral paragenesis during low-grade metamorphism at Teigarhorn, eastern Iceland. American Journal of Science 299, 467-501.

Neuhoff, P.S., Fridriksson, Th., and Bird, D.K., 2000. Zeolite Parageneses in the North Atlantic Igneous Province: Implications for Geotectonics and Groundwater Quality of Basaltic Crust. International Geology Review, v. 42, p. 15-44. Reprinted in Ernst, W.G., Ed., Frontiers in Geochemistry: Global Inorganic Geochemistry (Konrad Krauskopf Volume 1), Geological Society of America, International Book Series vol. 5, 271-300.

Ni, H., and Keppler, H., 2013. Carbon in silicate melts. Rev Mineral Geochem 75, 251-287.

Ni, S., Tan, E., Gurnis, M., and Helmberger, D., 2002. Sharp sides to the African superplume. Science 296, 1850-1852.

Niedermann, S., Graf, T., and Marti, K., 1993. Mass spectrometric identification of cosmic-ray produced neon in terrestrial rocks with multiple neon components. Earth Planetary Science Letters 118, 65–73.

Nishio, Y., Ishii, T., Gamo, T., Sano, Y., 1999. Volatile element isotopic systematics of the Rodriguez Triple Junction Indian Ocean MORB: implications for mantle heterogeneity, Earth Planet. Sci. Lett. 170, 241-253.

Nixon, P.H. (ed.), 1987. Mantle Xenoliths. XVII 844 pp. Wiley, Chichester.

Nyblade, A.A., and Robinson, S.W., 1994. The African Superswell. Geophys. Res. Lett., 21, 765–768.

Nyblade, A.A., 2011. The upper-mantle low-velocity anomaly beneath Ethiopia, Kenya, and Tanzania: Constraints on the origin of the African superswell in eastern Africa and plate versus plume models of mantle dynamics. The Geological Society of America Special Paper 478, 37-50.

Ongley, J.S., Basu, A.R., and Kyser, T.K., 1987. Oxygen isotopes in coexisting garnets, clinopyroxenes and phlogopites of Roberts Victor eclogites: implications for petrogenesis and mantle metasomatism. Earth and Planetary Science Letters 83, 80–84.

O'Nions, R.K., and Oxburgh, E.R., 1988. Helium volatile fluxes and the development of continental crust. Earth and Planetary Science Letters 90, 331-347.

Orlando, A., Abebe, T., Manetti, P., Santo, A.P., and Corti, G., 2006. Petrology of mantle xenoliths from Megado and Dilo, Kenya Rift, Southern Ethiopian. Ofioliti 31, 71-87.

Ozima, M., and Podosek F.A., 2002. Noble Gas Geochemistry, 2nd ed., Cambridge Univ. Press, New York. 286 pp.

Palot, M., Cartigny, P., Harris, J.W., Kaminsky, F.V., Stachel, T., 2012. Evidence for deep mantle convection and primordial heterogeneity from nitrogen and carbon stable isotopes in diamond. Earth and Planetary Science Letters 357–358, 179–193.

Parman, S.W., Kurz, M.D., Hart, S.R., and Grove T.L., 2005. Helium solubility in olivine and implications for high ^{3}He/^{4}He in ocean island basalts. Nature 437, 1140-1143.

Pearson, D.G., Davies, G.R., Nixon, P.H., Greenwood, P.B., and Mattey, D.P., 1991. Oxygen isotope evidence for the origin of pyroxenites in the Beni Bousera peridotite massif N. Morocco: derivation from subducted oceanic lithosphere. Earth Planet. Sci. Lett. 102, 289–301.

Pearson, D.G., Canil, D., and Shirey, S.B., 2003. Mantle samples included in volcanic rocks: xenoliths and diamonds. In: Carlson, R.W. (ed.) Treatise on Geochemistry, Volume 2-The Mantle and Core. Amsterdam: Elsevier Pergamon, pp. 171-275.

Peate, D.W., Breddam, K., Baker, J.A., Kurz, M.D., Barker, A.K., Prestvik, T., Grassineau, N., Skovgaard, A.C., 2010. Compositional characteristics and spatial distribution of enriched Icelandic mantle components. J. Petrol. 51, 1447–1475.

Perkins, G.B., Sharp, Z.D., Selverstone, J., 2006. Oxygen isotope evidence for subduction and rift-related mantle metasomatism beneath the Colorado Plateau–Rio Grande rift transition. Contrib. Mineral. Petrol. 151, 633–650.

Peters, K.E., Sweeny, R.E., Kaplan, I.R., 1978. Correlation of carbon and nitrogen stable isotope ratios in sedimentary organic matter. Limnol. Ocean, 23, 598-604.

Pik, R., Marty, B., and Hilton, D.R., 2006. How many mantle plumes in Africa? The geochemical point of view. Chemical Geology 226, 100–114.

Pinti, D.L., Hashizume, K., Matsuda, J.I., 2001. Nitrogen and argon signatures in 3.8 to 2.8 Ga metasediments: Clues on the chemical state of the Archean ocean and the deep biosphere. Geochim. Cosmochim. Acta 65, 2301-2316.

Pinti, D.L., Hashizume, K., Orberger, B., Gallien, J.-P., Cloquet, C., and Massault, M., 2007. Biogenic nitrogen and carbon in Fe– Mn-oxyhydroxides from an Archan chert, Marble Bar, Western Australia. Geochem. Geophys. Geosyst. 8, Q02007.

Pinti, D.L., and Hashizume, K., 2010. Early life recorded by nitrogen isotopes. In: Golding, S., Glikson, M. (Eds.), Earliest Life on Earth: Habitats, Environments and Methods of Detection. Springer-Verlag, The Netherlands, pp. 183–205.

Porcelli, D., O'Nions, R.K., and O'Reilly, S.Y., 1986. Helium and strontium isotopes in ultramafic xenoliths. Chem. Geol. 54, 237-249.

Porcelli, D.R., O’Nions, R.K., Galer, S.J.G., Cohen, A.S., and Mattey,D.P., 1992. Isotopic relationships of volatile and lithophile trace elements in continental ultramafic xenoliths. Contrib. Mineral. Petrol. 110, 528– 538.

Porcelli, D., and Wasserburg G.J., 1995. Mass transfer of helium, neon, argon, and xenon through a steady state upper mantle. Geochimica Cosmochimica Acta 59, 4921-4937.

Porcelli, D. and Halliday, A.N., 2001. The core as a possible source of mantle helium. Earth Planet. Sci. Lett. 192, 45-56.

Porcelli, D., and Ballentine, C.J., 2002. Models for the distribution of terrestrial noble gases and evolution of the atmosphere. Rev. Mineral. Geochem., 47, 411– 480.

Poreda, R.J., Jenden, P.D., Kaplan, I.R., and Craig, H., 1986. Mantle helium in Sacramento basin natural gas wells. Geochimica et cosmochimica Acta 50, 2847–2853.

Poreda, R.J., Jeffrey, A.W.A., Kaplan, I.R., and Craig, H., 1988. Magmatic helium in subduction zone natural gases. Chemical Geology 71, 199-210.

Poreda, R.J, Shilling, J.G., and Craig, H., 1986. Helium and hydrogen isotopes in ocean-ridge basalts north and south of Iceland. Earth Planet. Sci. Lett. 78, 1-17.

Poreda, R.J, and Craig, H., 1989. Helium isotope ratios in circum-Pacific volcanic arcs. Nature 338, 473-478.

Raquin, A., and Moreira, M., 2009. Atmospheric $^{38}Ar/^{36}Ar$ in the mantle: implications for the nature of the terrestrial parent bodies. Earth Planetary Science Letters 287, 551-558.

Ray, M.C., Hilton, D.R., Munoz, J., Fischer, T.P. and Shaw, A.M., 2009. The effects of volatile recycling, degassing and crustal contamination on the helium and carbon geochemistry of hydrothermal fluids from the Southern Volcanic Zone of Chile. Chemical Geology 266, 38-49.

Reisberg, L., Lorand, J.P., and Bedini, R.M., 2004. Reliability of Os model ages in pervasively metasomatized continental mantle lithosphere: a case study of Sidamo spinel peridotite xenoliths (East African Rift, Ethiopia). Chem Geol 208, 119-140.

Richet, P., Bottinga, Y., and Javoy, M., 1977. A review of hydrogen, carbon, nitrogen, oxygen, sulphur and chlorine stable isotope fractionation among gaseous molecules. Annu. Rev. Earth Planet. Sci. 82, 269-279.

Ritsema, J., van Heijst, H.J., and Woodhouse, J.H., 1999. Complex shear wave velocity structure imaged beneath Africa and Iceland. Science 286, 1925-1928.

Roger, S., Dautria, J.M., Coulon, C., Pik, R., Yirgu, G., Michard, A., Legros, P., and Ayalew, D., 1999. An insight on the nature, composition and evolution of the lithospheric mantle beneath in the north-western Ethiopian plateau: the ultrabasic xenoliths from the Tana Lake Province. In: Boccaletti, M., Peccerillo, A., (eds) The Ethiopian rift system, Acta Vulcanol 11, 161–168.

Rogers, N.W., De Mulder, M., and Hawkesworth, C.J., 1992. An enriched mantle source for potassic basanites - evidence from Karisimbi volcano, Virunga volcanic province, Rwanda. Contrib. Mineral. Petrol. 11, 543-556.

Rogers, N.W., James, D., Kelley, S.P., and De Mulder, M., 1998. The generation of potassic lavas from the eastern Virunga province, Rwanda. J. Petrol. 39, 1223-1247.

Rogers, N.W., McDonald, R., Fitton, J.G., George, R., Smith, M., and Barreeiro, B., 2000. Two mantle plumes plumes beneath the East African rift system: Sr, Nd and Pb isotope evidence from Kenya Rift basalts. Earth Planet. Sci. Lett. 176, 387-400.

Rogers, N.W., 2006. Basaltic magmatism and the geodynamics of the East African Rift. Geological Society Special Publication 259, 77–93.

Rogers, N.W., Davies, M.K., Parkinson, I.J., and Yirgu, G., 2010. Osmium isotopes and Fe/Mn ratios in Ti-rich picritic basalts from the Ethiopian flood basalt province: no evidence for core contribution to the Afar plume. Earth and Planetary Science Letters 296, 413–422.

Rooney, T.O., Herzberg, C. and Bastow, I.D., 2012a. Elevated mantle temperature beneath East Africa. Geology 40, 27-30.

Rooney, T.O., Hanan, B.B., Graham, D.W., Furman, T., Blichert-Toft, J., and Schilling, J.-G., 2012b. Upper mantle pollution during Afar plume–continental rift interaction. Journal of Petrology 53, 365-389.

Rosenthal, A., Foley, S.F., Pearson, D.G., Nowell, B.M., and Tappe, S., 2009. Petrogenesis of strongly alkaline primitive volcanic rocks at the propagating tip of the western branch of the East African Rift. Earth and Planetary Science Letters 284, 236-248.

Roskosz, M., Mysen, B.O., and Cody, G.D., 2006. Dual speciation of nitrogen in silicate melts at high pressure and temperature: An experimental study. Geochim. Cosmochim. Acta 70, 2902-2918.

Roskosz, M., Bouhifd, M.A., Jephcoat, A.P., Marty, B. and Mysen, B.O., 2013. Nitrogen solubility in molten metal and silicate at high pressure and temperature. Geochim. Cosmochim. Acta 121, 15-28.

Roulleau, E., Pinti, D.L., Stevenson, R.K., Takahata, N., Sano, Y., and Pitre, F., 2012. N, Ar and Pb isotopic co-variations in magmatic minerals: Discriminating fractionation processes from magmatic sources in Monteregian Hills, Québec, Canada. Chem. Geol. 326-327, 123-131.

Rudnick, R.L., McDonough, W.F., and Chappell B.W., 1993. Carbonatite metasomatism in the Northen Tanzanian mantle: petrographic and geochemical characteristics. Earth. Planet. Sci. Lett. 114, 463–475.

Rudnick, R.L., McDonough, W.F., and Orpin, A., 1994. Northern Tanzanian peridotite xenoliths: a comparison with Kaapvaal peridotites and inferences on metasomatic interactions, in Proceedings of the 5th International Kimberlite Conference, edited by H.O.A. Meyer and O. Leonardos, pp. 336–353, Companhia de Pesquisa de Recursos Minerais, Rio de Janeiro.

Saal, A.E., Hauri, E.H., Langmuir, C.H., and Perfit, M.R., 2002. Vapour undersaturation in primitive mid-ocean-ridge basalt and the volatile content of Earth’s upper mantle. Nature 419, 451-455.

Sadofsky S.J., and Bebout G. E., 2004. Nitrogen geochemistry of subducting sediments: new results from the Izu Bonin-Mariana margin and insights regarding global nitrogen subduction. Geochem. Geophys. Geosyst. 5, Q03l15. doi:10.1029/ 2003GC000543.

Sakai, H., Des Marais, D.J., Ueda, A., and Moore, J.G., 1984. Concentrations and isotope ratios of carbon, nitrogen and sulfur in ocean-floor basalts. Geochim. Cosmochim. Acta 48, 2433- 2441.

Sano, Y., Nakamura, Y., Wakita, H., Urabe, A., and Tominaga, Y., 1984. ^{3}He emission related to volcanic activity. Science 224, 150-151.

Sano, Y., and Marty, B., 1995. Origin of carbon in fumarolic gas fromisland arcs, Chem.Geol. 119, 265-274.

Sano, Y., and Williams, S. N., 1996. Fluxes of mantle and subducted carbon along convergent plate boundaries, Geophys. Res. Lett. 23, 2749–2752.

Sano, Y., Takahata, N., Nishio, Y., and Marty, B., 1998. Nitrogen recycling in subduction zones, Geophys. Res. Lett. 25, 2289–2292.

Sano, Y., Furukawa, Y., and Takahata, N., 2010. Atmospheric helium isotope ratio: Possible temporal and spatial variations. Geochimica et Cosmochimica Acta 74, 4893-4901.

Sarda, P., Staudacher, T., and Allègre, C.J., 1988. Neon isotopes in submarine basalts. Earth Planet. Sci. Lett. 91, 73-88.

Sarda, P., and Graham, D., 1990. Mid-ocean ridge popping rocks: implications for degassing at ridge crests. Earth Planet. Sci. Lett. 97, 268-289.

Sarda, P., and Moreira, M., 2002. Vesiculation and vesicle loss in mid-ocean ridge basalt glasses: He, Ne, Ar elemental fractionation and pressure influence. Geochimica et Cosmochimica Acta 66, 1449-1458.

Scarsi, P., and Craig, H., 1996. Helium isotope ratios in Ethiopian Rift basalts. Earth Planetary Science Letters 144, 505-516.

Scarsi, P., 2000. Fractional extraction of helium by crushing of olivine and clinopyroxene phenocrysts: Effects on the ^{3}He/^{4}He measured ratio. Geochimica Cosmochimica Acta 64, 3751-3762.

Schiano, P., Clocchiatti, R., Shimizu, N., Weis, D. and Mattielli, N., 1994. Cogenetic silica-rich and carbonate-rich melts trapped in mantle minerals in Kerguelen ultramafic xenoliths: Implications for metasomatism in the oceanic upper mantle. Earth and Planetary Science Letters 123, 167-178.

Schilling, J.G., Kingsley, R.H., Hanan, B.B., and Mccully, B.L., 1992. Nd-Sr-Pb isotopic variations along the Gulf of Aden Evidence for Afar mantle plume continental lithosphere interaction. Journal of Geophysical Research: Solid Earth 97(B7), 10927-10966.

Schoell, M., 1988. Multiple origins of methane in the earth. Chem. Geol. 78, 1–10.

Sharp, Z.D., 1990. A laser based microanalytical method for the in situ determination of oxygen isotope ratios of silicates and oxides. Geochim. Cosmochim. Acta 54, 1353-1357.

Sharp, Z.D., 2006. Principles of Stable Isotope Geochemistry. Prentice Hall, 344 pp.

Shaw, A.M., Hilton, D.R., Macpherson, C.G., and Sinton, J.M., 2004. The CO_2-He-Ar-H_2O systematics of the Manus back-arc basin: resolving source composition from degassing and contamination effects. Geochim. Cosmochim. Acta 68, 1837-1856.

Shaw, A.M., Hilton, D.R., Fischer, T.P., Walker, J.A. and De Leeuw, G.A. (2006). Helium isotope variations in mineral separates from Costa Rica and Nicaragua: Assessing crustal contributions, time scale variations and diffusion-related mechanisms. Chemical Geology, 230, 124-139.

Shervais, J.W., Taylor, L.A., Lugmair, G.W., Clayton, R.N., Mayeda, T.K. and Korotev, R.L., 1988. Early proterozoic oceanic crust and the evolution of subcontinental mantle: eclogites and related rocks from southern Africa. Geological Society of America Bulletin 100, 411-423.

Shibata, T., Takahashi, E., and Matsuda J.-I., 1998. Solubility of neon, argon, krypton, and xenon in binary and ternary silicate systems: A new view on noble gas solubility. Geochemica Cosmochimica Acta 62, 1241-1253.

Shilobreeva, S., Martinez, I., Busigny, V., Agrinier, P., and Laverne, C., 2011. Insights into C and H storage in the altered oceanic crust: results from ODP/IODP Hole 1256D. Geochimica et Cosmochimica Acta 75, 2237–2255.

Sieh, K., Natawidjaja, D., 2000. Neotectonics of the Sumatran fault, Indonesia. J. Geophys. Res.105, 28295–326.

Simmons, N.A., Forte, A.M., and Grand, S.P., 2007. Thermochemical structure and dynamics of the African superplume. Geophysical Research Letters 34, doi:10.1029/2006GL028009

Singh, S.C., Hananto, N., Mukti, M., Robinson, D.P., Das, S., Chauhan, A., Carton, H., Gratacos, B., Midnet, S., Djajadihardja, Y., and Harjono, H., 2011. Aseismic zone and earthquake segmentation associated with a deep subducted seamount in Sumatra. Nature Geosci. 4, 308-311.

Skovgaard, A.C., Storey, M., Baker, J.A., Blusztajn, J., and Hart, S.R., 2001. Osmium-oxygen isotopic evidence for a recycled and strongly depleted component in the Iceland mantle plume. Earth and Planetary Science Letters 194, 259-275.

Smithsonian Institution, 2011. Marapi. Bulletin of the Global Volcanism Network, v. 36 no. 7.

Snyder, G., Poreda, R., Fehn, U. and Hunt, A., 2003. Sources of nitrogen and methane in Central American geothermal settings: Noble gas and 129I evidence for crustal and magmatic volatile components. Geochem. Geophys. Geosyst., 4(1), 9001, doi:10.1029/2002GC000363.

Sobolev, A.V., Hofmann, A.W., Sobolev, S.V., and Nikogosian, I.K., 2005. An olivine-free mantle source of Hawaiian shield basalts. Nature 434, 590-597.

Sobolev, A.V., Hoffman, A.W., Kuzmin, D.V., Yaxley, G.M., Arndt, N.T., Chung, S-L., Danyushevsky, L.V.,, Elliot, T., Frey, F.A., Garcia, M.O., Gurenko, A.A., Kamenetsky, V.S., Kerr, A.C., Krivolutskaya, N.A., Matvienkov, V.V., Nikogosian, I.K., Rocholl, A., Sigurdsson, I.A., Sushchevskaya, N.M., & Teklay, M. 2007. The amount of recycled crust in sources of mantle derived melts. Science 316, 412–417.

Sobolev, A.V., Hofmann, A.W., Brügmann, G., Batanova, V.G., and Kuzmin, D.V., 2008. A quantitative link between recycling and osmium isotopes. Science 321, 536.

Sobolev, A.V., Hofmann, A.W., Jochum, K.P., Kuzmin, D.V., and Stoll, B., 2011. A young source for the Hawaiian plume. Nature 476, 434-437.

Soper, N.J., Strachan, R.A., Holdsworth, R.E., Gayer, R.A., and Greiling, R.O., 1992. Sinistral transpression and the Silurian closure of Iapetus. J. Geol. Soc. (Lond.) 149, 871–880.

Spera, F.J., 1984. Carbon dioxide in petrogenesis III: role of volatiles in the ascent of alkaline magma with special reference to xenolith-bearing mafic lavas. Contrib Mineral Petrol 88, 217-232.

Sun, W.D., Bennett, V.C., and Kamenetsky, V.S., 2004. The mechanism of Re enrichment in arc magmas: evidence from Lau Basin basaltic glasses and primitive melt inclusions. Earth Planet. Sci. Lett. 222, 101-114.

Staudacher, T., and Allègre, C.J., 1988. Recycling of oceanic crust and sediments: The noble gas subduction barrier. Earth Planet. Sci. Lett. 89, 173-183.

Staudigel, H., Hart, S.R., Schmincke, H.U., and Smith, B.M., 1989. Cretaceous ocean crust at DSDP sites 417 and 418: carbon uptake from weathering versus loss by magmatic outgassing. Geochim. Cosmochim. Acta 53, 3091–3094.

Stracke, A., Zindler, A., Salters, V.J.M., McKenzie, D., Blichert-Toft, J., Albarede, F. and Grönvold, K., 2003. Theistareykir revisited.Geochemistry, Geophysics, Geosystems 4(2), 8507, doi:10.1029/2001GC000201.

Stuart, F., Turner, G., and Taylor, R., 1994. He–Ar isotope systematics of fluid inclusions; resolving mantle and crustal contributions to hydrothermal fluids. In Noble Gas Geochemistry and Cosmochemistry (ed. J. Matsuda). Terra Scientific Publishing Company, Tokyo, pp. 261 277.

Stuart, F.M., Lass-Evans, S., Fitton, J.G., and Ellam, R.M., 2003. High $^3He/^4He$ ratios in picritic basalts from Baffin Island and the role of a mixed reservoir in mantle plumes. Nature 424, 57-59.

Taran, Y.A., Fischer, T.P., Porovsky, B., Sano, Y., Armienta, M.A., and Macias, J.L., 1998. Geochemistry of the volcano-hydrothermal system of El Chichón volcano, Chiapas, Mexico. Bull. Volcanol. 59, 436-449.

Taran Y.A., and Giggenbach W.F., 2003. Geochemistry of light hydrocarbons in volcanic and hydrothermal fluids. Society of Economic Geologists Special Publication 10, 61–74.

Taylor, Jr., H.P., and Sheppard, S.M.F., 1986. Igneous rocks: I. Processes of isotopic fractionation and isotope systematics. In Stable isotopes in high temperature geological processes, editors H. W. Valley, H. P. Taylor, Jr., and 207 J. R. O'Neil, volume 16 of Rev. Mineral. Geochem., 227–271. Mineral. Soc. Am., Washington, DC.

Tedesco, D., Tassi, F., Vaselli, O., Poreda, R.J., Darrah, T., Cuoco, E., and Yalire, M.M., 2010. Gas isotopic signatures (He, C, and Ar) in the Lake Kivu region (western branch of the East Africa rift system): Geodynamic and volcanological implications, J. Geophys. Res., 115, B01205, doi:10.1029/2008JB006227.

Teklay, M., Scherer, E.E., Mezger, K., and Danyushevsky, L., 2010. Geochemical characteristics and Sr-Nd-Hf isotope compositions of mantle xenoliths and host basalts from Assab, Eritrea: implications for the composition and thermal structure of the lithosphere beneath the Afar Depression. Contrib Mineral Petrol 159, 731–751.

Tera, F., Brown, L., Morris, J., Sacks, I.S., Klein, J., and Middleton, R., 1986. Sediment incorporation in island-arc magmas: inferences from ^{10}Be. Geochim Cosmochim Acta 50, 535-550.

Thirlwall, M.F., 1995. Generation of the Pb isotopic characteristics of the Iceland plume. J. Geol. Soc. 152, 991–996.

Thirlwall, M.F., 1997. Pb isotopic and elemental evidence for OIB derivation from young HIMU mantle. Chemical Geology 139, 51-74.

Thirlwall, M.F., Gee, M.A.M., Taylor, R.N., and Murton, B.J., 2004. Mantle components in Iceland and adjacent ridges investigated using double-spike Pb isotope ratios. Geochim. Cosmochim. Acta 68, 361-386.

Thirlwall, M.F., Gee, M.A.M., Lowry, D., Mattey, D.P., Murton, B.J., and Taylor, R.N., 2006. Low δ^{18}O in the Icelandic mantle and its origins: evidence from Reykjanes Ridge and Icelandic lavas. Geochim. Cosmochim. Acta 70, 993–1019.

Thomas, J.B., Cherniak, D.L., and Waston, E.B., 2008. Lattice diffusion and solubility of argon in forsterite, enstatite, quartz, and corundrum. Chemical Geology 253, 1-22.

Thorseth, I.H., Furnes, H., and Heldal, M., 1992. The importance of microbiological activity in the alteration of natural basaltic glass. Geochim. Cosmochim. Acta 56, 845–850.

Tolstikhin, I.N., and Marty, B., 1998. The evolution of terrestrial volatiles: a view from helium, neon, argon and nitrogen isotope modelling. Chem. Geol. 147, 27–52.

Tucker, J.M., and Mukhopadhyay, S., 2013. Evidence for multiple giant impacts and magma oceans from mantle noble gases. Lunar & Planetary Science Conference, Abs. 2990.

Turner, S., and Foden, J., 2001. U-Th-Ra disequilibria, Sr-Nd-Pb isotope and trace element variations in Sunda arc lavas: predominance of a subducted sediment component. Contributions to Mineralogy and Petrology. 142, 43-57.

Trieloff, M., Kunz, J., Clague, D.A., Harrison, D., and Allègre, C.J., 2000. The nature of pristine noble gases in mantle plumes. Science 288, 1036-1038.

Trieloff, M., and Kunz, J., 2005. Isotope systematics of noble gases in the Earth's mantle: possible sources of primordial isotopes and implications for mantle structure. Phys. Earth Planet. Inter. 148, 13–38.

Trull, T., Nadeau, S., Pineau, F., Polvé, M., and Javoy, M., 1993. C–He systematics in hotspot xenoliths: implications for mantle carbon contents and carbon recycling. Earth Planet. Sci. Lett. 118, 43–64.

Tuffen, H., Owen, J., and Denton, J., 2010. Magma degassing during subglacial eruptions and its use to reconstruct palaeo-ice thicknesses. Earth-Sci Rev. 99, 1–18.

Ulianov, A., Kalt, A., and Pettke, T., 2006. Aluminous websterite and granulite xenoliths from the Chyulu Hills volcanic field, Kenya: gabbro-troctolitic cumulates subjected to lithospheric foundering. Contrib Mineral Petrol 152, 459–483.

Valbracht, P.J., Honda, M., Matsumoto, T., Mattielli, N., McDougall, I., Ragettli, R., and Weis, D., 1996. Helium, neon and argon isotope systematics in Kerguelen ultramafic xenoliths: implications for mantle source signatures. Earth and Planetary Science Letters 138, 29–38.

van Achterbergh, E., Griffin, W.L., Ryan, C., O'Reilly, S.Y., Pearsone, N., Kivi. K., and Doyle. B., 2002. Subduction signature for quenched carbonatites from the deep lithosphere. Geology 30, 743–746.

van Soest, M.C., Hilton, D.R., and Kreulen, R., 1998. Tracing crustal and slab contributions to arc magmatism in the Lesser Antilles island arc using helium and carbon relationships in geothermal fluids. Geochimica et Cosmochimica Acta 62, 3323–3335.

Veizer, J. and Mackenzie, F.T., 2003. Evolution of sedimentary rocks. In: Sediments, Diagenesis and Sedimentary Rocks, In: ed. F. T. Mackenzie, Treatise on Geochemistry, Volume 7-Sediments, Diagenesis and Sedimentary Rocks. Amsterdam: Elsevier Pergamon, pp. 369-407.

Varekamp, J.C., Kreulen, R., Poorter, R.P.E., and van Bergen, M.J., 1992. Carbon sources in arc volcanism with implications for the carbon cycle. Terra Nova 4, 363–373.

Vazquez, J.A., and Reid, M.R., 2004. Probing the accumulation history of the voluminous Toba magma. Science 305, 991-994.

Virrueta, C., 2013. Origin of Methane and Other Hydrocarbons in Magmatic Systems. Report for the Ronald E. McNair Postbaccalaureate Achievement Program, University of California, San Diego, August, 2013.

von Huene, R., and Scholl, D.W., 1991. Observations at convergent margins concerning sediment subduction, subduction erosion, and the growth of continental crust, Rev. Geophys. 29, 279–316.

Walter, M.J., Kohn, S.C., Araujo, D., Bulanova, G.P., Smith, C.B., Gaillou, E., Wang, J., Steele, A. and Shirey, S.B., 2011. Deep mantle cycling of oceanic crust: Evidence from diamonds and their mineral inclusions. Science 334, 54-57.

Watson, E.B., Thomas, J.B., and Cherniak, D.J., 2007. ^{40}Ar retention in the terrestrial planets. Nature 449, 299-304.

Weiss, R.F., 1971. Solubility of Helium and Neon in Water and Seawater. J. Chem. Eng. Data, 16, 235–241.

Welhan, J.A., and Craig, H., 1983. Methane, hydrogen and helium in hydrothermal fluids at 21°N on the East Pacific Rise. In: Hydrothermal Processes at Seafloor Spreading Centers (eds Rona P.A., Bostrom K., Laubier L., Smith K.L.), pp. 391–409. Plenum Press, New York.

Welhan, J.A., 1988. Origins of methane in hydrothermal systems. Chem. Geol. 71, 183–198.

White, W.M., 2010. Oceanic Island Basalts and Mantle Plumes: The Geochemical Perspective. Annual Reviews of Earth & Planetary Sciences 38, 133-160.

Whitford, D.J., 1975. Strontium isotopic studies of the volcanic rocks of the Sunda arc, Indonesia, and their petrogenetic implications. Geochim Cosmochim Acta 39, 1287-1302.

Whitford, D.J., 1981. Neodymium isotopic composition of Quaternary island arc lavas from Indonesia. Geochimica et Cosmochimica Acta 45, 989-995.

Widiyantoro, S., and van der Hilst, R., 1996. Structure and evolution of lithospheric slab beneath the Sunda Arc, Indonesia. Science 271, 1566-1570.

Wolfe, C., Bjarnason, I., VanDecar, J., and Soloman, S., 1997. Seismic structure of the Iceland mantle plume. Nature 385, 245-247.

Wood, B.J., Li, J., and Shahar, A., 2013. Carbon in the core: its influence on the properties of core and mantle. Rev Mineral Geochem 75, 231-250.

Yamamoto, J., Kaneoka, I., Nakai, S., Kagi, H., Prikhodko, V.S., and Arai, S., 2004. Evidence for subduction-related components in the subcontinental mantle from low ^{3}He/^{4}He and ^{40}Ar/^{36}Ar ratio in mantle xenoliths from Far Eastern Russia. Chem. Geol. 207, 237-259.

Yamamoto, J., and Burnard, P., 2005. Solubility controlled noble gas fractionation during magmatic degassing: implications for noble gas compositions of primary melts of OIB and MORB.Geochimica et Cosmochimica Acta 69, 727-734.

Yamamoto, J., Nishimura, K., Sugimoto, T., Takemura, K., Takahata, N., and Sano, Y., 2009. Diffusive fractionation of noble gases in mantle with magma channels: Origin of low He/Ar in mantle-derived rocks. Earth and Planetary Science Letters 280, 167-174.

Yamamoto, J., Otsuka, K., Ohfuji, H., Ishibashi, H., Hirano, N., and Kagi, H., 2011. Retentiveity of CO_2 in fluid inclusions in mantle minerals, European Journal of Mineralogy 23, 805-815.

Yatsevich, I., and Honda, M., 1997. Production of nucleogenic neon in the Earth from natural radioactive decay. Journal of Geophysical Research 102, 10,291-10,298.

Yang, W., Teng, F.-Z., Zhang, H.-F., and Li, S., 2012. Magnesium isotopic systematics of continental basalts from the North China craton: Implications for tracing subducted carbonate in the mantle, Chemical Geology 328, 185-194.

Yirgu, G., Ebinger, C.J., and Maguire, P.K.H., (Eds.) 2006. The structure and evolution of the East African Rift System in the Afar Volcanic Province. Geological Society Special Publication 259, 1–327.

Yokochi, R., and Marty, B., 2004. A determination of the neon isotopic composition of the deep mantle. Earth and Planetary Science Letters 225, 77-88.

Yokochi, R., and Marty, B., 2006. Fast chemical and isotopic exchange of nitrogen during reaction with hot molybdenum, Geochem. Geophys. Geosyst., 7, Q07004, doi:10.1029/ 2006GC001253.

Yokochi, R., Marty, B., Chazot, G., and Burnard, P., 2009. Nitrogen in peridotite xenoliths: Lithophile behavior and magmatic isotope fractionation. Geochim. Cosmochim. Acta 73, 4843–4861.

Zimmer, M.M., Fischer, T.P., Hilton, D.R., Alvarado, G.E., Sharp, Z.D., and Walker, J.A., 2004. Nitrogen systematics and gas fluxes of subduction zones: insights from Costa Rica arc volatiles. Geochem. Geophys. Geosyst. 5, doi:10.1029/2003GC000651.